Enhancement of Ride and Directional Performances of Articulated Vehicles via Optimal Frame Steering and Hydro-Pneumatic Suspension

Yuming Yin

A Thesis
in
The Department
of
Mechanical, Industrial and Aerospace Engineering

Presented in Partial Fulfillment of the Requirements
For the Degree of
Doctor of Philosophy (Mechanical Engineering) at
Concordia University
Montreal, Quebec, Canada

October 2017

CONCORDIA UNIVERSITY
SCHOOL OF GRADUATE STUDIES

This is to certify that the thesis prepared

By: Yuming Yin

Entitled: Enhancement of Ride and Directional Performances of Articulated Vehicles via Optimal Frame Steering and Hydro-Pneumatic Suspension

and submitted in partial fulfillment of the requirements for the degree of

Doctor Of Philosophy (Mechanical Engineering)

complies with the regulations of the University and meets the accepted standards with respect to originality and quality.

Signed by the final examining committee:

Dr. Nizar Bouguila	Chair
Dr. Yuping He	External Examiner
Dr. Ciprian Alecsandru	External to Program
Dr. Rama Bhat	Examiner
Dr. Ramin Sedaghati	Examiner
Dr. Subhash Rakheja	Thesis Supervisor (s)
Dr. Paul-Emile Boileau	

Approved by

Dr. Ali Dolatabadi Chair of Department or Graduate Program Director

November 21, 2017
Date of Defence

Dr. Amir Asif Dean, Faculty of Engineering and Computer Science

ABSTRACT

Enhancement of Ride and Directional Performances of Articulated Vehicles via Optimal Frame Steering and Hydro-Pneumatic Suspension

Yuming Yin, Ph.D.

Concordia University, 2017

Off-road vehicles employed in agriculture, construction, forestry and mining sectors are known to exhibit comprehensive levels of terrain-induced ride vibration and relatively lower directional stability limits, especially for the articulated frame-steered vehicles (AFSV). The transmitted whole-body vibration (WBV) exposure levels to the human operators generally exceed the safety limits defined in ISO-2631-1 and the European Community guidelines. Moreover, the directional stability limits are generally assessed neglecting the contributions due to terrain roughness and kineto-dynamics of the articulated frame steering (AFS) system. Increasing demand for high load capacity and high-speed off-road vehicles raises greater concerns for both the directional stability limits and WBV exposure. The criterion for acceptable handling and stability limits of such vehicles do not yet exist and need to be established. Furthermore, both directional stability performance and ride vibration characteristics are coupled and pose conflicting vehicle suspension design requirements. This dissertation research focuses on enhancement of ride, and roll- and yaw-plane stability performance measures of frame-steered vehicle via analysis of kineto-dynamics of the AFS system and hydro-pneumatic suspensions.

A roll stability performance measure is initially proposed for off-road vehicles considering magnitude and spectral contents of the terrain elevations. The roll dynamics of an off-road vehicle operating on random rough terrains were investigated, where the two terrain-track profiles were synthesized considering coherency between them. It is shown that a measure based on steady-turning root-mean-square lateral acceleration corresponding to the sustained period of unity lateral-load-transfer-ratio prior to the absolute-rollover, could serve as a reliable measure of roll stability of vehicles operating on random rough terrains. The simulation results revealed adverse effects of terrain elevation magnitude on the roll stability, while a relatively higher coherency resulted in lower terrain roll-excitation and thereby higher roll stability. The yaw-plane stability limits of an AFSV are investigated in terms of free yaw-oscillations as well as transient steering characteristics through field measurements and simulations of kineto-dynamics of the AFS system.

It was shown that employing hydraulic fluid with higher bulk modulus and increasing the steering arm lengths would yield higher yaw stiffness of the AFS system and thereby higher frequency of yaw-oscillations. Greater leakage flows and viscous seal friction within the AFS system struts caused higher yaw damping coefficient but worsened the steering gain and articulation rate. A design guidance of the AFS system is subsequently proposed. The essential objective measures are further identified considering the AFSV's yaw oscillation/stability and steering performances, so as to seek an optimal design of the AFS system.

For enhancing the ride performance of AFSV, a simple and low cost design of a hydro-pneumatic suspension (HPS) is proposed. The nonlinear stiffness and damping properties of the HPS strut that permits entrapment of gas into the hydraulic oil were characterized experimentally and analytically. The formation of the gas-oil emulsion was studied in the laboratory, and variations in the bulk modulus and mass density of the emulsion were formulated as a function of the gas volume fraction. The model results obtained under different excitations in the 0.1 to 8 Hz frequency range showed reasonably good agreements with the measured stiffness and damping properties of the HPS strut. The results showed that increasing the fluid compressibility causes increase in effective stiffness but considerable reduction in the damping in a highly nonlinear manner. Increasing the gas volume fraction resulted in substantial hysteresis in the force-deflection and force-velocity characteristics of the strut.

A three-dimensional AFSV model is subsequently formulated integrating the hydro-mechanical AFS system and a hydro-pneumatic suspension. The HPS is implemented only at the front axle, which supports the driver cabin in order to preserve the roll stability of the vehicle. The validity of the model is illustrated through field measurements on a prototype vehicle. The suspension parameters are selected through design sensitivity analyses and optimization, considering integrated ride vibration, and roll- and yaw-plane stability performance measures. The results suggested that implementation of HPS to the front unit alone could help preserve the directional stability limits compared to the unsuspended prototype vehicle and reduce the ride vibration exposure by nearly 30%. The results of sensitivity analyses revealed that the directional stability performance limits are only slightly affected by the HPS parameters. Further reduction in the ride vibration exposure was attained with the optimal design, irrespective of the payload variations.

ACKNOLEDGEMENTS

The author wishes to express his sincere appreciation to his thesis supervisors, Dr. Subhash Rakheja and Dr. Paul-Emile Boileau, for initiating the study topic and for their great supports and continued guidance and efforts through the thesis work.

The author also wishes to acknowledge Chinese Government, Concordia University and CONCAVE center for their financial support, including the International Tuition Fee Remission, Mobility Award, Accelerator Award, Conference Award and Research Assistantship.

The author also thanks colleagues, faculty and staff at the department of Mechanical and Industrial Engineering, and CONCAVE center, for their contributions to this thesis work. The author also wishes to acknowledge Dr. Jue Yang from University of Science and Technology Beijing and XCMG Construction Machinery Co., Ltd for their great corporations.

Finally, the author would like to express his special thanks to his family and friends for their support and encouragement. The author would like to dedicate this thesis to the memory of his father who passed away in 2003 and his grandfather who passed away in 2017 to keep their spirits alive.

TABLE OF CONTENTS

CHAPTER 1

LITERATURE REVIEW AND SCOPE OF THE DISSERTATION

CHAPTER 2

A ROLL STABILITY PERFORMANCE MEASURE FOR OFF-ROAD VEHICLES

CHAPTER 3

EFFECTS OF ARTICULATED FRAME STEERING ON TRANSIENT YAW RESPONSES OF THE VEHICLE

CHAPTER 4

DESIGN OPTIMIZATION OF AN ARTICULATED FRAME STEERING SYSTEM

CHAPTER 5

CHARACTERIZATION OF A HYDRO-PNEUMATIC SUSPENSION STRUT WITH GAS-OIL EMULSION

CHAPTER 6

MULTI-PERFORMANCE ANALYSES AND DESIGN OPTIMIZATION OF HYDRO-PNEUMATIC SUSPENSION SYSTEM FOR AN OFF-ROAD WORK VEHICLE

CHAPTER 7

CONCLUSIONS AND RECOMMENDATIONS

LIST OF FIGURES

LIST OF TABLES

NOMENCLATURE

a	Tire force factor
$a_{0,m,v}$	Constant coefficients of the steering valve
a_v	Vector sum of weighted RMS accelerations
a_{wx}	Weighted RMS acceleration along x axis
a_{wy}	Weighted RMS acceleration along y axis
a_{wz}	Weighted RMS acceleration along z axis
A	Coefficient for tire cornering force
A_0	Initial angle of the strut mountings with respect to the articulation joint
A_b	Opening area of bleed orifices
A_c	Effective piston area of the steering struts
A_r	Effective annular area of the rod-side chamber of the steering struts
A_{hc}	Effective piston area of the hydro-pneumatic suspension strut
A_{hr}	Effective rod area of the hydro-pneumatic suspension strut
A_v	Opening area of check valves
$A(8)$	8-hour equivalent energy
b	Tire width
B	Coefficient for tire cornering force
B_{eff}	Effective bulk modulus of the hydraulic fluid
C	Soil cone index
C_b	Discharge coefficient of bleed orifices
C_α	Tire cornering stiffness
$C_{\alpha f}$	Tire cornering stiffness at front axle
$C_{\alpha r}$	Tire cornering stiffness at rear axle
C_{slip}	Tire longitudinal stiffness
C_v	Discharge coefficient of check valves
c_t	Tire vertical damping
d	Tire diameter
d_L	Displacement of left steering strut
d_R	Displacement of right steering strut

d_s	Peak-to-peak travel of hydro-pneumatic suspension strut
E_L	Extremity of engine supporting structure on the left side
E_R	Extremity of engine supporting structure on the right side
f	Temporal frequency
F	Composite objective function
F_c	Coulomb friction force
F_s	Stiction force
F_h	Total force of the hydro-pneumatic strut
F_f	Friction within the hydro-pneumatic strut
F_L	Steering force developed by the left strut
F_R	Steering force developed by the right strut
F_x	Tire traction force
F_y	Tire cornering force
F_{y0}	Initial tire cornering force
F_{y1}	Steady-state tire cornering force
F_{zt}	Tire normal force
G_d, P, Q	Power spectra density of the terrain elevation
h	Tire section height
h_L	Steering arm length of the left strut
h_R	Steering arm length of the right strut
i	Tire longitudinal slip ratio
I_f	Yaw mass moment of inertia of the front unit
I_r	Yaw mass moment of inertia of the rear unit
k	Terrain correlation constant
k_l	Leakage flow coefficient
k_{l0}	Additional constant leakage coefficient
k_{lL}	Leakage coefficient of the left strut
k_{lR}	Leakage coefficient of the right strut
k_{mzf}	Aligning moment coefficient of tires at front axle
k_{mzr}	Aligning moment coefficient of tires at rear axle

k_s	Stribeck coefficient
k_t	Tire vertical stiffness
k_v	Flow area factor of the steering valve
k_x	Weighting constant of RMS acceleration along x axis
k_y	Weighting constant of RMS acceleration along y axis
k_z	Weighting constant of RMS acceleration along z axis
k_θ	Ratio of the gerotor volume displacement to its angular displacement
l_0	Initial length of the struts
l_1	Distance from the articulation joint to the front mounting points of the struts
l_2	Distance from the articulation joint to the rear mounting points of the struts
l_L	Instantaneous length of the left strut
l_R	Instantaneous length of the right strut
L	Initial strut length
L_L	Instantaneous length of the left strut
L_R	Instantaneous length of the right strut
L_{max}	Maximum strut length
L_{min}	Minimum strut length
L_1	Mounting point of the left steering strut on the front unit
L_2	Mounting point of the left steering strut on the rear unit
L_{f1}	Longitudinal distance from the mass center of front unit to the front axle
L_{f2}	Longitudinal distance from the mass center of front unit to the articulation joint
L_{r1}	Longitudinal distance from the mass center of rear unit to the rear axle
L_{r2}	Longitudinal distance from the mass center of rear unit to the articulation joint
m	Spatial frequency
m_f	Mass of the front unit
m_r	Mass of the rear unit
M_2	Pairwise comparison matrix for level II
$M_{3/A(k)}$	Pairwise comparison matrix for level III, k=1,2,3
M_{zi}	Aligning moment developed by tire i (i=1,..,4)
n	Polytropic exponent
n_0	Reference spatial frequency

n_b	Number of bleed orifices
n_v	Number of check valves
OS	Yaw response overshoot
p	Terrain elevation
P_0	Fluid pressure in the reservoir
$P_{1,2}$	Tire-terrain intersection point
P_c	Fluid pressure in piston-side chamber of the left steering strut and rod-side chamber of the right steering strut
P_r	Fluid pressure in rod-side chamber of the left steering strut and piston-side chamber of the right steering strut
P_{h0}	Initial pressure in the hydro-pneumatic suspension strut
P_{hc}	Fluid pressure in piston-side chamber of the hydro-pneumatic suspension strut
P_{hr}	Fluid pressure in rod-side chamber of the hydro-pneumatic suspension strut
q	Terrain elevation
q_1	Rate of fluid flow from the steering valve to the steering struts
q_2	Rate of fluid flow from the steering struts to the reservoir
q_b	Flow rate through the bleed orifices
q_c	Flow rate through the check valves
q_l	Leakage flow rate within the hydro-pneumatic suspension strut
q_{lL}	Rate of leakage flow within the left strut
q_{lR}	Rate of leakage flow within the right strut
R_1	Mounting point of the right steering strut on the front unit
R_2	Mounting point of the right steering strut on the rear unit
T	Half-track width
T_L	Extremity of front tire on the left side
T_R	Extremity of front tire on the right side
T_s	Steering torque generated by the steering struts about the articulation joint
u	Vehicle forward speed
u_f	Body-fixed longitudinal velocity of the front unit
u_r	Body-fixed longitudinal velocity of the rear unit
U_{max}	Static friction coefficient

U_{min}	Dynamic friction coefficient
v_h	Hysteresis transition velocity of the hydro-pneumatic strut
v_f	Body-fixed lateral velocity of the front unit
v_r	Body-fixed lateral velocity of the rear unit
V	Vector of the normalized objective measures
V_0	Initial fluid volume of the piston-side chamber of left-strut, the rod-side chamber of right strut and the connecting pipes
V_{1L}	Volume of fluid in the piston-side chamber of left strut
V_{1R}	Volume of fluid in the rod-side chamber of right strut
V_{2L}	Volume of fluid in the rod-side chamber of left strut
V_{2R}	Volume of fluid in the piston-side chamber of right strut
V_c	Volume of the emulsion within the piston-side chamber
V_g	Gas volume within the piston-side chamber
V_r	Volume of the emulsion within the rod-side chamber
V_d	Effective tire deflection velocity
V_{sy}	Lateral velocity of tire-terrain contact center
V_x	Longitudinal velocity of wheel center
V_y	Lateral velocity of wheel center
w	Waviness exponent
W	Vector of weights
W_a	Additional weighting matrix
$W_{II/I}$	Weights for level II elements with respect to level I
$W_{III/II}$	Weights for level III elements with respect to level II
x	Terrain longitudinal coordinate
X	Relative angular displacement of the steering valve
X_0	Dead-band of the steering valve
Y_i	Cornering force developed by tire i (i=1,..,4)
z_{oi}	Effective terrain elevation
$z_{P1,P2}$	Terrain elevation
z_s	Deflection of the hydro-pneumatic suspension strut

z_u	Vertical motion of the wheel center
α, α_i	Tire lateral slip angle (i=1,..,4)
α_{si}	Steady-state side-slip angle of tire i (i=1,..,4)
α_r	Roughness coefficient
β_c	Effective bulk modulus of the emulsion within the piston-side chamber
β_h	Bulk modulus of pure hydraulic oil
β_r	Effective bulk modulus of the emulsion within the rod-side chamber
γ	Coherence function
γ_i	Gas volume fraction of the emulsion
γ_0	Initial gas volume fraction of the emulsion
$\mathit{\Gamma}$	Articulated steering gain
δ	Tire deflection
ζ	Yaw damping ratio
η_g	Efficiency of the gerotor
θ	Articulation angle
θ_h	Steering valve housing displacement
θ_{sw}	Steering wheel displacement
ϑ	Slope of the terrain profile
μ_v	Viscous damping coefficient due to strut seal friction
ρ_c	Mass density of the emulsion within the piston-side chamber
ρ_h	Mass density of pure hydraulic oil
ρ_r	Mass density of the emulsion within the rod-side chamber
σ_y	Tire lateral relaxation length
φ_f	Body-fixed yaw velocity of the front unit
φ_r	Body-fixed yaw velocity of the rear unit
χ	Design variable vector
ψ	Yaw response rate
ω	Yaw mode frequency
$\mathit{\Omega}$	Angular spatial frequency
$\mathit{\Omega}_0$	Reference angular spatial frequency

ACRONYMS

AFS	Articulated Frame Steering
AFSV	Articulated Frame Steered Vehicles
AHP	Analytic Hierarchy Process
ARIMA	Autoregressive Integrated Moving Average
cg	Center of Gravity / mass center
CAD	Computer-Aided Design
CTC	Center of Tire Contact
DAQ	Data Acquisition
DRT	Dynamic Rollover Threshold
DOF	Degree of Freedom
EC	European Community
ELA	Effective Lateral Acceleration
GA	Genetic Algorithm
HGCZ	Health Guidance Caution Zone
HHT	Hilbert-Huang Transformation
HPS	Hydro-Pneumatic Suspension
LBP	Low Back Pain
LQR	Linear Quadratic Regulator
LSM	Least Square Method
LTR	Load Transfer Ratio
MO	Mobility Number
MVEE	Military Vehicle Engineering & Establishment
PI	Proportional-Integral
PS	Pattern search
PSD	Power Spectral Density
RAR	Rearward Amplification Ratio
RCF	Rollover Critical Factor
RMS	Root Mean Square
RPER	Rollover Prevention Energy Reserve
RSF	Roll Safety Factor

RSM	Response Surface Method
SSF	Static Safety Factor
SQP	Sequential quadratic programming
TTR	Tilt-Table Ratio
WBV	Whole-Body Vibration

CHAPTER 1

LITERATURE REVIEW AND SCOPE OF THE DISSERTATION

1.1 Introduction

Vehicles employed in off-road sectors such as agricultural, construction, forestry and mining regions are known to exhibit relatively lower directional stability limits and high levels of whole-body vibration (WBV). The WBV exposure levels generally exceed the safety limits for the human operators defined in ISO-2631-1 [1] and the European Community (EC) guidelines [2]. Epidemiological studies have shown direct associations between prolonged WBV exposure and operator health risks and reduced work rate [3-5]. Surveys of overturning accident conducted by Health and Safety Executive in United Kingdom [6] and Scottish Institute of Agricultural Engineering [7] have reported high tractor accident rates on rough terrains, which have been attributed to lower overturning limits of such vehicles. National Institute for Occupational Safety and Health in United States has also reported higher frequency of fatal rollover accidents of mining trucks, especially in the loaded case [8, 9].

The articulation degree-of-freedom of the widely-used articulated frame-steered vehicles (AFSV) further contributes to yaw divergence or snaking behavior of the vehicle when operating above a critical speed [10-12]. Increasing demand for high load capacity and high-speed vehicles raises greater concerns for both the directional stability limits and WBV exposure. The enhancement of operational safety of off-road vehicles, especially the AFSVs, thus necessitates designs for improved roll- and yaw-plane stability limits together with the attenuation of terrain-induced ride vibration.

Current designs of low to medium size off-road vehicle generally rely on ride vibration attenuation through soft and large size tires and a seat suspension. The tires are designed/selected to support the vehicle weight and fulfill required traction performance on different terrains, while offering very light damping and thereby limited control of terrain-induced vibration. Moreover, the soft and large size tires may cause greater roll and pitch motions of the vehicle, as well as greater fore-aft and lateral WBVs attributed to high driver location. Further, a seat suspension generally limits the transmission of vertical vibration only, when adequately tuned for the target vehicle [13, 14], while the ride vibration environment of off-road work vehicles comprises equally large magnitudes of horizontal and rotational vibrations [15, 16]. Based on the field-measured data, it has been shown that a seat suspension may offer little attenuation of vertical vibration and it may even amplify the cabin vibrations under some operating situations [17]. Many designs of axle suspensions have also been proposed to enhance the vehicle ride performance, while their implementations in off-road vehicles have been limited due to the reduced roll- and tip-over stability, and increased jackknife and snaking potential of the suspended vehicles particularly for the AFSVs [18]. The roll- and yaw-plane stability limits of off-road vehicles can be improved to some extent via the anti-roll bars, friction damping and leakage flows within the articulated steering struts [10, 18, 19]. Their robustness to variations in load, speed and off-road terrain conditions, however, are not yet known. Further, the effects of kinematic layout, hydraulic fluid properties and steering valve flow characteristics of the articulated frame steering (AFS) system on the yaw oscillation/stability of the vehicle are usually overlooked. Although off-road vehicles operate under substantially different terrain conditions compared to the road vehicles, their stability performance is invariably assessed on the basis of measures defined for road vehicles [18, 20, 21]. A knowledge gap exists on directional stability measures for off-road vehicles incorporating the tire interactions with off-road rough terrains.

The developments in innovative linkage [22] and cross-coupled hydro-pneumatic suspensions [23] offer good potential to achieve enhanced vibration safety of the operators, while preserving the operational safety of the vehicle. Such developments, however, involve numerous complex challenges in view of conflicting ride and stability performance measures, lack of well-defined stability measures and various design constraints. Thus far, only limited efforts have been made with regards to coupled ride and handling performance of the suspended off-road vehicles, especially the AFSVs. The limited reported studies on AFSVs focus either on vehicle ride performance, mostly through the field measurements [3, 24], or on the snaking stability limits [19, 25]. The designs of advanced suspensions together with appropriate articulated frame steering system may help tackle the conflicting design requirements, and improve ride and directional stability performance of the frame-steered off-road work vehicles.

This dissertation research focuses on enhancement of ride, and roll- and yaw-plane stability performance measures of frame-steered vehicle via analysis of kineto-dynamics of the frame steering system and hydro-pneumatic axle suspension. A roll stability performance measure is proposed for off-road vehicles considering magnitude and spectral contents of the terrain. The free yaw-oscillations as well as transient steering characteristics of an articulated frame-steered vehicle are investigated through field measurements and simulations of the yaw-plane dynamic model.

The essential objective measures are subsequently identified considering the AFSV's yaw oscillation/stability and steering performances, so as to seek an optimal design of the articulated frame steering system. The stiffness and damping characteristics of a hydro-pneumatic suspension strut design are also investigated experimentally and analytically. The validated suspension model and optimal AFS system are integrated to the three-dimensional model of the AFSV in the ADAMS platform to analyze the ride and roll/yaw stability performance of the vehicle. An optimal design of the hydro-pneumatic axle suspension system is subsequently proposed for realizing a better compromise between ride and directional performances of the AFSV.

1.2 Review of relevant literature

The state-of-the-art developments in off-road vehicles' ride, directional dynamics analyses and suspension designs are reviewed in order to build essential knowledge on integrated analysis and design methods, and to formulate the scope of the dissertation research. The reported studies focusing on: ride and handling dynamics of off-road work vehicles, including the performance measures; modelling of vehicle system and subsystems, and the tire-terrain interactions; kineto-dynamics of articulated steering system; and design and analyses of axle suspension systems are reviewed and discussed in the following subsections.

1.2.1 Ride and handling dynamics of off-road work vehicles

Analysis of ride vibration and handling performance of an off-road work vehicle involves integration of rigid body dynamic model of the vehicle with various subsystem models such as the tires, suspension systems and the articulated frame steering mechanism in addition to the terrain profiles. Furthermore, the assessments of ride and handling dynamics of vehicles involves the formulations of relevant performance measures.

Various studies on human responses to whole-body vibration have evolved into generally acceptable and standardized measures of ride performance considering the human drivers' health, safety and performance rate. Considerable gap in knowledge, however, exists for measures related to handling and directional stability performance of off-road vehicles. The significance of the WBV environment of off-road vehicles, primarily arising from tires' interactions with rough terrains, can be evidenced from the various epidemiology studies on health effects of WBV among the exposed operators. An EC study estimated that 4 to 7% of all employees in some European countries and North America are exposed to potentially harmful WBV [26]. Exposure to high magnitudes of WBV on a daily basis has been associated with discomfort, interference with activities and various health risks such as nervous, circulatory and digestive system disorders, noise-induced hearing loss and degenerative changes to the spine, particularly the low back pain (LBP) [27]. The focus groups in these epidemiological studies have been the vehicle drivers, which constitute the largest population of workers exposed to WBV [28]. Occupationally induced LBP has been further associated with excessive financial costs, and loss of workdays and quality of life. The total cost of LBP in Sweden was estimated in the order of 1860 million Euros in 2001, where the lost productivity accounted for 84% of the total cost [29]. Another study attributed 101.8 million lost workdays to LBP in 1988 in the USA [30]. Some European countries like Belgium, Germany, Netherland and France recognize the low back pain and/or back disorders due to exposure to WBV as an occupational disease. Considering the increasing drive for productivity growth, particularly in the developing economies, it would be reasonable is speculate that the occupationally WBV-exposed population will continue to grow.

The WBV levels of a large number of off-road work vehicles either approach or exceed the 8-hour health guidance caution zone (HGCZ), defined in ISO 2631-1 [1]. The WBV levels of such vehicles are either close to or exceed the action limiting values defined in the EC guideline [2]. The ride vibration environment of a vehicle is generally assessed in terms of frequency-weighted root mean square (RMS) acceleration at the driver seat. The standardized measurement methods have been described in ISO 2631-1 [1] and BS 6841 [31]. The ISO 2631-1 defines the frequency weightings to derive the weighted RMS accelerations along the horizontal (a_{wx}, a_{wy}), vertical (a_{wz}) and rotational axes. The total WBV exposure a_v is subsequently obtained from the weighted sum of frequency-weighted RMS accelerations along the translational axes alone:

$$a_v = \sqrt{k_x^2 a_{wx}^2 + k_y^2 a_{wy}^2 + k_z^2 a_{wz}^2} \tag{1.1}$$

where k_x, k_y and k_z are the weighting constants. The standard further provides the HGCZ to assess the potential health effects of WBV. The 2002/44/EC [2] recommends the use of daily exposure A(8) in terms of 8-hour equivalent energy representing the equivalent continuous exposure. The directive recommends the exposure limit value of 1.15 m/s^2 and an action value of 0.5 m/s^2.

The reported exposure levels of some of the off-road vehicles are summarized Table 1.1. Despite their operations at relatively low speeds, the WBV levels of vast majority of the off-road work vehicles exceed the HGCZ, which is mostly due to vehicle interactions with rough terrains.

Furthermore, many of these vehicles transmit equally high magnitudes of horizontal and vertical vibration, as seen in Table 1.1. A number of studies have shown that the WBV levels of a vehicle are related to various driver-, operation-, design- and environmental-related factors such as speed [5] , terrain roughness [32], cab and cab mounts, axle locations [33], vehicle load and dimensions [3], and driving style and experience [34].

When the WBV exposure is deemed as a health risk for the workers, the primary actions to take into consideration aim at elimination or reduction of vibration at source such as proper maintenance (or replacement) of older vehicles, routine upkeep of tracks and trails, and reductions in vehicle speed and load. The secondary actions involve the engineering solutions aimed at reducing the vibration along the transmission path through suspensions or vibration isolators inserted between the source of vibration and the operator, namely tires, body suspension, and cab and seat suspension [17, 35]. A third group of actions for WBV-related health risk reductions include optimizing the driver posture considering cab ergonomics, seat profile and visibility, and work organization so as to reduce the exposure duration. Reported studies have shown that the vibration levels on the seat pan exceed those at the base of the seat, suggesting that current seat suspension mechanisms may not be effective for a class of vehicles [4, 17].

Table 1.1: Summary of WBV levels of off-road work vehicles

Vehicle (Model)	Terrain	Task	Speed (km/h)	Average $a_{wx}(m/s^2)$	Average $a_{wy}(m/s^2)$	Average $a_{wz}(m/s^2)$	Average $a_v(m/s^2)$	Exceed HGCZ	Source
Articulated dumper	Quarry	-	-	0.14	0.18	**0.38**	0.50	No	[24]
Agricultural tractor	Workplace	-	5	-	-	-	0.89	Yes	[36]
	Road	-	20	-	-	-	0.55	No	
Backhoe	-	-	-	-	-	**1.0-1.1**	1.05	Yes	[5]
Bulldozer	-	Pushing	-	**1.96**	1.4	1.64	3.75	Yes	[16]
Crawler loader	-	-	-	**0.8-1.1**	-	-	1.33	Yes	[5]
Drill-jumbo	-	Drilling	-	0.03	0.02	**0.08**	0.09	No	[16]
Dump truck	-	Various	-	0.67	0.71	**1.2**	1.82	Yes	
Excavator (CAT 330C)	Unpaved	Haulage	10-15	0.21-0.34	0.17-0.30	**0.53-1.05**	0.94	Yes	[4]
		Material shifting		0.12-0.13	0.08	**0.15-0.21**	0.27	No	
Forklift	Quarry	-	-	0.3	0.28	**0.95**	1.11	Yes	[24]
	Mill		-	0.11	0.11	**0.3**	0.37	No	
	Dockyard		-	0.2	0.15	**0.4**	0.53	No	
Forwarder	-	-	-	0.29-1.36	**0.43-1.79**	0.21-1.00	2.03	Yes	[37]
Grader	-	Pushing leveling	-	0.38	0.45	**0.79**	1.14	Yes	[16]
Harvester	-	-	-	0.216	0.22	**0.386**	0.58	No	[38]
Loader-wheeled (Volvo L110F)	Unpaved	Haulage	10-15	0.32-0.44	0.43-0.5	**0.43-0.61**	0.99	Yes	[4]
		Material shifting		0.35-0.62	0.22-0.53	**0.37-1.02**	1.10	Yes	
LHD truck	-	Various	-	0.87-0.97	0.49-0.63	**1.4-1.7**	2.17	Yes	[3]
Mower (Toro 40000D)	-	-	-	0.83	**0.87**	0.56	1.77	Yes	[39]
Skidder	-	Various	-	0.28-1.02	**0.22-1.18**	0.25-0.87	1.51	Yes	[15]

Unlike the ride vibration, the dynamic safety or directional performance measures have not been well defined for off-road vehicles. Off-road vehicle dynamic safety limits generally include the roll stability, slope stability and yaw stability limits, also referred to as the snaking and jackknife stability limits for articulated vehicles [12, 18, 40]. Some of the measures defined for road vehicles have been used to assess dynamic safety limits of off-road vehicles, although their validity is questionable due to large variations in the tire forces on rough terrains. The specific measures reported in the literature are summarized below.

The roll stability limits can be evaluated in terms of static and dynamic measures commonly used to describe relative roll stability of heavy commercial road vehicles [40, 41]. The static roll stability has been described in terms of different measures such as static safety factor (SSF) and tilt-table ratio (TTR), while the dynamic roll stability is assessed in terms of the Lateral Load Transfer Ratio (LTR), Roll Safety Factor (RSF), Rearward Amplification Ratio (RAR) and Rollover Prevention Energy Reserve (RPER). Li et al. [21] investigated rollover risk of vehicle negotiating a fishhook maneuver on a random terrain profile. The study assessed the roll stability in terms of peak normalized rollover critical factor (RCF) as a function of the vehicle roll angle and instantaneous position of the mass center (cg). Pazooki et al. [10] assessed the dynamic roll stability of an AFSV in terms of the RSF (LTR of the rear unit), during constant-speed turning and path-change maneuvers. The vehicle is considered to approach its relative roll instability limit when RSF value approaches unity, which corresponds to loss of contact of tires on inside track of the vehicle. The study also expressed the dynamic rollover threshold of the vehicle in terms of effective lateral acceleration (ELA) based on the lateral accelerations of the sprung and unsprung masses. In addition, the absolute rollover criterion has been described as the lateral distance between vehicle mass center and the line joining the contact centers of outside tires of the front and rear axles [41]. There studies have invariably shown that terrain roughness adversely affects the roll stability limit of the vehicle. The validity of the measures defined for road vehicles is thus questioned, since these are defined for perfectly smooth roads.

Hunter [42] and Yisa et al. [43] have presented the static and dynamic slope stability measurements of agriculture and forestry vehicles. The static slope stability refers to the maximum slope of the terrain prior to overturning of the vehicle, which directly relates to instantaneous normal loads on different wheels. European and Japanese regulations recommend the minimum wheel load requirements as 20%, 19% and 18% for small, medium and large-size tractors [44].

The dynamic slope stability, on the other hand, is related to loss of control, and is described by the limiting speed corresponding to vehicle sliding or overturning.

The articulation joint in an AFSV introduces an additional yaw degree-of-freedom (DOF) apart from compliance in the roll and pitch axis, which results in snaking behavior of the rear unit and jackknife under extreme maneuvers. Crolla and Horton [12], He et al. [19] and Azad et al. [25, 45] investigated the snaking mode stability limits in terms of critical speed through eigenvalue analysis. Alternatively, Pazooki et al. [10], Rehnberg et al. [46] and Dudziński et al. [11] assessed the snaking mode stability in terms of articulation angle together with its oscillation frequency and the rate of decay under a pulse steering input. These studies have shown lower snaking stability with reduced articulation stiffness and damping, tire cornering stiffness, yaw inertia of the rear unit and higher yaw inertia of the front unit. Pazooki et al. [10] also showed that the yaw stability limits of the vehicle strongly depend upon steering struts kinematics. He et al. [19] concluded that lowering the articulation stiffness causes over-steering of the vehicle, which may evolve into jackknife instability, and the leakage flows within the steering struts enhance the snaking mode limit but deteriorate the jackknife limit.

1.2.2 Vehicle modeling

The ride vibration responses of a vehicle, in-general, strongly depends upon various design and operating factors such as inertial properties, vehicle dimensions, terrain roughness, speed, and suspension and tire properties. Although the ride dynamic models of different road vehicles have been extensively investigated, such efforts in off-road work vehicles have been mostly limited to agricultural vehicles and tracked military vehicles. Such efforts are even minimal for AFSVs despite their high levels of ride vibrations, which may in-part be due to complex dynamics of AFSVs, particularly with regards to kinematics and dynamics of the steering system. Moreover, the reported models generally focus either on ride analysis or handling analysis. Only a few have attempted the coupled ride and handling analyses. The reported studies on off-road work vehicles models may be grouped into two categories: lumped-parameter and multi-body dynamic models. The lumped-parameter models provide the ride and directional responses in a highly efficient manner but may involve several simplifying assumptions. The multi-body dynamic models, on the other hand, are computationally demanding but consider detailed vehicle components kinematics and dynamics, and could provide more accurate predictions of the responses.

The reported ride dynamic models of different off-road work vehicles have provided considerable insight into the significance of axle suspensions, and the roles of various design and operating factors on the ride performance. The majority of these consider only planar dynamics assuming constant forward speed, while neglecting the fore-aft and lateral tire-terrain interactions and the contributions of the articulated steering mechanism [47]. Only a few studies have implemented three-dimensional tire-terrain models to study the fore-aft and lateral ride dynamics of off-road tractors. Pazooki et al. [48] proposed a three-dimensional lumped-parameter model of an AFSV (Fig. 1.1(a)) with a rear-axle torsio-elastic suspension together with a three-dimensional tire model to evaluate the ride responses along the lateral, fore-aft, vertical, roll and pitch axes. Rehnberg and Drugge [49] developed 19- and 22-DOF multi-body models of a wheel loader (Fig. 1.1(b)) with and without axle suspensions, respectively, in the ADAMS platform and presented the effects of suspension on ride dynamics of the vehicle.

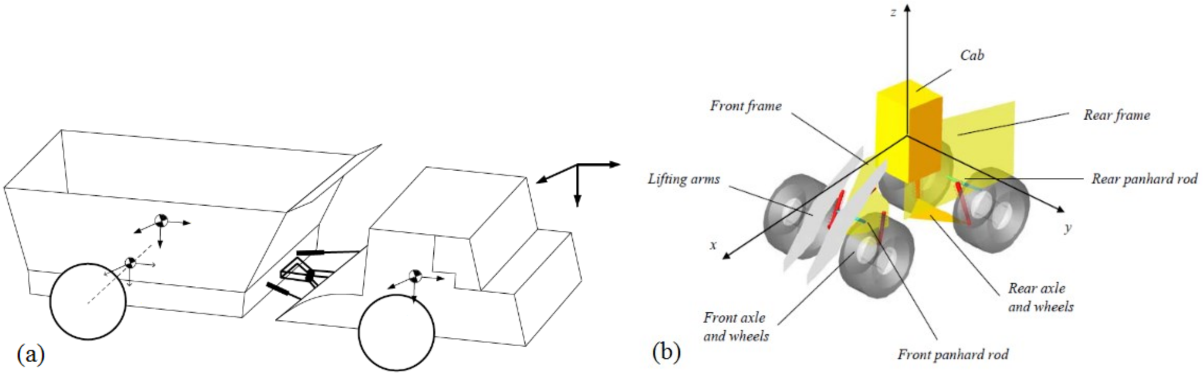

Figure 1.1: (a) Lumped-parameter vehicle model [48] and (b) multi-body vehicle model [49]

The directional stability analyses of off-road work vehicles have also been addressed in only a few studies, although the directional responses of commercial road vehicles have been extensively investigated. This is likely due to low speed operations of most of the off-road work vehicles. A class of off-road work vehicles, including some of the AFSVs, however, are designed to operate at relatively higher speeds, where the roll and yaw stability limits would be of greater concern [19]. Furthermore, such vehicles also operate on highly rough off-road terrains with substantial slopes and cross-slopes, and thereby may experience tip-over or rollover. Tire interactions with terrains with cross-slope, and uneven penetrations of the left- and right-wheels into deformable terrains, could also lead to substantial lateral load transfers and thus lower roll stability even at low speeds.

A simple 3-DOF yaw-plane linear vehicle model has been commonly used to investigate the yaw and snaking stability limits of AFSVs, while neglecting kinematics and dynamics of the frame steering, the effect of lateral load transfer, roll motions of the articulated units and vertical tire-terrain interactions [12, 19, 50]. The steering system has been mostly characterized by equivalent linear torsional stiffness and damping constants neglecting kinematic motions of the steering struts. These studies have employed different tire cornering models ranging from a linear model to a mobility index-based tire model with tire lag [51].

Azad [50] developed a linear single-DOF model of an AFSV by constraining the front unit along the lateral and yaw directions to analyze the vehicle snaking mode. He et al. [19] developed a linear 2-DOF (lateral and yaw) bicycle model of an AFSV assuming constant forward speed, small articulation angles and rigidly coupled front and rear sections, to evaluate understeer gradient of the vehicle. Azad [50] also analyzed a nonlinear 12-DOF multi-body dynamic model developed in the ADAMS platform. The steering struts in the multi-body model were also represented by a torsional spring and a damper with allowable steering angle of $\pm 45^{\circ}$. The Fiala tire model [52] was used to derive rolling resistance, longitudinal force, lateral force and aligning moment due to the tires, while the vertical forces were obtained from a linear point-contact tire model. Li et al. [53, 54] derived a nonlinear 7-DOF three-dimensional model of an AFSV considering prescribed articulation angle in an open-loop manner, while neglecting kinematics and dynamics of the steering struts. The model was used to evaluate roll and slope stability limits of the vehicle, which was validated through measurements performed on a scaled wheel loader subject to turning maneuvers on slopes and on a terrain surface with obstacles.

The above-stated studies have represented the steering mechanism by an equivalent torsional spring and damping element, which may not accurately describe the kinematics and dynamics of the struts. In a recent study, Pazooki et al. [10] investigated the effects of steering kinematics on the yaw dynamic responses, and it was shown that the yaw stability limit of an AFSV is strongly related to effective damping of the steering mechanism, which is further related to the steering valve characteristics and the leakage flows apart from the struts kinematics. It was further shown that effective torsional stiffness and damping due to AFS struts is highly nonlinear and cannot be adequately described by equivalent constants used in [19, 50]. Dudziński [11] developed a multi-body model of an AFSV considering the hydraulic fluid compressibility, pipes flexibility and steering struts geometry to study the snaking behavior of the vehicle. The study also measured the torsional stiffness of the steering mechanism, and tire flexibility of a wheeled loader, and demonstrated model validity using the data obtained for the vehicle negotiating an obstacle at its right front wheel.

Pazooki et al. [48] also derived a nonlinear 13-DOF three-dimensional model of an AFSV to study its ride as well as handling properties. The model incorporated the nonlinear kinematics and dynamics of the steering struts together with fluid compressibility, leakage flows and idealized steering valve characteristics. The vertical tire-terrain interaction was modeled using a nonlinear point-contact model, while the lateral tire force was obtained as a nonlinear function of the side-slip angle considering first order lag. The correlations between the right- and left-track elevations were modeled, assuming a cut-off frequency of 1 Hz, so as to generate roll mode excitation of the vehicle. The study showed that the yaw stability limits of the vehicle strongly depend upon steering struts kinematics and damping, which depend on leakage flows and steering valve characteristics.

Among the various subsystems, the modeling of tires and tire-terrain interactions is known to be most challenging. The reported studies have employed widely different tire models. Off-road vehicle tires are mostly selected to support the vehicle load and provide the tractive and cornering forces to achieve desired mobility performance [55]. The tire properties, however, strongly affect the ride and handling performance of the vehicle [56]. A tire model, in general, implies various structure-related simplifying assumptions, namely, the belts, rim, carcass, sidewalls and tread, apart from the tire-terrain contact. A number of proven regression-based models of road vehicle tires have evolved over past many decades, which have been derived on the basis of the laboratory-measured data such as magic-formula tire model [57] and Unitire [58]. The measurements with off-road tires, however, are most challenging due to their excessive load rating and sizes. The lack of reliable data for off-road work vehicle tires is the primary source of uncertainties in the reported ride and directional dynamic responses.

Many reported off-road work vehicle ride dynamics models have employed the simple linear point-contact tire model, represented by the equivalent linear stiffness and damping elements either in parallel (Kelvin unit) or in series. Crolla et al. [59] demonstrated that the series arrangement yields more accurate results for an agricultural tractor. It has been shown that this simple model overestimates the contact pressure, while loss of tire-terrain contact is entirely ignored. The single contact point has been extended to a roller contact, a fixed footprint and an adaptive footprint in different studies to achieve more accurate representation of the tire-terrain contact, as seen in Fig. 1.2 [60]. The linear point-contact, roller contact and fixed footprint models perform well only at low frequencies, while the adaptive footprint model yields better predictions in the entire frequency range with varying footprint size relative to the wheel center as a function of the tire deflection and the terrain profile. A three-dimensional point-contact tire model (Fig. 1.2(e)) has also been proposed to predict the vertical, lateral and longitudinal tire forces at the tire-terrain interface [59, 61].

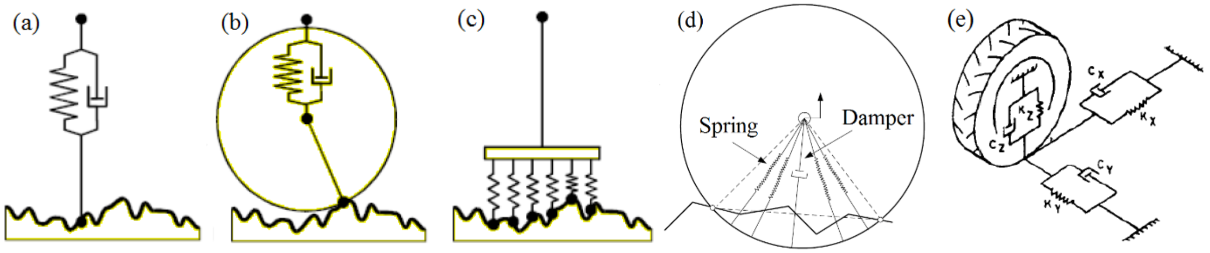

Figure 1.2: Off-road ride tire models: (a) point-contact; (b) roller contact; (c) fixed footprint; (d) adaptive footprint; (e) 3-dimentional point-contact [59, 60]

The vast majority of the off-road tire models focus only on the vertical dynamics. Only a few studies have attempted to formulate tire models for characterizing the longitudinal and cornering properties, such as the 3-dimentional point-contact model [59, 61]. Horton and Crolla [62] proposed a mobility index on the basis of limited measured data on lateral forces developed by the off-road tires, and the mobility number (MO), given by [63]:

$$MO = \frac{Cbd}{F_z}\sqrt{\frac{\delta}{h}}\left(\frac{1}{1+b/2d}\right) \tag{1.2}$$

where C is soil cone index, b is tire width, d is tire diameter, δ is tire deflection and h is the tire section height.

A number of empirical or semi-empirical off-road tire models have also been proposed in the reported studies, which may be considered valid for specific tires and test conditions. McAllister et al. [64] proposed a cornering force (F_y) model of the form:

$$F_y = A \times F_z(1 - e^{-B\alpha}) \tag{1.3}$$

where F_z is the normal load, α is the tire side-slip angle, and A and B are constants that depend upon the terrain profile and could be related to the tire mobility number. Using the measured lateral forces of various driven off-road tires, Krick [65] proposed the following relationship between the lateral and the tractive force:

$$F_y = (1 \pm aF_x)C_\alpha \alpha \tag{1.4}$$

where F_x is the tractive force, C_α is the cornering stiffness and a is a factor describing the variations in lateral force in the presence of a tractive or braking force. Janosi [66] also measured the off-road tire lateral and longitudinal forces, which were shown to follow friction ellipse relation that has been defined for road vehicle tires. Due to the large inertia of the tire segment within the contact patch, a rolling tire would exhibit certain delay in realizing the steady-state force. Ellis [67] assumed a first-order approximation to describe the off-road tire lag, where the cornering force developed by the tires is given by:

$$F_y = F_{y0} + \left(F_{y1} - F_{y0}\right)\left(1 - e^{-x/\sigma_y}\right) \tag{1.5}$$

where F_{y0} is the initial lateral force, F_{y1} is the steady-state force, x is the forward distance rolled and σ_y is the lateral relaxation length, which is considered to be approximately equal to the rolling radius of the off-road tire.

The vast majority of the empirical or semi-empirical off-road tire models are applicable under a pure slip condition, while only a few could describe the tire forces under combined slip conditions. Comprehensive models, however, have evolved for road vehicle tire models that incorporate more complex effects of camber, combined slip, inflation pressure, tire temperature, tread wear and more. Explorations of commercial vehicle tire models such as Ftire [52], RMOD-K [68], MF-SWIFT [51] and UATire [69], capable of ride and handling analyses on uneven terrains, would be desirable for applications in off-road vehicle tires, although challenging due to lack of reliable measured data. The Ftire model represents the tire belt flexibility with friction elements considering a large number of point masses (50-100) coupled to the rim through nonlinear spring-dampers elements to describe both in-plane and out-of-plane degrees of freedom, as illustrated by the model used in the ADAMS platform (Fig. 1.3) [70]. The RMOD-K model constitutes one or more flexible belt layers coupling the rim by the sidewall model. The RMOD-K thus requires relatively high computing time comparing to the Ftire model [52]. Both the models, however, require extensive inputs related tire modal properties to build the model, which would be most challenging for the off-road tires. MF-SWIFT model is an improvement over the widely used magic formula tire model, and it assumes a rigid belt coupled to the rim through the flexible and damped sidewall elements. The UATire model, on the other hand, represents the tire by radial, longitudinal and lateral spring elements. Apart from the pure slip and combined slip conditions, the RMOD-K and MF-SWIFT tire models consider effect of inflation pressure, while the RMOD-K and Ftire also incorporate the effects of temperature change. The Ftire further provides estimates of wear, which is an important issue for off-road tires. The developments in advanced computational methods have also resulted in a number of comprehensive finite element tire structure models, although the majority of these are not suited for vehicle dynamics analyses due to their high computing demands [71, 72].

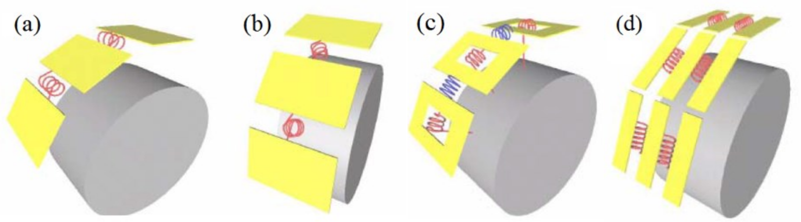

Figure 1.3: Representation of FTire belt stiffness assumption in ADAMS platform: (a) in plane; (b) out of plane; (c) torsional and twisting; and (d) lateral stiffness

In vehicle simulation models, terrain elevations constitute the primary excitation to land vehicles. Early studies in terrain-vehicle interactions date back to the military programs in 1940s, focusing on off-road deformable soil models, and interactions with rigid and deformable tires. These studies involved extensive field and laboratory measurements, which resulted in some empirical or semi-empirical relationships for tire sinkage and stresses development [73]. Furthermore, theories of elasticity, plastic equilibrium and critical soil state were introduced to analyze soil-tire or soil-wheel interactions, which involved numerical methods like Finite Element and Discrete Element methods [74]. Owing to the highly complex mechanics of deformable soils, the reported studies on ride analyses invariably describe the soft terrain elevations by an equivalent undeformable terrain profile [22], even though the terrain deformation during vehicle operation is high. The roughness indices of widely used terrain profiles, and the measurement and modeling methods have been reviewed in a recent study [75]. The study summarized various stochastic modelling methods such as power spectral density (PSD), Markov chains, autoregressive integrated moving average (ARIMA), wavelet transform, Hilbert-Huang transformation (HHT) and offset Rayleigh distribution models. In addition, stochastic partial differential equations have been formulated to describe the undeformable terrain profiles [76], as well as the vector space [77].

The ISO 8608 [78] recommend methods of reporting the terrain profile measurements in terms of displacement or acceleration PSD. The smoothed displacement spectra of various terrains have been described in the form of a power relation:

$$G_d(n) = G_d(n_0)(n/n_0)^{-w} \; or \; G_d(\Omega) = G_d(\Omega_0)(\Omega/\Omega_0)^{-w} \tag{1.6}$$

where G_d is PSD of the terrain roughness, n and Ω define the spatial frequency and angular spatial frequency, respectively, n_0(=0.1 cycles/m) and Ω_0(=1 rad/m) are the reference values, and w is the exponent. The roughness characteristics of many terrains have been reported on the basis of measurements namely the forestry terrains, plowed field, pasture, gravel roads, rough runways and the MVEE (Military Vehicle Engineering & Establishment) test track [79, 80]. Generalized regression functions relating power spectral density of the terrain elevation G_d to the spatial frequency n have also been reported [81], as:

$$G_Z(n) = \alpha_r n^{-\beta};\ \alpha_r > 0\ and\ \beta > 0 \tag{1.7}$$

where α_r is the roughness coefficient and β is the waviness of the terrain, which are identified from the field-measured data. Table 1.2 summarizes these constants for some of the terrains. The PSD of the terrain profile can also be expressed as a function of the temporal frequency f and vehicle speed u, using the relation $f = n \cdot u$.

Table 1.2: Roughness model coefficients for different off-road terrain profiles

Terrain	α_r	β
Forestry	1.00×10^{-4}	1.76
Plowed	6.50×10^{-4}	1.60
Pasture	3.00×10^{-4}	1.60
MVEE	3.16×10^{-4}	2.27

Equations (1.6) to (1.7) describe the average terrain elevation, while the cross-slope of the terrain that contributes to roll excitations of the vehicle is ignored. The ISO 8608 [78] suggests the coherence function to express the relationship between the two terrain tracks. A coherence function can be obtained on the basis of the isotropy assumption, i.e., all the profiles for a given road have the same properties, irrespective of the orientation and location. Figure 1.4 illustrates the spatial PSD properties of different terrains [20] and the isotropy coherency chart for a terrain profile with different track widths [82, 83]. Apart from the isotropic coherence model, Heath [84], and Sun and Su [85] proposed modified isotropic and non-parametric models, respectively, to describe the coherency. Zhang [86] proposed a simplified piecewise linear coherence frequency, assuming a cut-off frequency of 2 Hz, as:

$$\gamma^2(f) = \begin{cases} 1 - 0.45f, & f \le 2Hz \\ 0.1, & f > 2Hz \end{cases} \tag{1.8}$$

Alternatively, Bogsjo [87] proposed an exponential coherence function based upon 20 measured terrain profiles with varying roughness of the form:

$$\gamma(n) = e^{-2\rho T n} \tag{1.9}$$

where ρ is a constant and T is half-track width. The proposed parametric model revealed better accuracy than the isotropic model reported in [20, 85]. The above coherency functions have been applied to generate roughness profiles of two parallel tracks of off-road terrains [20, 88].

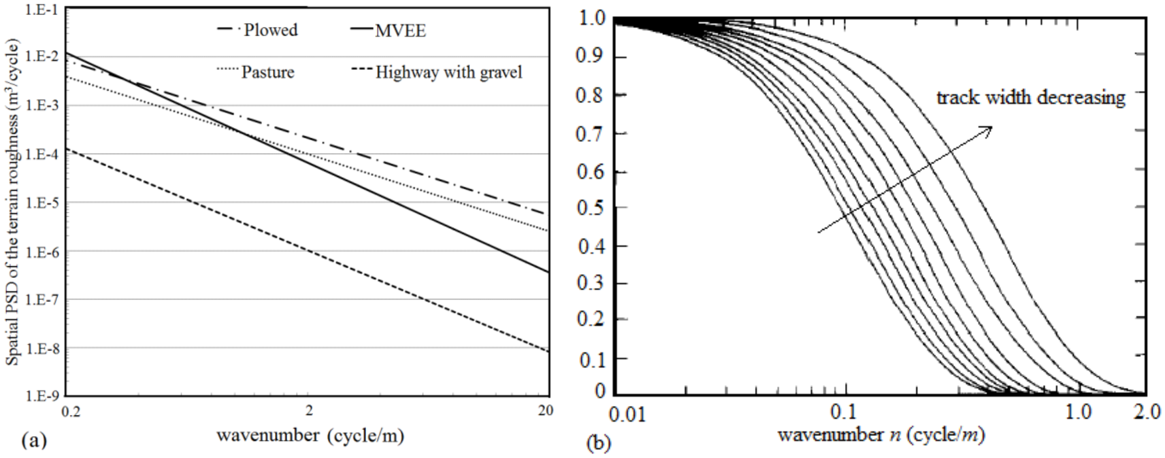

Figure 1.4: (a) Roughness characteristics of different terrains [20]; and (b) coherency based on isotropy [83]

1.2.3 Off-road vehicle suspension designs

Off-road vehicles generally employ secondary suspensions such as those at the seat and the cab. A number of primary axle suspensions have also been reported in some studies, although their implementations have been quite limited due to their adverse effects on the vehicle yaw and roll stability limits [18]. The performance analyses of axle suspensions have been mostly limited to the ride vibration control, while their effects on handling and stability performance have not been adequately addressed.

The terrain-induced vehicle vibrations generally dominate in the low frequency range up to 10 Hz. The lateral and vertical mode vibrations predominate near 1 Hz and in the 2-3 Hz frequency range, respectively, which are attributed the lateral and vertical mode resonances of the vehicle supported on large and soft tires [22, 89]. The attenuation of such low frequency vibration necessitates the designs of extremely low frequency cab and seat suspension (0.5-1Hz), which yield excessive static and dynamic deflections [13, 90]. Suspension seats with linkages, mechanical or air springs, dampers and elastic limit stops, used in off-road work vehicles, could attenuate approximately 50% of the bounce vibration, when adequately tuned for the target vehicle [14]. Optimal lateral seat suspensions with a vibration absorber has also been proposed to attenuate low frequency lateral vibration [91]. Hostens et al. [92] suggested that suspension seats require only minimal additional damping due to damping inherent to the air springs. Through a comprehensive nonlinear model of a suspension seat, it has been shown that design of a suspension seat involves difficult compromise between attenuation of continuous vibration and shock motions that may arise from vehicle interactions with tough terrains and end-stop impacts [93, 94]. A few studies have also suggested that a suspension seat needs to be tuned for specific vehicle vibration spectra. The component design in the absence of the total vehicle dynamics could yield relatively poor performance [17, 95]. Through field measurements on a forestry machine, it has been shown that a suspension seat offers very limited attenuation of vertical vibration and it may even amplify cab vibration under some operating situations [17].

Alternatively, a number of cab suspension designs have evolved to limit the transmission of multi-axis vibration to the driver [96]. Hilton and Moran [97] experimentally investigated a suspension cab with a torsional stiff frame, rubber torsion springs, Belleville springs and hydraulic dampers, and showed attenuation of vertical, pitch and roll vibration up to 70%. The suspension, however, was less effective on a relatively rough track and at low speeds. Similarly, Rakheja and Sankar [90] proposed an optimal cab suspension, which provided excellent ride in the longitudinal and pitch modes, while the isolation performance was quite poor in the bounce, roll and lateral modes. The structures of cab suspension proposed in these studies, however, were relatively complex for implementations in off-road vehicles. The cabs in most off-road work vehicles are either rubber mounted or rigidly connected to the frame and thus provide only negligible isolation of low frequency ride vibration.

Owing to high magnitudes of WBV and limitations of the secondary suspensions, a number of primary suspension designs have been proposed for off-road vehicles [98]. Considering the increasing demands for high-speed and high load capacity vehicles, the need for adequate axle suspensions has been widely recognized. Rehnberg and Drugge [99] investigated the ride performance potential of an axle suspension through analysis of multi-body models of a wheel loader with and without the axle suspensions. The study showed substantial reductions in the fore-aft and vertical accelerations of the suspended vehicle, while the high suspension roll stiffness resulted in only minimal improvement in the lateral acceleration. Pazooki et al. [80] proposed a passive rear-axle torsio-elastic suspension for a forestry skidder comprising a linkage and elastic torsion shafts, as seen in Fig. 1.5(a). The ride performance potential of the proposed suspension were investigated analytically and experimentally. The study showed nearly 35%, 43% and 57% reductions in the frequency weighted root mean square (RMS) accelerations along the x-, y- and z-axis, while a 20% reduction in the pitch acceleration was attained through design optimization.

Furthermore, the suspension revealed very low sensitivity to variations in the vehicle load. The suspension, however, was quite heavy and retrofitting the suspension involved complex alterations to the vehicle. It has been suggested that a soft rear axle suspension with light damping could provide good vibration reduction along the translational axes. Such a suspension, however, would require large suspension travel and thus affect the roll stability in an adverse manner [100]. A number of semi-active and active suspension concepts have also been proposed for heavy road and off-road vehicles to achieve improved compromise between the vehicle ride, handling and roll stability performance [101, 102]. The high cost and weight of an active suspension, however, prohibits its application in heavy vehicles.

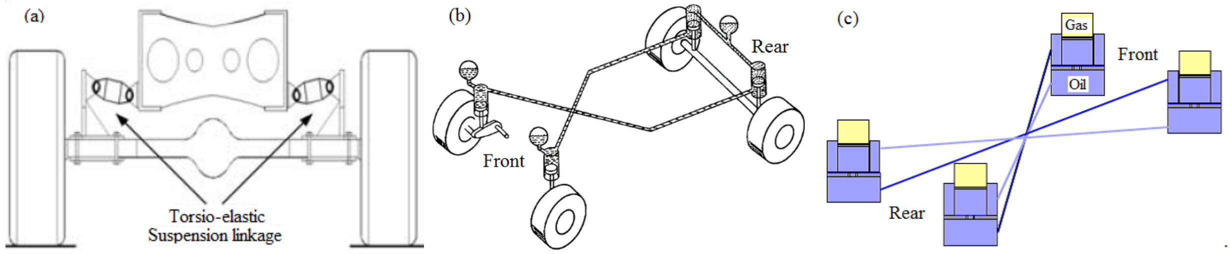

Figure 1.5: Innovative off-road vehicle suspensions: (a) torsio-elastic [80]; (b) hydro-mechanical [103] and (c) hydro-pneumatic [23]

Concepts in interconnected hydro-pneumatic axle suspensions with enhanced roll and pitch stiffness have been explored for applications in off-road vehicles. Horton and Crolla [103] proposed a semi-active hydraulically coupled axle suspension to achieve improved vehicle attitude control and ride comfort (Fig. 1.5(b)). Rehnberg [99] analyzed the ride vibration performance of a wheel loader equipped with a hydro-pneumatic front and rear axle suspensions. The vast majority of the hydro-pneumatic suspensions require high operating pressures due to lower effective working area, which may pose additional challenges on design of seals. Cao et al. [23, 104] proposed an alternate strut design with greater working area and different configurations of interconnected hydro-pneumatic suspensions (Fig. 1.5(c)). The studies demonstrated superior potentials of the cross-coupled suspensions in improving both the ride and handling performance, and introduced a simplified measure of desired suspension stiffness.

1.3 Scope and objectives of the dissertation

The primary objective of the dissertation research is to develop methods and subsystems for enhancement and assessment of ride and directional performances of the off-road vehicles, especially the articulated frame-steered vehicles, through design optimizations of articulated frame steering systems as well as the axle suspension systems. The specific goals of the dissertation research are summarized below:

(i) Propose analysis methods and performance measures for assessing the roll- and yaw-plane dynamic safety for off-road vehicles.

(ii) Develop a comprehensive model of the articulated frame steering (AFS) system considering its kinematic and dynamic properties, and optimize the AFS system design in order to enhance the vehicle's yaw-plane performances.

(iii) Characterize the nonlinear stiffness and damping properties of a low-cost and high load-capacity design of a hydro-pneumatic suspension (HPS) strut experimentally and analytically.

(iv) Develop and validate an integrated three-dimensional ride and yaw/roll plane directional dynamic model of an articulated frame-steered vehicle (AFSV) incorporating the AFS system's kineto-dynamic properties, tire interactions with the off-road rough terrain and the hydro-pneumatic suspension.

1.4 Organization of the dissertation – manuscript based format

This dissertation is prepared according to the manuscript-based format described in "Thesis Preparation, Examination Procedures and Regulations" guidelines of the School of Graduate Studies, Concordia University. This dissertation research is organized into 7 chapters, which address the research goals mentioned above, including the introduction and literature review chapter (Chapter 1). The first chapter mainly summarizes a comprehensive literature review of studies reporting the ride and directional dynamics analyses, and suspension designs for off-road vehicles. In Chapters 2, a roll-plane stability performance measure is defined considering terrain roughness and a single-unit mining truck model (goal (i)). Chapters 3 and 4 present the analyses of the AFS system coupled with the yaw-plane model of an articulated mining vehicle, and optimal design of the AFS to achieve improved yaw-plane performance of the AFSV (goals (i) and (ii)). Chapter 5 presents the experimental characterization and analytical modeling of a hydro-pneumatic suspension strut for off-road vehicles (goal (iii)). The three-dimensional model of the AFSV integrating the kineto-dynamic model of the AFS and hydro-pneumatic suspension is presented in Chapter 6 for analyses of both ride and directional stability performances (goal (iv)). Chapters 2 to 6 are compiled from 3 manuscripts published in international peer-reviewed journals, and 2 manuscripts submitted to the journals for review. These are further summarized below:

Chapter 2 presents the following paper published in the Journal of Terramechanics:

Y. Yin, S. Rakheja, P. Boileau (2016), A roll stability performance measure for off-road vehicles, Journal of Terramechanics, 64: 58-68.

This study proposed an alternative performance measure for assessing roll stability limits of off-road vehicles. The roll dynamics of an off-road mining vehicle operating on random rough terrains were investigated, where the two terrain-track profiles were synthesized considering coherency between them. It is shown that a measure based on steady-turning root-mean-square lateral acceleration corresponding to the sustained period of unity lateral-load-transfer-ratio prior to the absolute-rollover, could serve as a reliable measure of roll stability of the vehicle operating on random rough terrains. The robustness of proposed performance measure was demonstrated considering sprung mass center height variations and different terrain excitations. The simulation results revealed adverse effects of terrain elevation magnitude on the roll stability, while a relatively higher coherency resulted in lower terrain roll-excitation and thereby enhanced vehicle roll stability. Terrains with relatively higher waviness increased the magnitude of lower spatial frequency components, which resulted in reduced roll stability limits.

Chapter 3 presents the following paper published in the Proceedings of the Institution of Mechanical Engineers, Part D: Journal of Automobile Engineering:

Y. Yin, S. Rakheja, J. Yang, P. Boileau (2017), Effects of articulated frame steering on transient yaw responses of the vehicle, Proceedings of the Institution of Mechanical Engineers, Part D: Journal of Automobile Engineering (DOI: 10.1177/0954407017702987).

This study characterized both the free yaw-oscillation and transient steering responses of an articulated frame steering (AFS) mining vehicle considering kinematics of the steering struts together with the dynamics of the flow volume-regulated steering valve and the actuating system. The validity of the analytical vehicle and steering system model was demonstrated using the measured data acquired for the vehicle. The free-oscillation behavior of the AFS was characterized in terms of the yaw-mode natural frequency and yaw damping ratio. The transient responses of the AFS were assessed in terms of the steering gain, rate of articulation and articulation overshoot. The effects of variations in various AFS parameters on the free and transient responses were subsequently investigated and discussed so as to seek guidance for the AFS system design. It was shown that the greater bulk modulus of the hydraulic fluid and steering arm lengths would yield higher yaw stiffness of the AFS system and thereby higher frequency of yaw-oscillations. Greater leakage flows and viscous seal friction caused higher yaw damping coefficient but worsened the steering gain and articulation rate of the vehicle.

Chapter 4 presents the following paper accepted for publication in the Proceedings of the Institution of Mechanical Engineers, Part D: Journal of Automobile Engineering:

Y. Yin, S. Rakheja, J. Yang, P. Boileau (2017), Design optimization of an articulated frame steering system, Proceedings of the Institution of Mechanical Engineers, Part D: Journal of Automobile Engineering.

In this study, the yaw-plane model of the articulated vehicle coupled with the kinematic and dynamics properties of the steering struts, presented in Chapter 3, is utilized to identify objective measures of the articulated frame-steered vehicle (AFSV) under steering inputs. The results suggested that the vehicle yaw oscillation/stability, steering power efficiency and maneuverability could be objectively measured in terms of the strut length, yaw oscillation frequency, damping ratio, steering gain, and steering response rate and overshoot. The layout of the steering struts, and properties of the steering valve and hydraulic fluid are optimized using the weighted-sum method and a combination of pattern search and sequential quadratic programming algorithms. The relative weights of individual performance measures were obtained using the Analytic Hierarchy Process (AHP) model. The solutions of the optimization problem revealed more compact articulated frame steering (AFS) system design with over 20% reduction in strut length and 24% gain in the yaw oscillation frequency. Increasing the fluid bulk modulus resulted in more compact AFS layout and further increase in the yaw oscillation frequency with lower response overshoot. The optimal design based on weighted sum of various performance measures, however, revealed negligible changes in terms of the steering power efficiency.

Chapter 5 presents the following paper that has been submitted to Mechanical System and Signal Processing journal:

Y. Yin, S. Rakheja, J. Yang, P. Boileau (2017), Characterization of a hydro-pneumatic suspension strut with gas-oil emulsion, Mechanical System and Signal Processing.

In this paper, the nonlinear stiffness and damping properties of a simple and low-cost design of a hydro-pneumatic suspension (HPS) strut that permits entrapment of gas into the hydraulic oil were characterized experimentally and analytically. The formulation of gas-oil emulsion was studied in the laboratory, and the variations in the bulk modulus and mass density of the emulsion were formulated as a function of the gas volume fraction. An analytical model of the HPS was formulated considering polytropic change in the gas state, seal friction, and the gas-oil emulsion flows through orifices and valves. The model was formulated considering one and two bleed orifices configurations of the strut. The measured data acquired under a nearly constant temperature were used to identify gas volume fraction of the emulsion, and friction and flow discharge coefficients as functions of the strut velocity and fluid pressure. The results suggested that single orifice configuration, owing to high fluid pressure, caused greater gas entrapment within the oil and thus significantly higher compressibility of the gas-oil emulsion. The model results obtained under different excitations in the 0.1 to 8 Hz frequency range showed reasonably good agreements with the measured stiffness and damping properties of the HPS strut. The results showed that the variations in fluid compressibility and free gas volume cause increase in effective stiffness but considerable reduction in the damping in a highly nonlinear manner. Increasing the gas volume fraction resulted in substantial hysteresis in the force-deflection and force-velocity characteristics of the strut.

Chapter 6 presents the following paper that has been submitted to the Vehicle System Dynamics journal:

Y. Yin, S. Rakheja, P. Boileau (2017), Multi-performance optimization of a hydro-pneumatic suspension system for an off-road work vehicle, Vehicle System Dynamics.

This paper presented the three-dimensional multi-body model of an AFSV integrating the hydro-pneumatic suspension (HPS) strut, presented in Chapter 5, and the kineto-dynamics of the steering system. The model was developed in the ADAMS platform considering nonlinear tire interactions with the uneven terrain profiles. The field test data in terms of the ride vibrations and directional responses were used to demonstrate the model validity. An optimization problem was formulated to seek optimal suspension parameters considering the roll stability performance measure, proposed in Chapter 2, yaw-plane oscillation stability in Chapter 3 and 4, and the ride vibration attenuation performance. The structural parameters of the HPS struts were optimized using the integrated model in order to minimize the multi-axes vibrations while preserving the roll- and yaw-plane dynamic stabilities of the vehicle.

The contents of above-stated manuscripts are interrelated to ensure the flow of the dissertation according to the thesis regulations. A few repetitions in the analytical formulations and results, however, are evident. These manuscripts presented in the dissertation have been reformatted, while the references have been grouped together and renumbered according to the thesis regulations.

CHAPTER 2

A ROLL STABILITY PERFORMANCE MEASURE FOR OFF-ROAD VEHICLES

2.1 Introduction

The roll stability is among the most significant factors for commercial road as well as off-road vehicles, while the vast majority of reported studies focus on only road vehicles assuming negligible contributions of road roughness [105-107]. The maneuver-induced dynamic roll stability of commercial road vehicles has been widely investigated during cornering maneuver considering smooth road surface in addition to various design factors affecting the roll stability limits [105]. These have evolved in various performance measures to assess relative roll stability limits of vehicles such as static and dynamic rollover threshold, lateral load transfer ratio (LTR), roll safety factor (RSF), rearward amplification (RA) and rollover prevention energy reserve (RPER) [40, 108, 109]. Compared to road vehicles, only a few studies have reported roll stability analyses of off-road vehicles, which is partly due to relatively low speed operations of traditional off-road vehicles. High load-capacity and high-speed vehicles, however, are being increasingly employed in the resource and construction sectors to achieve enhanced productivity and operational efficiency [110]. The demand for high load-capacity and high-speed vehicles has been steadily growing, especially in the open-pit mining sector. A recent study has identified relatively higher frequency of fatal accidents of mining trucks, primarily attributed to vehicle rollover, apart from the structure failures and vehicle collisions [8]. In order to limit the frequency of mining vehicle accidents, especially the vehicle rollover, speed limits ranging from 30 to 60km/h have been widely reported in the mining sectors [111]. Both the greater load capacity and high operating speeds have contributed to greater concerns related to the operational safety of such vehicles.

Owing to tires' interactions with relatively rough terrains, the off-road vehicles exhibit considerably different roll dynamics compared to the road vehicles [56]. In the presence of the terrain roughness, the coupled vertical and lateral tire-road interactions could adversely affect the vehicle roll dynamics and thereby the stability limits [21]. The changes in terrain elevations cause not only considerable variations in restoring roll moment attributed to tires' normal forces, but also affect lateral forces developed by tires and thereby the directional performance of the vehicle. Moreover, tires' interactions with rough terrains could yield greater roll and pitch motions as well as load transfer between tires of different axles, which may adversely affect roll stability of the vehicle [20]. Considerations of tires' interactions with rough terrains would be important for assessing roll dynamic performance and stability limits of off-road vehicles.

A few studies have illustrated the adverse effects of terrain roughness on vehicle roll stability [20, 21, 112]. Gonzalez et al. [112] investigated roll dynamics of a vehicle where the random terrain excitation was represented by an equivalent force applied to the vehicle unsprung mass. The study concluded that in the presence of terrain roughness, the vehicle wheels may lift-off the ground before the vehicle approaches its rollover threshold limit. Li et al. [21] and Pazooki et al. [20] investigated terrain-induced vertical and roll responses of off-road vehicle models considering time history of the random terrain elevation and high coherency of low frequency components of the left- and right- terrain tracks. Li et al. [21] investigated rollover risk of the vehicle negotiating a fishhook maneuver at a constant forward speed of 54km/h on road surfaces B, C and D defined in ISO-8608 [78]. The study concluded that the roll stability limit decreases with increasing terrain roughness, which was assessed in terms of peak normalized rollover critical factor (RCF) as a function of the vehicle roll angle and instantaneous position of the mass center (cg). Pazooki et al. [20] investigated the static and dynamic rollover thresholds of an articulated frame steered vehicle during constant-speed turning and path-change maneuvers, considering different off-road terrains, namely, pasture, MVEE (Military Vehicles and Engineering Establishment) course and plowed-field. The study employed a roll stability measure based on effective lateral acceleration (ELA) at the instant of rear axle wheel lift-off when the roll safety factor approaches a unity value (RSF=1).

The roll stability limits of off-road vehicles in the aforementioned studies have been assessed using measures defined for heavy road vehicles. The validity of these measures, defined for road vehicles assuming negligible contributions due to tires' interactions with relatively rough terrains, may be questioned. Moreover, in off-road operations, the stability indicators based on peak ELA, RSF or RCF cannot be determined reliably due to large variations in these measures that are caused by tires' interactions with randomly distributed terrain roughness. Alternate measures thus need to be defined for assessing roll stability limits and rollover risks of off-road vehicles in the presence of terrain roughness. The above-stated studies have provided valuable insight into the effects of terrain elevation magnitude on the roll dynamics stability limits of off-road vehicles, while the effects of spectral distribution of terrain roughness have not been attempted. Moreover, these studies employed point-contact tire models neglecting the tire-terrain contact patch, which would likely yield errors in the roll stability measures due to more frequent wheel lift-off, particularly for shorter wavelength terrains [113].

In this study, a roll stability performance measure is proposed for off-road vehicles considering magnitude and spectral contents of the terrain. A comprehensive mining truck model is constructed in the TruckSim platform coupled with the Matlab/Simulink to evaluate its roll dynamic responses under different terrain excitations. The vehicle model considers the variation of tire footprint using circle-line approach, while the tire force is evaluated considering a non-linear point-contact tire model. The roll dynamic responses obtained during cornering maneuver are analyzed to derive the roll stability performance measure. The robustness of proposed performance measure is subsequently assessed, and the effects of magnitude and frequency components of the terrain on roll stability limits of the off-road vehicle are studied as well.

2.2 Vehicle model formulation

A multi-body dynamic model of a 50 tons mining truck is constructed in the TruckSim simulation platform to study its roll dynamics behavior. The TruckSim platform permits modelling and integration of various vehicle subsystem models, such as tire, suspension and steering, in a convenient manner using either lumped-parameters or mathematical models or datasets [114]. The vehicle model is pictorially illustrated in Fig. 2.1. The maximum load capacity of the target mining truck is 50 tons. The rear axle of the vehicle is supported on a set of dual tires, while the front axle comprises a set of single tires. The dimensional and inertial parameters of the vehicle are listed in Table 2.1, which were obtained from the design manual [115] and a published study [116]. The mass moments of inertia of subsystems are defined with respect to the mass center (cg) of each component.

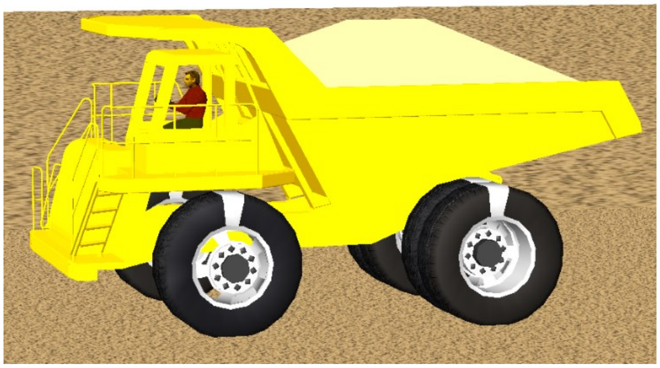

Figure 2.1: Simulation model of a 50 tons mining truck in the TruckSim platform

Table 2.1: Dimensional and inertial parameters of the 50 tons mining truck [115, 116]

Parameters	Unloaded	Loaded
Wheel base (m)	4.02	
Front track (m)	3.3	
Rear track (m)	2.8	
Rear axle dual tire space (m)	0.69	
Front axle unsprung mass (kg)	3,900	
Rear axle unsprung mass (kg)	7,800	
- roll mass moment inertia (kgm^2)	13,701	
Sprung mass (kg)	23,400	73,840
- cg height (m)	2.35	3.15
- cg to front axle (longitudinal, m)	1.31	2.57
- roll mass moment inertia (kgm^2)	43,401	119,652
- pitch mass moment inertia (kgm^2)	115,700	286,761
- yaw mass moment inertia (kgm^2)	89,400	194,030

The candidate vehicle is equipped with an independent front-axle suspension and a solid rear-axle suspension. The suspension parameters are linearized at loaded equilibrium condition based on the design parameters [115, 116], and listed in Table 2.2. The suspension bump stops are considered as high stiffness clearance springs in order to limit the suspension travel. The vehicle driving torque developed at the rear axle is regulated using a proportional-integral (PI) controller, in order to maintain a specified constant forward speed of the vehicle during simulation.

Table 2.2: Suspension parameters of the 50 tons mining truck [115, 116]

Parameters	Value
Front suspension stiffness (kN/mm)	1.1
Front suspension damping coefficient (kNs/m)	10
Front suspension travel (cm)	30
Rear suspension stiffness (kN/mm)	5.2
Rear suspension damping coefficient (kNs/m)	15
Rear suspension travel (cm)	22

2.2.1 Tire model

The off-road tire is modelled considering the effect of tire-terrain contact patch. The circle-line interaction representation [117] is implemented in order to obtain the effective contact patch, as seen in Fig. 2.2, which is indicated as the line between the intersection points P_1 and P_2. The tire vertical compliance and dissipative characteristics are simplified as a linear spring and damper, such that the tire normal force F_{zt} is calculated considering the possible loss of contact of tire with the terrain, as:

$$F_{zt} = \begin{cases} k_t\delta + c_t\dot{\delta}; & \delta > 0 \\ 0 & ; \delta \leq 0 \end{cases} \tag{2.1}$$

where k_t and c_t are the tire vertical stiffness and damping coefficients, respectively; δ is tire deflection, which is determined considering effective tire-terrain contact [117], as:

$$\delta = (z_{oi} - z_u)/\cos\vartheta \tag{2.2}$$

where z_u is the vertical motion of the wheel center, z_{oi} is the effective terrain elevation defined over the instantaneous contact patch and considered as average of the terrain elevation at the intersection points $P_1(z_{P1})$ and $P_2(z_{P1})$, as shown in Fig. 2.2, such that:

$$z_{oi} = (z_{P1} + z_{P2})/2 \tag{2.3}$$

The coordinates of the intersection points P_1 and P_2 on the wheel circumference are determined using the circle-line intersection algorithm and the terrain profile points in the immediate vicinity of P_1 and P_2 [117, 118]. In Equation (2.2), ϑ is slope of the linear terrain profile P_1P_2, such that:

$$\vartheta = \tan^{-1}\left((z_{P2} - z_{P1})/\Delta x\right) \tag{2.4}$$

where Δx is length of the instantaneous contact patch length, which is obtained through projection of linear terrain profile P_1P_2 along the x-axis, as shown in Fig. 2.2.

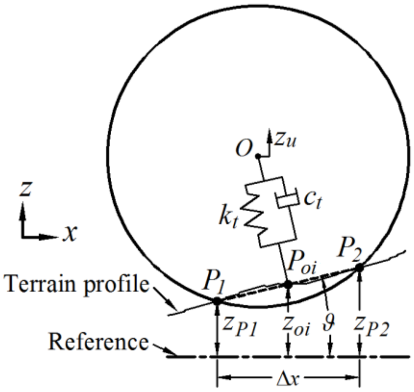

Figure 2.2: Effective tire-terrain contact patch

The tire cornering force F_{yt} is defined as a linear function of the tire slip angle α for the given normal load. Since the cornering stiffness k_{ty} is positively correlated with the tire normal force F_{zt} [79], k_{ty} during a steering maneuver will change due to dynamic load transfer between the inside and outside tires. In the TruckSim platform, the linear interpolation/extrapolation is utilized to calculate the cornering stiffness corresponding to instantaneous tire normal loads. The cornering force developed by a vehicle tire is obtained from:

$$F_{yt} = k_{ty}\alpha \tag{2.5}$$

The tire slip angle α is defined as the angle between the lateral velocity of tire-terrain contact center (V_{sy}) and the longitudinal velocity of wheel center (V_x):

$$\alpha = \tan^{-1}\left(V_{sy}/|V_x|\right) \tag{2.6}$$

A first order tire lag, proposed in [119], is also employed in the TruckSim platform, in order to represent the tire lateral transient response, such that:

$$\dot{V}_{sy} = \frac{|V_x|}{\sigma_y}\left(V_y - V_{sy}\right) \tag{2.7}$$

where σ_y is the tire lateral relaxation length and V_y is the lateral velocity of wheel center. V_{sy} approaches V_y after a certain time lapse. Table 2.3 lists the physical properties of the off-road tire (21-35) including the dimensions, effective vertical stiffness and damping coefficients, cornering stiffness and tire lateral relaxation length [115, 116].

Table 2.3: Simulation parameters of the off-road tire [115, 116]

Parameters	Values
Free radius (m)	1.06
Effective rolling radius (m)	0.955
Tire width (m)	0.575
Vertical spring rate (kN/mm)	1.8
Vertical damping coefficient (kN.s/m)	6.0
Cornering stiffness (kN/mm, F_{zt}=140kN)	4.0
Lateral relaxation length (m)	1.0

2.2.2 Off-road terrain model

The off-road terrain roughness is usually described by an equivalent undeformable profile elevation for the purpose of vehicle dynamic analyses [20, 21]. The terrain profile can be effectively generated from the displacement power spectral density (PSD) function, widely defined as function of the terrain waviness w and spatial frequency n, as [56, 78, 79]:

$$G_d(m) = \alpha_r \cdot m^{-w} \tag{2.8}$$

where G_d is the one-sided spatial PSD of the terrain elevation and α_r is the roughness coefficient. The ISO-8608 [78] describes the spatial PSD of different road profiles ranging from smooth (class A) to very rough (class E) considering a reference spatial frequency m_0 (=0.1 cycles/m) and constant waviness of 2.0. The roughness coefficient α_r and waviness w of the standardized terrain classes A to E and several other reported off-road terrains are compared in Table 2.4 [78, 79, 81]. The off-road terrains generally exhibit higher roughness coefficients compared to the road profiles, which implies greater elevations. The limited data available for a haul road in a mining site suggest that the haul road elevation is comparable to that of class E terrain (very poor) in ISO/TC108/SC2/WG4 N57 [120], near the reference special frequency, as seen in Fig. 2.3 [121, 122]. While the terrain waviness of the haul road in Fig. 2.3 is higher than that of the class E terrain, which contributes to higher roughness magnitudes at lower spatial frequency components ($m < m_0$) and lower magnitudes at higher frequency components ($m > m_0$). The low frequency components generally govern the elevation of the off-road haul terrain, especially the cross-slope contributing to roll excitations [20, 123].

Table 2.4: The reported roughness coefficients and waviness of different terrains [78, 79, 81]

Terrain	α_r (geometric mean)	w	Off-road terrain	α_r	w
Class A	1.6×10^{-7}	2.0	Forestry	1.00×10^{-4}	1.76
Class B	6.4×10^{-7}	2.0	Pasture	3.00×10^{-4}	1.60
Class C	2.56×10^{-6}	2.0	MVEE	3.16×10^{-4}	2.27
Class D	1.024×10^{-5}	2.0	Plowed	6.50×10^{-4}	1.60
Class E	4.096×10^{-5}	2.0			

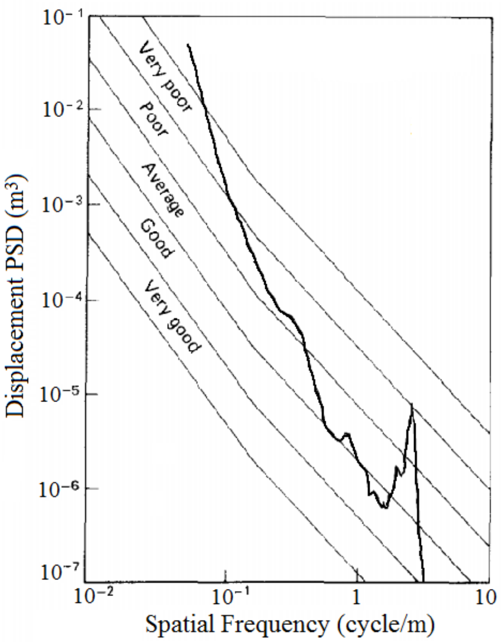

Figure 2.3: Displacement PSD of a haul road for heavy-duty dumpers [122]

The elevation histories of terrain have been obtained through processing a zero-mean white noise random signal with a frequency response function [20, 78, 124]. In this study, two unity power band-limited white noise signals, $wn_1(x)$ and $wn_2(x)$, are utilized to obtain the profiles of two terrain tracks $q(x)$ and $p(x)$, as shown in Fig. 2.4, where x is longitudinal coordinate of the terrain. Since the PSD functions of $q(x)$ and $p(x)$, $Q(m)$ and $P(m)$, are governed by $G_d(m)$ described in Equation (2.8), a frequency response function $\sqrt{G_d(m)}$ is employed to obtain $q(x)$

and $p(x)$ [125]. The relation between the profiles of two terrain tracks is dependent upon the coherence function, defined as [78]:

$$\gamma^2(m) = \frac{G_{qp}^2(m)}{Q(m) \cdot P(m)} \tag{2.9}$$

where $G_{qp}(m)$ is the cross-spectral density function of $q(x)$ and $p(x)$. As shown in Fig. 2.4, the frequency response function $\sqrt{\gamma^2(m)}$ determines the correlated components of the two tracks and $\sqrt{1-\gamma^2(m)}$ determines the uncorrelated components of $q(x)$ and $p(x)$ [125]. The coherency between the two tracks $\gamma^2(m)$ determines the roll excitations due to the terrain. A piecewise linear coherence function can be formulated on the basis of the reported experimental results [86, 87], so as to describe the roll excitation due to elevation differences of the two tracks, in the form of [86]:

$$\gamma^2(m) = \begin{cases} 1 - 0.9m/m_c, & m \leq m_c \\ 0.1, & m > m_c \end{cases} \tag{2.10}$$

where m_c is the cut-off spatial frequency after which the coherency between the two tracks is a small constant.

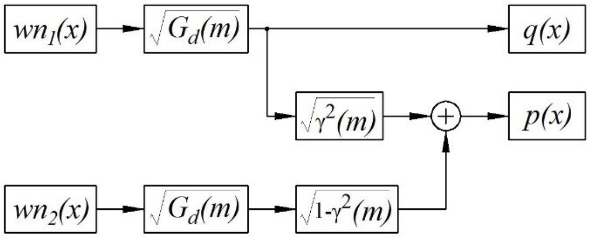

Figure 2.4: Schematic to synthesis left and right terrain profiles

Bogsjö [87] presented the coherency between the measured elevations of two tracks of three different roads, including a gravel road, as shown in Fig. 2.5. The results suggest that for the gravel road, the coherence decreases to 0.1 at around 0.4 cycles/m. A higher coherence implies greater similarity of the two tracks and thereby less roll excitation. The off-road terrains generally exhibit higher magnitude of cross-slope, especially in the lower spatial frequency range [22, 123], which suggest lower coherence in the lower spatial frequency range. In this study, the cut-off spatial frequency is taken as 0.3 cycles/m, while the elevations of the off-road terrain are estimated assuming the spectrum of the class E profile, described in ISO-8608. The range of the spatial frequency is selected as 0.02 to 5 cycles/m, which relates to relatively large range of excitation frequencies (0.03 to 70 Hz) in the 5 to 50 km/h speed range.

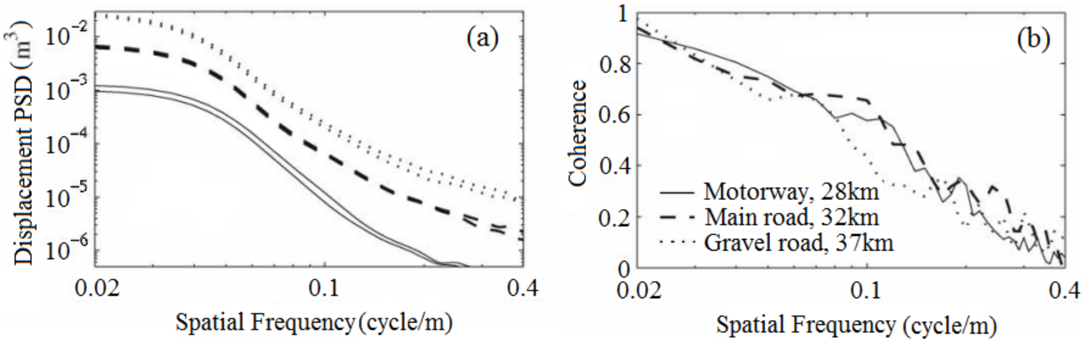

Figure 2.5: The PSD and coherency of the measured road elevations: (a) displacement PSDs; and (b) coherence between two tracks [87]

The elevations of the two tracks are generated using the method described in Fig. 2.4, where the functions $\sqrt{G_d(m)}$, $\sqrt{\gamma^2(m)}$ and $\sqrt{1-\gamma^2(m)}$ are represented by the third-order system functions. Figures 2.6(a) and 2.6(b), respectively, illustrate the generated profile, $q(x)$ and $p(x)$, and their PSD spectra, $Q(m)$ and $P(m)$. The displacement PSD of the standardized class E profile is also presented in Fig. 2.6(b). The coherence between the two track elevations is presented in Fig. 2.6(c) together with the assumed coherence function (m_c=0.3 cycles/m). The results clearly show that the displacement spectra of the two tracks' elevation are comparable with PSD of the standardized road profile, while the coherence between the two tracks' elevation closely follows the assumed coherence function. The PSD of the cross-slope between the tracks' elevation is also computed and presented in terms of the roll angle excitation in Fig. 2.7, considering different cut-off frequencies, ranging from 0.3 to 0.9 cycles/m. The results show that a higher cut-off frequency yields lower roll excitation in the lower frequency range due to greater coherence between the two tracks.

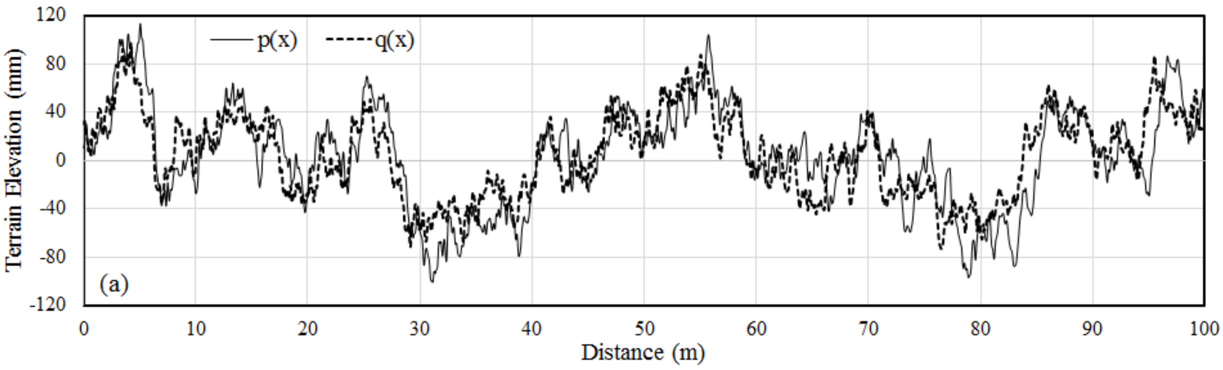

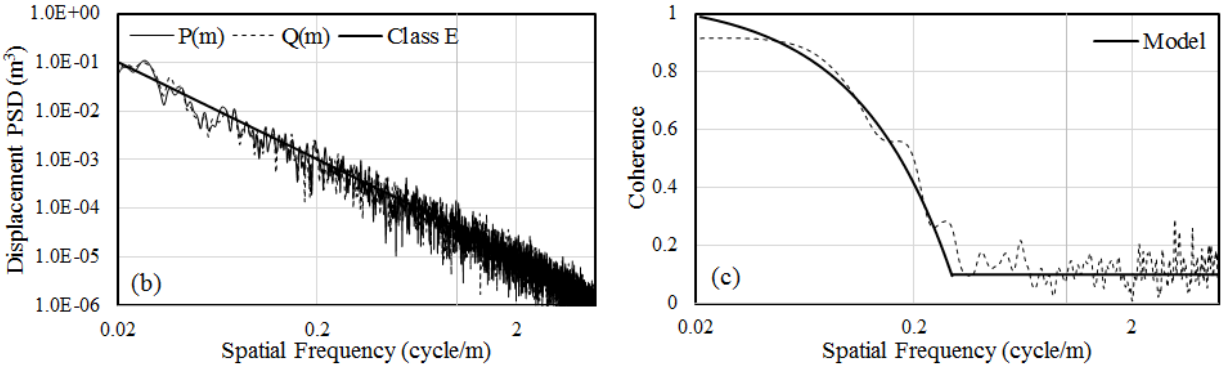

Figure 2.6: (a) Elevations of the two tracks of the terrain; (b) comparison of displacement PSD of the two tracks, $P(m)$ and $Q(m)$, with that of standardized profile; and (c) comparison of coherence between the two tracks with the coherence model

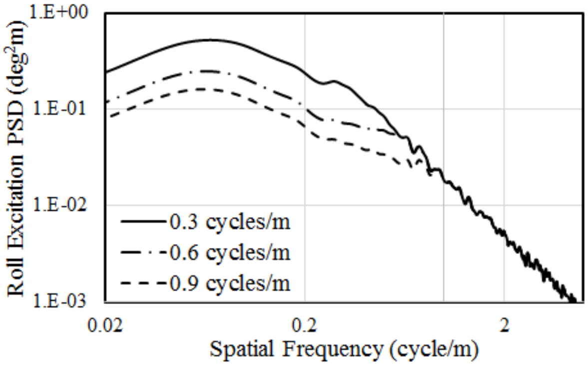

Figure 2.7: Effect of cut-off frequency on the PSD of cross-slope between the two tracks (roll excitations)

2.3 Roll dynamic analyses and stability performance measure

The dynamic relative roll stability limits of road vehicles have been widely defined in terms of dynamic rollover threshold (DRT) corresponding to wheels lift-off during cornering maneuvers, expressed in terms of lateral load transfer ratio (LTR) [41, 105]. In case of off-road vehicles involving tires' interactions with rough terrains, the determination of LTR poses considerable challenges due to large oscillations in the instantaneous tire forces. The applicability of the LTR measure to predict the roll stability limit of the two-axles mining truck, considered in this study, is investigated using the definition:

$$LTR = \left| \frac{\left(F_{zLf} - F_{zRf}\right) + \left(F_{zLr} - F_{zRr}\right)}{\left(F_{zLf} + F_{zRf}\right) + \left(F_{zLr} + F_{zRr}\right)} \right| \tag{2.11}$$

where F_{zij} is the normal force of tires i (i=R, L) of axle j (j=f, r), where R and L respect the right- and left- track tires, respectively, and f and r respect the front- and rear- axles, respectively. It is evident that the LTR approaches unity when the tires on a given track lift-off the terrain.

The roll dynamic responses of the vehicle model are evaluated during cornering maneuvers, idealized by a ramp steering wheel input. The simulations are performanced for a perfectly smooth road profile and the synthesized terrain profiles presented in Fig. 2.6(a). The vehicle forward speed is maintained around 40 km/h, which is close to the maximum possible speed for the candidate vehicle in the open-pit mining regions. The simulations are terminated when the vehicle approaches the absolute rollover as the vehicle mass center aligns vertically above the line joining the contact centers of outside tires of the front and rear axles [41].

Figure 2.8 illustrates the time-histories of lateral acceleration and LTR responses of the loaded vehicle model traversing the smooth as well as off-road terrain. Both the lateral acceleration and LTR trend to increase gradually with increasing steering input, irrespective of the terrain. The responses on the off-road terrain, however, exhibit considerable high-frequency oscillations, which make it difficult to identify the onset of a roll instability, and the corresponding lateral acceleration and LTR. The responses on the smooth road surface also exhibit some oscillation near t=30s, which are attributed to suspension strut topping/bottoming, prior to the vehicle approaching absolute rollover indicated by point B in Fig. 2.8. It is further seen that the LTR approaches unity, at point A, slightly before the absolute rollover and remains near 1 until absolute rollover. Beyond this point, the lateral acceleration decreases sharply as the vehicle approaches absolute rollover. The lateral acceleration corresponding to point A can be considered as the relative dynamic rollover threshold (DRT=0.279g) for the vehicle operating on smooth surface.

In the presence of terrain roughness, the LTR response momentarily approaches unity value, as seen in Fig. 2.8(a), although the corresponding lateral acceleration may be quite low. The LTR therefore cannot serve as a reliable measure of dynamic roll stability. Figure 2.9 illustrates the LTR and lateral acceleration responses zoomed over short intervals around t=14.5s and t=35s. The results, however, show that the LTR remains unity after t=39.29s, indicated by A^4, as it was observed in the responses with smooth road surface. This event is followed by absolute rollover and rapid decrease in the lateral acceleration (point B’). The lateral accelerations corresponding to A^4 and B’, however, are relatively low as 0.174g and 0.135g, respectively, compared to the peak acceleration (0.53g). These acceleration values therefore may not adequately relate to dynamic rollover thresholds. The dynamic roll stability criterion developed for road vehicles [105] thus cannot be considered reliable for off-road vehicles.

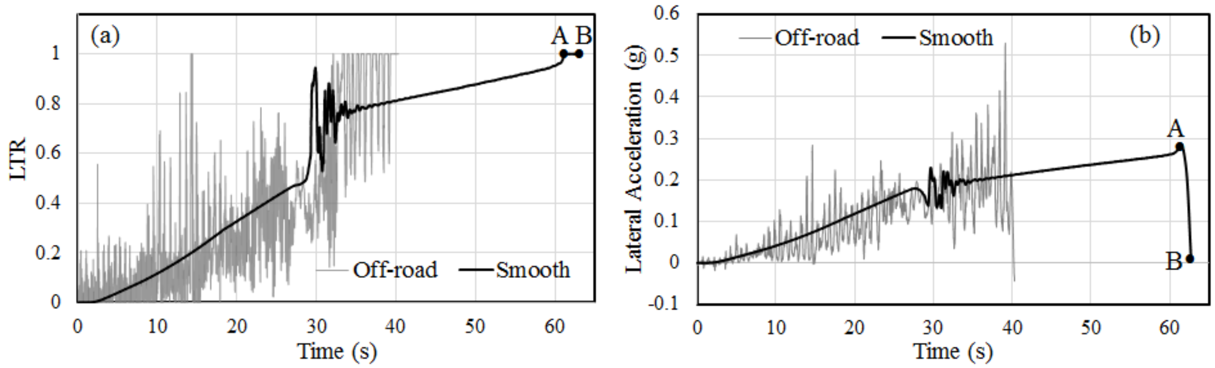

Figure 2.8: Cornering maneuver responses: (a) LTR and (b) lateral acceleration

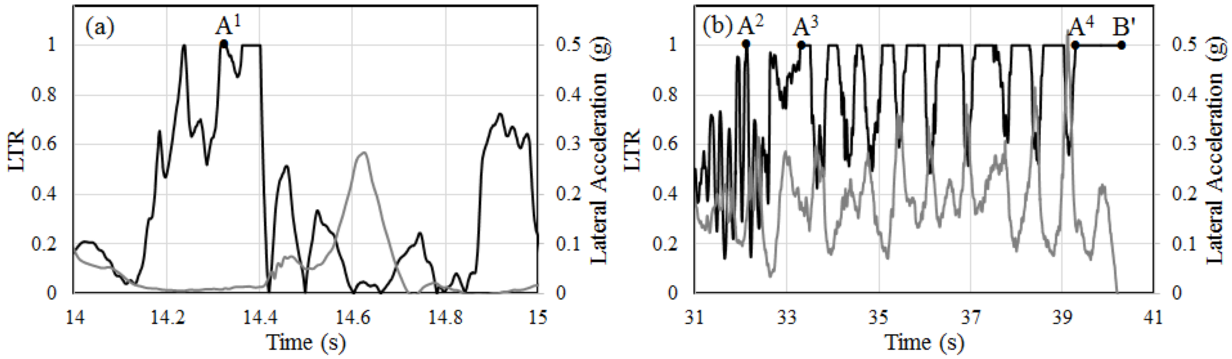

Figure 2.9: LTR (──) and lateral acceleration (──) responses during cornering maneuver on the synthesized off-road terrain: (a) 14≤ t ≤15s and (b) 31≤ t ≤41s

The results presented in Fig. 2.9(b), however, suggest that the LTR value mostly remains near 1 in the interval between point A^3 to A^4. The vehicle can be interpreted as within the critical roll stability margin during this period. The lateral acceleration during this period, however, varies considerably from 0.17g to 0.53g. The root mean square (RMS) acceleration response during the period of sustained unity value of LTR may be considered as the DRT acceleration of the off-road vehicle, which was obtained as 0.203g. The duration of sustained unity LTR value is also significant considering that the LTR also approaches 1 at relatively lower acceleration (e.g., A^1). This duration should be sufficiently long so as to obtain a reliable indication of relative roll stability. The sustained period ΔT (from A^3 to A^4) is in the order of 9.6s, which indicates the likelihood of vehicle rollover. The roll stability measure of the off-road vehicle is thus proposed as the RMS lateral acceleration response over the sustained period of unity LTR value.

The proposed measure is further assessed considering variations in the sprung mass cg height. The sprung mass cg height is varied by ±0.15 and ±0.3m about the nominal height of 3.15m. Figure 2.10(a) illustrates variations in the proposed dynamic rollover threshold acceleration measure over the sustained period with varying sprung mass cg height together with the DRT obtained for the smooth road and the Static Stability Factor (SSF, ratio of half wheel track to cg height). The SSF is obtained considering the overall vehicle cg height. The proposed DRT, DRT on the smooth road and SSF gradually decrease with increasing cg height, as expected. Similar trends are evident in all the three measures with increasing cg height. The DRT obtained for the off-road terrain, however, is consistently lower than that for the smooth road. When the cg height is 2.85 m, the DRT obtained for the off-road terrain is 22.3% lower than that for the smooth surface. With cg height increased to 3.5 m, the DRT on the rough terrain is 16% lower than that on the smooth surface. This is attributed to lower sustained period of LTR for the higher cg vehicle, as seen in Fig. 2.10(b). The results show that increasing the cg height from the nominal value yields substantial smaller ΔT suggesting rapid transition from a relative rollover to absolute rollover. Furthermore, the proposed DRT obtained for the off-road terrain is directly correlated with the DRT for the smooth road ($r^2 > 0.97$), as seen in Fig. 2.11.

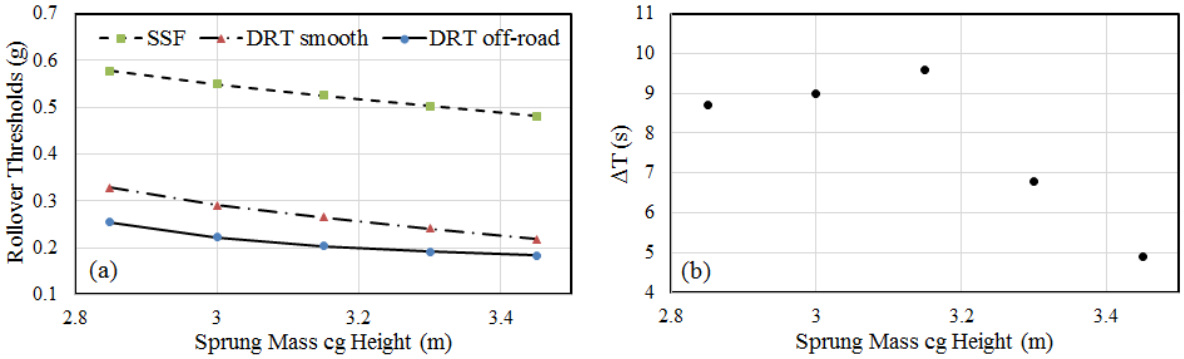

Figure 2.10: Variations in (a) DRT obtained for off-road and smooth surfaces, and SSF with sprung mass cg height; (b) sustained period of LTR on the off-road terrain with sprung mass cg height

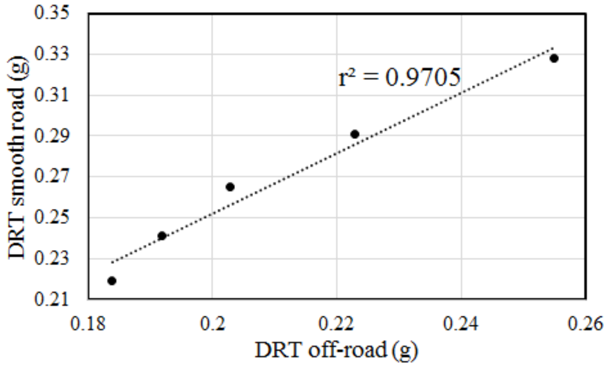

Figure 2.11: Correlation between DRT acceleration obtained for the off-road and smooth road surfaces over the range of sprung mass cg height

2.4 Parametric analyses and discussions

The roll dynamics of the vehicle are strongly affected by properties of the off-road terrain such as roughness, waviness, spectral components and coherency between the two tracks. The reliability of the proposed DRT measure and the method is investigated considering variations in the properties of the off-road terrain. The roll dynamic responses of the loaded vehicle model are evaluated in the similar manner, while the off-road terrain properties are varied. These include the roughness coefficient α_r, terrain waviness w, and spatial frequency range m in Eq. (2.8) and cut-off frequency m_c in the coherence function in Eq. (2.10). The simulation results are obtained by varying only one of the terrain parameters at one time so as to study the effect of each parameter on the DRT and sustained period ΔT. The results are discussed to highlight the influences of terrain properties on the roll stability of the off-road vehicle.

On the basis of reported terrain properties in Table 2.4, five different values of the α_r (1.6×10^{-7}, 6.4×10^{-7}, 2.56×10^{-6}, 1.024×10^{-5} and 4.096×10^{-5}) and terrain waviness w (1.6, 1.8, 2.0, 2.2 and 2.4) are considered. Different ranges of spatial frequency are considered to study the effect of frequency of terrain excitations, these included: 0.02-1, 0.02-3, 0.02-5, 0.02-10, 0.05-5, 0.15-5, 0.25-5 cycles/m. The terrain excitation in the 0.02-1 cycles/m frequency range represents dominantly low frequency components, while the range 0.02-10 cycles/m is used to study the effect of additional higher frequency components. The frequency range 0.25-5 cycles/m, on the other hand, is used to investigate the effect of relatively higher frequency components with lower emphasis on the low frequency components. The coherency between the two tracks is varied by varying the cut-off frequency m_c (0.3, 0.6 and 0.9 cycles/m), which directly affect the magnitude of low frequency roll excitations due to terrain, as seen in Fig. 2.7. The roll dynamic responses are analyzed to determine sustained period ΔT of unity value of LTR and the DRT based on RMS lateral acceleration responses over ΔT. Figures 2.12 to 2.14 illustrate the relations between the DRT measure and sustained period with various terrain parameters.

Figure 2.12 illustrates the effect of terrain roughness coefficient on DRT and ΔT, considering different cut-off frequencies of the coherence function. An increase in the roughness coefficient α_r leads to lower DRT but higher ΔT, irrespective of the cut-off frequency m_c. Increasing the terrain roughness causes greater oscillations in the LTR, which contribute to relatively higher sustained period. For m_c=0.3 cycles/m, the DRT value decreases by nearly 17% when α_r is increased from 1.6×10^{-7} (Class A) to 4.096×10^{-5} (Class E), while the corresponding ΔT increases nearly 6.4 times. The adverse effect of terrain roughness magnitude on roll stability of the vehicles has also been reported by Li et al. [21] and Pazooki et al. [20], for standardized and off-road surfaces, respectively. The results further show notable effect of coherency between the two terrain tracks on the DRT and ΔT, especially under higher roughness terrains. Increasing the cut-off frequency of the coherence function reduces the magnitude of roll excitation (Fig. 2.7), which results in relatively higher DRT and lower ΔT.

An increase in the terrain waviness w, also adversely affect the roll stability of the vehicle. The DRT decreases with higher waviness, while ΔT increases, as shown in Fig. 2.13. An increase in the waviness yields higher roughness magnitude at relatively lower spatial frequencies ($m < m_0$), thereby higher low frequency roll excitation due to terrain. This results in lower DRT, which is also observed from the effect of frequency range of terrain roughness in Fig. 2.14. The results suggest lower DRT when terrain elevations comprise lower spectral components ($0.02 \leq m \leq 1$). While the obtained DRT decreases by only 4% with waviness increasing from 1.6 to 2.4, it decreases by nearly 10% when the terrain profile contains lower spatial frequency components ($0.02 \leq m \leq 5$), as seen in Fig. 2.14(c). Relatively smaller in DRT occur when the higher frequency components of the terrain are included, as seen in Fig. 2.14(a). The results thus further confirm that roll stability of the vehicle is strongly affected by lower frequency components of terrain elevation. This is evident in Figs. 2.14(c) and 2.14(d), which suggest lower DRT and higher ΔT when lower frequency components of the terrain are considered ($0.02 \leq m \leq 5$).

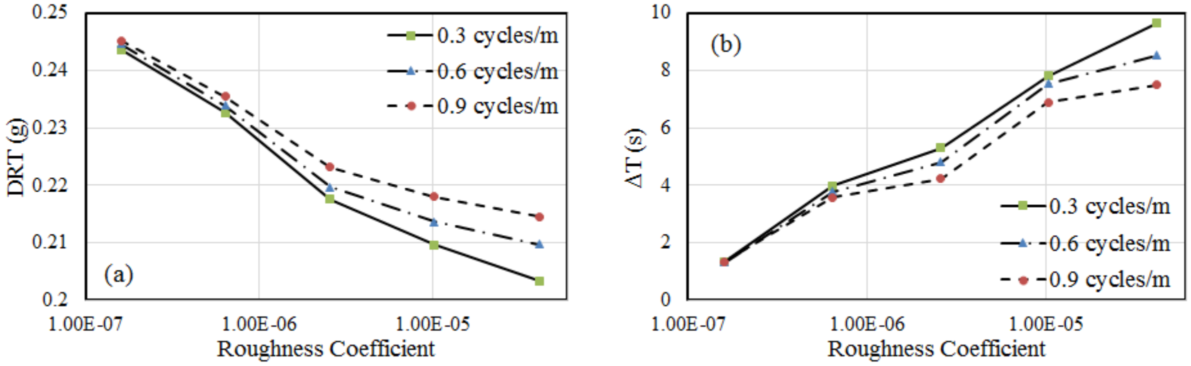

Figure 2.12: Effect of variation in roughness coefficient and coherence function cut-off frequency on the rollover threshold acceleration, DRT, and sustained period, ΔT (w=2.0, m=0.02-5 cycles/m)

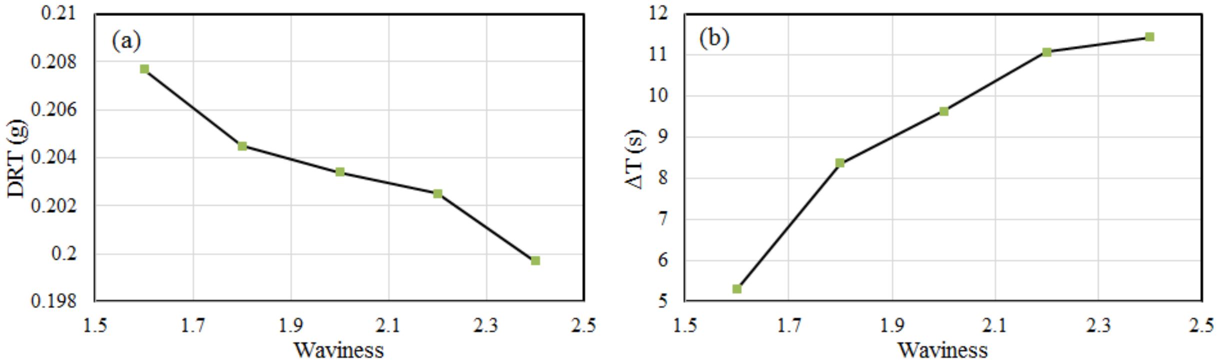

Figure 2.13: Effect of variation in waviness on the rollover threshold acceleration, DRT, and sustained period, ΔT (α_r=4.096×10^{-5}, m_c=0.3 cycles/m, m=0.02-5 cycles/m)

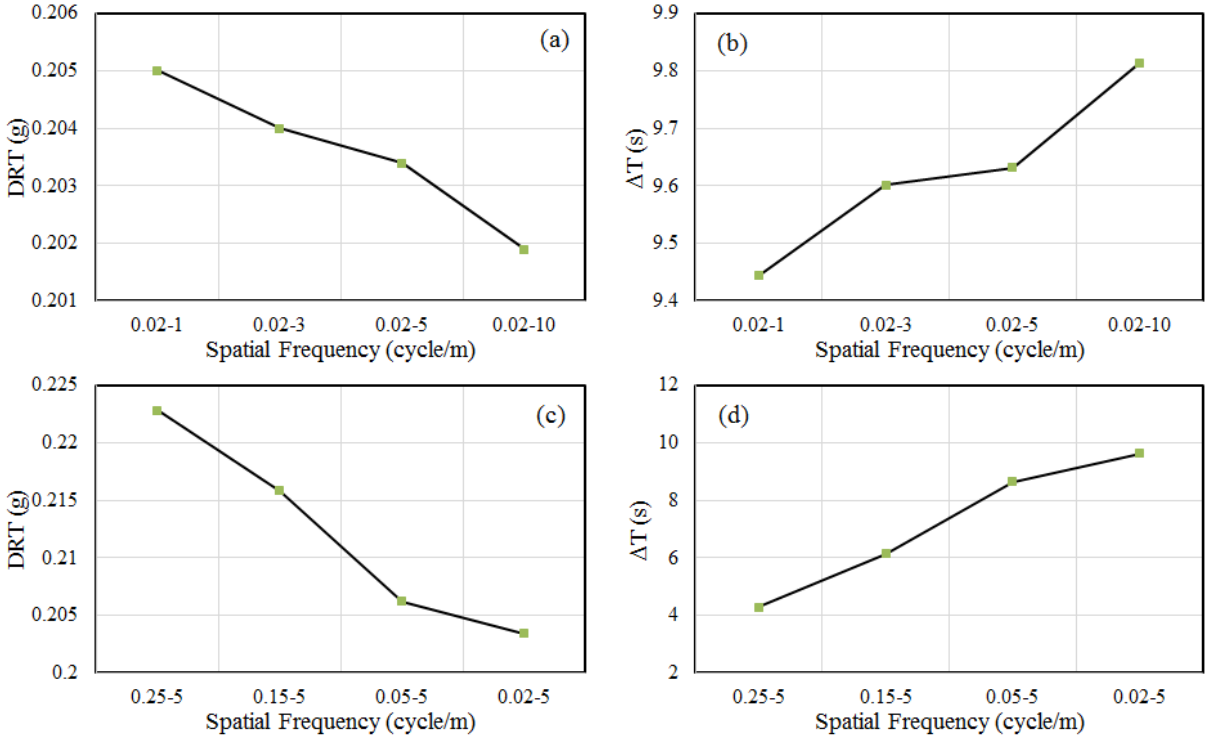

Figure 2.14: Effect of variation in spatial frequency range on the rollover threshold acceleration, DRT, and sustained period, ΔT (α_r=4.096×10^{-5}, w=2.0, m_c=0.3 cycles/m)

2.5 Conclusions

The roll stability of off-road vehicles cannot be reliably predicted using the measures defined for road vehicles, due to large oscillations in the LTR and lateral acceleration responses in the presence of terrain roughness. The dynamic rollover threshold (DRT) of vehicle operating on rough terrains can be estimated as the RMS lateral acceleration over the period when the LTR remains near unity, prior to the absolute rollover. The DRT estimated considering terrain elevations showed very good correlation with the conventional DRT values that are obtained for smooth road surface ($r^2 > 0.97$) over a wide range of sprung mass cg heights. The DRT on the rough terrains, however, was consistently lower than the DRT for smooth road surface. The vehicle operations on terrains with higher elevations adversely affected the DRT, while it increased the sustained period of unity LTR value. Greater roll excitations of the terrain also yielded lower DRT due to larger vehicle roll oscillations. The results further suggested that the DRT was strongly influenced by the lower spatial frequency components of the terrain elevation. Higher terrain waviness also caused higher magnitudes of lower frequency components and thereby the lower DRT. The relatively higher spatial frequency components of terrain elevation, however, affected the dynamic rollover threshold only slightly.

CHAPTER 3

EFFECTS OF ARTICULATED FRAME STEERING ON TRANSIENT YAW RESPONSES OF THE VEHICLE

3.1 Introduction

Vehicles employing articulated frame steering (AFS) systems are widely employed in construction, forestry and mining sectors to achieve improved traction and mobility/maneuverability performances [12, 126-128]. Compared to the conventional front wheel steered vehicles, the articulated frame-steered vehicles (AFSV) use relatively large diameter tires, and yield lower off-tracking between the two axles and thus reduced rate of tire wear and improved maneuverability, especially at low speeds [126, 129, 130]. Furthermore, the relative roll motion between the front and rear units of the AFSV could yield better terrain contact of the wheels and thereby relatively lower wheel-load transfers, when compared to conventional front-steered vehicles, which may contribute to improved traction performance [12, 131].

The articulated frame steering system, however, introduces considerable yaw oscillations between the front and rear units of the vehicle, which may cause vehicle yaw divergence beyond a critical speed [10, 45, 132, 133]. Additionally, the steering of the vehicle requires relatively large magnitude steering torque by the AFS system, which is usually powered by a closed-loop or a volume-regulated hydraulic steering system [12]. The kinematic and dynamic properties of the AFS system are known to significantly influence the performances of the AFSV [10]. A number of studies have investigated yaw stability of the AFSV based on the free yaw-oscillation responses, while simplifying the AFS system by the equivalent articulation stiffness and damping, and neglecting contributions due to its kinematics [12, 19, 132].

Horton and Crolla [12] and He et al. [19] analytically obtained the snaking critical speed when the real part of the eigenvalue corresponding to the snaking mode was observed positive. The eigenvalue analysis, however, is limited only to linear or linearized models, considered valid in the vicinity of the linearization point [12, 130]. Alternatively, Rhenberg et al. [132] and Pazooki et al. [10] have assessed the snaking behavior in terms of rate of decay of free oscillations in the articulation angle response following a lateral perturbation of the vehicle. The rate of decay, however, may not accurately describe the essential yaw-oscillation characteristics of the nonlinear vehicle model such as natural frequency and damping ratio, due to its sensitivity to the magnitude and duration of the pulse [134]. The critical speeds reported in different studies vary widely, from

43.2 km/h to 120 km/h [10, 12, 19, 25]. The yaw divergence of the AFSV may also be measured in terms of the yaw damping ratio, as in the cases of articulated road vehicles and railway cars [40, 135-137].

The natural frequency of yaw oscillations is related to the effective yaw stiffness of the AFSV and the AFS system. The equivalent torsional stiffness of AFS system is generally linearized about zero articulation angle, which can range from 1.1×10^5 Nm/rad to 2×10^8 Nm/rad considering the compliance of the hydraulic fluid, connecting pipes and entrapped air [11, 19, 25, 132]. The instantaneous effective stiffness of the AFS system, however, would vary with the struts' orientations and actuating forces of the steering struts in a nonlinear manner, which is widely ignored in the aforementioned studies.

The AFS systems also exhibit considerable damping due to leakage flows across the piston seals and friction between the cylinder and rod [19, 138, 139]. Greater leakage flows and fluid bulk modulus were believed to increase the damping coefficient and stiffness of the steering system, respectively, which have been reported to attenuate the free-oscillation of the articulation angle and increase the critical speed of the vehicle [10, 12, 19, 132]. Horton and Crolla [12], Pazooki et al. [10] and He et al. [19] invariably assumed the leakage flows within the struts to be proportional to the pressure difference across the seal. The leakage flows, however, depend on the relative velocity between the cylinder and rod, which affects the seal clearance in a nonlinear manner [140, 141]. The reported studies also neglected the contributions due to friction generated between the steering strut cylinder and the rod. The articulated frame-steered vehicles in the aforementioned studies are mostly modeled in the yaw plane [10, 12, 19]. Rhenberg et al. [132] and Pazooki et al. [22, 48] have also developed the 3-dimentional models of the AFSV in order to investigate the effects of axle suspension system on its ride vibration and directional stability.

Furthermore, the transient steering responses of the AFSV have not been adequately addressed in the reported studies, which are related to dynamic properties and yaw responses of the vehicle units apart from the AFS system. Pazooki et al. [10, 48] investigated the transient steering responses of an AFSV model under idealized steady-turning and path-change maneuvers. Moreover, the articulation angle and strut deflection responses of the vehicle trend to vary with the vehicle load due to changes in the flow demand [10]. It has also shown that an increase in the maximum steering valve flow rate can yield relatively rapid steering torque and articulation angle responses, while the leakage flows affect the transient articulation angle response only slightly.

The study also demonstrated that steering arm lengths of the struts contribute to a higher decay rate of the articulation angle oscillations. This vehicle model employed a closed-loop AFS system to regulate the hydraulic flows in response to the steady-state articulation angle and the steering wheel input considering idealized valve flow characteristics. Many AFSVs, however, employ the flow volume-regulated AFS system, while the flow volume is governed by the steering wheel input alone [12, 131].

In this study, the free yaw-oscillations as well as transient steering characteristics of an articulated frame-steered vehicle with a flow volume-regulated AFS system are investigated. The kinematic and dynamic properties of steering system are formulated in conjunction with a yaw-plane vehicle model. The model incorporates fluid compressibility, leakage flows, viscous friction within the steering struts, and volume-regulated steering valve flow characteristic. The measured data acquired for a 35-tonne articulated mining truck are used to examine validity of the established model. The free-oscillation and transient articulation angle responses are evaluated under a pulse and a step steering wheel input, respectively. A parameter sensitivity analysis is conducted to study the influences of selected steering system design parameters, namely, the effective fluid bulk modulus, the leakage flows and viscous friction coefficients, and kinematic angle of the struts layout, on the steering characteristics of the AFSV. The results obtained through parametric sensitivity analyses are used to discuss design guidance for the articulated frame steering system in view of its kineto-dynamic characteristic.

3.2 Model development

3.2.1 Articulated frame steering system model

Figure 3.1 schematically illustrates the two steering struts coupling the AFSV mining vehicle considered in the study. The left- and right- steering struts, as shown in Fig. 3.1(a), are mounted between the front unit (at L_1 and R_1, respectively) and the rear unit (at L_2 and R_2, respectively). The hydraulic steering circuit, shown in Fig. 3.2, actuates the steering struts to generate the steering torque following a steering command. The hydraulic flows to and from the struts are controlled by the steering valve driven by the steering wheel. The gerotor within the steering valve rotates proportionally to the fluid volume passing through it, which offers the feedback for the steering system [131]. The steering torque T_S generated by the steering struts about the articulation joint can be expressed as:

$$T_s = F_L h_L - F_R h_R \tag{3.1}$$

where F_L and F_R are forces developed by the left- and right-strut, respectively; h_L and h_R are kinematic steering arm lengths of the left- and right-strut, respectively, measured from the articulation joint, as seen in Fig. 3.1(a).

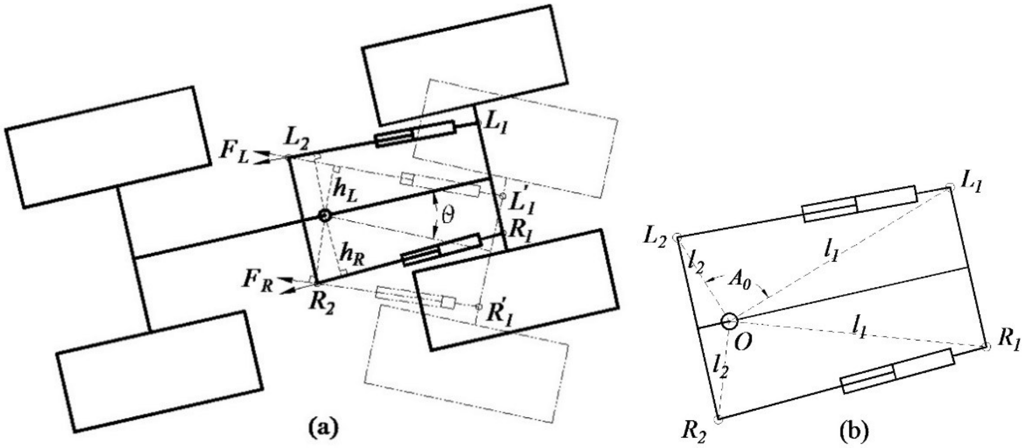

Figure 3.1: (a) Schematic of the AFSV units coupled via steering struts; and (b) layout of steering struts

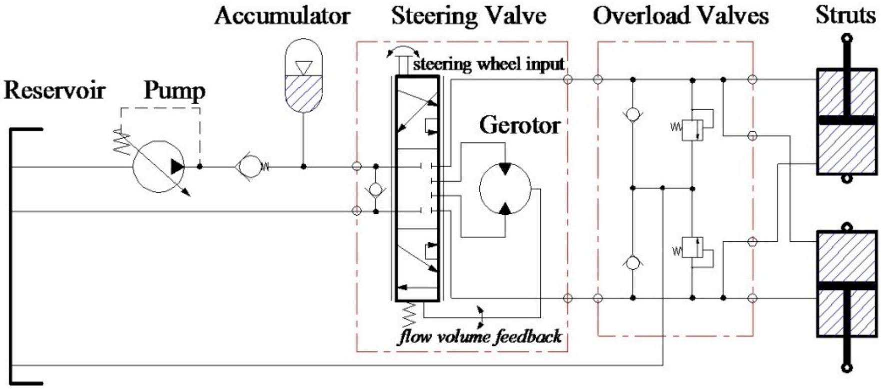

Figure 3.2: Hydraulic steering circuit [131]

The instantaneous steering arm lengths, h_L and h_R, vary during steering, and can be related to the articulation angle θ, and the geometry, such that:

$$\begin{aligned} h_L(\theta) &= \frac{l_1 l_2 \sin(A_0+\theta)}{\sqrt{l_1^2 + l_2^2 - 2 l_1 l_2 \cos(A_0+\theta)}} \\ h_R(\theta) &= \frac{l_1 l_2 \sin(A_0-\theta)}{\sqrt{l_1^2 + l_2^2 - 2 l_1 l_2 \cos(A_0-\theta)}} \end{aligned} \tag{3.2}$$

The geometric parameters, l_1, l_2 and A_0, as shown in Fig. 3.1(b), are kinematic constants related to layout of the two steering struts. l_1 and l_2 define the distances from the articulation joint to the front and rear mounting points of the struts, respectively. A_0 is the initial angle of the strut mountings with respect to the articulation joint, indicated by lines *OL₁* (l_1) and *OL₂* (l_2), shown in

Fig. 3.1(b).

The steering forces developed by the struts are calculated from the instantaneous fluid pressures within two chambers of each strut and the viscous friction due to hydraulic seals. The friction force due to seal is considered as a viscous force, and expressed as a linear function of relative piston velocity with respect to the cylinder. For the left- and right-struts, these can be expressed as a function of the articulation rate, $h_L\dot{\theta}$ and $h_R\dot{\theta}$, respectively. The strut forces, F_L and F_R, can thus be expressed as:

$$\begin{aligned} F_L &= A_c P_c - A_r P_r - \mu_v h_L \dot{\theta} \\ F_R &= A_c P_r - A_r P_c + \mu_v h_R \dot{\theta} \end{aligned} \qquad (3.3)$$

where A_c is effective piston area; A_r is effective annular area of the rod-side chamber; P_c is fluid pressure in piston-side chamber of the left strut and rod-side chamber of the right strut; P_r is fluid pressure in rod-side chamber of left strut and piston-side chamber of the right strut, as seen in Fig. 3.3; and μ_v is viscous damping coefficient due to seal friction.

The hydraulic fluid pressures are derived on the basis of the fluid continuity considering fluid compressibility and leakage flows within the steering struts. Figure 3 illustrates the fluid flow path during a right-hand turning maneuver, including the flows through the valve spool and housing. The fluid entering the steering valve from the pump via an accumulator flows into the strut chambers through the gerotor. The fluid flows also occur from the other chamber of each strut to the reservoir through another path inside the steering valve. The flow continuity equations within the two steering struts can thus be expressed as:

$$\begin{aligned} q_1 &= A_c h_L \dot{\theta} + A_r h_R \dot{\theta} + q_{lL} + q_{lR} + \frac{V_{1L} + V_{1R}}{B_{eff}} \dot{P}_c \\ q_2 &= A_r h_L \dot{\theta} + A_c h_R \dot{\theta} + q_{lL} + q_{lR} - \frac{V_{2L} + V_{2R}}{B_{eff}} \dot{P}_r \end{aligned} \qquad (3.4)$$

where q_1 is rate of fluid flow from the steering valve to the steering struts; q_2 is rate of fluid flow from the steering struts to the reservoir; q_{lL} and q_{lR} are leakage flows within the left- and right-struts, respectively; B_{eff} is effective bulk modulus of the hydraulic fluid; V_{1L} and V_{2R} are volumes of fluid in the piston-side chambers of left- and right-struts, respectively; and V_{1R} and V_{2L} are those of fluid in the rod-side chambers of right and left-struts, respectively, as shown in Fig. 3.3.

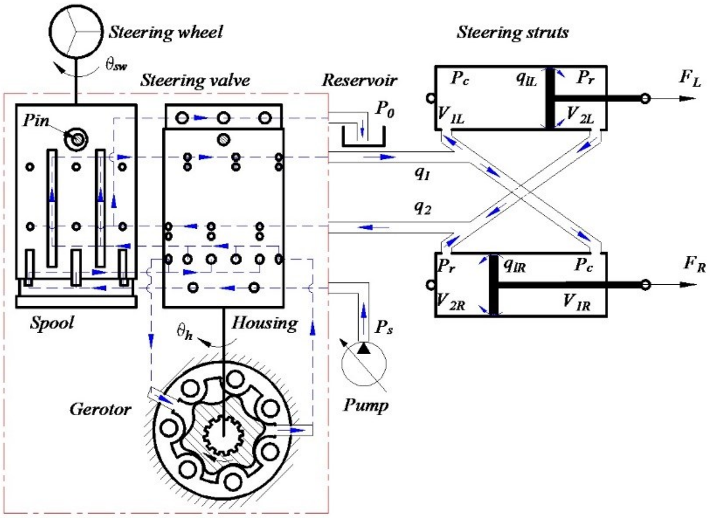

Figure 3.3: Hydraulic fluid flow paths during a right-hand turn

The leakage flows between the two strut chambers, attributed to the piston seal, can be computed from the pressure difference across the piston, such that [10, 12, 19]:

$$\begin{aligned} q_{lL} &= k_{lL}(P_c - P_r) \\ q_{lR} &= k_{lR}(P_c - P_r) \end{aligned} \tag{3.5}$$

where k_{lL} and k_{lR} are leakage coefficients of the left- and right-strut, respectively. Considering the symmetry of the AFS system, these have been assumed as identical constants in the reported studies [10, 12, 19]. The leakage flows through the generally implemented rectangle cross-section hydraulic seals, however, have been reported to strongly correlate with the relative velocity [140, 141]. The instantaneous leakage coefficient is thus expressed by a velocity-related coefficient k_l in addition to the constant coefficient k_{l0}, such that:

$$\begin{aligned} k_{lL} &= k_{l0} + k_l h_L |\dot{\theta}| \\ k_{lR} &= k_{l0} + k_l h_R |\dot{\theta}| \end{aligned} \tag{3.6}$$

The volumes of fluids in the interconnected strut chambers in Eq. (3.4) are calculated neglecting the deformation of the struts and connecting tubes, as:

$$\begin{aligned} V_{1L} + V_{1R} &= V_0 + A_c(l_L - l_0) + A_r(l_0 - l_R) \\ V_{2L} + V_{2R} &= V_0 - A_r(l_L - l_0) - A_c(l_0 - l_R) \end{aligned} \tag{3.7}$$

where V_0 is initial fluid volume of the piston-side chamber of left-strut, the rod-side chamber of right strut and the connecting pipes, which is identical to the initial fluid volume of the piston-side chamber of right strut, the rod-side chamber of left strut and the connecting pipes; l_0 is initial length of the struts, which equals $\sqrt{l_1^2 + l_2^2 - 2l_1 l_2 \cos(A_0)}$; and l_L and l_R are instantaneous lengths of the left- and right-struts, respectively, which can be expressed as a function of the articulation angle θ, as:

$$\begin{aligned} l_L(\theta) &= \sqrt{l_1^2 + l_2^2 - 2l_1l_2\cos(A_0+\theta)} \\ l_R(\theta) &= \sqrt{l_1^2 + l_2^2 - 2l_1l_2\cos(A_0-\theta)} \end{aligned} \tag{3.8}$$

The flow through the steering valve is related to relative angular displacement of the valve spool with respect to its housing. The valve spool is directly coupled to the steering wheel, while the housing displacement θ_h is identical to that of the gerotor, as shown in Fig. 3.3. For a given steering wheel displacement θ_{sw}, the relative angular displacement of the steering valve, X, during a right-hand turning maneuver is thus given by:

$$X = \theta_{sw} - \theta_h \tag{3.9}$$

where the angular displacement of the housing, θ_h, is regulated by the volume flow from the steering valve to the steering strut chambers [131], such that:

$$\theta_h = \frac{\int q_1 dt}{k_\theta \eta_g} \tag{3.10}$$

where k_θ is ratio of the gerotor volume displacement to its angular displacement and η_g is efficiency of the gerotor.

Since a higher pressure difference would yield greater hydraulic flow rate and thereby cause the flow transition from laminar to turbulence [142], the fluid flow through the steering valve of the AFS system can be assumed as a laminar-turbulent transition flow within the working pressure range. While the rate of laminar flow through the orifices is proportional to the pressure difference $(P_s - P_c)$, the rate of turbulent flow is related to root of the pressure difference $(\sqrt{P_s - P_c})$ [142], where P_s is the supply pressure. Considering the dead-band X_0 of the steering valve, the rate of flow from the steering valve to the steering struts, q_1, during a right-hand turn can be expressed in terms of the relative valve displacement X, as:

$$q_1 = \begin{cases} 0 & 0° \le X \le X_0 \\ a_m(X - X_0)\sqrt{P_s - P_c} + a_v(X - X_0)(P_s - P_c)\cdot e^{a_0(P_s - P_c)} & X > X_0 \end{cases} \tag{3.11}$$

where the exponential term $(e^{a_0(P_s-P_c)})$ represents the laminar-turbulent transition with increase in pressure difference and a_i (i=0, m and v) are the constant coefficients related to the effective flow area and discharge coefficient. These coefficients were identified on the basis of flow rate and pressure differential characteristics of the valve specified by the manufacturer [143]. Figure 3.4 compares the flow and pressure characteristics of the valve obtained from the model with the manufacturer's specifications for the fully opened valve. The comparison suggests that the model can accurately describe the valve flow characteristics in the selected pressure range.

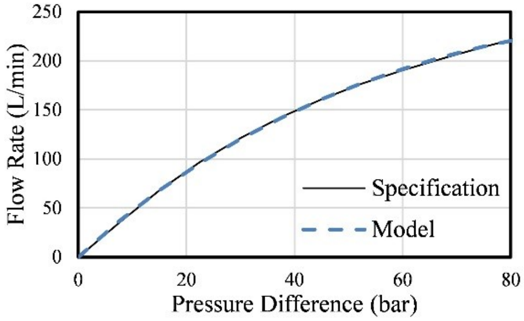

Figure 3.4: Comparison of flow rate versus pressure difference characteristics obtained from the model with the manufacturer's specification for the fully opened steering valve

Similarly, the rate of flow from the steering struts to the reservoir, q_2, is calculated with the multiplication of a flow area factor k_v, such that:

$$q_2 = \begin{cases} 0 & 0° \leq X \leq X_0 \\ k_v a_m (X - X_0)\sqrt{P_r - P_0} + k_v a_v (X - X_0)(P_r - P_0) \cdot e^{a_0 (P_r - P_0)} & X > X_0 \end{cases} \tag{3.12}$$

where k_v is the flow area factor, which accounts for the difference in the effective areas for flows between the struts and the reservoir, and between the pump and the struts. For the AFS system design of the mining vehicle, k_v<1. P_0 in the above equation denotes the fluid pressure in the reservoir, taken as atmospheric pressure.

Furthermore, the relative angular displacement of the valve spool with respect to the housing, X, is limited to ±8.1 degrees via a pin located in the valve housing. After reaching the limit position, the steering wheel drives the valve spool, the valve housing and the gerotor at the same rate. The gerotor then functions as a pump, and the flow rate through the steering valve directly relates to the driver's steering rate. This enables the vehicle to steer even without the hydraulic power supply, although this feature is not considered in the model in order to avoid discontinuity in the flow rate.

3.2.2 Vehicle model

The kinematic and dynamic responses of the AFSV and the AFS system are evaluated from the yaw plane model of the vehicle (Fig. 3.5) in conjunction with that of the AFS system model. The roll and pitch motions of the vehicle are assumed to be small and their contribution to the steering responses are neglected. The longitudinal dynamics of the AFSV is further neglected assuming constant forward speed. The governing equations of motion of the yaw plane model used in the reported studies [12, 131], are given by:

$$\begin{gathered}m_f(\dot{v}_f + u_f\varphi_f) + m_r(\dot{v}_r + u_r\varphi_r)\cos\theta - m_r(\dot{u}_r - v_r\varphi_r)\sin\theta - Y_1 - Y_2 - (Y_3 + Y_4)\cos\theta = 0\\ (I_f + m_f L_{f2}^2)\dot{\varphi}_f + m_f(\dot{v}_f + u_f\varphi_f)L_{f2} - (Y_1 + Y_2)(L_{f1} + L_{f2}) + (M_{z1} + M_{z2}) - T_s = 0\\ (I_r + m_r L_{r2}^2)\dot{\varphi}_r - m_r(\dot{v}_r + u_r\varphi_r)L_{r2} + (Y_3 + Y_4)(L_{r1} + L_{r2}) + (M_{z3} + M_{z4}) + T_s = 0\end{gathered} \tag{3.13}$$

where (u_f, v_f, φ_f) and (u_r, v_r, φ_r) are the body-fixed longitudinal, lateral and yaw velocities of the front and rear units, respectively; m_f and m_r are masses of the front and rear units, respectively; I_f and I_r are yaw mass moment of inertia of the two units about their respective mass center (cg); Y_i and M_{zi} are the cornering force and aligning moment developed by tire *i* (i=1,..,4) of the vehicle, respectively; L_{f1} and L_{f2} are longitudinal distances from the mass center of front unit to the front axle and the articulation joint, respectively; L_{r1} and L_{r2}. are longitudinal distances from the mass center of rear unit to the rear axle and the articulation joint, respectively.

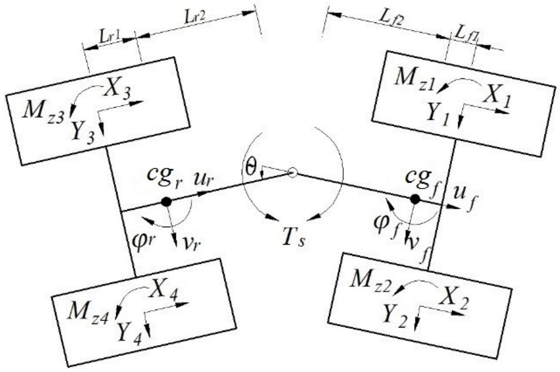

Figure 3.5: Yaw-plane model of the articulated frame-steered vehicle

The relative lateral and longitudinal motions between the front and rear units are constrained by the articulation joint, while it permits relative yaw plane motions of the units, which yield:

$$\begin{gathered}u_r = u_f\cos\theta - (v_f - L_{f2}\varphi_f)\sin\theta\\ v_r = u_f\sin\theta + (v_f - L_{f2}\varphi_f)\cos\theta - L_{r2}\varphi_r\\ \dot{\theta} = \varphi_f - \varphi_r\end{gathered} \tag{3.14}$$

The tire cornering forces, Y_i, are considered as linear function of the tire side-slip angle α_i for a given normal load. Since the tire aligning moment, M_{zi}, is related to the tire side-slip angle, the pneumatic trail as well as the tire lateral and longitudinal forces [79], the aligning moment is described as a linear function of the tire side-slip angle and an effective aligning moment coefficient. The cornering forces and aligning moments generated by the tires are thus given by:

$$Y_i = \begin{cases} C_{\alpha f}\alpha_i; & i = \text{ 1 and 2} \\ C_{\alpha r}\alpha_i; & i = \text{ 3 and 4} \end{cases}$$
$$M_{zi} = \begin{cases} k_{mzf}\alpha_i; & i = \text{ 1 and 2} \\ k_{mzr}\alpha_i; & i = \text{ 3 and 4} \end{cases} \tag{3.15}$$

where $C_{\alpha f}$ and $C_{\alpha r}$ are cornering stiffness of tires at front and rear axle, respectively, and k_{mzf} and k_{mzr} are the respective aligning moment coefficients.

A first-order dynamic lag in the tire side-slip angle is considered to account for the transient effect of the tire, where the delay is defined by the tire lateral relaxation length σ_y and the vehicle forward speed u_f, such that [51]:

$$\frac{\sigma_y}{u_f} \cdot \frac{d\alpha_i}{dt} + \alpha_i = \alpha_{si}; \quad i = 1, 2, 3 \; and \; 4 \tag{3.16}$$

where α_{si} is the steady-state side-slip angle of the tire, α_{si}, given by:

$$\alpha_{si} = \begin{cases} -\,tan^{-1}\left(\dfrac{v_f + L_{fi}\varphi_f}{u_f + (-1)^{i+1}T\varphi_f}\right); & i = 1 \text{ and } 2 \\ -\,tan^{-1}\left(\dfrac{v_r - L_{ri}\varphi_r}{u_r + (-1)^{i+1}T\varphi_r}\right); & i = 3 \text{ and } 4 \end{cases} \tag{3.17}$$

where T is the half-track of the vehicle axle.

3.3 Method of analysis

The reported studies on articulated frame-steered vehicles are mostly focused on identification of the yaw stability limits or snaking tendency of the vehicle using either eigen-analyses of the linear or linearized vehicle models [12, 19] or divergence in the free oscillations in the articulation angle responses [10, 12, 19, 25, 132]. The AFS in these studies, however, is described by the equivalent torsional stiffness and damping, neglecting the contributions due to kinematics of the steering struts and dynamics of the steering valve, which could yield important effects of the steering responses of the vehicle [10]. Dudziński and Skurjat [11] showed that directional dynamic performance of an AFSV is strongly dependent upon the equivalent torsional stiffness, which is governed by torsional flexibility of the AFS and the tires. The studies on directional dynamics of articulated freight vehicles have emphasized the significance of yaw damping ratio of the vehicle [40]. Although the lateral and yaw stability characteristics of articulated freight vehicles have been widely evaluated in terms of articulation angle gain and articulation rate under step steer inputs

[79, 144], the transient steering response analysis of AFSVs have been limited only to a few studies [10], which are also related to kineto-dynamic properties of the AFS.

In this study, the effects of steering strut parameters are investigated in terms of both the free yaw-oscillation and transient directional responses of the vehicle model. The free oscillation responses of the model are evaluated under a $0.2s$ half-sine steering pulse disturbance, as in [40, 132], at a constant forward speed of 50 km/h, which is generally the upper speed limit in the open-pit mining operations. The free oscillations responses are analyzed to determine the overall yaw mode stiffness and damping properties of the vehicle model in terms of yaw-mode natural frequency and damping ratio, assuming single-degree-of-freedom (DOF) system response. The transient yaw responses of the vehicle model are evaluated under a 30 degrees step steer input at the forward speed of 50 km/h, which resulted in peak articulation angle comparable to that obtained under the pulse input. The results are analyzed to study the effects of AFS design parameters on: (i) steering gain, defined as the ratio of articulation angle to the steering wheel angle; (ii) rate of articulation, defined as 100% rise rate in the articulation angle response; and (iii) percent articulation overshoot.

3.4 Results and discussions

3.4.1 Model validation

The model validity was examined using the data acquired through measurements performed on a 35-tonne mining AFSV. The vehicle parameters also served as nominal simulation parameters for the vehicle and the AFS system models, which are listed in Table 3.1 [131, 145]. These are acquired partly from the vehicle design manual [145], manufacturer documentations and partly identified through minimizing the difference between simulation and measured responses. In particular, the tire properties are identified using the measured responses during steady-turning maneuvers of the vehicle, while using the measured strut chambers’ fluid pressures. The field test program has been described in [131]. Briefly, the mining vehicle was operated on a relatively smooth concrete surface to reduce the effects of terrain roughness on the vehicle and the AFS responses. The measurements were performed on a 13.5 m radius steady-turning course, and a path-change course with 4.5 m lateral offset and 18 m gate, which were realized through placements of cones, as shown in Fig. 3.6. The measurements were conducted for the loaded and unloaded vehicles. The measurements of the unloaded vehicle were attempted at two different speeds, while that of the loaded vehicle were performed at a single speed (Table 3.2). The vehicle was instrumented to measure vehicle speed and steering wheel angle, and responses in terms of articulation angle, left strut displacement, strut fluid pressures and front unit yaw rate. Although, the driver was advised to maintain steady speed during a given test, notable variations were observed in the measured speed. Table 3.2 summarizes the mean and standard deviation of the speed measured during each test. The measured data revealed relatively smaller speed variations during the steady-turning maneuver compared to the path-change maneuver.

Table 3.1: Nominal simulation parameters of the 35 tons articulated frame-steered vehicle (AFSV) and the frame steering system (AFS) [131, 145]

Vehicle Model Parameters			Steering Model Parameters	
Variable	Loaded	Unloaded	Variable	Value
m_f (kg)	21,000	21,000	A_0 (deg)	76.5
m_r (kg)	52,220	18,500	X_0 (deg)	2.1
I_f (kgm^2)	42,000	42,000	l_1 (m)	1.96
I_r (kgm^2)	104,000	31,000	l_2 (m)	0.64
L_{f1} (m)	-0.45	-0.45	A_c (cm^2)	95
L_{f2} (m)	2.13	2.13	A_r (cm^2)	57
L_{r1} (m)	1.13	0.60	V_0 (L)	7.6
L_{r2} (m)	2.31	2.84	P_s (Mpa)	13.5
$C_{\alpha f}$ (kN/deg)	4.5	4.1	P_0 (Mpa)	0.1
$C_{\alpha r}$ (kN/deg)	4.9	2.54	B_{eff}(Gpa)	1.6
k_{mzf} (kNm/deg)	3.8	2.35	μ_v	0.06
k_{mzr} (kNm/deg)	4.7	1.43	k_{l0}	1.3×10^{-13}
σ_y (m)	0.4	0.4	k_l	1.8×10^{-10}
T (m)	1.14	1.14	k_θ (mL/deg)	8.34
			k_v	0.7
			η_g	0.9

Figure 3.6: Test courses: (a) steady-turning maneuver; (b) path-change maneuver [131]

Table 3.2: Mean and standard deviation of the speed measured during the two test maneuvers

	Steady-Turning			Path-Change		
	Loaded	Unloaded		Loaded	Unloaded	
Speed (km/h)	13.4 ± 0.3	18.5 ± 0.3	24 ± 0.4	15.3 ± 1.9	19.2 ± 1.1	22.8 ± 1.5

For the purpose of model verifications, simulations were conducted under the mean measured speed and steering wheel angle. The steady-state and transient responses of the vehicle and steering system model were comparabled to the mean measured responses, as shown in Figs. 3.7 and 3.8, in terms of articulation angle, left steering strut displacement, fluid pressures in the strut chambers and front unit yaw rate. The comparisons under the steady-turning maneuvers are presented for both the unloaded and loaded vehicles operating at forward speeds of 18.5 km/h and 13.4 km/h, respectively, as seen in Fig. 3.7. The model yields steady responses, which decrease slightly due to the leakage flows within the steering struts, such as the articulation angle responses in Figs. 3.7(a) and 3.7(b). The measured strut displacement responses of the loaded as well as unloaded vehicles also decrease slightly during steady turning, as seen in Figs. 3.7(c) and 3.7(d). The mean measured strut displacements, however, are nearly 10% lower than those obtained from the model. This difference is likely due to the simplifications associated with the yaw-plane model. Unlike the model responses, the mean measured data exhibit notable fluctuations in the articulation angle, fluid pressure (Figs. 3.7(e) and 3.7(f)) and yaw rate responses (Figs. 3.7(g) and 3.7(h)) of the vehicle, which are attributed to steering wheel angle corrections, forward speed variations and vehicle yaw oscillations. The mean values of the measured data, however, are in good agreement with those obtained from the model for both the loaded and unloaded vehicles. Similar degree of agreement between the model and measured responses was also observed for the unloaded vehicle operating at the mean speed of 24 km/h.

The model responses under the path-change maneuvers are compared with the measured data in Fig. 3.8, for both the unloaded and loaded vehicles operating at the speed of 19.2 km/h and 15.3 km/h, respectively. The articulation angle response of the loaded vehicle model (Fig. 3.8(a)) reveals good agreement with the corresponding measured data, while notable deviations are evident in the articulation angle response of unloaded vehicle model (Fig. 3.8(b)). Further analysis of the measured data revealed measurement errors caused by loosening of the link rods used to attach the articulation potentiometer. The strut displacement responses of the loaded and unloaded vehicle models, however, show very good agreement with the measured data, which seem to be well correlated with the measured and model's articulation angle responses, as expected and shown in Figs. 3.8(c) and 3.8(d). The comparisons also show reasonable good agreements between the yaw rate responses of the model (Figs. 3.8(i) and 3.8(j)). The observed differences between the strut chambers' fluid pressures obtained from the model and the measured data, as seen in Figs.

3.8(g) and 3.8(h), are believed to be caused by variations in the vehicle forward speed, which directly contributes to variations in the fluid supply pressure. Despite the observed discrepancies, the comparisons in Figs. 3.7 and 3.8 suggest that the model could yield reasonably good predictions of steady-state and transient steering responses of the loaded as well as unloaded vehicle.

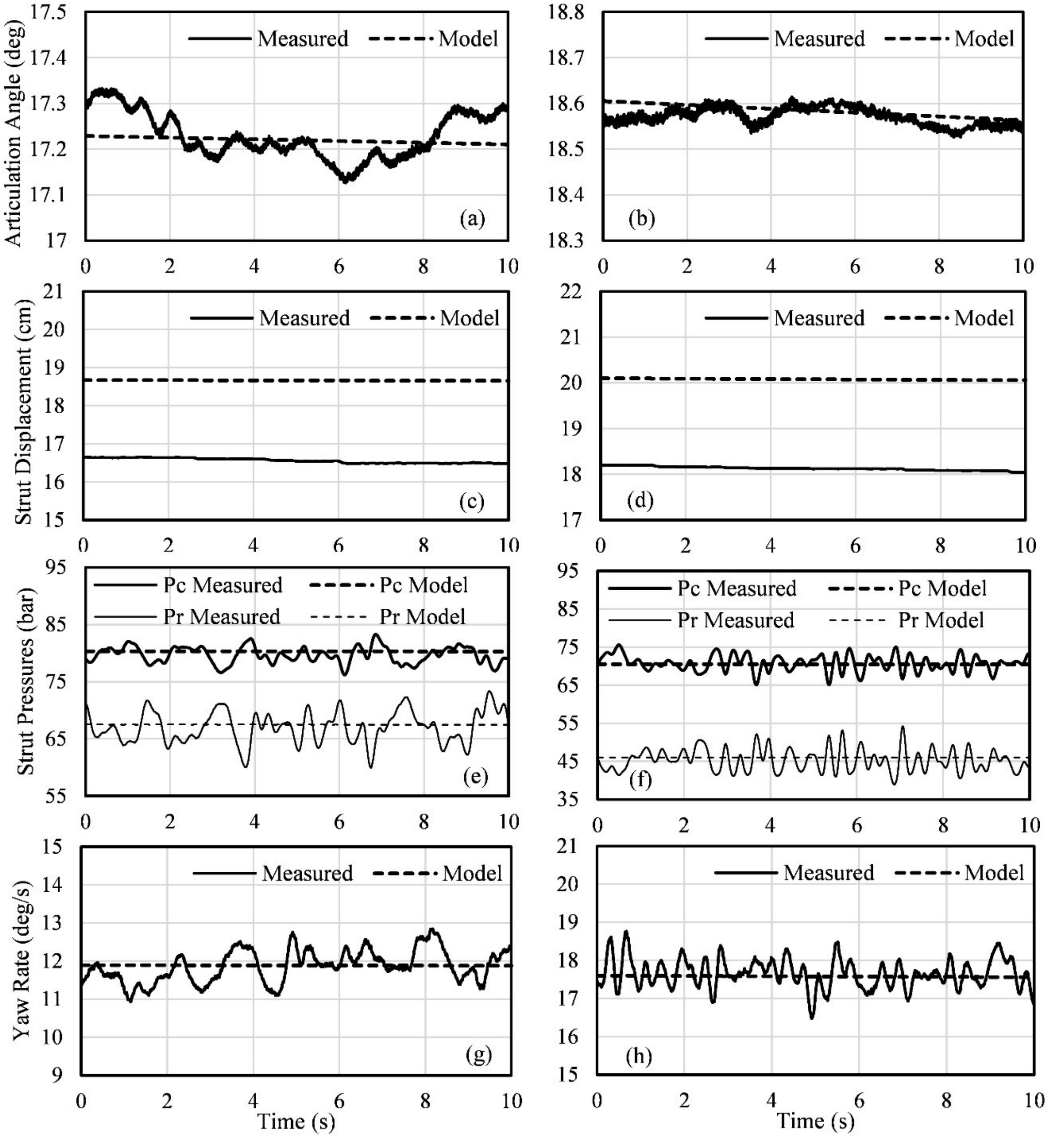

Figure 3.7: Comparisons of steady-turning responses of the model with the measured responses: (a, c, e, g) loaded (13.4 km/h); (b, d, f, h) unloaded (18.5 km/h)

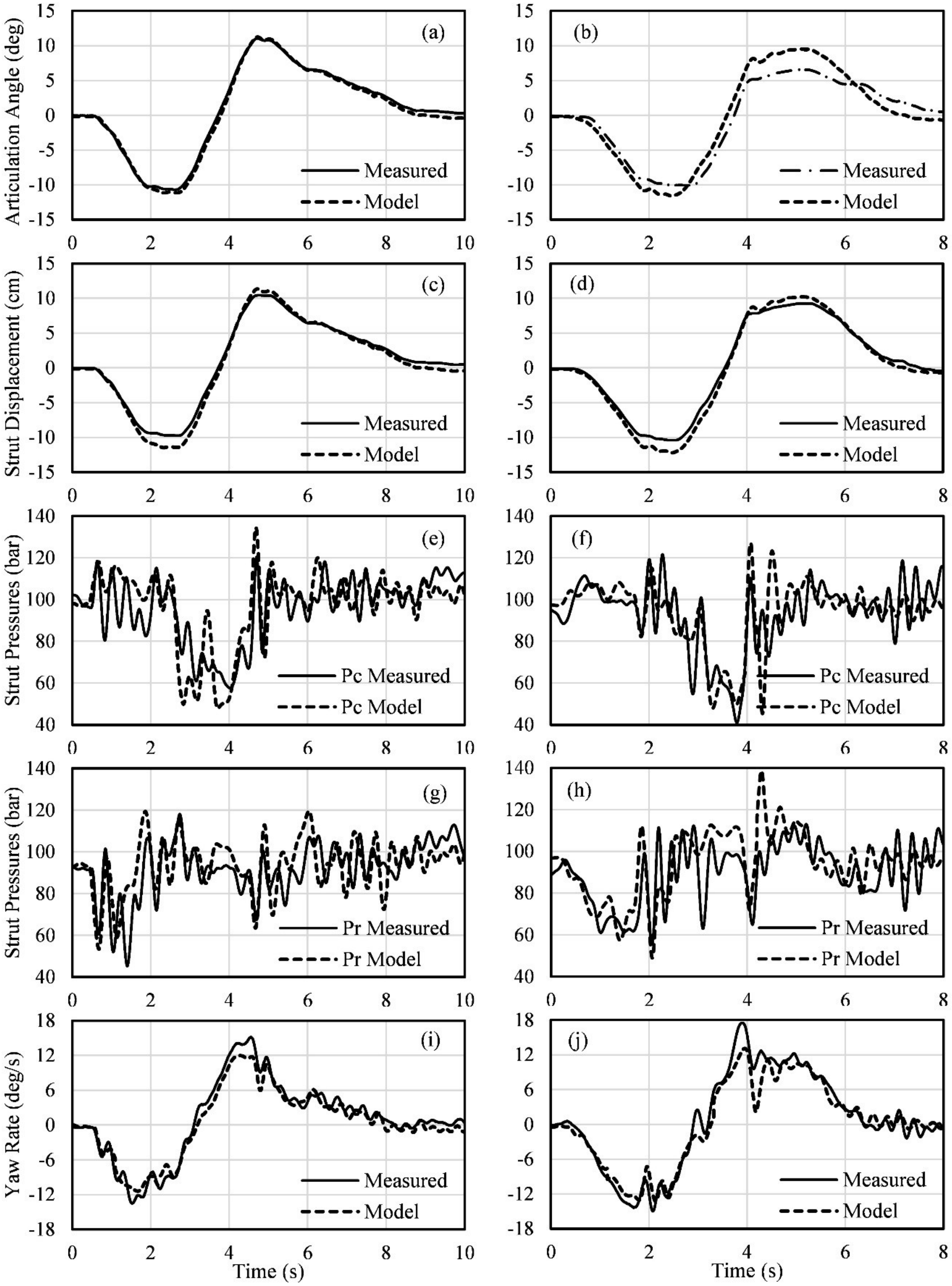

Figure 3.8: Comparisons of path-change responses of the model with the measured responses: (a, c, e, g and i) loaded (15.3 km/h); (b, d, f, h and j) unloaded (19.2 km/h)

3.4.2 Responses to pulse and step steering inputs

Figure 3.9(a) illustrates the pulse steering input and the resulting articulation angle response of the nominal vehicle model corresponding to a forward speed of 50 km/h. The results show free oscillations in the articulation angle response following the pulse excitation. There exists a considerable time lag between the articulation response and the steering input due to delays in the steering valve flows, tire lag, and kineto-dynamics of the steering struts. Following the initial oscillation caused by the steering input, the response oscillations occur at nearly constant but relatively higher frequency. While the frequency of oscillations relates to equivalent torsional stiffness of the AFS and the vehicle, the gradual decline in the amplitude of oscillations is a measure of the equivalent yaw damping. Both the equivalent torsional stiffness and damping are strongly affected by kineto-dynamic characteristics of the AFS system. The reported studies have used the free oscillation responses to demonstrate snaking tendency of the AFSV [10, 25, 132]. Additionally, such responses could also provide estimates of the equivalent torsional stiffness and damping of the AFS system. The oscillation frequency and damping ratio of the AFSV model with AFS can be identified by fitting the articulation time-history to the response function of a linear single-DOF system, as recommended for articulated freight vehicles [40]. The results further show that the articulation angle tends to converge to a non-zero value, which may be attributed to two design factors of the AFS: (i) dead-band in the steering valve flow; and (ii) fluid compressibility, which causes asymmetric flow rates during steering and correction phases.

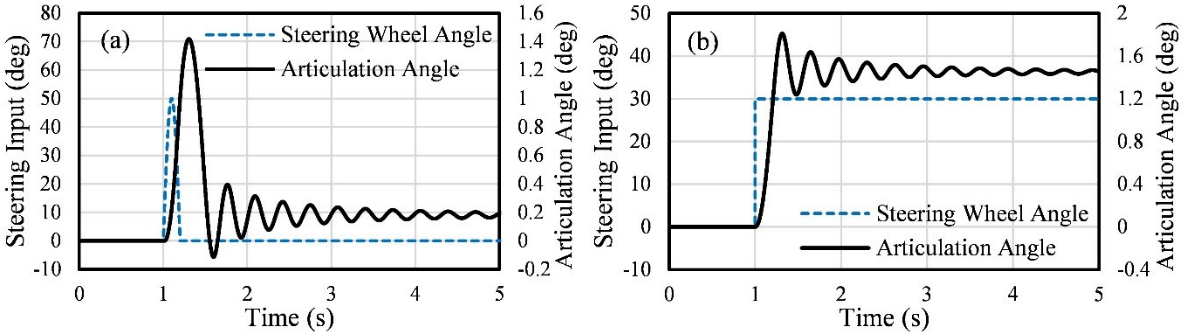

Figure 3.9: Articulation angle response of the vehicle model subject to: (a) 0.2*s* pulse steering input; and (b) 30 degrees step steering input (50 km/h)

Figure 3.9(b) illustrates the transient articulation angle response of the nominal vehicle model subject to a 30 degrees step steering input at a constant speed of 50 km/h. The chosen speed is the maximum permissible speed in many open-pit mining sites. The results show a degree of overshoot in the response and gradually decaying oscillations similar to those observed under the pulse steering input. The articulation angle response is analyzed to evaluate the steering response rate in terms of 0-to-100% rise time, and the percent overshoot of the articulation angle, which may be related to transient path deviation and thus the handling quality of the AFSV. The steering gain, the ratio of the steady-state articulation angle to the steering wheel angle, is further evaluated. The magnitude of the step input determines the total fluid volume flow from the volume-regulated steering valve to the struts and thus the hydraulic power consumption by the AFS. The amount of useful work, however, is determined by the fluid volume contributing to the vehicle steering, i.e., the steady-state articulation angle. The steering gain thus relates to the efficiency of the AFS. The simulations were performed to assess the effects of the AFS design parameters on the equivalent stiffness (oscillation frequency) and yaw damping from the vehicle responses to the pulse steering input. The step steer responses are used to evaluate the effects of design parameters on the steering response rate, percent overshoot and the steering gain. The results are discussed in the following subsection.

3.4.3 AFS design parameter sensitivity analyses

The parameter sensitivity analyses are performed considering variations in the AFS design parameters for the vehicle model with the rated load and no load. These include: (i) the kinematic angle A_0, which relates to the length and mounting positions of the struts, and thereby affects the steering arm lengths, as seen in Eq. (3.2) and Fig. 3.1(b); (ii) the effective bulk modulus B_{eff} of the fluid, which may affect the equivalent stiffness of the AFS [12, 19]; (iii) the viscous damping coefficient μ_v; and (iv) the velocity-related leakage coefficient k_l, which is known to affect the equivalent yaw damping due to AFS [19]. The results are obtained considering variations in only one design parameter at one time, in order to study the effect of each parameter on the AFS performance. The variations are limited to ±15% and ±30% about the corresponding nominal values.

It should be noted that a change in kinematic angle A_0 would cause variations in the initial arm lengths of the steering system, h_L and h_R, and thus the steering torque, in a highly nonlinear manner, as seen in Eqs. (3.2) and (3.1), respectively. Figure 3.10 illustrates the change in the initial effective steering length corresponding to changes in the kinematic angle within ±30% range. The results show that the steering arm length approaches its maximum value, when the kinematic angle of the struts layout is decreased by about 7.5% from the nominal value.

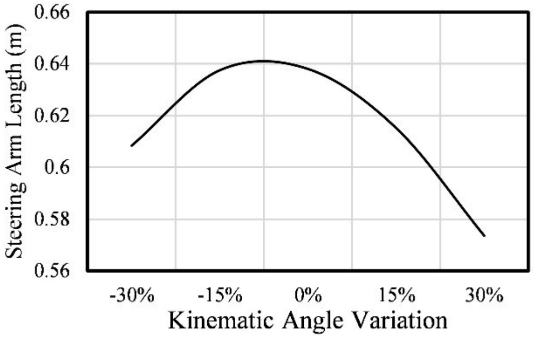

Figure 3.10: The relation between the variation in kinematic angle (A_0) and initial steering arm length of the steering struts

Figure 3.11 illustrates the effects of variations in the selected design parameters on percent changes in the resulting natural frequency and damping ratio of the AFSV model relative to those obtained for the nominal design parameters. The results obtained for the loaded and unloaded conditions exhibit similar trends, which is more evident in the articulation oscillation frequency. It is evident that the stiffness of AFS system is most significantly affected by the fluid bulk modulus. The observed trend is consistent with that reported in [12, 19]. Decreasing the effective fluid bulk modulus would yield substantial reduction in the articulation angle oscillation frequency and thus the equivalent torsional stiffness of the AFS system. This may also arise from entrapped air in the struts or operations under relatively higher fluid temperatures.

The effect of variation in the kinematic angle on the yaw oscillation frequency is nonlinear and highly asymmetric, which correlates with the variation in struts' steering arm length, shown in Fig. 3.10. The equivalent torsional stiffness of the AFS system is thus strongly influenced by the kinematic angle and thus the steering arm length. Increasing or decreasing the kinematic angle yields reduction in the oscillation frequency. The AFS system design considered in this study resulted in highest oscillation frequency, when the kinematic angle was lowered by about 7.5% from the nominal value, although the relative change is quite small. This also corresponds to the maximum initial steering arm length, as seen in Fig. 3.10. Relatively smaller kinematic angle also reduces the initial length of the steering struts (l_0 in Eq. (3.7)), which would contribute to higher column stability of the steering struts and relatively lower fluid volume demand. The results also show negligible effects of variations in the leakage and viscous damping coefficients on the oscillation frequency, suggesting that these do not contribute to the equivalent torsional stiffness of the AFS system.

The yaw damping ratio of the AFS system, however, is most significantly influenced by variations in the leakage and viscous damping coefficients. Greater leakage flows contribute to higher effective yaw damping, which has also been reported in [12, 19, 132]. The effect of leakage coefficient on the yaw damping ratio, however, is nonlinear but nearly insensitive to variations in the vehicle load. The viscous damping coefficient, on the other hand yields nearly linear variations in the damping ratio, especially for the loaded vehicle, and exhibits strong dependence on the vehicle load. For the loaded vehicle, increasing the leakage and viscous damping coefficients by 30% yields nearly 6.7% and 10% gain in the yaw damping ratio, respectively. The corresponding change for the unloaded vehicle due to 30% higher viscous damping coefficient, however, reduces to about 6.7%. It is further seen that 30% reduction in the leakage coefficient causes relatively greater reduction of about 9.5% in the damping ratio.

The results also show very small effects of variations in the kinematic angle and the fluid bulk modulus on the equivalent yaw damping ratio. For instance, a 30% increase in the fluid bulk modulus yields about 1% reduction in the yaw damping ratio, which is partly due to increase in the equivalent stiffness and thus the oscillation frequency.

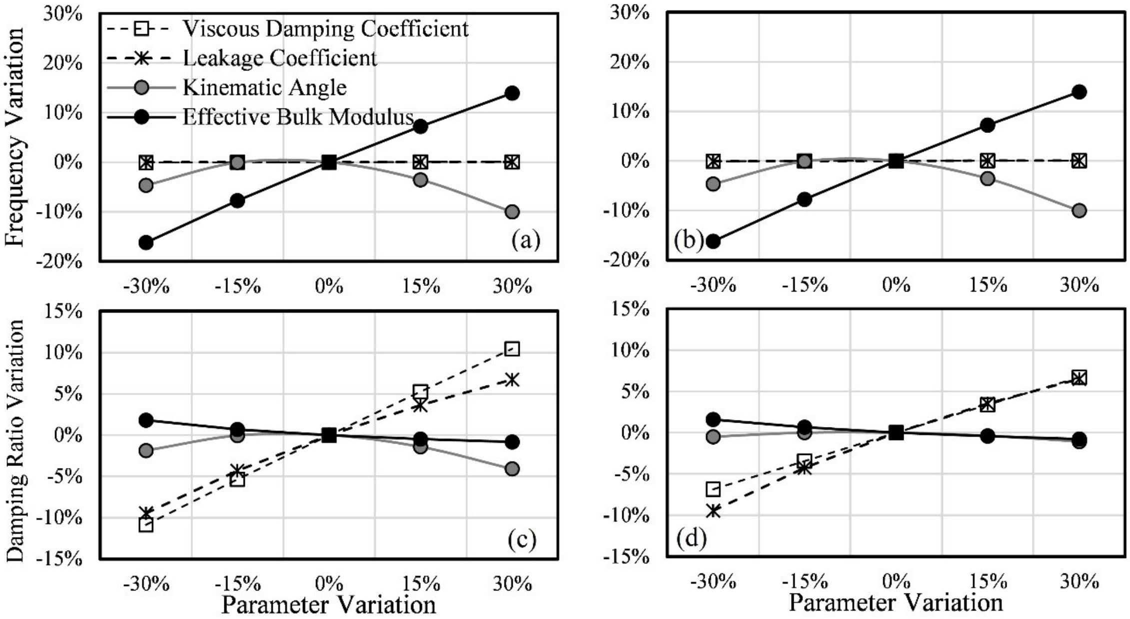

Figure 3.11: Parameter sensitivity of yaw-mode frequency and damping ratio: (a and c) loaded; (b and d) unloaded

Figure 3.12 illustrates the effects of variations in the selected design parameters on the transient response characteristics of the AFSV in terms of the steering gain, rate of articulation and articulation overshoot, which are obtained from the responses to a step steering input. The results also show similar trends for the loaded and the unloaded vehicles. The nonlinear effects of variations in the kinematic angle on the transient response measures are also evident, which are correlated with variations in struts' steering arms lengths shown in Fig. 3.10. Strong correlations between the steering gain and rate of articulation are also evident, which suggest their strong dependence on the steering arms lengths and thereby the kinematics of the AFS system. With shorter steering arm lengths, the strut displacement and strut velocity resulting from a given steering wheel angle input, would contribute to greater articulation angle and articulation rate, which leads to a higher steering gain and a faster steering response, as seen in Fig. 3.12. The steering wheel angle input simultaneously determines the fluid volume and rate of flow from the pump into the steering struts, as shown in Fig. (3.3) and Eqs. (3.9) to (3.11), and thereby affects the strut displacement and strut velocity, respectively. In particular, increasing the kinematic angle by 30% can increase the steering gain by about 10.5% for both the loaded and unloaded vehicles. The effect of variations in the other parameters on the steering gain, however, is very small, as seen in Fig. 3.12. Greater leakage and viscous damping coefficients decrease the steering gain and rate of articulation in a nearly linear manner, which is as expected since the leakage flows and friction within the steering struts would lead to the power dissipation. Increasing the fluid bulk modulus also contributes to slightly higher steering gain and rate of articulation. Moreover, the response of the unloaded vehicle is more sensitive to the effective bulk modulus, partly due to relatively lower pressure difference within the steering struts compared to the loaded condition.

The effect of variation in the kinematic angle on the articulation overshoot is very small compared to the dominant effects observed on the steering gain and rate of articulation. Increasing the fluid bulk modulus yields considerable reduction in the articulation overshoot, which is likely attributed to a higher resultant oscillation frequency. A 30% increase in the effective bulk modulus yields nearly 18% to 20% lower articulation overshoot of the loaded and unloaded vehicles, respectively. Nearly 30% increase in the overshoot is observed when the bulk modulus is lowered by 30%. Increasing the leakage and viscous damping coefficients, on the other hand, yield slightly lower articulation overshoot, which is nearly identical for both the loaded and unloaded vehicles. A 30% increase in the leakage and viscous damping coefficients yields about 8% and 2% reductions in the articulation overshoot, respectively. The leakage flows and frictions within the steering struts can thus help limit the transient path deviations as well as the free yaw-oscillations, with slight deterioration in the steering gain and articulation rate performance.

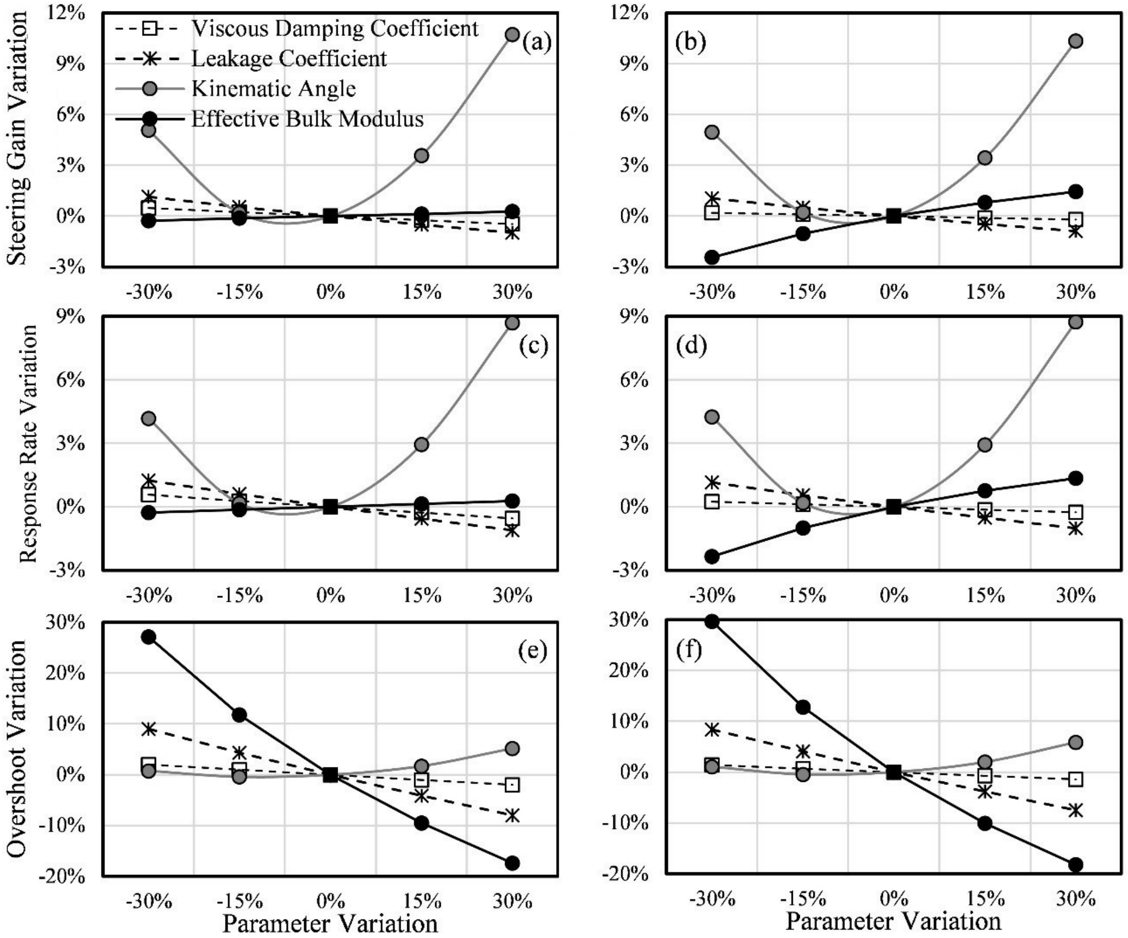

Figure 3.12: Parameter sensitivity of steering gain, rate of articulation and articulation overshoot: (a, c and e) loaded; (b, d and f) unloaded

The results suggest strong effects of the AFS system kinematics on the free oscillations and transient response characteristics of the AFSV. Moreover, contradictory effects of some of the design parameters are also evident in view of the free-oscillation and transient steering characteristics. A design optimization study is thus considered essential to derive an optimal layout of the steering struts apart from the optimal valve flow characteristics and the fluid bulk modulus. This may be formulated on the basis of the design guidance obtained from Figures 3.10 to 3.12, which are summarized below:

- The free oscillations and the transient responses of the AFS system are strongly affected by the kinematic angle and the effective arms lengths. Longer steering arms contribute to greater effective torsional stiffness, but lower steering gain and response rate. The length of the steering struts, however, should be limited to ensure greater column stability and reduced fluid volume demand, while the effective arm lengths be maximized to achieve superior performance. Further efforts in realizing an optimal layout of the struts would thus be worthy.

- The hydraulic fluid with relatively lower bulk modulus tends to reduce the articulation stiffness and response rate with higher response overshoot. The hydraulic circuit should thus be designed to ensure minimal entrapped air in the fluid. Operations under extreme temperatures could also lead to greater fluid compressibility.
- Increasing the leakage flows helps to limit the free oscillations and the articulation overshoot, while these would cause slightly lower steering gain and response rate. Higher leakage, however, will contribute to higher hydraulic losses.

3.5 Conclusions

The major conclusions of the study are summarized below:

1. The performance characteristics of the articulated frame-steered vehicles are related to the free-oscillation behavior as well as the transient steering responses.
2. The yaw-mode natural frequency and yaw damping ratio of the AFS can be identified from the articulation angle response following a steering perturbation. The transient steering performances including the steering efficiency, response speed and path deviations can be obtained from the steering gain, articulation rate and articulation angle overshoot, respectively. These characteristics are strongly dependent on the kineto-dynamic properties of the AFS system, although some of the design parameters suggest contradictory effects on different performance measures.
3. Greater fluid bulk modulus was shown to increase the yaw stiffness and slightly decrease the yaw damping ratio, while it contributed to greater steering gain and rate of articulation and significantly reduced the articulation overshoot.
4. The leakage flows and viscous seal friction within the struts attenuated the yaw-oscillations without affecting the yaw stiffness. These also contribute to power dissipation and thereby lower steering gain and rate of articulation.
5. The steering gain and rate of articulation were shown to be dominated by the strut kinematics. Longer steering arm lengths of the struts reduced the steering gain and articulation rate of the AFSV significantly, while increasing the equivalent torsional stiffness of the AFS system.

CHAPTER 4

DESIGN OPTIMIZATION OF AN ARTICULATED FRAME STEERING SYSTEM

4.1 Introduction

Articulated frame steering (AFS) systems, widely implemented on construction, forestry and mining vehicles, are known to enhance the traction and mobility/maneuverability performances of the vehicle [19, 126, 128]. The articulated frame-steered vehicles (AFSV) comprise front and rear units coupled by an articulation joint and frame mounted left and right steering struts. The roll degree-of-freedom (DOF), apart from the yaw-DOF, introduced by the articulation joint, however, may lead to reduced roll stability and yaw divergence of the AFSVs [11, 128, 132, 133]. The steering of the AFSV also requires relatively large magnitude of steering torque generated by the two hydraulic-powered steering struts. The essential yaw stability, steering power consumption and maneuverability performance characteristics of the AFSVs are known to be strongly affected by the kinematic and dynamic properties of the steering system. Furthermore, various design parameters of the AFS system exhibit contradictory effects on its performance characteristics [146].

A few studies have suggested that the critical speed of an AFSV can be enhanced by increasing the equivalent torsional stiffness and damping at the articulation joint. Horton and Crolla [12] and He et al. [19] suggested that increasing the effective bulk modulus of the hydraulic fluid within the steering struts can yield higher effective stiffness. Higher fluid bulk modulus, however, can lead to lower torsional damping ratio [146]. Permitting higher leakage flows across the strut piston seals could provide higher articulation damping [10, 12, 19]. Pazooki et al. [10] showed that steering response rate of AFSV could be enhanced by increasing the maximum flow rate of the steering valve. The study was based on yaw plane model of the vehicle with a closed-loop AFS system. Increasing the flow rate, however, will impose higher power requirement and may lead to higher response overshoot while maneuvering. Increasing the leakage flows will also contribute to higher power demand and lower efficiency of the AFS.

A few studies have attempted to seek optimal designs of different AFS systems using yaw-plane model of the AFSV. The majority of these have focused on identification of optimal mounting positions of the steering struts considering AFS kinematics in the yaw-plane to achieve certain performance measures such as minimal fluid pressure, minimal power, desired articulation angle, articulation torque and steering rate [126, 147, 148]. Dudziński [126] obtained a Pareto-optimal set of design parameters to achieve a compromise between the maximum steering arm length and maximum transmission angle of the steering struts over the entire range of the articulation angle. The optimal solutions were obtained to satisfy target steering torque, steering rate and a certain articulation angle. Wei at al. [147] identified optimal strut layout to achieve minimum pressure oscillation within the steering struts by minimizing the differences between the right- and left-strut's displacements and the resulting arm lengths. The proposed optimization problem helped limit the kinematic asymmetry under extreme steering maneuvers. Zhao and Wang [148] proposed an optimal strut layout to minimize the steering power consumption for an articulated dump truck in addition to the minimum difference between displacements of the two struts. The multi-objective fuzzy optimization design theory was used in an effort to reduce the kinematic asymmetry and power consumption simultaneously. Thulasiraman et al. [149] used a quasi-static model of the vehicle to identify minimal actuating fluid pressure within the struts to overcome motion resistances encountered during wheels alignment, rolling and wheel dragging. The effectiveness of the resulting optimal strut layout and fluid pressure was illustrated through field measurements conducted on a wheel loader.

The aforementioned design optimization studies, invariably, were based only on kinematics of the AFS system, while the contributions due to dynamics of the coupled AFS-vehicle system were neglected. A number of studies have established that the dynamics of the AFS and the vehicle strongly affect the AFS responses, and yaw stability limit and transient directional behavior of the vehicle [10, 12, 19, 131]. The stability and direction performance of the vehicle are thus not addressed in the kinematic-based optimal designs. Furthermore, the relatively long steering struts employed in the AFS system may interfere with other subsystems, especially under extreme steering maneuvers. The constraints imposed by the other vehicle design factors on the struts' geometry and layout have not been addressed in the above studies.

The above design optimization studies obtained optimal solutions to minimize different objective functions. The solutions thus represent a compromise between multiple objectives in terms of a Pareto-optimal set of the design parameters [126], or through minimization of a weighted sum of the objective functions [150, 151]. The specific weights applied to various objectives pose considerable challenges, and are generally governed by the designer's preference [152]. This is usually performed posteriorly on the Pareto-optimal set or a priori using the efficient weighted-sum method [152, 153]. Alternatively, the Analytic Hierarchy Process (AHP) can be applied to determine the relative weights in a reliable manner considering the pairwise comparisons and hierarchical weighting process [152, 154].

In this study, a comprehensive model of an articulated frame steering system is formulated considering kinematics and dynamic properties of the actuating struts in conjunction with the yaw-plane model of an articulated mining truck. The validity of the coupled AFS and vehicle model is illustrated through comparisons of the steering responses with the field-measured data. The essential objective measures are identified considering yaw oscillation/stability, steering power efficiency and maneuverability of the vehicle under pulse and step steering inputs. An Analytic Hierarchy Process (AHP) model is subsequently developed to determine the weights to be applied to the selected objective measures, namely, strut length, yaw oscillation frequency, yaw damping ratio, steering gain, response overshoot and response rate. The weighted-sum method is used to formulate a composite minimization function subject to various limit constraints, which is solved using a combination of direct- and gradient-based search algorithms in the Matlab platform. The merits of the solutions comprising optimal steering struts' layout, steering valve flow characteristics and fluid bulk modulus are discussed through model simulations.

4.2 Model formulation and validation of coupled AFS and AFSV system

4.2.1 Modeling of the AFS kinematics and AFS-vehicle dynamics

The directional responses of an AFSV under a steering input are primarily governed by the steering torque developed by the frame steering system. Under a given steer input, the steering torque developed by the steering struts is strongly related to both the kinematics of the AFS and dynamics of the actuating system, apart from lateral and yaw motions of the two vehicle units. Figure 4.1 illustrates yaw plane model of an articulated frame steered vehicle (AFSV) subject to a steering torque, T_s, about the articulation joint, which leads to an articulation angle, θ, between the front and rear units of the vehicle. Assuming constant forward speed, the governing equations of the lateral and yaw motions of the vehicle units are obtained as [146]:

$$\begin{gathered}
m_f\left(\dot{v}_f + u_f\varphi_f\right) + m_r(\dot{v}_r + u_r\varphi_r)\cos\theta - m_r(\dot{u}_r - v_r\varphi_r)\sin\theta - Y_1 - Y_2 - (Y_3 + Y_4)\cos\theta = 0 \\
\left(I_f + m_f L_{f2}^2\right)\dot{\varphi}_f + m_f\left(\dot{v}_f + u_f\varphi_f\right)L_{f2} - (Y_1 + Y_2)\left(L_{f1} + L_{f2}\right) + (M_{z1} + M_{z2}) - T_s = 0 \\
(I_r + m_r L_{r2}^2)\dot{\varphi}_r - m_r(\dot{v}_r + u_r\varphi_r)L_{r2} + (Y_3 + Y_4)(L_{r1} + L_{r2}) + (M_{z3} + M_{z4}) + T_s = 0
\end{gathered} \tag{4.1}$$

where (u_f, v_f, φ_f) and (u_r, v_r, φ_r) are the body-fixed longitudinal, lateral and yaw velocities of the front and rear units, respectively, denoted by the subscripts *f* and *r*; m_f and m_r are masses of the front and rear units, respectively; I_f and I_r are yaw mass moment of inertia of two units about their respective mass center (cg); Y_i and M_{zi} are the cornering force and aligning moment developed by tire i (i=1,..,4), as functions of the tires' side-slip angles together with the first-order lag, as detailed in[146]; L_{j1} and L_{j2} are longitudinal distances from the cg of unit j (j=f, r) to the axle attached to the same unit and the articulation joint, respectively.

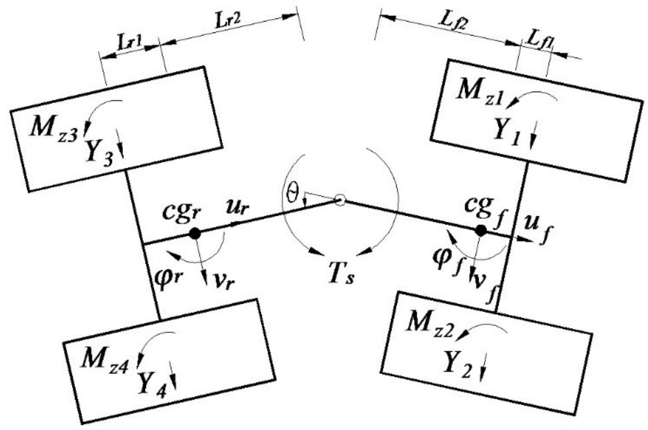

Figure 4.1: Yaw-plane model of the articulated frame-steered vehicle (AFSV)

Apart from the articulation joint, the two vehicle units are coupled via the left- and right-steering struts, which are mounted between the front unit (at L_1 and R_1) and the rear unit (at L_2 and R_2), as seen in Fig. 4.2. The two steering struts are also coupled hydraulically, where the piston- and rod-side chambers of one strut are connected to the rod- and piston-side chambers, respectively of the other strut. The steering valve, which is driven by the steering wheel, directs the fluid flow from the accumulator to one of the strut chambers as well as from the other strut chamber to the reservoir. A hydraulic pump is used to charge the accumulator; the fluid pressure in the accumulator, P_s, is held near 100 bars. The fluid pressure in the reservoir, P_0, is nearly atmosphereic. During a steering input, the forces developed by the left- and right-struts (F_L and F_R, respectively) contribute to the steering torque about the articulation joint, as shown in Fig. 4.1, such that:

$$T_s = F_L h_L + F_R h_R \tag{4.2}$$

From the above relation, it is evident that the resultant steering torque is directly related to the steering arm lengths, h_L and h_R, of the left- and right-struts, respectively, which are further influenced by kinematics of the AFS, especially the lengths and layout of the struts (Fig. 4.2).

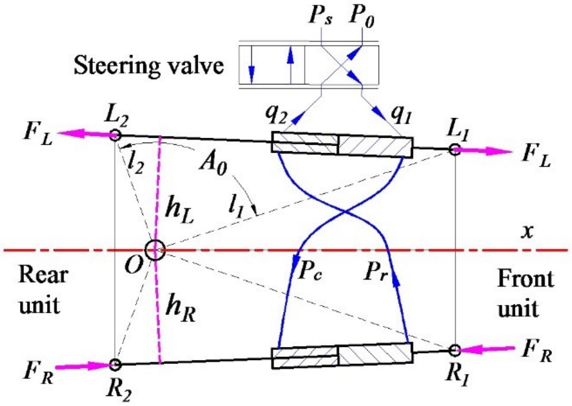

Figure 4.2: Layout of the steering struts and the hydraulic actuating circuit of the AFS system

The variations in the instantaneous steering arm lengths (h_L and h_R) and the struts' lengths (L_L and L_R) are strongly influenced by the struts' layout apart from the articulation angle. The steering arm lengths and the resulting steering torque are determined as functions of the articulation angle θ, and the kinematic constants A_0, l_1 and l_2 shown in Fig. 4.2. Constants l_1 and l_2 define coordinates of the front and rear mounting points of the struts, respectively, with respect to the articulation joint. A_0 defines the initial angle of the strut mounts with respect to the articulation joint, when the two units are aligned along the centerline *x* (Fig. 4.2). For the left- and right-struts, this angle is formed by lines *OL₁* (l_1) and *OL₂* (l_2), and *OR₁* (l_1) and *OR₂* (l_2), respectively, such that:

$$\begin{aligned} L_L(\theta) &= \sqrt{l_1^2 + l_2^2 - 2l_1 l_2 \cos(A_0 + \theta)} \\ L_R(\theta) &= \sqrt{l_1^2 + l_2^2 - 2l_1 l_2 \cos(A_0 - \theta)} \\ h_L(\theta) &= l_1 l_2\, sin(A_0 + \theta)\,/l_L \\ h_R(\theta) &= l_1 l_2\, sin(A_0 - \theta)\,/l_R \end{aligned} \tag{4.3}$$

The force developed by a steering strut is determined from the flow characteristics of the steering valve and the resulting pressure differences across the piston. Considering the friction due to strut seals as a viscous force, the forces developed by the left- and right-struts can be expressed as a function of the pressure difference, articulation rate $\dot{\theta}$ and the steering arm lengths, such that:

$$\begin{aligned} F_L &= P_c A_c - P_r A_r - \mu_v h_L \dot{\theta} \\ F_R &= P_c A_r - P_r A_c - \mu_v h_R \dot{\theta} \end{aligned} \tag{4.4}$$

where P_c is the fluid pressure in the piston-side chamber of the left strut and rod-side chamber of the right strut, P_r is the fluid pressure in rod-side chamber of the left strut and piston-side chamber of the right strut (Fig. 4.2), A_c is the piston area, A_r is the annular area of the rod-side chamber, and μ_v is the viscous damping coefficient due to seal friction.

The fluid pressures within the steering struts are derived on the basis of the fluid compressibility and fluid continuity. Considering the leakage flows between each chamber, the fluid continuity of the strut chambers can be expressed as:

$$\begin{aligned} \frac{V_1}{B_{eff}} \dot{P}_c &= q_1 - A_c h_L \dot{\theta} - A_r h_R \dot{\theta} - q_l \\ \frac{V_2}{B_{eff}} \dot{P}_r &= A_r h_L \dot{\theta} + A_c h_R \dot{\theta} + q_l - q_2 \end{aligned} \tag{4.5}$$

where B_{eff} is the effective bulk modulus of the hydraulic fluid; V_1 is total volume of fluid in the piston-side chamber of the left strut and rod-side chamber of the right strut; V_2 is total volume of fluid in the rod-side chamber of the left strut and piston-side chamber of the right strut; q_l is the leakage flow within the struts, assumed as a linear function of the pressure difference across the piston [19, 138]; and q_1 and q_2 are the rates of fluid flows from steering valve to the steering struts, and from steering struts to the reservoir, respectively.

Fluid flow rates through the steering valve are evaluated from specifications characteristics of the valve [143]. These suggested laminar flows through the valve under relatively low pressures and transition to turbulent flows under higher pressure difference. The fluid flow through the steering valve, q, is thus modeled as a laminar-turbulent transition flow within the working pressure range [142], as:

$$q = a_m X \sqrt{\Delta P} + a_v X \Delta P e^{a_0 \Delta P} \tag{4.6}$$

where ΔP is the fluid pressure difference across the steering valve, X is the effective opening area of the steering valve, a_m is the coefficient determining the maximum flow rate, a_0 is the coefficient determining the transition from the laminar- to turbulent-flow, a_v is the coefficient determining the initial rise rate of the fluid flow. The valve opening is related to the steering command, which exhibits dead-band and saturation nonlinearities [146]. The flow rate coefficients, a_0, a_v and a_m, in Eq. (4.6) are identified on the basis of the valve specifications from the manufacturer [143]. Figure 4.3 compares the flow rate and pressure difference characteristics of the valve obtained from the model with the manufacturer's specifications for the fully opened valve. The comparison suggests that the model can accurately describe the valve flow characteristics in the specified pressure range (0 - 80 bars).

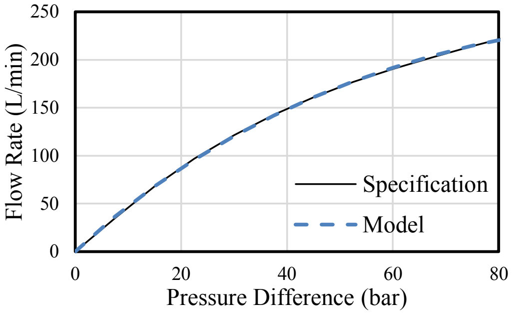

Figure 4.3: Comparison of flow rate versus pressure difference characteristics obtained from the model with the manufacturer’s specification for fully opened steering valve

4.2.2 Model validation

The validity of the coupled AFS-vehicle system model is initially examined using the data acquired through measurements performed on a 35 tons mining AFSV. The vehicle parameters also served as nominal simulation parameters for the coupled system model, which are summarized in Table 4.1 [131, 145]. The field test program has been described in [131]. Briefly, the kinematic and dynamic responses of the vehicle and the AFS system were measured during nearly-constant speed cornering and path-change maneuvers, while operating on a relatively smooth concrete surface. Figure 4.4 illustrates comparisons of articulation angle responses of the model with the measured data obtained for the unloaded and loaded vehicle. The test speeds for the unloaded and loaded vehicles, however, differed. These were 18.5 and 13.5 km/h, respectively, during the cornering maneuver, and 19.2 and 15.3 km/h during the path-change maneuver. The results are presented for constant speed cornering and path-change maneuvers. The model yields steady articulation angles of the loaded and unloaded vehicle during cornering, which decrease slightly due to leakage flows within the steering struts. The mean measured values are comparable with those predicted from the model for both the unloaded and loaded vehicles, as shown in Figs. 4.4(a) and 4.4(b), respectively. The measured data, however, exhibit some oscillations in the articulation angle, which are not observed in the model responses. Such oscillations are attributed to slight variations in the steering wheel angle and forward speed, and tires’ interactions with the random road surface during the field measurements, which are not considered in the model.

Figure 4.4(c) and 4.4(d) compare the articulation angle responses of the unloaded and loaded vehicle models, respectively, subject to the path-change maneuver, with the corresponding measured responses. The comparisons show very good agreement between the two for the loaded vehicle, with notable differences for the unloaded vehicle. The peak measured articulation angle of unloaded vehicle is observed to be lower than that predicted from the model, as illustrated in

Fig. 4.4(c). Further analysis of the measured data revealed that measurement errors had occurred due to loosening of the link rods used to attach the articulation potentiometer [131]. Despite the observed discrepancies, the results suggest that the AFSV model could yield reasonably good predictions of the steady-state and transient steering responses of the loaded as well as unloaded vehicle.

Table 4.1: Nominal simulation parameters of the 35 tons AFSV and the AFS system [131, 145]

Vehicle Model Parameters			Steering Model Parameters	
Variable	Loaded	Unloaded	Variable	Value
m_f (kg)	21,000	21,000	A_0 (deg)	76.5
m_r (kg)	52,220	18,500	l_1 (m)	1.96
I_f (kgm^2)	42,000	42,000	l_2 (m)	0.64
I_r (kgm^2)	104,000	31,000	a_0	-0.0074
L_{f1} (m)	-0.45	-0.45	a_m	0.94
L_{f2} (m)	2.13	2.13	a_v	4.8
L_{r1} (m)	1.13	0.60	A_c (cm^2)	95
L_{r2} (m)	2.31	2.84	A_r (cm^2)	57
			B_{eff}(Gpa)	1.6

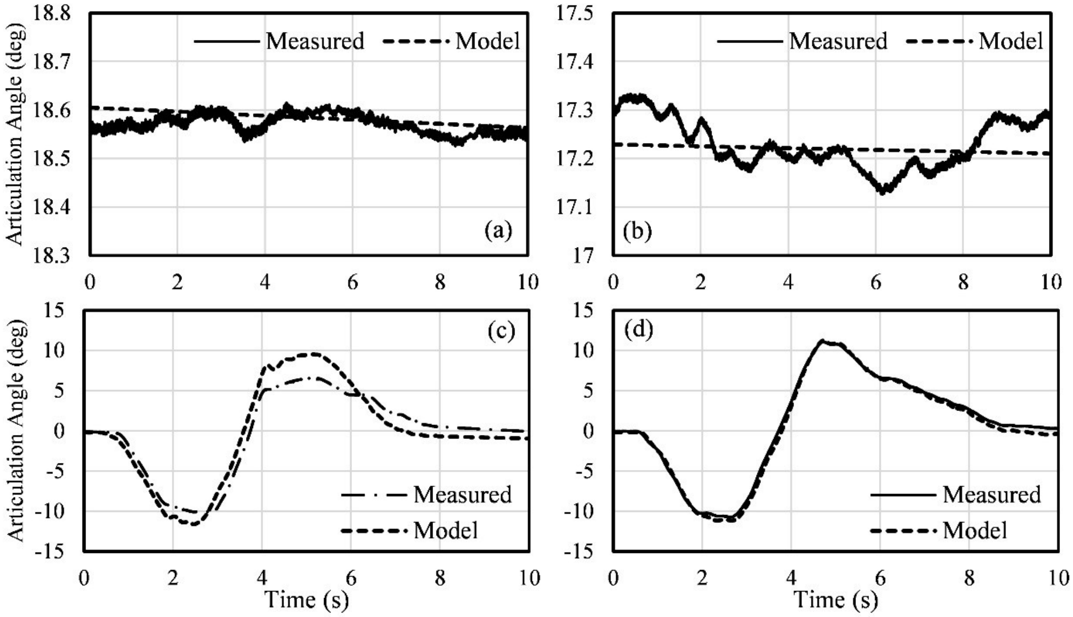

Figure 4.4: Comparisons of the articulation angle responses of the unloaded and loaded vehicle models with the measured responses: (a) cornering, unloaded (18.5km/h); (b) cornering, loaded (13.4km/h); (c) path-change, unloaded (19.2km/h) and (d) path-change, loaded (15.3km/h)

4.3 Design optimization of the AFS system

The kinematics and dynamics of the AFS system are primarily influenced by the struts layout, steering valve flow characteristics and fluid bulk modulus as evidenced from Eqs. (4.3), (4.5) and (4.6). A few studies have attempted optimal designs of the AFS system considering specific performance measures such as minimal fluid pressure and power consumption [148, 149], and desired articulation angle, articulation torque and steering rate [126]. These are based on geometry and kinematic responses of the AFS, while the contributions due to steering valve, fluid properties and dynamics of the steering struts and the vehicle are neglected. Moreover, the optimal parameters identified to satisfy a defined performance measure may affect other measures in a contradictory manner.

The aforementioned studies have shown that increasing the steering arm length can help achieve the desired articulation response and steering torque with lower fluid pressure and thus power demand. This relatively longer struts, however, may pose implementation challenges due to potential interference with other components during turning, apart from the potential column instability issue. Increasing the fluid bulk modulus contributes to improved yaw stability limit by increasing the effective articulation stiffness, while it leads to reduced effective damping [146]. The studies reporting design parametric sensitivity analyses have shown that the leakage flows help reduce yaw oscillations and increase the yaw stability limit by improving yaw damping [12, 19]. Leakage flows, however, will lead to higher power consumption by the AFS system. Increasing the maximum steering valve flow rate results in rapid steering response [10] at the expense of higher power consumption and larger response overshoot. The design optimization study thus necessitates identification of essential objective measures related to power consumption, maneuverability and yaw oscillation/stability behavior of the vehicle, and the key design parameters, which are discussed below.

4.3.1 Identification of the objective measures

In this study, the design optimization of the AFS is attempted considering a range of objective measures, which affect yaw oscillation/stability, power consumption and steering efficiency, and maneuverability of the AFSV in a coupled manner, as seen in Fig. 4.5. The objective measures can be identified from steady-state and transient articulation angle responses of the yaw-plane vehicle model to step and pulse steering inputs, shown in Figs. 4.6(a) and 4.6(b), respectively. The results are obtained for the loaded vehicle model using the nominal parameters (Table 4.1), while subjected to 30-degree step steering and 0.2*s* half-sine steering pulse inputs, respectively. The steering inputs are applied at a constant forward speed of 50 km/h, which is generally the upper speed limit in the open-pit mining operations.

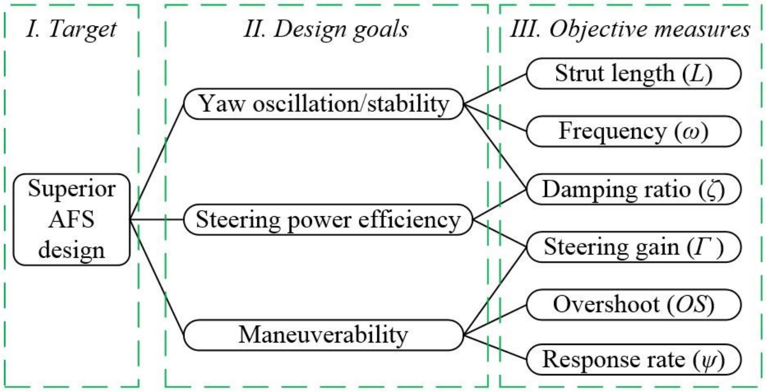

Figure 4.5: Objective measures related to performances of the articulated frame steering vehicle

It has been reported that the yaw stability limit of an AFSV can be enhanced by increasing the yaw mode stiffness and damping ratio properties of the AFSV [12, 19]. For a nonlinear vehicle model, these properties can be estimated from the frequency and rate of decay of free oscillations in the articulation angle response following the pulse input (Fig. 4.6(b)) [10, 132, 155]. The higher yaw oscillation frequency (ω) and damping ratio (ζ) are thus considered as the essential objective measures to realize improved yaw oscillation/stability performance of an AFS design. The strut length (L) forms an additional measure considering its notable effect on the overall articulation stiffness, as seen in Fig. 4.5. The strut length should be minimized to facilitate implementation, and to ensure column stability and absence of interference with other subsystems.

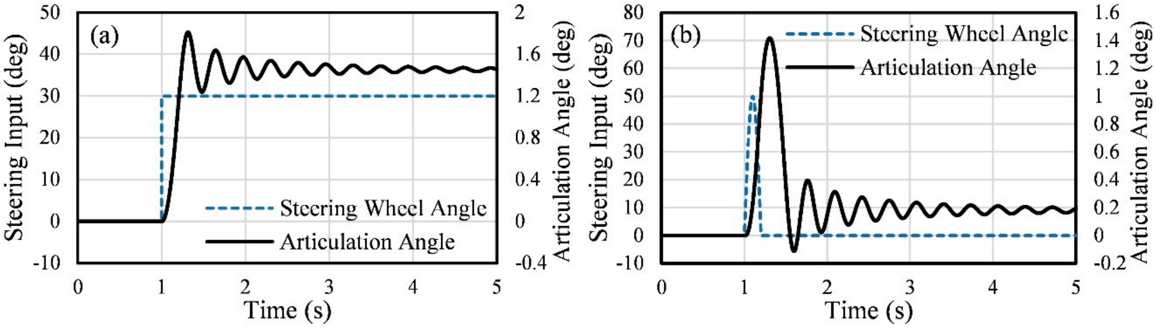

Figure 4.6: Articulation angle response of the loaded vehicle model subject to: (a) 30 degrees step steering input; and (b) 0.2s pulse steering input (50km/h)

Greater damping within the AFS system, however, also implies greater power dissipation and reduced steering power efficiency. The steering power efficiency (η) of the hydraulic-powered AFS system can be obtained from the useful work done by the AFS struts and the total hydraulic power consumption, such that:

$$\eta = \frac{\int T_s \dot{\theta} dt}{\int P_s q dt} \tag{4.7}$$

In Eq. (4.7), $\int qdt$ defines the total fluid volume flow from the steering valve to the struts. For given flow characteristics of the steering valve, the fluid volume is determined by the valve spool displacement and thus the magnitude of the steering input [131]. The amount of useful work, on the other hand, is related to the resulting articulation angle (θ) response. The ratio of the steady-state articulation angle under a step steer input to the steering wheel angle, defined as the steering gain Γ, thus relates to the average power efficiency of the AFS system. The steering gain is also related to the overall steering ratio of the AFS system and can be estimated from the articulation response to a step steer input, as shown in Fig. 4.6(a).

Both the steering power efficiency and the steering gain are strongly related to effective yaw damping, which is mostly attributed to the leakage flows within the struts. Figure 4.7 illustrates variations in the steering gain obtained from the steady-state step-steering response considering ±15% and ±30% variations in the leakage flow coefficient relative to the nominal value. The results suggest strong correlation (r^2>0.99) between them over the entire range of leakage flows considered. Increasing the leakage flows results in lower steering gain, which is consistent with the observation in [10], as well as lower steering power efficiency. Lower yaw-mode damping ratio and higher steering gain are thus considered as the objective measures related to steering power efficiency of the AFSV (Fig. 4.5).

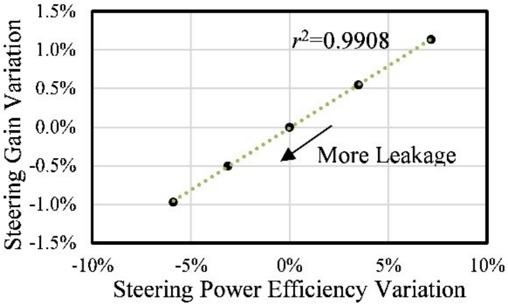

Figure 4.7: Correlation between the steering gain and steering power efficiency over a range of leakage flows

Moreover, good vehicle maneuverability generally implies short turning radius, rapid turning and ability to follow the desired trajectory [126]. The turning ability of the vehicle can be obtained from the steady-state articulation angle response to a step steer input. The step steer response in Fig. 4.6(a) further yields steering response rate in terms of 0-to-100% rise time and the overshoot, considered as a measure of the turning speed and path deviation, respectively. Higher steering gain, higher response rate and lower response overshoot thus form the objective measures related to enhanced manoeuvrability of the AFSV.

4.3.2 Optimization problem formulation

The design optimization problem is formulated considering the design goals and the corresponding objective measures, summarized as levels II and III, respectively, in the hierarchy scheme in Fig. 4.5. As discussed above, the essential objective measures related to enhanced yaw oscillation/stability, steering power efficiency and maneuverability performances of the coupled AFS-vehicle system include: (i) shorter strut length L, (ii) higher oscillation frequency ω, (iii) higher damping ratio ζ, (iv) higher steering gain $\varGamma$, (v) lower response overshoot OS and (vi) higher response rate ψ. The design optimization problem is thus formulated to minimize a composite objective function $F(\chi)$ of weighted objective measures, such that:

$$F(\chi) = \text{Minimize}[V \cdot W] \tag{4.8}$$

where V is a vector of the objective measures normalized with respect to those corresponding to the nominal parameters, $V = [L/L_0 \quad \omega_0/\omega \quad \zeta_0/\zeta \quad \varGamma_0/\varGamma \quad OS/OS_0 \quad \psi_0/\psi]$, where the nominal values are denoted with subscript '*0*' obtained using the nominal parameters (Table 4.1). In the above equation, W is a coulomb vector of weights and χ is a vector of design variables, which are identified considering both the kinematic and dynamic response of the AFS and the vehicle. These include: (i) the steering struts layout parameters (A_0, l_1 and l_2), which directly relate to lengths of the struts, steering gain, and effective articulation stiffness and damping; (ii) the rate of change of steering valve flow (a_v), which determines the steering response rate; and (iii) effective fluid bulk modulus (B_{eff}), which influences the equivalent stiffness of the AFS system and the response rate [10, 19]. The fluid bulk modulus and strut kinematics also affect the yaw stability limits of the AFSV. The maximum flow rate of the steering valve, leakage flows and the friction due to struts' seals are held to the nominal values, since these directly relate to the power consumption.

4.3.3 Design constraints

Limit constraints, defined for each design variable on the basis of reported parameter sensitivity analyses and geometric design constraints, are summarized in Table 4.2. It is reported that the effective hydraulic fluid bulk modulus could increase with the fluid pressure and saturate at about 1.7 GPa [156, 157], while it may decrease considerably in the presence of entrapped air [12, 158]. The limit constraints on the effective fluid bulk modulus is thus defined as, $0.6 \leq B_{eff} \leq 1.7$ GPa.

The valve coefficient, a_v, affecting the rate of change of steering valve flow is permitted to vary within ±50%, such that $2.4 \leq a_v \leq 7.2$.

The constraints on the struts' layout parameters (A_0, l_1 and l_2) are defined considering the feasible mounting locations (L_1, R_1) and (L_2, R_2) on the lead and trailing units, respectively (Table 4.2). As shown in Fig. 4.8, the center line of main beams and front cross beam define the extreme mounting locations (L_1, R_1) of struts on the front unit. On the rear unit, the struts are mounted close to the articulation joint beside the engine so as to reduce the overall strut length and to minimize potential interference due to struts. The limit constraints, summarized in Table 4.2, are identified to ensure absence of interference with the large size tires considering extremities of the front tires (T_L, T_R) and the engine supporting structure (E_L, E_R), as shown in Fig. 4.8. Additional limit constraints are thus defined to ensure that the left- and right-strut axes do not coincide with L_1T_L and L_1E_L, and R_1T_R and R_1E_R, respectively, during steering, such that:

$$\begin{aligned} \angle OL_1E_L < \angle OL_1L_2(\theta) < \angle OL_1T_L \\ \angle OR_1E_R < \angle OR_1R_2(\theta) < \angle OR_1T_R \end{aligned} \tag{4.9}$$

In addition, the minimum strut length must satisfy the following inequality to achieve maximum articulation angle of about 45 degrees [126]:

$$L > (L_{max} - L) + 2(L - L_{min}) \tag{4.10}$$

where L_{max} and L_{min} represent maximum and minimum strut lengths, respectively, when fully extended and compressed.

Table 4.2: Nominal values and upper and lower bounds of the design parameters

Parameters	Lower bound	Nominal value	Upper bound
A_0 (deg)	45	76.5	130
l_1 (m)	0.8	1.96	3.0
l_2 (m)	0.35	0.64	0.95
a_v	2.4	4.8	7.2
B_{eff} (Gpa)	0.6	1.6	1.7

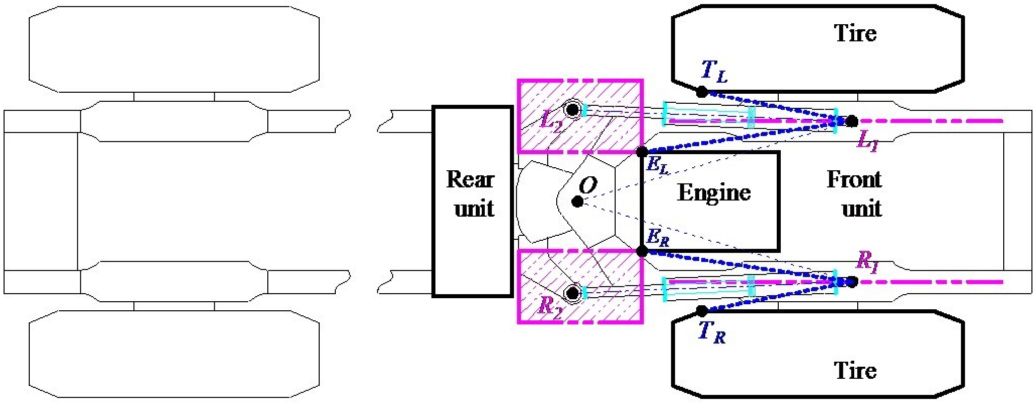

Figure 4.8: Representation of the articulated frame-steered vehicle and configuration of the steering struts

4.3.4 Weight determination of the objective measures

As illustrated in Fig. 4.5, the selected objective measures intrinsically form a hierarchal relationship with the AFS system design (level I) and the design goals (level II). The Analytic Hierarchy Process (AHP) modeling approach [154] is used to identify appropriate weights for different design goals in level II and the objective measures in level III. The weights within each hierarchy level, with respect to the preceding level, are obtained as the normalized principal eigenvector of a reciprocal pairwise comparison matrix [154, 159]. This matrix is defined considering relative importance of different elements within a level, which can vary from 1 (identical importance) to 9 (high importance) [159]. In level II, the vehicle yaw oscillation/stability is considered 3 times as important as the steering power efficiency, and 2 times as important as the maneuverability. The maneuverability is considered 2 times as important as the steering power efficiency, which yields the pairwise comparison matrix for level II, M_2, as:

$$M_2 = \begin{bmatrix} 1 & 3 & 2 \\ 1/3 & 1 & 1/2 \\ 1/2 & 2 & 1 \end{bmatrix} \tag{4.11}$$

The principal eigenvector of M_2 is normalized to yield weights for level II elements with respect to level I, $W_{II/I}$, such that:

$$W_{II/I} = [0.54 \quad 0.16 \quad 0.3]^T \tag{4.12}$$

where ‘T’ designates the transpose.

Similarly, the pairwise comparison matrix of the objective measures in level III is formulated to determine the weights for the objective measures vector V with respect to the design goals in level II, $W_{III/II}$. The reciprocal pairwise comparison matrix is formulated considering relative importance of element $V(i)$ with respect to $V(j)$ and the linearized gradient $dV(j)/dV(i)$ obtained from fitting of their possible values within the constrained design space [15]. The relations between the selected objectives are generally nonlinear, and the pairwise comparison values between these objective measures are considered to be bounded by 5, which indicates a relatively strong importance [159], such that:

$$\frac{w_{V(i)}}{w_{V(j)}} = \begin{cases} 1, & \dfrac{dV(j)}{dV(i)} \geq 0 \\ -\dfrac{dV(j)}{dV(i)}, & -5 < \dfrac{dV(j)}{dV(i)} < 0, \\ 5, & \dfrac{dV(j)}{dV(i)} \leq -5 \end{cases} \qquad i,j = 1,..,6 \tag{4.13}$$

where $w_{V(i)}/w_{V(j)}$ is relative importance of $V(i)$ over $V(j)$. The relative weights between two independent elements, for instance, *Γ* vs *L* (Fig. 4.5), are taken as 0. The pairwise comparison matrices are obtained considering relative significance of the elements with respect to each design goal in level II, as:

$$M_{3/A(1)} = \begin{bmatrix} \begin{bmatrix} 1 & 1/5 & 1 \\ 5 & 1 & 1.59 \\ 1 & 0.63 & 1 \end{bmatrix} & \mathbf{0}_{3\times3} \\ \mathbf{0}_{3\times3} & \mathbf{0}_{3\times3} \end{bmatrix};\ M_{3/A(2)} = \begin{bmatrix} \mathbf{0}_{2\times2} & \mathbf{0}_{2\times2} & \mathbf{0}_{2\times2} \\ \mathbf{0}_{2\times2} & \begin{bmatrix} 1 & 1.76 \\ 0.57 & 1 \end{bmatrix} & \mathbf{0}_{2\times2} \\ \mathbf{0}_{2\times2} & \mathbf{0}_{2\times2} & \mathbf{0}_{2\times2} \end{bmatrix};\ M_{3/A(2)} = \begin{bmatrix} \mathbf{0}_{3\times3} & \mathbf{0}_{3\times3} \\ \mathbf{0}_{3\times3} & \begin{bmatrix} 1 & 1.25 & 1 \\ 0.8 & 1 & 1.3 \\ 1 & 0.77 & 1 \end{bmatrix} \end{bmatrix} \tag{4.14}$$

where *M*$_{3/A(k)}$ is the pairwise comparison matrix defining relative significance of the objective measures in level III with respect the design goal *A*(*k*), *k*=1,2,3 in level II. The principal eigenvectors of each matrix define the relative weights of measures in level III with respect to the goals in level II, *W*$_{III/II}$, such that:

$$W_{III/II} = \begin{bmatrix} 0.17 & 0 & 0 \\ 0.58 & 0 & 0 \\ 0.25 & 0.64 & 0 \\ 0 & 0.36 & 0.36 \\ 0 & 0 & 0.34 \\ 0 & 0 & 0.30 \end{bmatrix} \tag{4.15}$$

Since some of the elements in level III are not coupled to certain elements in level II, the AHP model is considered 'not complete' [159]. The proportions of the number of elements of *V* related to the each element in level II are used to define an additional weighting matrix *W*$_a$ as [154, 159]:

$$W_a = \begin{bmatrix} 3/6 & 0 & 0 \\ 0 & 2/6 & 0 \\ 0 & 0 & 3/6 \end{bmatrix} \tag{4.16}$$

The weights of the objective measures in Fig. 4.5 with respect to the AFS design (level I), *W*, are subsequently obtained from:

$$W = \text{Normalize}\big(W_{III/II} \cdot W_a \cdot W_{II/I}\big) = [0.1\ 0.33\ 0.21\ 0.15\ 0.11\ 0.1]^T \tag{4.17}$$

In the above equation, the weighting vector is normalized so as achieve the sum of weights as unity. The resulting weighting vector suggest highest relative significance of the yaw oscillation frequency (0.33) followed by the yaw damping ratio (0.21), the steering gain (0.15) and response overshoot (0.11). The relative significance of the strut length and the response rate are equal and lowest (0.1).

4.3.5 Optimization strategy

For nonlinear engineering optimization problems, a gradient-based search method may more likely yield a local optima than the direct-search optimization method [160]. In this study, the optimization problem is solved in two stages to approach a global solution, which involved pattern search (PS) followed by the sequential quadratic programming (SQP) algorithm available in Matlab/Simulink Design Optimization toolbox [161]. The PS algorithm, integrating the Latin hypercube search method, is utilized in order to effectively search for a preliminary optimal solution starting from a starting design vector [162]. The solutions obtained for different starting vectors converged to very similar optimal values. In the second stage, the SQP algorithm was used to further refines the PS algorithm solution to obtain the optimal articulated frame steering system design in the design space listed in Table 4.2.

4.4 Results and discussions

The optimization problem for the AFS system was solved considering fully loaded condition. Table 4.3 summarizes the optimized design parameters and the resulting values of the objective measures normalized with respect to those of the nominal design. The table compares the solutions obtained from PS method alone and the combined (PS/SQP) method. The combined PS/SQP method converges to only slightly lower weighted sum value compared to that obtained from the PS alone. The two methods, however, result in considerably different optimal solutions for individual measures. The preliminary solution converges to nearly nominal strut length while emphasizing the measures with relatively higher weights, namely the yaw mode frequency and the damping ratio. The combined method yields considerably lower optimal strut length with enhanced values of steering gain and the response rate, while maintaining comparable emphasis on the yaw frequency and damping ratio. This suggests that the PS algorithm yields an acceptable preliminary solution, while the combined PS/SQP algorithm further refines the optimal solution, as reported in

[163].

The combined algorithm yields substantially different layout of the steering struts with lower values of A_0, l_1 and l_2 compared to the PS method. The optimal design parameters A_0 and l_1 are substantially smaller than those of the current design, which translate to a compact AFS system design with substantially smaller strut length and thereby greater column stability. Despite the relatively lower weighting on the strut length, the combined PS/SQP method converged to 21% reduction in the strut length, which is due to its complex contributions to nearly all the other performance measures in the level III (Fig. 4.5). The parameter l_2, however, converges to a relatively higher value to achieve greater steering arms' length, h_L and h_R, and thereby greater steering torque. The optimal values of A_0 and l_1, obtained from the PS method, however, are comparable to the current design parameters, while a higher value of l_2 is chosen so as to enhance the steering arm length and the torque. The compact AFS design obtained from the combined method also yields relatively lower steering gain and response rate compared to the nominal design, but superior than those of the PS solution which converges closer to the current struts layout.

Both the methods converge towards upper bounds of the valve flow coefficient a_v and the fluid bulk modulus B_{eff}. This is due to relatively higher weighting imposed on the yaw mode frequency and damping, while approaching higher steering gain and response rate. The PS and combined PS/SQP methods yield normalized yaw oscillation frequencies of 1.35 and 1.24, respectively, which is due to combined effect of higher fluid bulk modulus, faster steering valve response and AFS kinematics (greater steering arms' length). Although the damping ratio is inversely affected by the increasing yaw mode frequency, the PS and combined PS/SQP methods yield 10% and 7% gain in the damping ratio. Moreover, the convergence towards higher steering system stiffness and higher flow coefficient would contribute to relatively higher response overshoot and response rate. The optimal solutions, however, yield lower response overshoot (3 to 6%) and rate (13 to 19%), which is due to relatively lower weights (0.10) imposed on these measures. The lower response rate together with lower steering gain also lead to reduced steering power efficiency and vehicle maneuverability.

Table 4.3: Optimal design parameters and normalized performance measures obtained from the pattern search (PS) and combined pattern search (PS) and sequential quadratic programming (SQP) methods

Parameter	Current design	Optimal design		Normalized Objective	Optimal value	
		PS	PS/SQP		PS	PS/SQP
A_0 (deg)	76.5	74.4	56.4	Strut length	0.95	0.79
l_1 (m)	1.96	1.86	1.79	Yaw frequency	1.35	1.24
l_2 (m)	0.64	0.85	0.77	Damping ratio	1.10	1.07
a_v	4.8	7.189	*7.200*	Steering gain	0.77	0.84
B_{eff} (GPa)	1.6	*1.700*	*1.700*	Overshoot	0.94	0.97
				Response rate	0.81	0.87
				Function $F(\chi)$	0.95	0.94

The results shown in Table 4.3 suggest that both the methods converge to upper bound of the effective bulk modulus, which is primarily due to higher weighting imposed on the yaw mode frequency and thus the steering stiffness. The solutions of the optimization problem were obtained by relaxing the upper bound on B_{eff} by 30% (B_{eff}=2.08 GPa) in order to achieve improved yaw oscillation frequency and response rate. The resulting optimal design parameters and performance measures values obtained from the PS and combined PS/SQP methods are summarized in Table 4.4. Both the methods yield relatively lower weighted sum values and either comparable or improved performance measures compared to those in Table 4.3. This suggests that relaxing the effective bulk modulus can lead to a more favorable AFS system design. Both the methods converge to the upper bound of B_{eff} but lead to more compact AFS system design compared to that presented in Table 4.3. The PS method, particularly, converges to considerably lower strut length and A_0. The combined PS/SQP method resulted in notable gains in nearly all the performance measures. Relaxing the upper bound on B_{eff} resulted in nearly 6% reduction in strut length, 2.4% increase in yaw frequency, 7% higher steering gain, 11% lower overshoot and 6% increase in the response rate. Increasing the steering system frequency, however, caused a slight reduction in the damping ratio, in the order of 3%. These are consistent with the trends in studies reporting the effect of fluid bulk modus on the equivalent torsional stiffness of AFS [12, 19]. Despite the higher effective torsional stiffness, the optimal solutions show reductions in the response overshoot, which is attributed to kineto-dynamics of the AFS system. Although the effective fluid bulk modulus of generally used hydraulic fluids has been reported to be limited to about 1.7 GPa [156, 157], the results suggest that use of alternate hydraulic fluids with greater bulk modulus can enhance the overall performances of the AFSV.

Table 4.4: Optimal design parameters and normalized performance measures obtained from the pattern search (PS) and combined pattern search (PS) and sequential quadratic programming (SQP) methods with relaxed upper bound of fluid bulk modulus

Parameter	Current design	Optimal design		Normalized Objective	Optimal value	
		PS	PS/SQP		PS	PS/SQP
A_0 (deg)	76.5	55.7	56.9	Strut length	0.85	0.74
l_1 (m)	1.96	1.95	1.67	Yaw frequency	1.49	1.27
l_2 (m)	0.64	0.84	0.72	Damping ratio	1.08	1.04
a_v	4.8	7.198	*7.200*	Steering gain	0.77	0.90
B_{eff} (GPa)	1.6	*2.080*	*2.080*	Overshoot	0.81	0.86
				Response rate	0.81	0.92
				Function $F(\chi)$	0.91	0.90

The simulations were performed to obtain articulation angle responses of both the current and optimal AFS designs to step and pulse steering inputs, which are compared in Fig. 4.9. The results are obtained using the optimal parameters obtained from the combined PS/SQP method with relaxed fluid bulk modulus (Table 4.4). The response to the step input clearly shows considerably higher oscillation frequency, lower peak magnitudes and lower response overshoot of the optimal design compared to the current design. The higher yaw oscillation frequency of the optimal design is also evident from the pulse steering response shown in Fig. 4.9(b). These suggest enhanced yaw stability limit and maneuverability performance of the AFSV with the optimal AFS system. Apart from these, optimal design yields significant decrease in the steering struts length (26%) leading to enhanced column stability of the steering struts and a more compact layout of the AFS system. The responses in Fig. 4.9 also show comparable response rates of the optimal and current designs, while the optimal design yields relatively lower steering gain compared to the current design. The optimal design thus does not provide benefits in terms of the steering power efficiency.

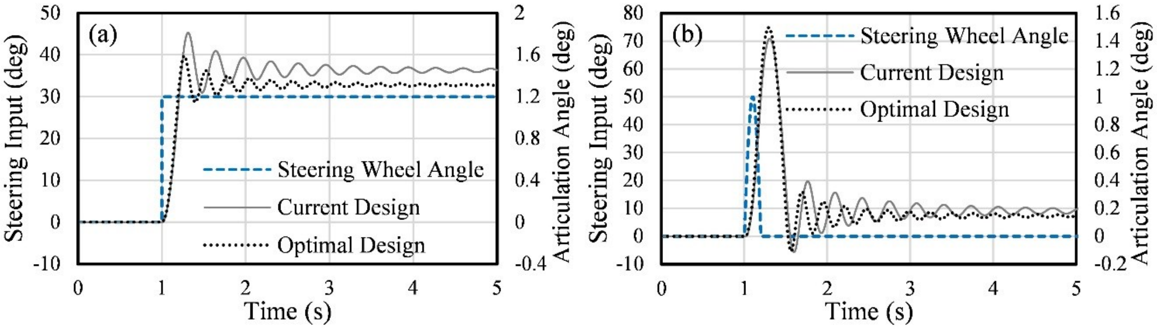

Figure 4.9: Comparisons of articulation angle responses of the optimal and current designs subject to (a) step and (b) pulse steering input

4.5 Conclusions

The design, and kinematics and dynamics of the articulated frame steering system affect the vehicle performances in terms of yaw oscillation/stability, steering gain, steering power efficiency and maneuverability in a highly complex and contradictory manner. The yaw oscillation/stability behavior of the vehicle is directly related to the strut length, fluid bulk modulus and effective yaw damping. The steering power efficiency was found to be strongly correlated (r^2>0.99) with the steering gain under a step steering input. The solutions of the three-level Analytic Hierarchy Process model revealed greatest weight for the equivalent yaw stiffness or oscillation frequency compared to the other measures, namely, strut length, damping ratio, steering gain, and response overshoot and rate.

The solutions of the design optimization problem suggested that the direct pattern search method can yield acceptable optimal design, while the combined pattern search and sequential quadratic programming method could provide more global optimal solution. The optimal solutions revealed 24% gain in the yaw oscillation frequency, 7% gain in the yaw damping ratio and a more compact AFS system design with over 20% reduction in the strut length. The results with relaxed the upper bound of fluid bulk modulus suggested further benefits in nearly all the performance measures, especially the 11% lower response overshoot attributing to kineto-dynamics of the AFS system. The steering power efficiency of the AFS system, however, was negligibly changed for the obtained optimal design based on the weighted sum of various objective measures.

CHAPTER 5

CHARACTERIZATION OF A HYDRO-PNEUMATIC SUSPENSION STRUT WITH GAS-OIL EMULSION

5.1 Introduction

Hydro-pneumatic suspensions (HPS), owing to their compact design and superior design flexibility, are increasingly being implemented in commercial road and off-road vehicles [164-168]. Their nonlinear pneumatic-stiffness and hydraulic-damping properties could provide enhanced attenuation of ride vibrations under large payload variations [124, 167], while offering improved handling performance through cross-axle interconnections [23, 169] or control interventions [170, 171]. Various designs of the HPS struts have evolved over the past few decades, which generally comprise a number of gas and oil chambers [23, 172, 173]. The strut chambers containing hydraulic oil are usually coupled via bleed orifices and/or damping or check valves. The gas may be separated from oil by a floating piston [23, 174] or a diaphragm [172], or the gas and oil may be contained within the same chamber [173, 175].

The separation of the gas from the oil via a floating piston or a diaphragm requires additional chambers within the strut and increases the design complexity, seal friction and cost of the HPS strut. Struts with chambers shared by the gas and oil may offer low cost and simpler designs. Such a design, however, permits gas entrapment within the oil and may yield highly complex variations in stiffness and damping properties of the strut. The entrapment of gas in the oil results in gas-oil emulsion within the strut leading to greater variations in the gas and oil properties, namely, the mass density and bulk modulus [142, 176, 177]. During operation, the gas-oil emulsion may also occur in high pressure struts with separated gas and oil chambers due to leakage through the floating piston seals [172]. This tends to alter the suspension performances, which has not been thoroughly investigated. Characterization of the HPS systems thus necessitates considerations of the effects of gas-oil emulsion, which could provide important design guidance for the HPS struts.

The characteristics of the HPS systems with separated oil and gas chambers have been investigated in a number of studies, while considering nominal gas and hydraulic oil properties [172, 174, 178]. The stiffness and damping coefficients of a HPS strut generally increase with increasing gas pressure and strut velocity, respectively. Els and Grobbelaar [174] analyzed a HPS strut with two oil chambers and a separated gas chamber. The strut damping effect was shown to increase the strut temperature in a laboratory test, which resulted in relatively greater strut stiffness and ride height. During the field test, the oil temperature saturated at about 85°C, although only negligible variation in gas temperature was observed due to good heat dissipation of the gas chamber. The reported laboratory results also revealed approximately adiabatic gas process under sinusoidal excitations at relatively higher frequencies. It was suggested that the heat transfer between the gas and its surroundings should be considered at relatively lower frequencies (<0.5Hz). Van Der Westhuizen and Els [179] compared the results obtained from real gas equations considering the heat transfer with the ideal gas law. Ideal adiabatic approach was shown to be appropriate within excitation cycles at relatively higher strut velocities. Moreover, relatively higher hysteresis was observed in the gas pressure measured at lower excitations frequencies compared to the higher frequencies, which was attributed to the heat transfer and thereby additional contribution to the energy dissipation of the HPS strut [174, 179].

Guo et al. [172] and Küçük et al. [180] analyzed the HPS strut comprising three oil chambers and a separated gas chamber assuming adiabatic gas process, turbulent fluid flows through the orifices and check valves, and negligible leakage flows. The three oil chambers, however, involved complex fluid flows among them and one of the chambers approached vacuum at a high velocity, as reported by Guo et al. [172]. Cao et al. [178] proposed an analytical model of a twin-gas-chamber HPS strut design with two gas chambers and two oil chambers. This novel HPS strut offered greater effective working area than the conventional strut designs and thereby relatively lower operating pressure for a given load capacity. The twin-gas-chamber design also revealed relatively lower asymmetry in the suspension rates during compression and extension.

In comparison to the struts with separated gas and oil chambers, only a few studies have explored the properties of strut designs with chambers shared by both the gas and the hydraulic oil. Yang et al. [173] and Shen et al. [175] analyzed a HPS strut with one mixed gas-oil chamber and an oil chamber. The studies reported hardening tendency in stiffness and reduced damping force during compression. Shen et al. [175] investigated the effect of varying the bleed orifices size, while Yang et al. [173] suggested that the variations in oil temperature affected the HPS properties only slightly. The effects of gas and oil mixing on the strut properties, however, were neglected in these studies. Within the mixed gas-oil chamber, the entrapped gas has been reported to dissolve into the oil and/or exist as gas bubbles [142]. The resulting gas-oil emulsion possesses lower mass density and bulk modulus compared to those of the hydraulic oil, which may affect the rates of fluid flows and effective volumes of the gas and the fluid. When considerable gas is entrapped within the hydraulic oil, the bulk modulus of the emulsion may be significantly reduced and highly sensitive to the fluid pressure [176, 177]. The properties of the mixed fluid such as bulk modulus and mass density are strongly influenced by the gas volume fraction, which have not yet been adequately addressed.

Furthermore, the aforementioned studies have generally assumed Coulomb [179] or negligible [178, 180] seal friction within the HPS strut. Owing to the high pressure design, the sealing of the gas chamber from the oil chamber generally involves substantial seal friction. The magnitude of the seal friction may be significant compared to the hydraulic damping force at a relatively lower velocity [179]. Various friction models have been proposed for characterizing seal friction considering pre-sliding hysteresis, stick-slip and Stribeck effects [181-183]. It would be worthy to investigate the significance of seal friction on the HPS characteristics over a range of strut operating velocity.

In this study, the characteristics of a simple and low cost HPS strut design with one mixed gas-oil chamber and one separate oil chamber are experimentally and analytically investigated. The static and dynamic pressure/force-deflection and force-velocity properties of a prototype strut are characterized in the laboratory under a nearly constant temperature, in the 0.1 to 8 Hz frequency range with peak velocity ranging from 0.05 to 0.24 m/s. An analytical model is formulated considering the seal friction, polytropic change in the gas state, entrapped gas within the hydraulic oil, mixed fluid flows through the bleed orifices and the check valves. The model validity is subsequently examined using the measured fluid pressures within the two strut chambers and the total strut force over the range of excitation velocities. The measured data and the model are analyzed and discussed to highlight the effects of gas-oil emulsion on the stiffness and damping properties of the HPS strut.

5.2 Strut design and laboratory measurements

The hydro-pneumatic suspension (HPS) strut, considered in this study, comprises two chambers connected via two bleed orifices and two check valves, as illustrated in Fig. 5.1. The piston-side chamber is shared by both the gas and the hydraulic oil, and the annular rod-side chamber is filled with only the hydraulic oil. The initial volume and pressure of the gas are selected to achieve desired HPS static stiffness and the load capacity considering the cross-section areas of the piston and the rod (Fig. 5.1(a)). During operation, the entrapment of gas within the oil would result in the gas-oil emulsion, as seen in Figs. 5.1(b) (compression) and 5.1(c) (extension). The effective mass density and bulk modulus of the gas-oil emulsion would thus be lower than those of the hydraulic oil, depending on the volume fraction of the entrapped gas [142, 176, 177]. The emulsion can flow from the piston-side chamber to the rod-side chamber via the check valves and bleed orifices installed on the strut rod during compression (Fig. 5.1(b)), apart from the leakage flow through the piston seal. The check valves, however, remain closed during the extension stroke (Fig. 5.1(c)), which contributes to relatively higher damping force in extension. The rates of fluid flows are related to the pressures within the two chambers, strut velocity as well as the properties of the gas-oil emulsion. The variations in the pressure difference between the two strut chambers and the seal friction force at different strut velocities determine the damping property of the HPS strut.

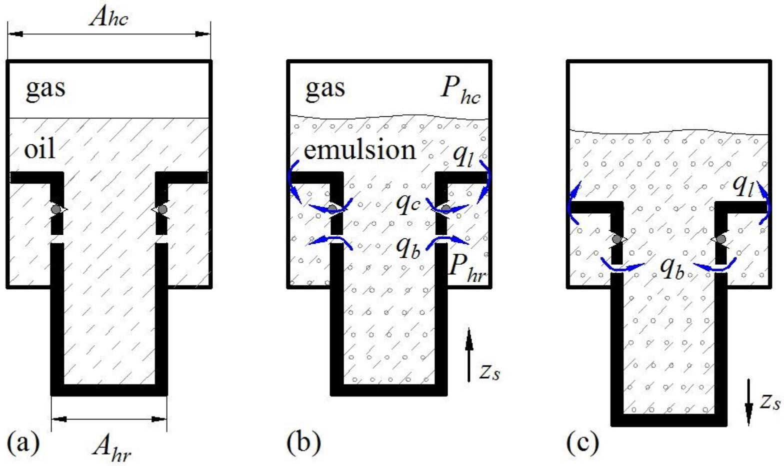

Figure 5.1: Schematics of the hydro-pneumatic suspension (HPS) strut: (a) static (mid-) position; (b) gas-oil emulsion during compression; and (c) gas-oil emulsion during extension

In order to investigate the stiffness and damping properties of this HPS strut with gas-oil emulsion, laboratory experiments were conducted on a prototype HPS strut to acquire its response characteristics under pseudo-static and dynamic excitations. The HPS strut was installed vertically between a fixed cross-beam via a 45 kN force transducer and an electro-hydraulic shaker, as illustrated in Fig. 5.2. The force transducer was mounted between the fixed cross beam and the strut to acquire the total strut force, while the strut deflection was measured using a linear variable differential transformer (LVDT) installed within the electro-hydraulic exciter. Two pressure sensors were installed on the strut to measure pressures of fluids within the rod- (#1 in Fig. 5.2) and piston-side (#2 in Fig. 5.2) chambers. The temperature of oil in the piston-side chamber was also measured during the experiments using a resistance temperature detector (RTD) inserted from the bottom of the strut rod. A thermocouple was further attached to exterior surface of the strut to monitor the strut body temperature.

The temperature of the HPS strut during the tests was maintained within certain desired ranges via a cooling fan, as seen in Fig. 5.2. The data from these sensors were acquired using a multi-channel data acquisition (DAQ) system. The strut was filled with 1 liter of hydraulic oil via a high pressure ball valve mounted at the top of the strut cylinder, as also shown in Fig. 5.2. The ball valve was subsequently connected to a nitrogen tank for charging the gas at a pressure of 0.68 Mpa (100 psi) via a pressure regulator.

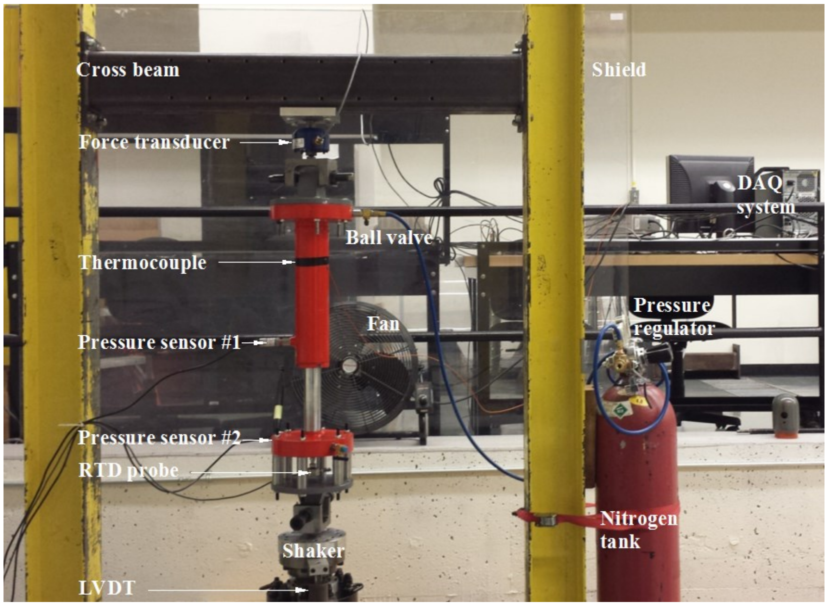

Figure 5.2: Experimental setup of the hydro-pneumatic suspension strut

Three series of experiments were conducted to study the effects of entrapped gas in the hydraulic oil, and to characterize the stiffness and damping properties of the strut. The first series of experiments was conducted to study the mixing of gas in the oil under a static deflection, which caused reduction in the gas pressure at a very slow rate due to gradual dissolving of gas in the oil. A static displacement was applied to the strut piston and the fluid pressures in the two chambers were monitored over a period of more than 1.5 hours. The strut deflection was applied in a ramp-step manner, while the ramp rate was approximately 70 mm/min. The strut was subsequently returned to the initial position and the fluid pressures were monitored in a similar manner. The experiment was repeated for three different static displacements (75, 100, 115 mm). In the second series, the strut piston was positioned near the mid-stroke of the strut for about 1 hour. The strut was then subjected to a harmonic excitation to examine the effect of entrapped gas on the fluid pressure during operation. The experiment was conducted for nearly 2.5 hours until the mean pressures of fluids in both the chambers approached steady values. The strut piston was then brought back to the bottom position. The harmonic excitation was applied at low frequencies of 0.1 and 1 Hz in order to minimize the heat build-up. The cylinder temperature was continuously monitored and held in the 21±2°C range using a large size fan. During the first and second series of experiments, the signals from the pressure transducers, force transducer, thermocouple and the LVDT were continuously acquired in the multi-channel data acquisition system at a sampling frequency of 10 Hz.

In the third series, the pressure-deflection, force-deflection and force-velocity characteristics of the strut were measured under different harmonic excitations. The measurements were performed for two different strut body temperatures (30±2°C and 50±2°C). The strut was displaced to achieve its mid-position, and the selected harmonic excitation was applied to the strut piston. The sensors' signals were acquired when the body temperature approached the desired value. The measurements were initially conducted at a low frequency of about 0.1 Hz in order to measure the force-deflection properties of the gas and the friction force under pseudo-static conditions. The force due to gas and seal friction was measured under 5, 25 and 50 mm amplitude excitations. The measurements were subsequently performed under excitations in the 1 to 8 Hz range and varying amplitudes to characterize the force-velocity properties of the strut. For this purpose, the experiments were repeated under different excitation amplitudes so as to achieve constant peak velocities ranging from 0.05 to 0.24 m/s over the selected frequency range. The peak amplitude, however, was limited to 45 mm. The data from the pressure, temperature, force and displacement sensors were acquired for analysis of strut properties under different excitations at a sampling frequency of 360 Hz. Additionally, the third series of experiments was repeated with one of the bleed orifices blocked, in order to investigate its effects on the strut stiffness and damping properties.

5.3 Model formulation and parameters identification

5.3.1 Hydro-pneumatic suspension model

An analytical model of the HPS strut is formulated considering the entrapped gas to investigate its performance characteristics as functions of the design parameters and external excitation. The stiffness property of the strut and its ride height are determined from the gas volume and gas pressure, which may be reduced by the gas entrapment within the hydraulic oil. The strut damping property, on the other hand, is related to the fluid pressures within the two strut chambers, which are related to strut deflection and velocity, and properties of the gas-oil emulsion (gas volume fraction, mass density and bulk modulus). As illustrated in Fig. 5.1, the total force developed by the HPS strut, F_h, can be obtained from the fluid pressures within the piston- and rod-side chambers and the friction due to the seals between the strut cylinder and strut rod, as:

$$F_h = P_{hc}A_{hc} - P_{hr}(A_{hc} - A_{hr}) + F_f \tag{5.1}$$

where P_{hc} and P_{hr} are pressures of fluid within the piston- and rod-side chambers, respectively; A_{hc} and A_{hr} are effective areas of the piston and rod, respectively, as shown in Fig. 5.1(a); and F_f is the friction force.

It has been shown that the seal friction force during periodic motions exhibits stick-slip, Stribeck effect and hysteresis behaviour. The friction force can thus be expressed as a combination of Coulomb, Stribeck and viscous components, as a function of the strut velocity ($\dot{z}_s$) [181, 183-185]. Furthermore, linear force transition in the vicinity of zero velocity ($|\dot{z}_s| < v_h$), is introduced to describe the hysteresis behavior of the friction force, as illustrated in Fig. 5.3. In the figure, the upward strut motion z_s from the static position (Fig. 5.1(a)) is considered positive ($z_s > 0$). When the strut velocity exceeds the hysteresis transition velocity v_h ($|\dot{z}_s| \geq v_h$), the friction force can be expressed as:

$$F_f = \mu_v \dot{z}_s + F_c sgn(\dot{z}_s) + F_s e^{-k_s|\dot{z}_s|} sgn(\dot{x});\ |\dot{z}_s| \geq v_h \tag{5.2}$$

where F_c is Coulomb friction force, F_s is stiction force, k_s is Stribeck coefficient, μ_v is viscous friction coefficient, and sgn represents the sign function. The friction force within the linear transition band, $|\dot{z}_s| < v_h$, which describes the hysteresis effect as the direction of velocity changes ($z_s\dot{z}_s < 0$), can be expressed as:

$$F_f = \mu_v \dot{z}_s + F_c\left(\frac{2}{v_h}\dot{z}_s - sgn(\dot{z}_s)\right) + F_s\left(\frac{1 + e^{-k_s v_h}}{v_h}\dot{z}_s - sgn(\dot{z}_s)\right);\ z_s\dot{z}_s < 0\ and\ |\dot{z}_s| < v_h \tag{5.3}$$

When the strut maintains the same direction of velocity within the linear transition band ($z_s\dot{z}_s \geq 0$ and $|\dot{z}_s| < v_h$), the friction force is obtained from Eq. (5.2). It has been further shown that width of the hysteresis loop in the transition region increases with increasing peak strut velocity [181]. The transition velocity band is thus expressed as a function of the peak strut velocity.

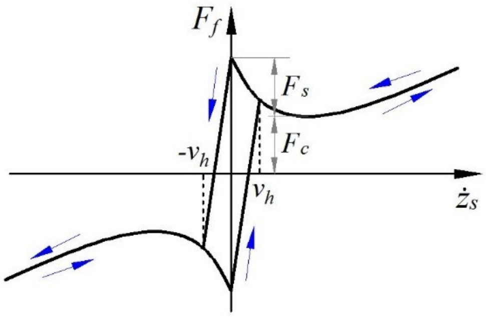

Figure 5.3: Friction model of the strut seals

The instantaneous pressures of the gas and emulsion within the piston-side chamber are assumed to be identical neglecting the effect of fluid inertia. Assuming polytropic process of the gas, P_{hc} can be obtained from the initial gas pressure P_{h0} and volume V_{g0}, and the instantaneous gas volume V_g, such that:

$$P_{hc} = P_{h0}\left(V_{g0}/V_g\right)^n \tag{5.4}$$

where n is the polytropic exponent. The instantaneous gas volume V_g in the piston-side chamber is obtained from the continuity equation considering compressibility of the gas-oil emulsion, which can be expressed as:

$$A_{hc}\dot{z}_s + \dot{V}_g = q_b + q_c + q_l + \frac{V_c}{\beta_c}\dot{P}_{hc} \tag{5.5}$$

where q_b, q_c, and q_l are rates of fluid flows through the bleed orifices, the check valves and the clearance between the strut piston and the cylinder, respectively; V_c and β_c are instantaneous volume and effective bulk modulus of the emulsion within the piston-side chamber, respectively. The pressure of fluid in the rod-side chamber, P_{hr}, is obtained from the volume continuity equation within the rod-side chamber. Since the mass density of the emulsion within each chamber may be different, the continuity within the rod-side chamber is formulated considering the mass density variation of the fluid flows between the two chambers, such that:

$$(A_{hc} - A_{hr})\dot{z}_s = \frac{\rho_c}{\rho_r}(q_b + q_c + q_l) - \frac{V_r}{\beta_r}\dot{P}_{hr} \tag{5.6}$$

where ρ_c and ρ_r are instantaneous mass densities of the emulsion within the piston- and rod-side chambers, respectively; V_r and β_r are the volume and effective bulk modulus of emulsion within the rod-side chamber, respectively. The volumes of emulsion in the two chambers of the strut can be obtained from:

$$\begin{gathered} V_c = V_{c0} + V_{g0} - A_{hc}x - V_g \\ V_r = V_{r0} + (A_{hc} - A_{hr})z_s \end{gathered} \tag{5.7}$$

where V_{i0} $(i = c, r)$ is the initial volume of the emulsion within the piston- (c) or rod-side (r) chamber.

The mass density and bulk modulus of the gas-oil emulsions in the two chambers of the HPS strut depend on the volume fraction of entrapped gas within the hydraulic oil as well as the fluid pressure [142]. The gas volume fraction of the emulsion, defined as the ratio of the entrapped gas volume to the hydraulic oil volume ($\gamma_i = V_{gi}/V_{hi}\,; i = c, r$) also varies with the fluid pressure due to compressibility of both the entrapped gas and the hydraulic oil. The instantaneous volumes of entrapped gas V_{gi} and hydraulic oil V_{hi} of the emulsion in chamber i can be expressed as:

$$\begin{aligned} V_{gi} &= \left(\frac{P_{h0}}{P_{hi}}\right)^{\frac{1}{n}} V_{gi0};\ i = c, r \\ V_{hi} &= \left(1 - \frac{P_{hi} - P_{h0}}{\beta_h}\right) V_{hi0};\ i = c, r \end{aligned} \tag{5.8}$$

where V_{gi0} and V_{hi0} are initial volumes of entrapped gas and hydraulic oil within the emulsion, respectively; and β_h is bulk modulus of pure hydraulic oil. The instantaneous gas volume fractions of the emulsions in the piston- and rod-side chambers can thus be obtained from:

$$\gamma_i = \frac{\left(\frac{P_{h0}}{P_{hi}}\right)^{\frac{1}{n}} V_{gi0}}{\left(1 - \frac{P_{hi} - P_{h0}}{\beta_h}\right) V_{hi0}} = \frac{\left(\frac{P_{h0}}{P_{hi}}\right)^{\frac{1}{n}}}{1 - \frac{P_{hi} - P_{h0}}{\beta_h}} \gamma_0;\ i = c, r \tag{5.9}$$

where γ_0 $(V_{gi0}/V_{hi0}\,; i = c, r)$ is the initial gas fraction of the emulsion in chamber i.

Assuming negligible mass of the entrapped gas, the mass density of the emulsion in each chamber ($\rho_i;\ i = c, r$) can be obtained from [142]:

$$\rho_i = \frac{\rho_h V_{hi0}}{V_{hi} + V_{gi}} = \frac{\rho_h}{\left(1 - \frac{P_{hi} - P_{h0}}{\beta_h}\right)(1 + \gamma_i)};\ i = c, r \tag{5.10}$$

where ρ_h is mass density of the hydraulic oil.

Similarly, the effective bulk modulus of the emulsion within each chamber ($\beta_i;\ i = c, r$) can be derived as a function of the instantaneous pressure considering the compressibility of both the entrapped gas ($-\frac{V_{gi} dP_{hi}}{dV_{gi}} = nP_{hi};\ i = c, r$) and the hydraulic oil ($-\frac{V_{hi} dP_{hi}}{dV_{hi}} = \beta_h;\ i = c, r$), as:

$$\beta_i = -\frac{V_{gi} + V_{hi}}{\frac{d}{dP_{hi}}\left(V_{gi} + V_{hi}\right)} = \frac{n(1 + \gamma_i) P_{hi} \beta_h}{nP_{hi} + \gamma_i \beta_h};\ i = c, r \tag{5.11}$$

Assuming turbulent flows through the bleed orifices (q_b) and check valves (q_c), and laminar leakage flow (q_l), the relations between the fluid flows and pressures can be expressed as:

$$\begin{aligned} q_b &= C_b(n_b A_b)\sqrt{\frac{2|P_{hc}-P_{hr}|}{\bar{\rho}_i}}\cdot sgn(P_{hc}-P_{hr}) \\ q_c &= \begin{cases} C_v(n_v A_v)\sqrt{\dfrac{2(P_{hc}-P_{hr})}{\bar{\rho}_i}} & ; P_{hc} > P_{hr} \\ 0 & ; P_{hc} \le P_{hr} \end{cases} \\ q_l &= k_l(P_{hc}-P_{hr}) \end{aligned} \tag{5.12}$$

where (C_b, A_b, n_b) and (C_v, A_v, n_v) are discharge coefficient, opening area and number of bleed orifices and check valves, respectively; $\bar{\rho}_i$ $(= (\rho_c + \rho_r)/2)$ is the average mass density of the emulsions within the two chambers; and k_l is the leakage flow coefficient. It should be noted that the check valves remain closed when P_{hr} is greater than P_{hc}.

5.3.2 Model parameters identification

The parameters of the HPS strut model are obtained partly from its design dimensions and nominal properties of the hydraulic oil, and partly identified from the measured data acquired during the third series of experiments. Table 5.1 summarizes the constant model parameters, which include geometric parameters of the strut, and mass density and bulk modulus of the hydraulic oil. The force-deflection and pressure-deflection data obtained from the pseudo-static experiments (excitation frequency: 0.1 Hz) for the body temperature of 30±2°C, are used to identify polytropic exponent of the gas n in Eq. (5.4) and Coulomb friction F_c in Eq. (5.2), assuming negligibly small hydraulic damping force. The exponent n was identified via minimizing the error between the measured and model-predicted gas pressure under different strut deflections. The value of F_c was obtained from the force-deflection data under 25 mm displacement excitation considering negligible contributions due to viscous coefficient at low velocities. These revealed similar values of F_c in the vicinity of the peak velocity, which was greater than v_h.

The data acquired under different peak velocity excitations in the 1-8 Hz range are used to identify the viscous friction coefficient, stiction force and Stribeck coefficient (μ_v, F_s and k_s, respectively, in Eq. (5.2)), initial gas volume fraction of the gas-oil emulsion (γ_0 in Eq. (5.9)), leakage flow coefficient, and discharge coefficients of the bleed orifices and the check valve (C_b and C_v, respectively, in Eq. (5.12)). For this purpose, the gas spring force predicted from the model was subtracted from the measured total force to obtain the force due to hydraulic damping and friction. The resulting force in the vicinity of zero velocity is analyzed to obtain the Stribeck coefficient k_s and the stiction force F_s. The results revealed nearly constant value of coefficient k_s of 50 s/m in the considered velocity range. A nearly constant value of the viscous friction coefficient (50 Ns/m) was also identified from the force-velocity data. The stiction force, however, decreased monotonically with increasing strut velocity, as shown in Fig. 5.4(a). This tendency has also been reported in [181, 182]. The figure illustrates the mean values of F_s corresponding to each velocity excitation magnitude for different excitation frequencies for one and two bleed orifices configurations. The results suggest comparable values of F_s for both cases (one and two bleed orifices), especially at velocities exceeding 100 mm/s.

The flow-related parameters, namely, k_l, C_b, C_v, are further identified by minimizing the error between the measured fluid pressures with those obtained from Eqs. (5.5) and (5.6). The results showed nearly constant leakage flow coefficient ($k_l \approx 5\times10^{-12}$ m^3/Pa.s) for the range of strut velocity considered. Since the entrapped gas within the hydraulic oil significantly increases the compressibility of the fluid, the pressure within the piston-side chamber (P_{hc}) may exhibit considerable hysteresis during harmonic strut motion. The initial gas volume fraction γ_0 is thus determined for the range of velocity excitations considered. The instantaneous gas volume fraction, mass density and effective bulk moduli of the gas-oil emulsions in the two chambers are subsequently obtained using Eqs. (5.9) to (5.11). Figure 5.4(b) illustrates variations in the mean value of γ_0 with the peak velocity excitation for one as well as two bleed orifices configurations. The results show only minimal dependence of γ_0 on the strut velocity excitation for two bleed orifices. The γ_0, however, increases in a nearly quadratic manner with velocity for the single bleed orifice strut, which is due to higher fluid pressures at the higher velocity. The higher value of γ_0 of the single orifice strut is due to higher difference between pressures of emulsions in the piston and rod-side chambers compared to the two-orifices strut.

The discharge coefficient for flows across the bleed orifices, identified from pressure variations during extension alone, revealed notable variations with the peak pressure difference and thereby the strut velocity, as seen in Figs. 5.4(c). For both one- and two-bleed orifices, C_b increases with pressure difference and approach saturation to near 0.74 and 0.76, respectively, at pressures above about 0.8 MPa. Flows through single bleed orifice suggest slightly smaller value of C_b compared to that for the two bleed orifices. The mean discharge coefficient for flows across the check valves, identified from pressure variations during compression and shown in Fig. 5.4(d), show even greater variations with the pressure difference. The values of C_v are lower than those of C_v in the entire range of pressure difference, which is likely due to valve construction and dynamics that cause greater flow resistance. The C_v increases with the pressure difference and approaches saturation at a higher pressure difference, as observed in case of C_b. Moreover, the results suggest only small differences in C_v for the one and two bleed orifice struts. From the results in Figs. 5.4(c) and 5.4(d), it is deduced that values of C_b of 0.74 and 0.76 may be considered for the one and two-bleed orifice flows, respectively. An average value of 0.6 for C_v may be used for estimating the flows through the check valves.

Table 5.1: Constant parameters of the hydro-pneumatic suspension (HPS) strut

Parameter	Description	Value
A_{hc} (cm^2)	Area of the strut piston	44.179
A_{hr} (cm^2)	Area of the strut rod	19.635
A_b (cm^2)	Area of one orifice	0.0707
A_v (cm^2)	Area of one check valve	0.041
β_h (Mpa)	Hydraulic oil bulk modulus	1700
ρ_h (kg/m^3)	Hydraulic oil mass density	850
F_c (N)	Coulomb friction	110
μ_v (Ns/m)	Viscous friction coefficient	50
k_s (s/m)	Stribeck coefficient	50
k_l (m^3/Pa.s)	Leakage flow coefficient	5×10^{-12}
n	Polytropic exponent of gas	1.4

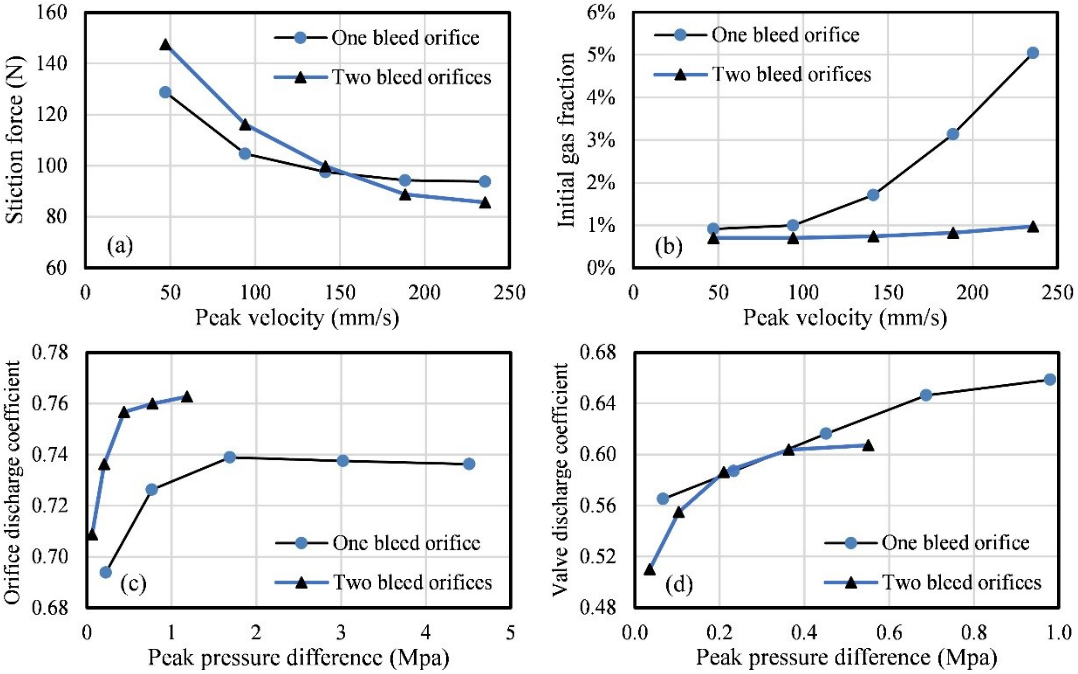

Figure 5. 4: Variations in the mean values of identified HPS strut model parameters (1-8 Hz): (a) stiction force, F_s; (b) initial gas volume fraction of the emulsion, γ_0; (c) discharge coefficient of the bleed orifice flows, C_b; and (d) discharge coefficient of the check valve flows, C_v

5.4 Results and discussions

5.4.1 Gas-oil emulsion formulation

The fluid pressures measured from the first and second series of experiments are examined to build an understanding of rate of mixing of gas and oil, and the formulation of gas-oil emulsion. Figure 5.5 illustrates the time-histories of fluid pressure, P_{hc}, measured during the first series of experiments under three levels of ramp-step strut displacements (75, 100 and 115 mm). The figure also illustrates the time-histories of the displacements applied to the strut. The pressure of fluid in the rod-side chamber, P_{hr}, was identical to P_{hc}, and thereby not illustrated. The fluid pressure increased from the initial pressure of 0.68 MPa to nearly 1.43, 2.05 and 2.74 MPa in a ramp manner due to compression of the gas, when the strut was displaced by 75, 100 and 115 mm, respectively. Although the strut position was maintained for a long period, ranging from 1 to 2 hours depending on the strut displacement magnitude, the fluid pressure decreased at a very slow rate. This suggested that the gas tends to dissolve into the oil at a very slow rate when the gas pressure is increased. The fluid pressure decreased at a higher rate (0.82 kPa/min) under higher gas pressure (115 mm displacement) compared to that at a lower gas pressure (0.31 kPa/min under 75 mm displacement). This trend suggested that a higher gas pressure can cause greater amount of gas entrapment into the oil. The dispersion of the gas into the oil will reduce the mass of the free gas within the strut, while only negligible change in the volume of hydraulic oil (emulsion) occurs due its increased compressibility, as reported in [142]. As the strut piston is restored to its bottom position, the fluid pressure decreases rapidly to a value slightly below the initial pressure of 0.68 Mpa. The fluid pressure, however, gradually increases to the initial pressure, suggesting the gradual release of gas from the oil.

Figure 5.6 illustrates variations in the pressure P_{hc} measured under 0.1 Hz (30 mm amplitude) and 1 Hz (15 mm amplitude) harmonic excitations during the second series of experiments. The harmonic excitation was applied to the strut positioned near its mid-position. The fluid pressure increased to about 1.4 MPa when the strut was displaced to its mid-position. The strut position was held for some period prior to application of the harmonic input. Under harmonic excitation, oscillations in P_{hc} were observed at the excitation frequency, while a gradual decrease in equilibrium (mean) pressure is evident due to mixing of gas in the oil. Moreover, the variations in fluid pressure are asymmetric about the equilibrium pressure, which is attributed to compressibility of the gas. The 0.1 Hz and 1 Hz excitations were maintained for about 140 and 75 minutes, respectively, until a near saturation of P_{hc} was observed. The strut body temperature was continuously monitored and maintained at 21±2°C. The results suggest relatively faster decrease in P_{hc} at the higher frequency of 1 Hz compared to that at 0.1 Hz. The rate of pressure decrease in both cases is substantially higher than that observed under static displacement of the strut, shown in Fig. 5.5. Moreover, higher frequency excitation (1 Hz) resulted in substantially faster saturation of the pressure compared to the 0.1 Hz excitation. This suggests higher volume of gas entrapment and rapid formulation of the gas-oil emulsion under a higher frequency excitation. The pressure saturation was observed near 50 minutes under 1 Hz excitation and more than 2 hours under 0.1 Hz excitation. This is also evident from the relatively higher gas volume fraction at a higher strut velocity, especially in case of the single bleed orifice configuration, as seen in Fig. 5.4(b).

The considerable decrease in the fluid pressure is clearly evident when the harmonic excitation is terminated (points B^1 and B^2 in Fig. 5.6). The steady-state pressures under both excitations were nearly identical, and 23% lower than the pressure measured prior to the excitations (point A). Only minimal change in the fluid pressure was observed when the strut was held to its mid-position following the harmonic excitations. The fluid pressures approached a value below the initial pressure, as the strut was restored to its bottom position (point D). The pressure, however, gradually increased to the initial value after a period of more than 2 hours, as seen in Fig. 6. This was attributed to slow separation of the dissolved gas from the hydraulic oil, as the fluid pressure decreased. The presence of numerous minute gas bubbles was clearly observed within the hydraulic oil, when the gas-oil emulsion was released from the strut through a high-pressure ball valve after completion of the experiments. From the results, it is deduced that the gas-oil emulsion may be formulated rapidly under typical excitations encountered during vehicle operation, and suspension strut will likely operate with nearly saturated gas-oil emulsion and saturated fluid pressure.

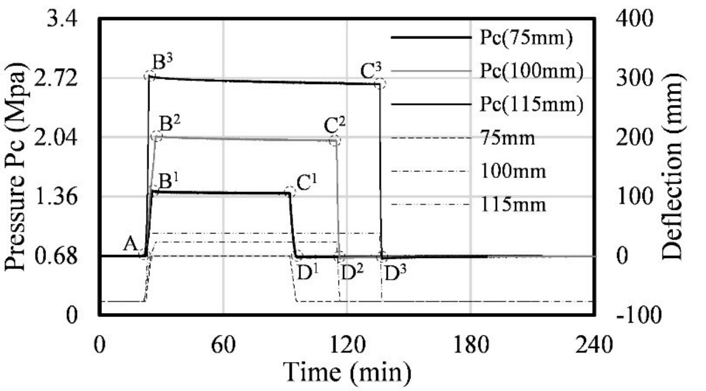

Figure 5.5: Time-histories of strut piston deflections (dashed lines) and resulting variations in fluid pressure P_{hc} in the piston-side chamber (solid lines)

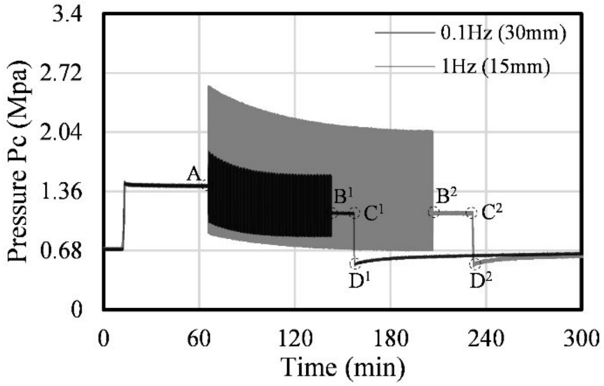

Figure 5.6: Variations in fluid pressure P_{hc} in the piston-side chamber under 0.1 Hz (30 mm amplitude) and 1 Hz (15 mm amplitude) harmonic excitations

5.4.2 Stiffness and damping characteristics of HPS strut

The nonlinear stiffness and damping characteristics of the HPS strut with gas-oil emulsion are obtained from the analytical model and the data acquired during the third series of experiments corresponding to the strut body temperature of 30±2°C. The model responses in terms of total force and fluid pressures are evaluated under different harmonic excitations. The model results are initially obtained at a low frequency excitation of 0.1 Hz to examine the pseudo-static stiffness and friction property of the strut. Subsequently, the responses are obtained under excitations in the 1 to 8 Hz frequency range. In each case, the model results are compared with the measured data to illustrate validity of the model. The measured data under each excitation were acquired only after the saturation of the gas entrapment, which was determined from the steady mean pressure of the gas-oil emulsion. The pressure saturation occurred quite rapidly under higher frequency excitations.

Figures 5.7 and 5.8 compare the pseudo-static responses of the model of the HPS strut with one and two bleed orifices with the measured data under two different excitation amplitudes (25 and 50 mm). Owing to very low magnitude of the strut velocities, both the one and two bleed orifices configurations exhibit quite comparable responses. The mean values of the fluid pressure and total force for the two bleed orifice strut, however, are slightly higher than those of the single orifice strut. This was due to slightly higher charge pressure and thereby the saturation pressure of the two bleed orifice strut (1.02 MPa) compared to the single orifice strut (0.87 MPa). Figures 5.7(a) and 5.7(b) illustrate comparisons of the pressure-deflection responses of the one and two-orifice models, respectively, with the corresponding measured data for the 25 and 50 mm displacement magnitudes. The comparisons suggest reasonably good agreements between the model results and the measured data. The time-histories of fluid pressure obtained from the models also exhibit good agreement with the measured responses under different excitation magnitudes, as seen in Figs. 5.8(a) and 5.8(b). The measured pressure-deflection data, however, exhibit notable hysteresis, especially under higher excitation magnitudes, which is attributed to heat transfer between the gas and its surroundings, as reported in [174, 179]. The gas spring model in this study is based on adiabatic gas process neglecting the heat transfer. The model-predicted pressure-deflection responses thus follow the mean measured data with slight discrepancy in the phase, as seen in Figs. 5.7(a) and 5.7(b).

Figures 5.8(c) and 5.8(d) illustrate good agreements in the time-histories of the total force predicted from the single- and two-orifice strut models, respectively, and the corresponding measured data. Under the pseudo-static excitation, the force developed by the strut is primarily due to gas spring force apart from the seal friction. The force response is thus in phase with P_{hc} and could be estimated from $P_{hc}A_{hr}$. The force responses also show notable contributions of the friction force due to seals when the travel direction reverses. Figures 5.7(c) and 5.7(d) further illustrate the force-deflection responses of the two strut configurations. The results show that the friction model integrating the Coulomb, viscous and Stribeck components, presented in Eqs. (5.2) and (5.3), can adequately describe the seal friction. The model, however, slightly underestimates the friction force observed under extreme compression under the higher displacement excitation. This may in-part be due to structural asymmetry of the strut seals and in-part due to relatively higher gas pressure. Moreover, both the models and the measured data exhibit comparable friction force under 25 and 50 mm displacements. The friction force under 5 mm displacement, however, was observed to be slightly higher likely due to greater stiction force at lower relative velocity of the seals, as reported in [181, 182].

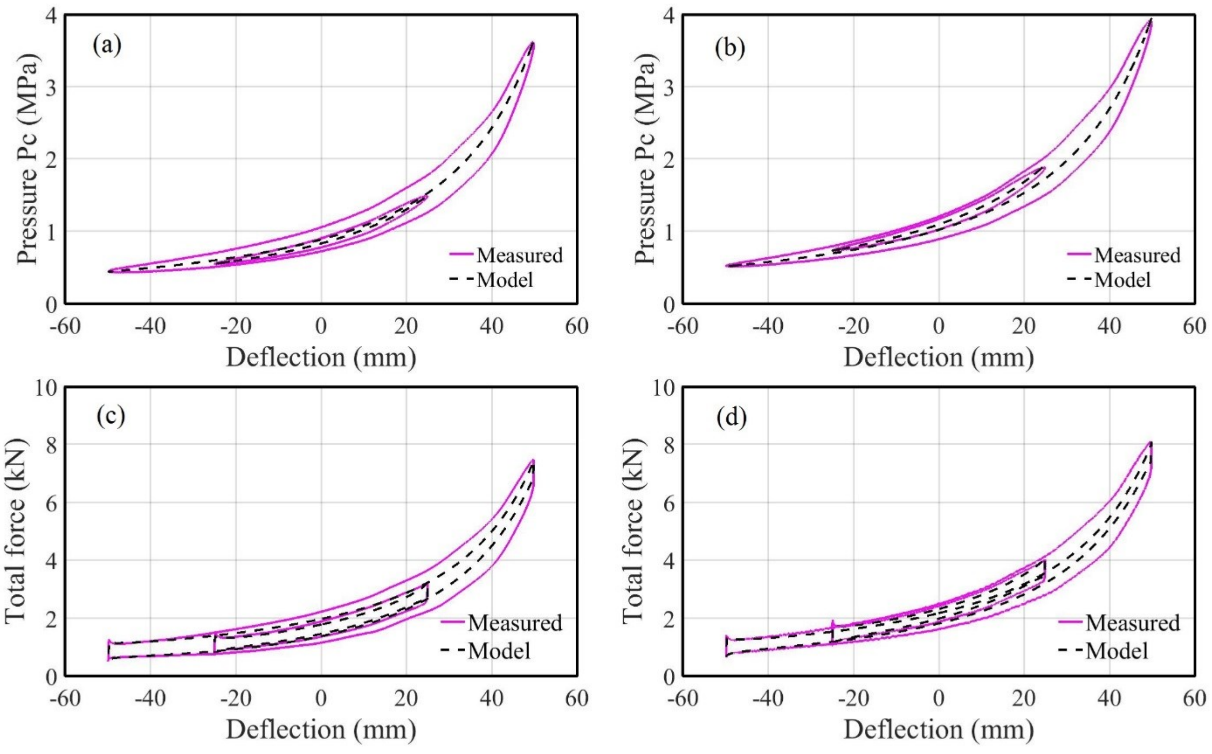

Figure 5.7: Comparisons of measured and model-predicted main chamber fluid pressure-deflection and force-deflection responses under pseudo-static excitations: (a, c) one bleed orifice strut, and (b, d) two bleed orifices strut (excitations: 25 and 50 mm at 0.1 Hz)

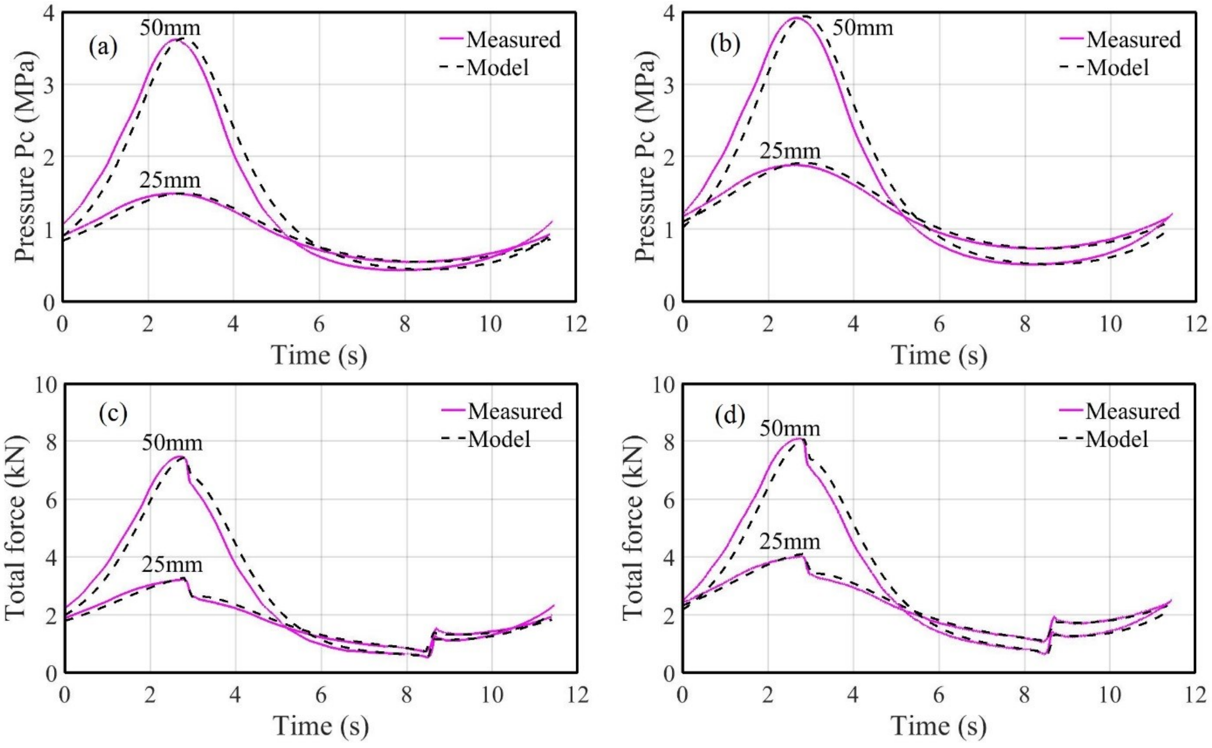

Figure 5.8: Comparisons of measured and model-predicted main chamber fluid pressure and total force under pseudo-static excitations: (a, c) one bleed orifice strut, and (b, d) two bleed orifices strut (excitations: 25 and 50 mm at 0.1 Hz)

Unlike the pseudo-static responses, the force developed by the single-orifice strut under excitations in the 1-8 Hz range differs significantly from that of the two-orifices strut. Figure 5.9 compare the pressure/force-deflection responses of the models with the measured data for 7.5 mm amplitude excitation at frequencies of 1, 3 and 5 Hz, as examples. Figure 5.10 compares the variations in damping force and total force developed by the two strut configurations as a function of the velocity under excitations at frequencies of 2, 5 and 8 Hz range. The peak velocity in this case is held at 235.6 mm/s, irrespective of the frequency. The effective damping force is obtained by subtracting the spring force ($P_{hc}A_{hr}$) from the total strut force.

The pressure/force-deflection responses of the single and two-orifice strut models generally show good agreements with the measured data, with notable deviations at the higher frequency of 5 Hz. The measured as well as model-predicted pressure-deflection responses of the strut with two bleed orifices seem to follow the polytropic gas process during compression as well as extension, irrespective of the excitation frequency, as seen in Fig. 5.9(b). Blocking one of the bleed orifices, however, resulted in considerable hysteresis, which tends to increase with increasing frequency, as seen in Fig. 5.9(a). This hysteresis of the single-orifice strut is due to large volume variations of the gas-oil emulsion and greater gas volume fraction when compared to the two-orifices strut, as seen in Fig. 5.4(b). Moreover, higher flow rate under higher piston velocity or excitation frequency could contribute to more entrapped gas and higher compressibility of the gas-oil emulsion. The variations in the volume of gas-oil emulsion in the piston-side chamber with strut deflection also revealed hysteresis due to changes in fluid compressibility during compression and extension.

Increase in the fluid flow rate between the two strut chambers under a higher velocity also caused relatively greater variations in the fluid pressure within the rod-side annular chamber, P_{hr}, during strut extension compared to those during compression, as shown in Figs. 5.9(c) and 5.9(d). The peak pressures during extension for the two-orifice strut, however, are considerably lower compared to the single-orifice strut. The minimum value of P_{hr} during strut compression seems to be bounded to 0.5 Mpa for the selected excitations. A few studies on multi-chamber hydro-pneumatic struts with separated gas and oil chambers have reported that the annular chamber pressure may approach vacuum [172]. The lowest pressure in the simple two-chamber strut design considered in this study was well above the vacuum.

The pressure/force-deflection responses of the two-orifice strut model are in close agreement with the measured responses, as seen in Figs. 5.9(b), 5.9(d) and 5.9(f). The responses of the single-orifice strut model, however, exhibit considerable deviations from the measured data at the higher frequency of 5 Hz. The differences, observed in Figs. 5.9(c) and 5.9(e), are mostly due to phase error in the model and measured responses. This is evident from comparisons of the time-history of the total force response with the measured data under 5 Hz excitation in Figs. 5.9(g) and 5.9(h) for the single- and two-orifices struts, respectively. The results clearly show greater phase deviation for the single-orifice strut, while the magnitudes of the model-predicted force are comparable with the measured force. It is further noted that the total force developed during extension by the single-orifice strut approaches considerably higher negative values due to substantially higher damping force. The results in Figs. 5.9(e) and 5.9(f) further show that the friction force is less significant compared to the hydraulic and gas spring forces at higher frequencies, especially for the single bleed orifice strut.

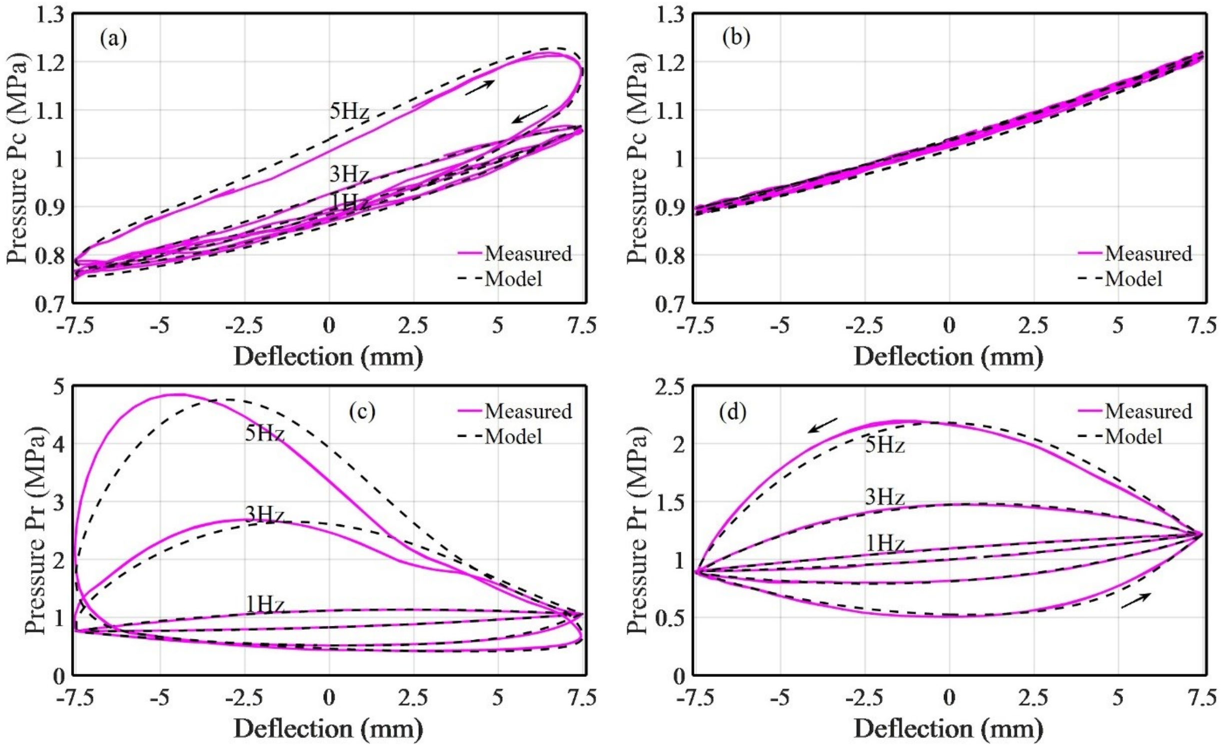

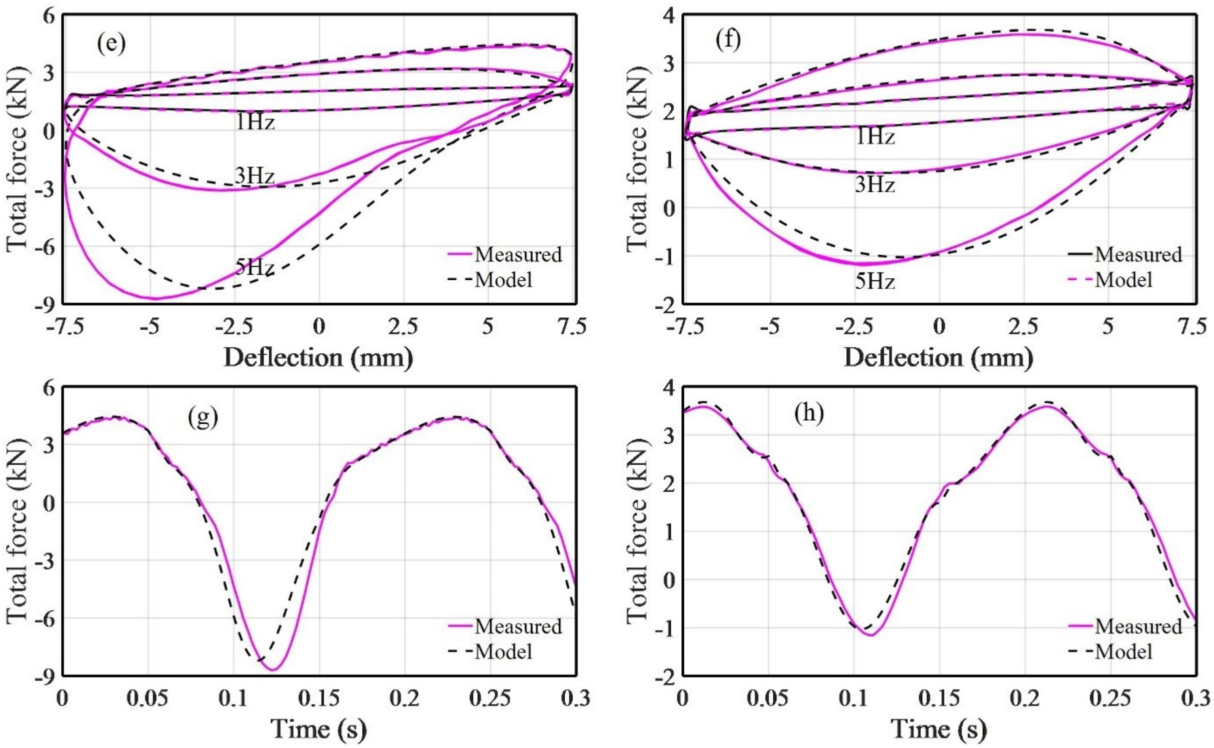

Figure 5.9: Comparisons of measured and model-predicted pressures and total force responses under 7.5 mm amplitude harmonic excitations at different frequencies: (a, c, e, g) one bleed orifice, and (b, d, f, h) two bleed orifices

The reasonably good agreements between the model-predicted and measured force-velocity characteristics are also evidenced in Fig. 5.10 for constant velocity excitations at 2, 5 and 8 Hz. The results show substantially higher total and effective damping force of the single-orifice strut when compared to the two-orifice strut. Figures 5.10(c) and 5.10(d) show that the effective damping force developed by the two-orifices strut is far less sensitive to excitation frequency compared to that of the single-orifice design. This is due to greater sensitivity of the fluid pressure to excitation frequency (Fig. 5.9) and greater gas volume fraction within the emulsion in the single-orifice design. Both the strut designs exhibit relatively higher damping in extension than in compression, as expected.

For the HPS strut with one bleed orifice (Fig. 5.10(c)), the peak total and damping force during extension decreases with increasing excitation frequency. Moreover, the peak damping force tends to shift away from the peak velocity, as the excitation frequency increases. This is due to greater phase difference between P_{hr} and velocity (Fig. 5.9(c)), which increases with increasing excitation frequency, and higher hysteresis in P_{hc} ((Fig. 5.9(a)). This also leads to considerable damping force near zero velocity. The hysteresis in the damping force of the two-orifices strut is also evident at higher excitation frequencies (Fig. 5.10(d)), although the hysteresis magnitude is substantially small. From the results, it may be deduced that the model can effectively predict the damping force and the hysteresis reasonably well under the excitations considered. Some discrepancies between the model results and measured data, however, are evident, especially during extension under higher frequency excitations. These are likely caused by complex variations in properties of the gas-oil emulsion under higher frequency excitations. The proposed model, however, can provide reasonably accurate predictions of the dynamic responses of the HPS strut with gas-oil emulsion, in terms of the fluid pressures and strut forces. The validated model could thus serve as a tool to study the effects of various parameters on the HPS strut's properties and to seek design guidance.

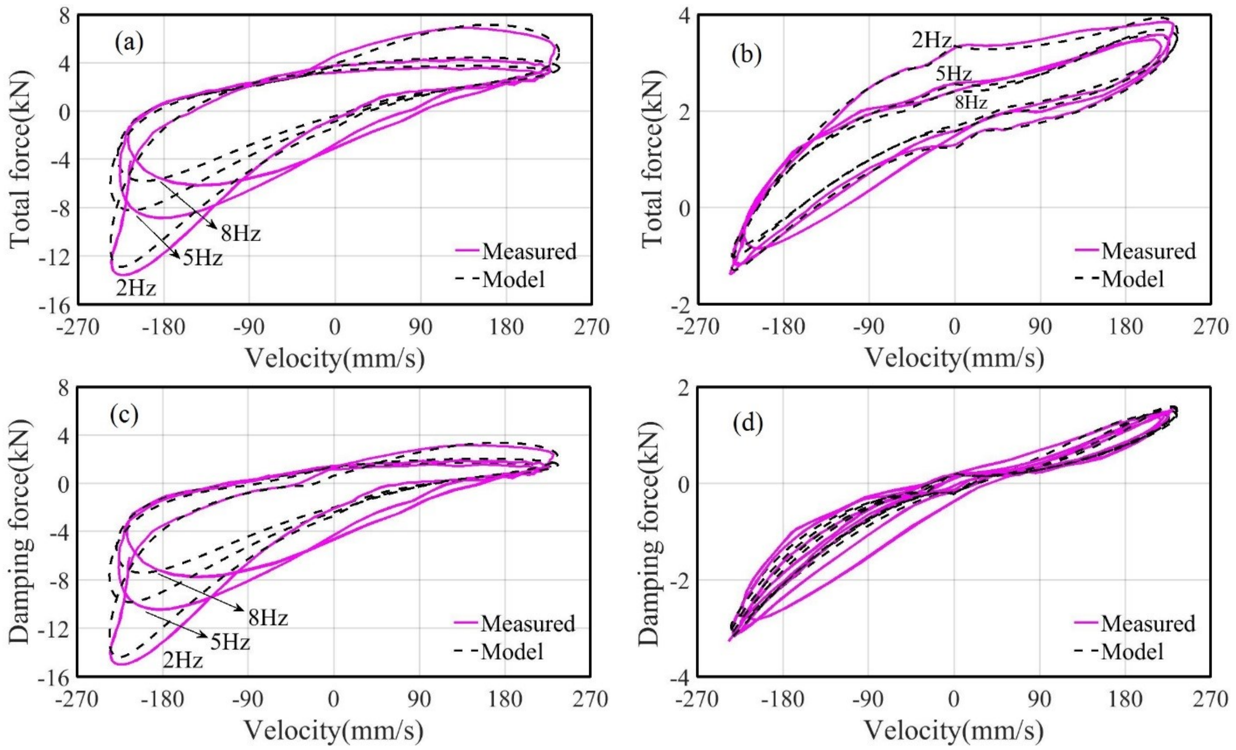

Figure 5.10: Comparisons of measured and model-predicted total force and damping force responses under constant peak velocity (235.6 mm/s) at different frequencies: (a, c) one bleed orifice, and (b, d) two bleed orifices

5.4.3 Effect of gas volume fraction

The properties of the gas-oil emulsion and thereby the stiffness and damping characteristics of the HPS strut are strongly dependent upon the gas volume fraction. This is evident from the effects of gas volume fraction on the fluid mass density and compressibility in Eqs. (5.10) and (5.11), which directly influence variations in fluid volume, fluid pressure and the flow rates. The effect of gas volume fraction on the resulting spring and damping forces are thus further investigated. Simulations are performed for the single and two-orifices strut models considering three different levels of steady-state gas volume fraction within the emulsion ($\gamma_0 = 0\%$, 3% and 6%). The results are obtained under constant peak velocity excitation (235.6 mm/s) and different frequencies. The steady-state pressure at mid-position of the strut is taken as 1 MPa. Other model parameters, such as the orifices' discharge coefficients and seal friction parameters, are set to the means of the identified values, as discussed earlier (Fig. 5.4).

As an example, Figure 5.11 illustrates the gas spring force-deflection and effective damping force-velocity response characteristics of the struts with one and two bleed orifices corresponding to 2 Hz excitation frequency for the three gas volume fractions (γ_0 = 0%, 3% and 6%). Figure 5.12 illustrates the effect of gas volume fraction on the responses under 5 and 8 Hz excitation frequencies. In the absence of the entrapped gas, different excitation frequencies yield nearly identical gas spring force characteristics for both the strut configurations. Slight hysteresis in the spring force, however, can be observed in the force-deflection responses of the single bleed orifice strut, as seen in Figs. 5.11(a) and 5.12 (a), which is due to its higher pressure and compressibility of the hydraulic oil. The force-deflection properties exhibit considerably larger hysteresis as the gas volume fraction is increased, irrespective of the excitation frequency. This is due to considerable increase in the fluid compressibility and is evident for both the single and two-orifices strut configurations. Increase in the gas volume fraction causes greater hysteresis in the force-deflection response due to relatively higher fluid pressure. Compared to the two orifices strut, the single orifice design yields considerably higher hysteresis. Increase in the gas volume also yields higher peak spring force and higher effective spring rate, with the exception of the two-orifice strut response under 2 Hz excitation. The change in spring rate is attributed to two phenomena: (i) gas volume entrapment in the oil reduces the volume of free gas, which contributes to increase in the spring rate; and (ii) increase in gas-oil emulsion compressibility, which would contribute to relatively lower stiffness. The effective spring rate tends to increase substantially when γ_0 is increased from 0% to 3%. Further increase in γ_0 to 6%, however, causes relatively smaller increase in the spring rate, which is likely due to more pronounced effect of higher compressibility. The effective spring rate also increases slightly with increase in the excitation frequency, as seen in Figs. 5.12(a) and 5.12(b).

In the absence of entrapped gas ($\gamma_0 = 0\%$), the force-velocity responses also exhibit slight hysteresis, especially during strut extension. This is mostly caused by the high fluid pressure within the rod-side chamber and compressibility of the oil. Higher compressibility of the emulsion with higher gas volume fraction significantly widens the hysteresis in the damping force, irrespective of the excitation frequency for both strut configurations, as seen in Figs. 5.11(c), 5.11(d), 5.12(c) and 5.12(d). Moreover, increasing the excitation frequency yields higher hysteresis in the damping force, as it was observed in Fig. 5.10. Increase in hysteresis is also associated with relatively higher phase between the damping force and strut velocity, which yields reduction in the peak damping force in a nonlinear manner, especially during strut extension. This is also evident in Fig. 5.10 and suggests reduced damping coefficient of the HPS strut in the presence of entrapped gas. It is further observed that the effective damping force response under 8 Hz excitation with $\gamma_0 = 3\%$ is quite comparable with that under 5 Hz excitation with $\gamma_0 = 6\%$, for both the single- and two-orifice strut configurations.

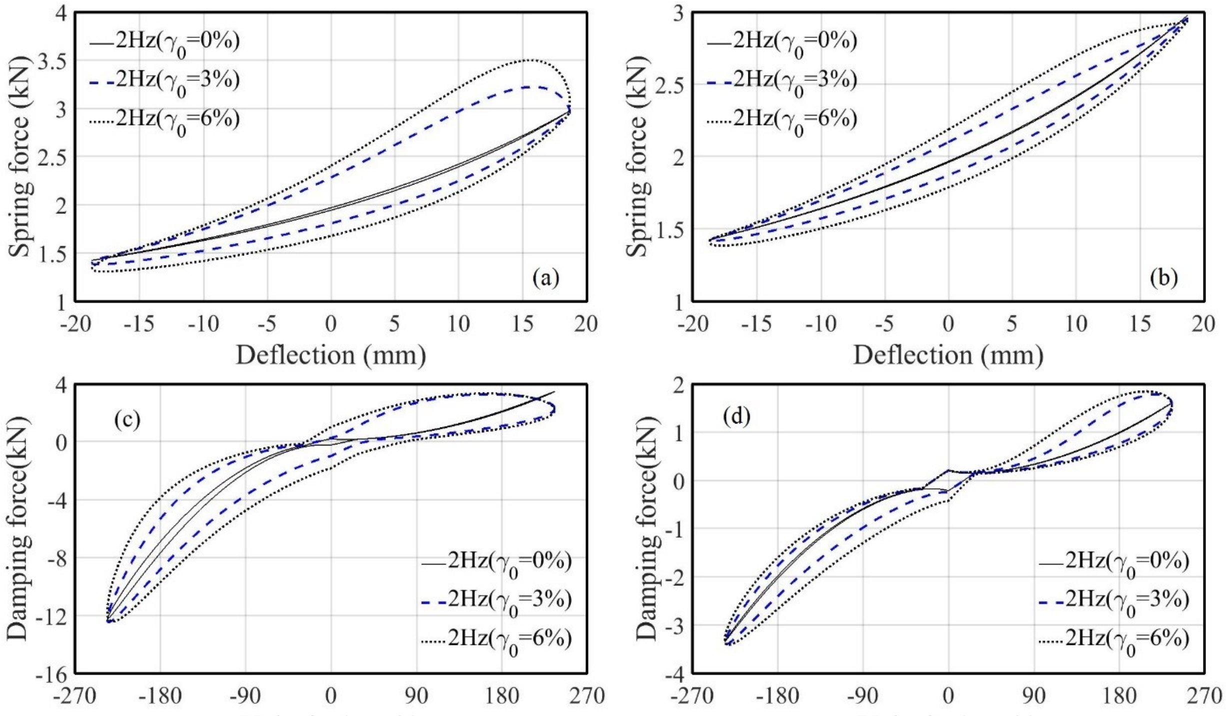

Figure 5.11: Effect of gas volume fraction on force-deflection and force-velocity responses of the struts: (a, c) one bleed orifice, and (b, d) two bleed orifices (peak velocity excitation of 235.6 mm/s at 2 Hz)

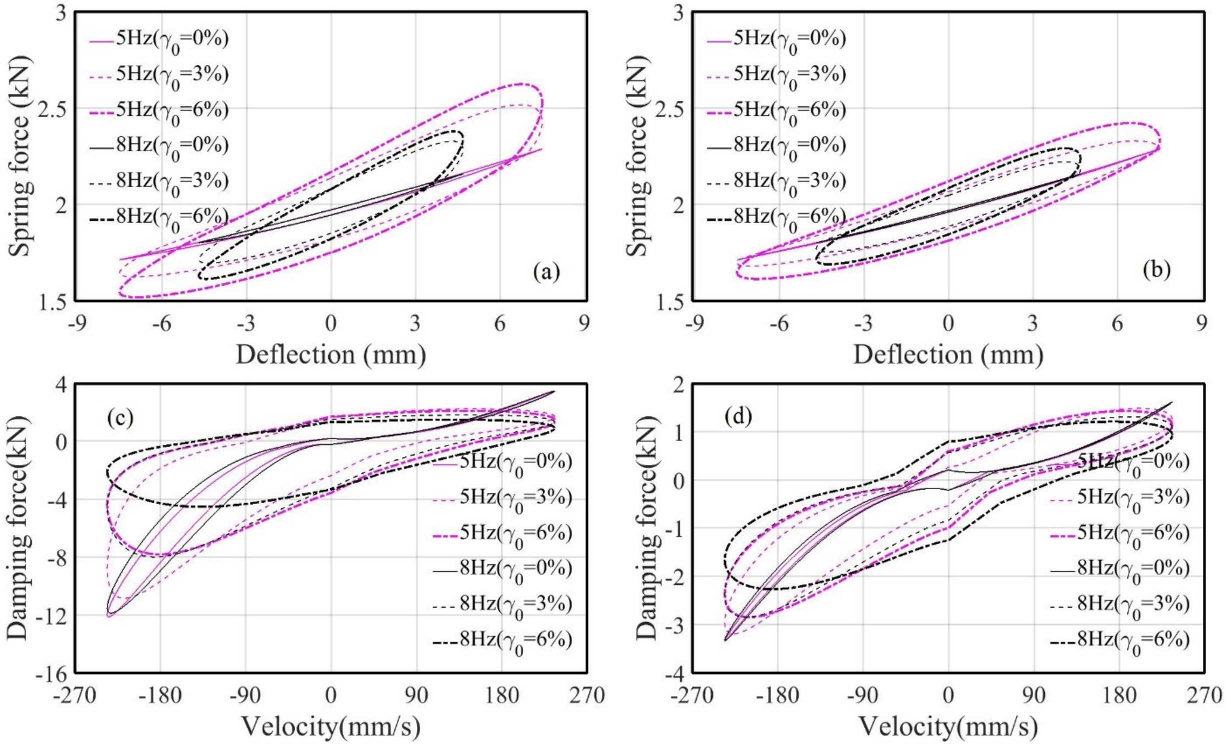

Figure 5.12: Effect of gas volume fraction on force-deflection and force-velocity responses of the struts: (a, c) one bleed orifice, and (b, d) two bleed orifices (peak velocity of 235.6 mm/s at 5 and 8 Hz)

5.5 Conclusions

The laboratory experiments revealed that the gas entrapment in the oil occurs rapidly under higher frequency operations and the mean gas volume fraction tended to saturate. The strut may thus be considered to operate with gas-oil emulsion and relatively lower free gas volume. The formulation of gas-oil emulsion within the HPS strut strongly affects its stiffness and damping properties due to significant variations in the fluid compressibility and free gas volume. The entrapped gas also contributes to notable hysteresis in both the stiffness and damping properties, especially under higher operating pressures in case of the single bleed orifice design. The effective stiffness tends to increase with increasing gas volume fraction due to lower gas volume, while the peak damping force and damping coefficient decrease due to higher compressibility of the emulsion. The reduced effective damping at higher velocities may be beneficial in enhancing the vibration isolation performance in the critical ride frequency range. The friction force introduced by strut seals was observed as relatively less significant especially at relatively higher strut velocities. The variations in the free gas volume and fluid compressibility would also affect the ride height. Ride height control mechanism is thus needed with such struts. Furthermore, variations in strut temperature could also affect the gas volume entrapment in the oil and the ride height. Owing to highly nonlinear variations in stiffness and damping properties with the gas volume fraction, further efforts are needed to identify relations among the gas volume fraction, properties of the emulsion and the fluid pressures.

CHAPTER 6

MULTI-PERFORMANCE ANALYSES AND DESIGN OPTIMIZATION OF HYDRO-PNEUMATIC SUSPENSION SYSTEM FOR AN OFF-ROAD WORK VEHICLE

6.1 Introduction

Articulated frame-steered vehicles (AFSV) are widely employed in the agricultural, construction, forestry and mining sectors for their enhanced traction and mobility/maneuverability performances on off-road terrains [11, 12, 80, 146]. Such vehicles are known to exhibit high magnitude ride vibration, and relatively lower roll- and yaw-plane stability limits attributed to the additional degrees-of-freedom (DOF) between the front and rear units. The directional stability limits are further reduced by tires interactions with the off-road terrains, which also induce considerable exposure of the human operators to low frequency whole-body vibration (WBV) [54, 168, 186]. The WBV exposure levels of AFSVs generally exceed the health caution guidance zone (HCGZ) defined in ISO-2631-1 [1] and the limits stipulated in the European Community (EC) guidelines [2], while the vertical ride vibration can be moderately attenuated through the large size tires and a seat suspension. Many designs of axle suspensions have been proposed to enhance the vehicle ride performance, while their implementations in off-road vehicles have been limited due to the reduced roll- and tip-over stability, and increased jackknife and snaking potential of the suspended AFSVs [48, 132, 168]. Increasing demand for high load capacity and high-speed work vehicles raises greater concerns for both the directional stability limits and the WBV exposure. The enhancement of operational safety of AFSVs, thus necessitates axle suspension designs for improved attenuation of terrain-induced ride vibration, while preserving roll- and yaw-plane stability limits.

The majority of the reported studies on AFSV focus only on the snaking tendency in the yaw plane on the basis of the rate of decay, frequency and damping ratio of the free yaw oscillations or eigenvalues of the linearized yaw-plane models [12, 18, 19, 146]. In these studies, the articulated frame steering (AFS) system is usually simplified as the equivalent torsional stiffness and damping about the articulation joint, while neglecting kinematics of the steering struts. Greater yaw-mode stiffness and damping coefficients have been suggested to increase the yaw stability limit. Yin et al. [146] showed significant effects of nonlinear kinematic and dynamic properties of the AFS system on the free and transient yaw oscillations. Rehnberg et al. [132] further investigated the effects of axle suspension's roll stiffness and roll damping coefficients on the snaking behavior, using a three-dimensional AFSV model with front- and rear-axle suspensions. The suspension kinematics were limited to roll motions about a predefined roll center, while the nonlinear kinematics and dynamics of the AFS, and the vertical DOF of the suspension system were not considered. The vehicle roll motion due to axle suspension was shown to slightly increase the snaking tendency of the vehicle. Greater roll stiffness and damping coefficients of the suspension, however, could attenuate the yaw oscillations to some extent.

Langer et al. [187, 188], Pazooki et al. [80] and Rehnberg and Drugge [167] investigated the multi-axes ride vibrations of AFSVs with the front-axle hydro-pneumatic suspension (HPS), rear-axle torsio-elastic suspension and both-axle linearized HPS, respectively. The proposed suspension systems could reduce the dominant ride vibration by nearly 50% when compared to the unsuspended vehicles. The AFS system, however, was simplified or neglected during the ride performance analyses on predefined terrains. The effective tire-terrain contact patch was considered by Langer et al. [187, 188], although the one-point contact method was generally used. The WBV responses of an AFSV (loader) model with a HPS suspension were evaluated while traversing a predefined 100 m working cycle at constant forward speeds (10 and 14 km/h). The study proposed optimal values for the initial gas volume/pressure, and cylinder and flow orifice sizes of the HPS, and the vehicle speed for limiting the WBV exposure below the HCGZ [1]. It was further shown that the HPS with higher gas volume can result in lower WBV exposure, while the effect of such low stiffness suspension on roll and yaw stability limits was not attempted. Pazooki et al. [80] proposed optimal stiffness and damping coefficients of a rear-axle torsio-elastic suspension for an articulated forestry vehicle using Genetic algorithm considering a low speed of 5 km/h. Rehnberg and Drugge [167] investigated sensitivity of ride performance to variations in vehicle forward speed and concluded that a higher speed may not necessarily lead to higher ride vibration due to reduced excitations near the dominant frequencies of the vehicle. These studies have also shown relatively lower vibration of the AFSV when loaded, irrespective of the vehicle speed.

The reported studies on AFSV generally focus either on the ride or yaw/roll directional responses, while the coupled analyses of ride and directional performances have been attempted in very few studies. Li et al. [53, 54] investigated the roll-plane and lateral stability of a scaled AFSV prototype. Pazooki et al. [48] explored the effects of the torsio-elastic suspension on both ride vibration, and roll- and yaw-plane stability of an articulated dump truck. The kineto-dynamics of AFS system was also considered assuming idealized flow characteristics of the steering valve. The proposed suspension resulted in substantial reduction in ride vibration with reduced directional stability limit of the vehicle. Moreover, the reported studies invariably assess the roll stability limit of off-road AFSVs using measures defined for road vehicles assuming negligible contributions due to terrain roughness. Such measures, however, may not be reliable for off-road vehicles, since the roll dynamic response is strongly affected by the vertical and roll excitations due to terrain elevations [168]. Considering that the suspension designs, invariably, involve complex compromise between the ride and directional performances, further efforts in ride height adjustment, cross-coupled HPS [23, 104, 169] and yaw stability control system [186] are considered worthy for the off-road AFSVs.

In this study, a three-dimensional multi-body dynamic model of an AFSV is formulated to investigate its coupled ride and directional performance characteristics. The model is formulated in the Adams platform, integrating the hydro-mechanical frame steering system and a hydro-pneumatic suspension (HPS) in the Matlab/Simulink platform. The unsuspended vehicle model is validated using the field measured data in terms of translational and rotational vibrations, and path-change directional responses. The parameters of the HPS subsystem are scaled from an experimentally validated model of a simple and low-cost HPS strut [189]. The HPS is implemented only at the front axle, which supports the driver cabin, which could help preserve high roll stiffness of the unsuspended rear unit. A sensitivity analyses is subsequently conducted to investigate the effects of HPS's parameters, namely, the piston area, and flow areas of the bleed orifices and check valves on the vehicles' ride vibration, and roll- and yaw-plane stability limits. The design optimization of the HPS system is also performed and analyzed.

6.2 Integrated model formulation

The AFSV considered in this study is a full-wheel electric-drive articulated mining dump truck with load capacity of 35 tons. A three-dimensional multi-body dynamic model of the vehicle is formulated in the ADAMS platform. In the model, the two hydraulic steering struts are symmetrically mounted between the front unit and the articulation joint, and the front-axle HPS struts are installed vertically between the vehicle frame and the axle, as seen in Fig. 6.1. The hydraulic frame steering system model is formulated considering kinematics and dynamics of the steering struts and flow properties of the steering valve [146]. The restoring and damping forces due to hydro-pneumatic suspension are derived from the suspension model, described in [189].

Both the suspension and the steering system models are developed in Matlab/Simulink platform and coupled to the AFSV model using co-simulation technique. The Matlab/Simulink solver is interfaced with the ADAMS platform using the C++ compiler. The displacement and velocity responses of the steering and suspension struts, evaluated from the multi-body vehicle model, are used as inputs to the steering and suspension subsystem models in the Matlab/Simulink. The resulting force responses of the steering and suspension struts are subsequently interfaced to the multi-body vehicle model via co-simulation. Detailed subsystem models of the AFSV are presented in the following subsections.

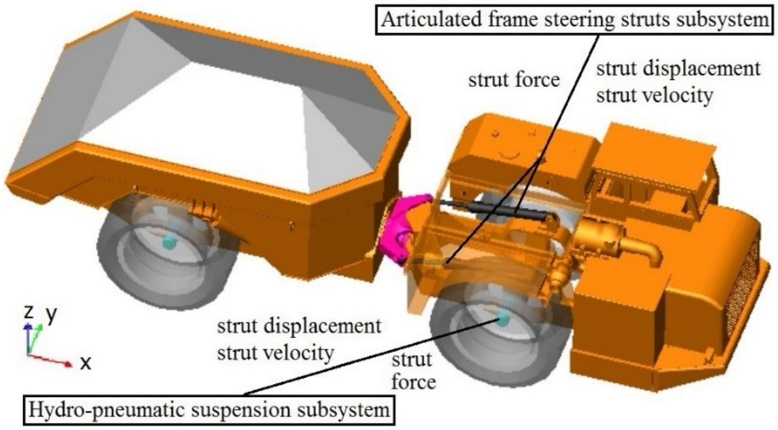

Figure 6.1: Three-dimensional multi-body model of the vehicle in ADAMS platform coupled with subsystems models in the Matlab/Simulink

6.2.1 Multi-body vehicle model

The AFSV prototype considered in the study is not equipped with axle or seat suspensions. Figure 6.2 illustrates the multi-body topology of the unsuspended AFSV model formulated in the ADAMS platform [190]. The loaded vehicle model is assembled with 12 bodies using 1 fixed joint, 2 translational joints, 6 revolute joints and 4 spherical joints. The articulation joint connects the front and rear units via the 2 revolute joints along x and z axis, which constrains the relative translational motions and the pitch motion between the front and rear units, while it permits relative roll and yaw plane motions of the units. The 4 spherical joints at the mounting points of the steering struts (Figs. 6.1 and 6.2) enable the three-axis rotations of the struts during the steering process and the three-dimensional kinematics of the AFS subsystem. The unsuspended multi-body vehicle model is thus formulated with a total of 14 degrees-of-freedom (DOF), which include 3 translational and 3 rotational DOFs of the front unit, 4 rotational DOFs of the wheels, 1 rotational DOF of the articulation joint in the yaw plane, 1 rotational DOF of the rear unit in the roll plane, and 2 rotational DOFs of the left and right steering struts along their respective center axis. When implementing the front-axle HPS system for the AFSV prototype, 2 translational joints are added vertically between the front unit and left- and right-wheel of the front axle. The additional vertical DOFs of the two front wheels account for the bounce and roll motions of the front axle with respect to the front unit. Moreover, the vehicle payload could be deactivated to simulate the unloaded cases.

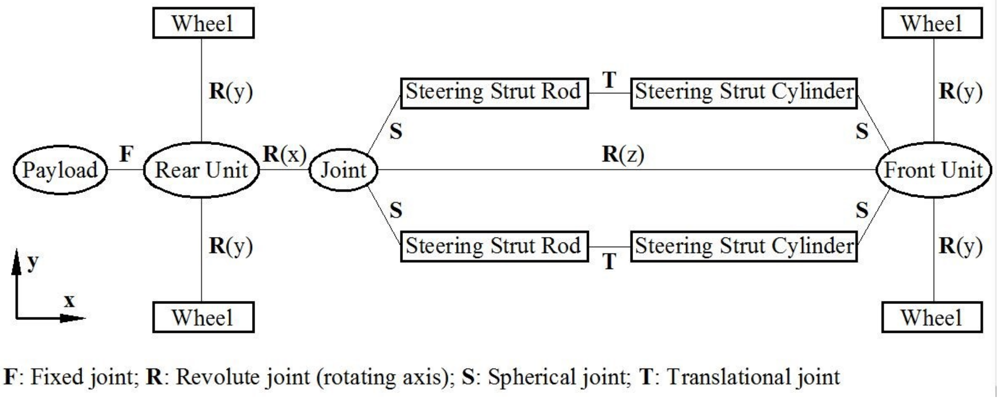

Figure 6.2: Topology of unsuspended articulated frame-steered vehicle model in the ADAMS platform

The vehicle model incorporates three-dimensional kinematics of the AFS subsystem during steering, and the dynamic forces developed by the steering struts applied to the strut mounting locations (Fig. 6.1). The strut forces yield an articulation moment about the articulation joint and steering of the articulated vehicle units. Identical driving torque is initially considered to be developed by each wheel, which is subsequently adjusted based on the difference between the actual and target speeds. For this purpose, a proportion-integral (PI) control scheme is used to ensure nearly constant forward speed during a given maneuver. The dimensional and inertial parameters of the vehicle, obtained from the computer-aided design (CAD) documents and the weighbridge measurements, are listed in Table 6.1. The moments of inertia of the two units and the payload are computed with respect to the center of gravity (cg) of each component.

Table 6.1: Dimensional and inertial parameters of the 35 tons articulated mining truck

Parameter	Value
Wheel base (m)	5.12
Front track (m)	2.28
Rear track (m)	2.28
Front axle to articulation joint longitudinal distance (m)	1.68
Rear axle to articulation joint longitudinal distance (m)	3.44
Front unit mass (kg)	21,000
- cg height (m)	1.36
- cg to articulation joint distance (longitudinal, m)	2.13
- roll mass moment inertia (kgm^2)	14,000

- pitch mass moment inertia (kgm^2)	41,000
- yaw mass moment inertia (kgm^2)	42,000
Rear unit mass (kg)	18,500
- cg height (m)	1.55
- cg to articulation joint distance (longitudinal, m)	2.84
- roll mass moment inertia (kgm^2)	12,000
- pitch mass moment inertia (kgm^2)	28,000
- yaw mass moment inertia (kgm^2)	31,000
Payload mass (kg)	33,720
- cg height (m)	2.4
- cg to articulation joint distance (longitudinal, m)	2.6
- roll mass moment inertia (kgm^2)	27,000
- pitch mass moment inertia (kgm^2)	72,000
- yaw mass moment inertia (kgm^2)	76,000

6.2.2 Tire model

The Fiala tire model together with the enveloping tire-terrain contact method available in the ADAMS platform [190] are customized to represent the AFSV off-road tires (29.5R29). Figure 6.3 illustrates the tire model interacting with the off-road terrain, where the tire periphery envelopes the terrain using two parallel tandem-cams. Each cam is in contact with the terrain at a single point, which are indicated as P_1 and P_2 in Fig. 6.3. The distance between contact points of the two cams ($\overline{P_1P_2}$), which defines the effective tire-terrain contact patch, is dependent on the tire radius and the tire deflection in addition to the terrain profile. The effective tire deflection is computed from:

$$\delta = (z_{oi} - z_u)/\cos\vartheta \tag{6.1}$$

where z_u is vertical motion of the wheel center, and z_{oi} is the effective terrain elevation defined over the instantaneous contact patch $\overline{P_1P_2}$ as an average of the terrain elevations at the cam-terrain contact points $P_1(z_{P1})$ and $P_2(z_{P2})$, such that:

$$z_{oi} = (z_{P1} + z_{P2})/2 \tag{6.2}$$

In Eq. (6.1), ϑ is slope of the terrain profile $\overline{P_1P_2}$, which can be expressed as:

$$\vartheta = \tan^{-1}\big((z_{P2} - z_{P1})/\Delta x\big) \tag{6.3}$$

where Δx is length of the instantaneous contact patch length along the longitudinal axis, which is obtained through projection of terrain profile $\overline{P_1P_2}$ along the x-axis, as shown in Fig. 6.3.

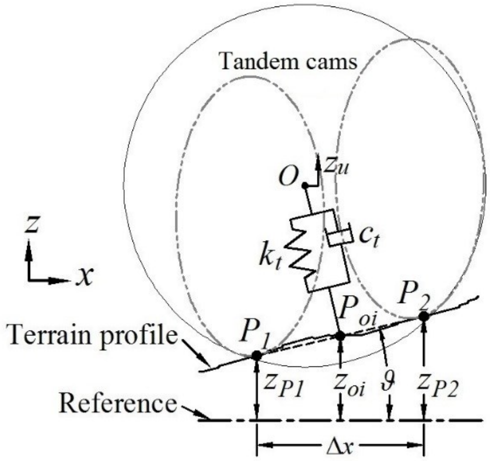

Figure 6.3: Schematic of the two-tandem-cams tire enveloping the off-road terrain [190]

The steady-state longitudinal force, lateral force, vertical force and aligning moment are governed by the Fiala model, as functions of the tire stiffness, tire load, tire width, tire-terrain friction coefficient, etc. [190]. The first-order dynamic lag of the tire is considered through the introduction of longitudinal and lateral relaxation lengths, as described in [51]. The nonlinear tire vertical stiffness is identified from the force-deflection characteristics obtained from the tire manufacturer's documentation and shown in Fig. 6.4. Table 6.2 lists other tire properties including the dimensions, vertical damping coefficient and load-dependent cornering stiffness, which are partly acquired from the tire manufacturer and partly identified on the basis of field-measured data [146].

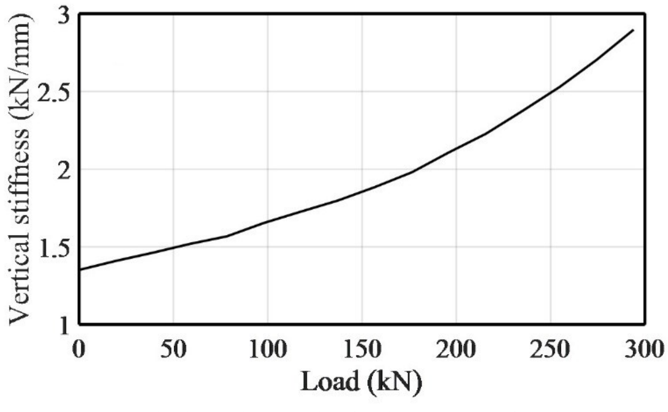

Figure 6.4: Variations in vertical stiffness of the tire with load

Table 6.2: Parameters of the radial-ply tire 29.5R29

Parameter	Value	
Free radius (m)	1.0	
Tire width (m)	0.7	
Charge pressure (bar)	5	
Vertical Damping coefficient (kN.s/m)	35	
Relaxation length (m)	1.2	
Front tire cornering stiffness (kN/deg)	6.8 (loaded)	6.1 (unloaded)
Rear tire cornering stiffness (kN/deg)	7.5 (loaded)	3.7 (unloaded)

6.2.3 Terrain profile

The terrain roughness in this study is represented by an equivalent undeformable profile for the purpose of vehicle dynamic analyses. The terrain profile is generated considering the displacement power spectral density (PSD) function in the form of [78, 79]:

$$G_d(m) = \alpha_r \cdot m^{-w} \tag{6.4}$$

where G_d is the one-sided spatial PSD of the terrain elevation, m is the spatial frequency, α_r is the roughness coefficient and w is the terrain waviness. The ISO-8608 [78] describes the spatial PSD of different road profiles ranging from smooth (class A) to very rough (class E) considering a constant waviness of 2.0. The off-road terrains generally exhibit relatively higher roughness coefficients and greater elevations. The limited data available for a haul road in a mining site suggest that the haul road elevation is comparable to that of class E profile [122, 168]. A simplified piecewise linear coherence function is further formulated so as to describe the roll excitation due to differences in elevations of the two tracks, such that [86]:

$$\gamma^2(m) = \begin{cases} 1 - 0.9m/m_c, & m \leq m_c\ cycle/m \\ 0.1, & m > m_c\ cycle/m \end{cases} \tag{6.5}$$

where m_c is the cut-off spatial frequency, which directly relates to magnitude of the cross-slope of the two terrain tracks [168].

The elevation histories of the two terrain tracks are synthesized using the method described in [168] and illustrated in Figure 6.5. Two unity power band-limited white noise signals, $wn_1(x)$ and $wn_2(x)$, are utilized to obtain the profiles of two terrain tracks $q(x)$ and $p(x)$, where x is longitudinal coordinate of the terrain, using the third-order frequency response functions $\sqrt{G_d(m)}$, $\sqrt{\gamma^2(m)}$ and $\sqrt{1-\gamma^2(m)}$. The method preserves the displacement PSD of the left and right terrain tracks as well as the coherence between them [168]. In this study, the cut-off spatial frequency is taken as 0.3 cycles/m, while the elevations of the off-road terrain are estimated assuming the spectrum of the class E profile.

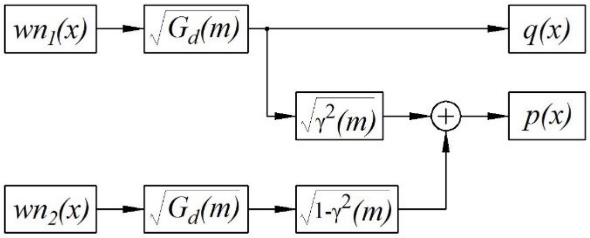

Figure 6.5: Synthesis of elevation-histories of left- and right-track terrain profiles [168]

6.2.4 Articulated frame steering system

The kineto-dynamics of a flow volume regulated frame steering system, illustrated in Fig. 6.6 [131, 146], is integrated to the AFSV multi-body model. The AFS system consists of a hydraulic pump, a steering valve, a reservoir and two steering struts. The steering valve directs the hydraulic fluid to the interconnected steering struts, and the gerotor serves as a steering feedback according to the flow volume. The steering forces developed by the left and right struts are calculated from instantaneous fluid pressures within two chambers of each strut and the viscous friction due to piston and rod seals, which are related to displacements (d_L and d_R) and velocities ($\dot{d}_L$ and $\dot{d}_R$) of the left- and right-struts obtained from the vehicle model. The fluid pressures are computed from the flow continuity equations within the two steering struts considering fluid compressibility and leakage flows within each strut, which can be expressed as:

$$\begin{aligned} q_1 &= A_c\dot{d}_L + A_r\dot{d}_R + q_{lL} + q_{lR} + \frac{V_{1L}+V_{1R}}{B_{eff}}\dot{P}_c \\ q_2 &= A_r\dot{d}_L + A_c\dot{d}_R + q_{lL} + q_{lR} - \frac{V_{2L}+V_{2R}}{B_{eff}}\dot{P}_r \end{aligned} \tag{6.6}$$

where A_c is effective piston area of the steering struts; A_r is effective annular area of the rod-side chamber; q_1 and q_2 are rates of fluid flows from steering valve to the steering struts and from the steering struts to the reservoir, respectively; q_{lL} and q_{lR} are leakage flows within the left- and right-struts, respectively; B_{eff} is effective bulk modulus of the hydraulic fluid; V_{1L} and V_{2R} are volumes of fluid in the piston-side chambers of left- and right-struts, respectively; and V_{1R} and V_{2L} are those of fluid in the rod-side chambers of the right and left-struts, respectively; P_c is fluid pressure in piston-side chamber of the left-strut and rod-side chamber of the right-strut; P_r is fluid pressure in rod-side chamber of left-strut and piston-side chamber of the right-strut, as shown in Fig. 6.6.

The volumes of fluids in the interconnected strut chambers in Eq. (6.6) are calculated neglecting the deformation of the struts and the connecting tubes, as:

$$\begin{aligned} V_{1L} + V_{1R} &= V_0 + A_c d_L + A_r d_R \\ V_{2L} + V_{2R} &= V_0 - A_r d_L - A_c d_R \end{aligned} \tag{6.7}$$

where V_0 is initial fluid volume of the piston-side chamber of the left-strut, rod-side chamber of the right strut and the connecting pipes, which is identical to the initial fluid volume of the piston-side chamber of right strut, the rod-side chamber of left strut and the connecting pipes.

The friction force due to struts' seals is considered as a viscous force, and expressed as a linear function of the relative strut velocity. The strut forces, F_L and F_R, are subsequently obtained from the fluid pressure and the friction force, as:

$$\begin{aligned} F_L &= A_c P_c - A_r P_r - \mu_v \dot{d}_L \\ F_R &= A_c P_r - A_r P_r + \mu_v \dot{d}_R \end{aligned} \tag{6.8}$$

where μ_v is the viscous damping coefficient due to seal friction.

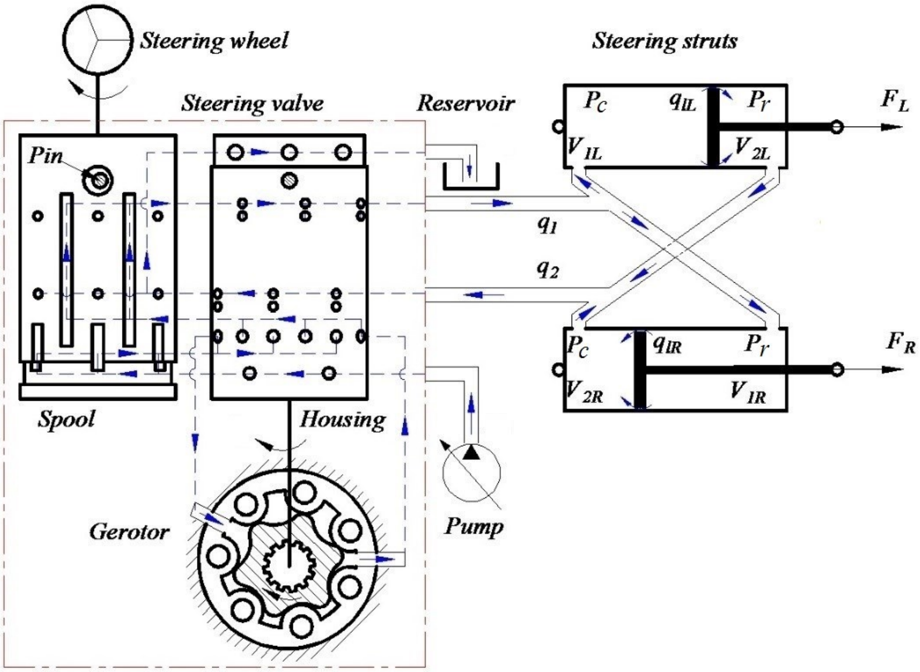

Figure 6.6: Flow volume-regulated frame steering system [146]

6.2.5 Hydro-pneumatic suspension system

Since hydro-pneumatic suspensions (HPS) are increasingly implemented in commercial road and off-road vehicles due to their compact design, ease of ride height control and enhanced attenuation of ride vibrations under large payload variations. The HPS model is formulated considering a simple and low-cost design, schematically illustrated in Fig. 6.7. The HPS strut comprises two chambers connected via bleed orifices and check valves. The piston-side chamber is shared by both the gas and the hydraulic oil, while the annular rod-side contains only the hydraulic oil (Fig. 6.7(a)). During operation, the entrapment of gas within the oil would result in the gas-oil emulsion, as seen in Figs. 6.7(b) and 6.7(c) during compression and rebound, respectively. The emulsion can flow from the piston-side chamber to the rod-side chamber via the check valves and bleed orifices installed on the strut rod during compression, apart from the leakage flow through the piston seal. The check valves, however, remain closed during the extension stroke, which contributes to relatively higher damping force in extension. The rates of fluid flows are related to the pressures within the two chambers, strut velocity as well as the properties of the gas-oil emulsion. The effective mass density and bulk modulus of the gas-oil emulsion would be lower than that of the hydraulic oil, depending on the volume fraction of the entrapped gas within the gas-oil emulsion [142, 176, 177].

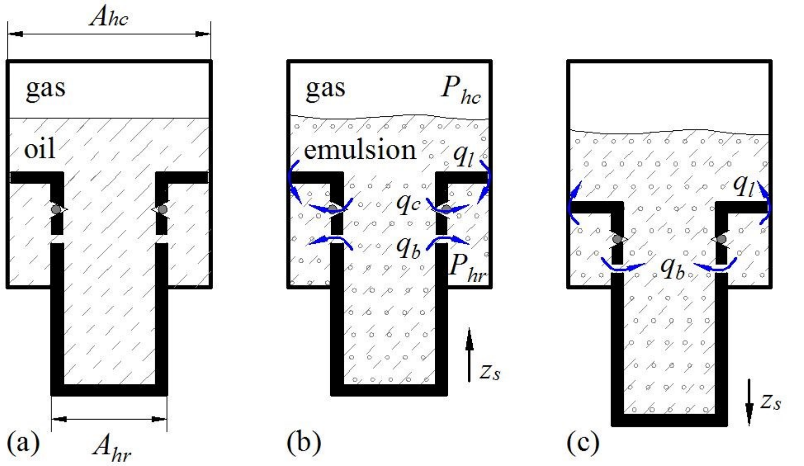

Figure 6.7: Schematic of the hydro-pneumatic suspension strut [189]

An analytical model of the HPS strut is formulated considering the entrapped gas within the oil, as functions of strut deflection and velocity, which can be imported from the multi-body vehicle model. The stiffness of the HPS and its ride height are determined from the strut deflection, gas volume and gas pressure, which may be lowered by the gas entrapment within the hydraulic oil. The strut damping property, on the other hand, is related to the fluid pressures within the two strut chambers and the flow areas, which are related to strut deflection and velocity, and properties of the gas-oil emulsion (gas volume fraction, and effective mass density and bulk modulus). As illustrated in Fig. 6.7, the total force developed by a HPS strut, F_h, can be obtained from the fluid pressures within the piston- and rod-side chambers, and the friction due to the seals between the strut cylinder and strut rod, as:

$$F_h = P_{hc}A_{hc} - P_{hr}(A_{hc} - A_{hr}) + F_f \tag{6.9}$$

where P_{hc} and P_{hr} are pressures of fluid within the piston- and rod-side chambers, respectively; A_{hc} and A_{hr} are effective areas of the piston and the rod, respectively, as shown in Fig. 6.7(a); and F_f is the friction force.

The instantaneous pressures of the gas and emulsion within the piston-side chamber are assumed to be identical neglecting the effect of fluid inertia. Assuming polytropic process of the gas, P_{hc} can be obtained from the initial gas pressure P_{h0} and volume V_{g0}, and the instantaneous gas volume V_g, such that:

$$P_{hc} = P_{h0}\left(V_{g0}/V_g\right)^n \tag{6.10}$$

where n is the polytropic exponent. The instantaneous gas volume V_g in the piston-side chamber is obtained from the continuity equation considering compressibility of the gas-oil emulsion, which can be expressed as:

$$A_{hc}\dot{z}_s + \dot{V}_g = q_b + q_c + q_l + \frac{V_c}{\beta_c}\dot{P}_{hc} \tag{6.11}$$

where $\dot{z}_s$ is relative velocity across the strut; q_b, q_c, and q_l are rates of fluid flows through the bleed orifices, the check valves and the clearance between the strut piston and the cylinder, respectively; V_c and β_c are instantaneous volume and effective bulk modulus of the emulsion within the piston-side chamber, respectively.

The pressure of fluid in the rod-side chamber, P_{hr}, is obtained from the volume continuity equation within the rod-side chamber. Since the mass density of the emulsion within each chamber may be different, the flow continuity equation for the rod-side chamber is formulated considering mass density variation of the fluid flows between the two chambers, such that:

$$(A_{hc} - A_{hr})\dot{z}_s = \frac{\rho_c}{\rho_r}(q_b + q_c + q_l) - \frac{V_r}{\beta_r}\dot{P}_{hr} \tag{6.12}$$

where ρ_c and ρ_r are instantaneous mass densities of the emulsion within the piston- and rod-side chambers, respectively; V_r and β_r are the volume and effective bulk modulus of the emulsion within the rod-side chamber, respectively. The volumes of emulsion in the two chambers of the strut can be obtained from:

$$\begin{gathered} V_c = V_{c0} + V_{g0} - A_{hc}z_s - V_g \\ V_r = V_{r0} + (A_{hc} - A_{hr})z_s \end{gathered} \tag{6.13}$$

where z_s is the strut deflection, and V_{i0} $(i = c, r)$ is the initial volume of the emulsion within the piston- (c) or rod-side (r) chambers.

The mass density and bulk modulus of the gas-oil emulsions in the two chambers of the HPS strut depend on the volume fraction of the entrapped gas within the hydraulic oil as well as the fluid pressure [142]. The gas volume fraction of the emulsion, defined as the ratio of the entrapped gas volume to the hydraulic oil volume ($\gamma_i = V_{gi}/V_{hi}\,; i = c, r$) also varies with the fluid pressure due to compressibility of both the entrapped gas and the hydraulic oil. The instantaneous volumes of entrapped gas V_{gi} and hydraulic oil V_{hi} of the emulsion in chamber i can be expressed as:

$$\begin{gathered} V_{gi} = \left(\frac{P_{h0}}{P_{hi}}\right)^{\frac{1}{n}} V_{gi0};\ i = c, r \\ V_{hi} = \left(1 - \frac{P_{hi} - P_{h0}}{\beta_h}\right) V_{hi0};\ i = c, r \end{gathered} \tag{6.14}$$

where V_{gi0} and V_{hi0} are initial volumes of the entrapped gas and hydraulic oil within the emulsion, respectively; and β_h is bulk modulus of pure hydraulic oil. The instantaneous gas volume fractions of the emulsions in the piston- and rod-side chambers can thus be obtained from:

$$\gamma_i = \frac{\left(\frac{P_{h0}}{P_{hi}}\right)^{\frac{1}{n}} V_{gi0}}{\left(1 - \frac{P_{hi} - P_{h0}}{\beta_h}\right) V_{hi0}} = \frac{\left(\frac{P_{h0}}{P_{hi}}\right)^{\frac{1}{n}}}{1 - \frac{P_{hi} - P_{h0}}{\beta_h}} \gamma_0;\ i = c, r \tag{6.15}$$

where γ_0 ($V_{gi0}/V_{hi0}\,; i = c, r$) is the initial gas fraction of the emulsion in chamber i.

Assuming negligible mass of the entrapped gas, the mass density of the emulsion in each chamber ($\rho_i;\ i = c, r$) can be obtained from [142]:

$$\rho_i = \frac{\rho_h V_{hi0}}{V_{hi} + V_{gi}} = \frac{\rho_h}{\left(1 - \frac{P_{hi} - P_{h0}}{\beta_h}\right)(1 + \gamma_i)};\ i = c, r \tag{6.16}$$

where ρ_h is mass density of the hydraulic oil.

Similarly, the effective bulk modulus of the emulsion within each chamber ($\beta_i;\ i = c, r$) can be derived as a function of the instantaneous pressure considering the compressibility of both the entrapped gas ($-\frac{V_{gi} dP_{hi}}{dV_{gi}} = nP_{hi};\ i = c, r$) and the hydraulic oil ($-\frac{V_{hi} dP_{hi}}{dV_{hi}} = \beta_h;\ i = c, r$), such that:

$$\beta_i = -\frac{V_{gi} + V_{hi}}{\frac{d}{dP_{hi}}\left(V_{gi} + V_{hi}\right)} = \frac{n(1+\gamma_i)P_{hi}\beta_h}{nP_{hi} + \gamma_i\beta_h};\ i = c, r \tag{6.17}$$

Assuming turbulent flows through the bleed orifices (q_b) and check valves (q_c), and laminar leakage flow (q_l), the relations between the fluid flows and pressures can be expressed as:

$$\begin{gathered} q_b = C_b(n_bA_b)\sqrt{\frac{2|P_{hc} - P_{hr}|}{\bar{\rho}_i}} \cdot sgn(P_{hc} - P_{hr}) \\ q_c = \begin{cases} C_v(n_vA_v)\sqrt{\frac{2(P_{hc} - P_{hr})}{\bar{\rho}_i}} & ; P_{hc} > P_{hr} \\ 0 & ; P_{hc} \leq P_{hr} \end{cases} \\ q_l = k_l(P_{hc} - P_{hr}) \end{gathered} \tag{6.18}$$

where (C_b, A_b, n_b) and (C_v, A_v, n_v) are discharge coefficient, opening area and number of bleed orifices and check valves, respectively; $\bar{\rho}_i = (\rho_c + \rho_r)/2$ is the average mass density of the emulsions within the two chambers; and k_l is the leakage flow coefficient. It should be noted that the check valves remain closed when P_{hr} is greater than P_{hc}.

The nominal parameters selected for the front-axle HPS of the considered AFSV, as listed in Table 6.3, are partly obtained from the vehicle configuration, and partly and the flow areas a scaled HPS strut, as reported in [189]. The cross-section areas of the piston and the rod are selected according to the weight and dimensional layout of the vehicle frame and the wheels. The initial volume and pressure of the gas are determined to achieve desired HPS static stiffness and the load capacity considering the cross-section areas of the piston and the rod. Due to the increased strut size compared to the scaled strut, more bleed orifices are introduced. The flow coefficients of the bleed orifices and check valves, are taken as 0.7 and 0.6, respectively, which are identified as mean value for the scaled strut. Although the initial gas fraction within the gas-oil emulsion in Eq. (6.16) has been observed to vary with the strut velocity [189], it is assumed as a constant of 2% for the front-axle HPS strut in this study. The polytropic exponent of gas, leakage flow coefficient and hydraulic oil properties remain the same as those of the scaled strut model, as listed in Table 6.3.

Table 6.3: Nominal parameters of the front-axle HPS

Parameter	Value
Piston area (m^2)	0.038
Rod area (m^2)	0.0254
Check valve area (mm^2)	8
Check valve flow coefficient	0.6
Check valve number	2
Bleed orifice area (mm^2)	11
Bleed orifice flow coefficient	0.7
Bleed orifice number	4
Strut travel (mm)	±120
Total oil volume (L)	11.4
Hydraulic oil bulk modulus (Mpa)	1700
Hydraulic oil mass density (kg/m^3)	850
Initial gas volume (L)	4.5
Initial gas pressure (MPa)	5.8
Initial gas fraction	2%
Polytropic exponent of gas	1.4
Leakage flow coefficient	5×10^{-12}

6.3 Validation of the unsuspended vehicle model

The validity of the vehicle model is examined using the field-measured data acquired for the AFSV prototype. The model validation, however, is limited to the unsuspended prototype vehicle, which is demonstrated in terms of the multi-axes ride vibration and path-change directional responses. The AFSV prototype was instrumented to measure the vehicle speed, steering wheel angle, articulation angle, left steering strut displacement and the steering struts' fluid pressures under a path-change maneuver, as shown in Figure 6.8(a). The path-change course with a 4.5 m lateral offset and an 18 m gate was realized by placements of cones. The ride vibration responses of the vehicle units were measured in terms of accelerations along the three-translational directions, and velocities along the three rotational directions. The vehicle ride vibration responses were measured during a straight-line vehicle motion, as shown in Fig. 6.8(b). The field experiment design has been described in details in [146].

The measurements were conducted on a paved test field for both the loaded and the unloaded vehicles at nearly-constant forward speeds. The roughness profiles of the test terrain tracks were synthesized using the class C spectrum and the method described in Fig. 6.5. The straight-line maneuvers of the unloaded vehicle were performed at three different average speeds: 8, 12 and 18 km/h, while those for the loaded vehicle were conducted at an average speed of 16 km/h. The path-change tests were performed at average speeds of 19.2 and 22.8 km/h for the unloaded vehicle and at 15.3 km/h for the loaded vehicle. Each measurement was repeated 3 times.

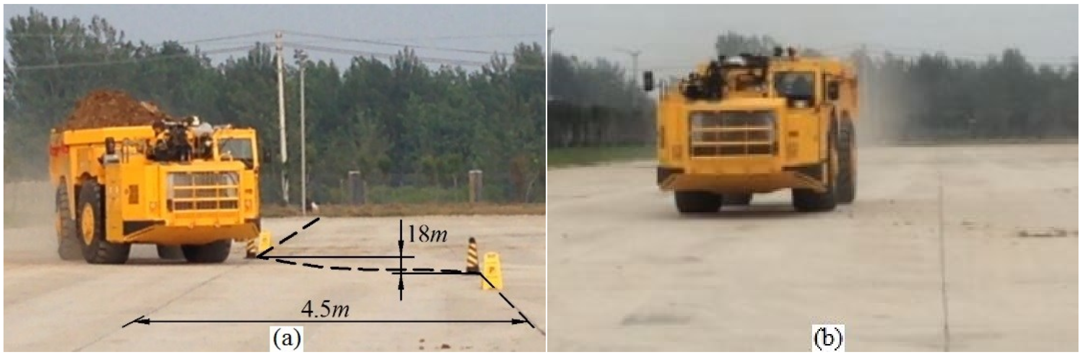

Figure 6.8: Test courses used in field measurements: (a) path-change maneuver; (b) straight-line maneuver

The measured rotational velocities during straight travels were differentiated to obtain the rotational ride accelerations. The time-histories of translational and rotational accelerations were transformed to the frequency domain using the Welch's power spectral density (PSD) estimation method. The repeatability of ride and directional responses measurements during different trials was also examined, which revealed relatively small differences due to slight variations in the path and speed of the AFSV. The mean of the acceleration spectra obtained from the repeated trials were also used to identify the dominant vibration modes frequencies.

The directional and ride dynamic responses of the unsuspended vehicle model incorporating kineto-dynamic model of the AFS system were obtained under excitations from the synthesized elevation histories of the two tracks and time-history of the measured steering wheel angle at the corresponding mean measured speed. Figures 6.9 and 6.10 illustrate comparisons of computed ride-vibration responses of the front unit of the vehicle with and without the payload with the mean measured responses at forward speeds of 16 and 18 km/h, respectively. The ride responses are presented in terms of PSD of accelerations along the translational and rotational axes. The comparisons show reasonable agreements between the computed and measured responses along all the directions, irrespective of the load condition, especially near the dominant ride frequencies. The results show relatively higher magnitude vibrations in the vertical direction of the loaded as well as unloaded vehicle, as shown in Figs. 6.9(a) and 6.10(a). The magnitude of the measured longitudinal acceleration of the unloaded vehicle, shown in Fig. 6.10(e), are also comparable with that of the vertical vibration. The longitudinal acceleration response of the vehicle model, for both the load conditions, however, are considerably lower than the measured responses, especially at frequencies above 2 Hz. This, in-part, is likely caused by the frequent acceleration and deceleration by the driver to maintain the desired speed. This is further evident from relatively higher magnitude of measured pitch accelerations at frequencies above 3 Hz (Figs. 6.9(b) and 6.10(b)). The results show strong coupling among the vertical and pitch modes, as seen in Figs. 6.9(a), 6.9(b), 6.10(a) and 6.10(b). The dominant vertical and pitch vibrations are observed near 1.7 Hz and 1.4 Hz, respectively, for the loaded vehicle, and near 2.2 Hz and 1.6 Hz, respectively, for the unloaded vehicle.

The measured as well as model responses also show strong coupling of the lateral and roll vibration modes. While notable discrepancies are evident between the lateral acceleration PSD obtained from the model and the measured data. This is likely due to lack of consideration of the tire's lateral compliance in the Fiala tire model. The magnitudes of yaw acceleration PSD responses obtained from the model and the measured data are relatively small for both the load conditions, as seen in Figs. 6.9(f) and 6.10(f).

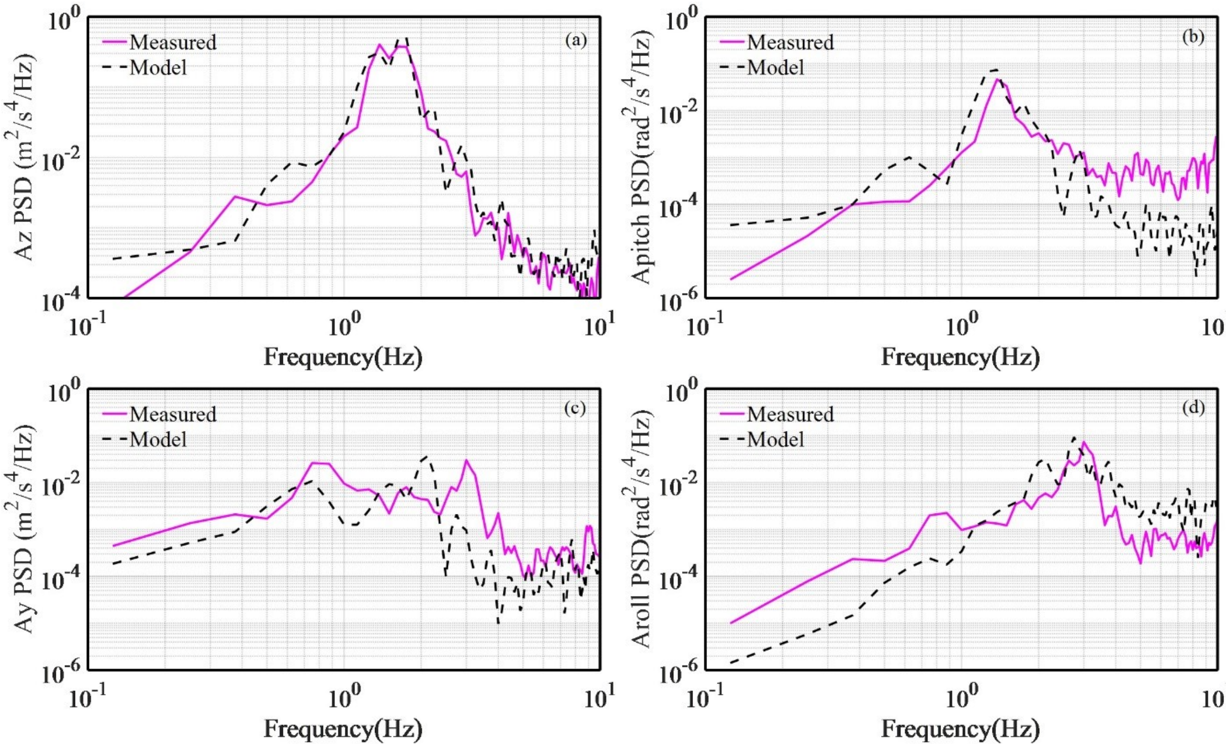

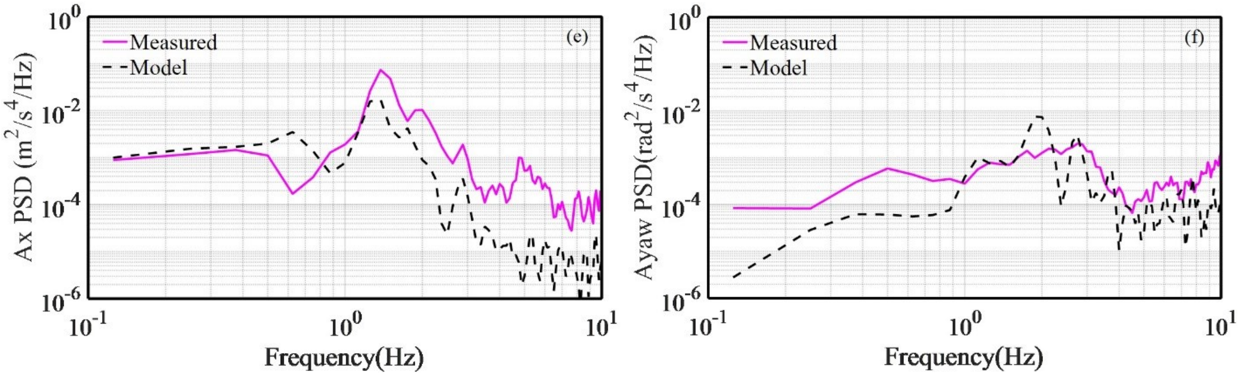

Figure 6.9: Comparisons of PSD of acceleration responses of the loaded vehicle model with the measured data (speed = 16 km/h)

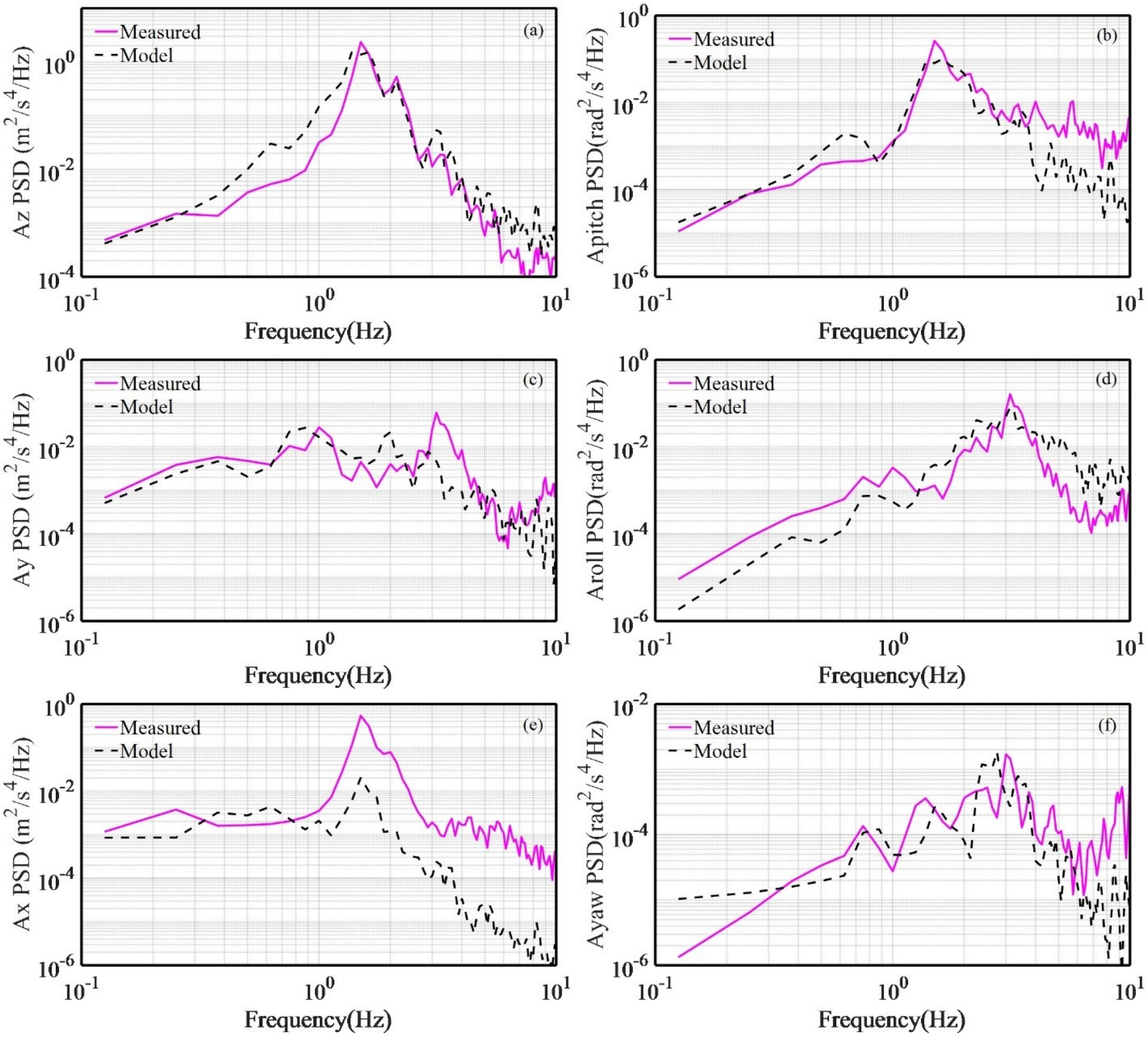

Figure 6.10: Comparisons of PSD of acceleration responses of the unloaded vehicle model with the measured data (speed = 18 km/h)

Figures 6.11(a) and 6.11(b) illustrate the measured steering wheel inputs corresponding to the path-change maneuvers for the vehicle with and without load at nearly-constant forward speeds of 15.3 and 19.2 km/h, respectively. The directional responses of the loaded and unloaded vehicle models are evaluated under these steering inputs. The responses in terms of the articulation angle, left strut displacement, and yaw rate and lateral acceleration of the front unit are compared with the measured responses in Fig. 6.12. The articulation angle and strut displacement response of the loaded vehicle model reveal good agreements with the corresponding measured data, although slight discrepancies are observed near the end of the path change maneuver, as seen in Figs. 6.12(a) and 6.12(c). The strut displacement response of the unloaded vehicle model also agrees well with the measured data, while notable deviations are evident in the corresponding articulation angle response (Figure 6.12(b)). Further analysis of the measured data revealed measurement errors caused by loosening of the link rods used to attach the articulation potentiometer, during measurements in the unloaded case. The comparisons also show reasonably good agreements in the yaw rate and lateral acceleration responses, whereas the peak responses of the model are slightly lower than those obtained from the measured data, which may be due to the simplified tire lateral dynamics considered in the model, as described in section 6.2.2. Despite the observed discrepancies, the comparisons in Figures 6.9, 6.10 and 6.12 suggest that the integrated vehicle model can yield reasonably good predictions of the ride vibration and the steering responses for both the loaded and unloaded conditions.

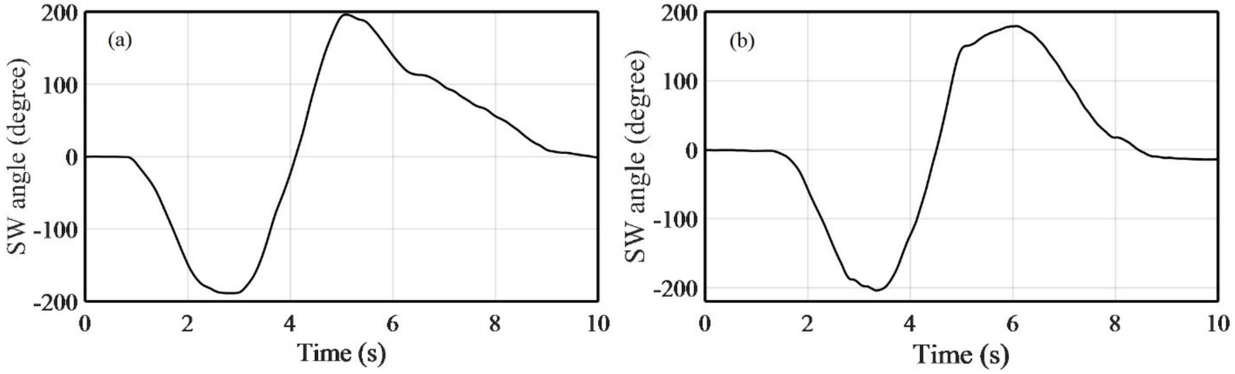

Figure 6.11: Measured steering wheel angle for the loaded (a) and unloaded (b) vehicle

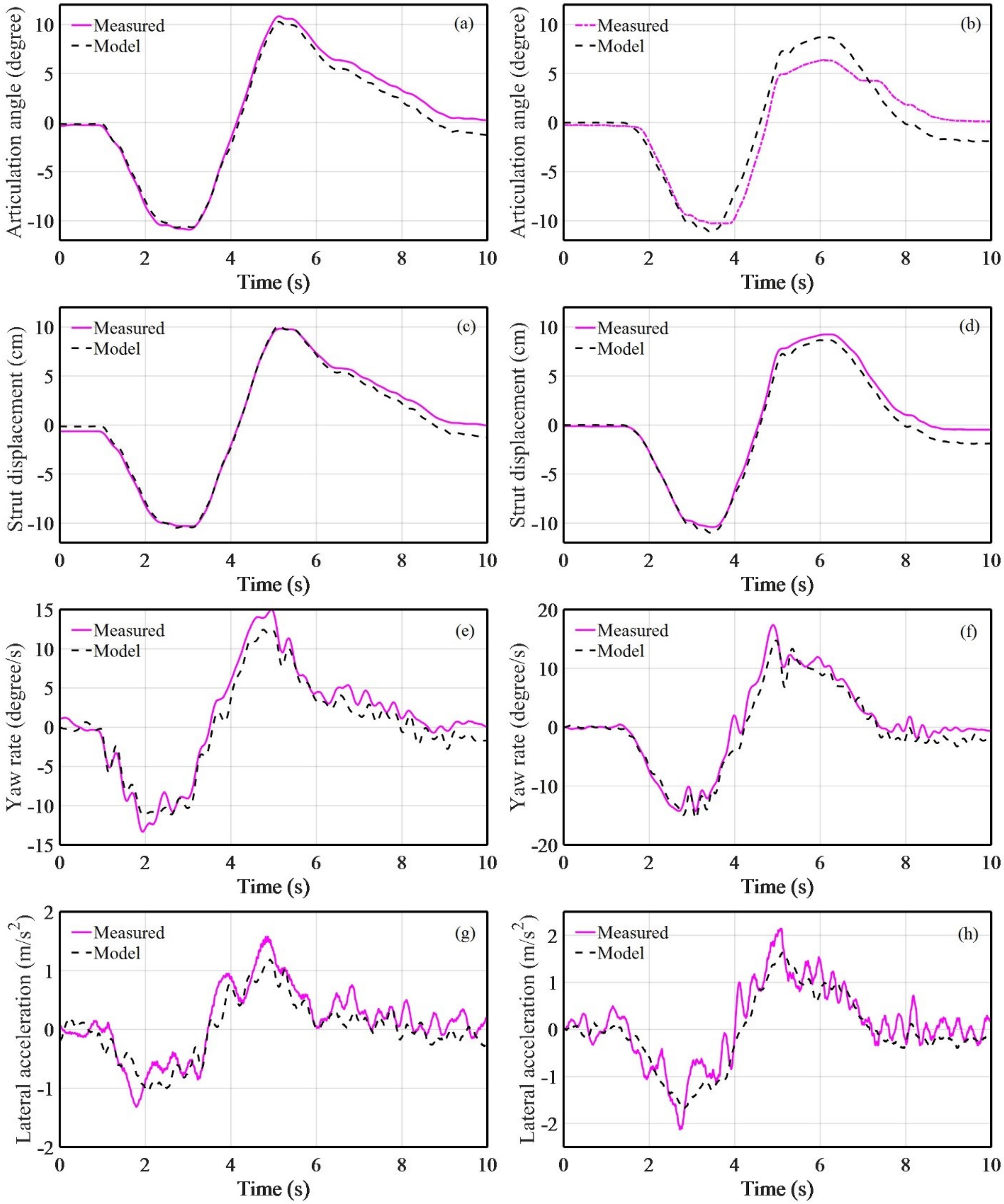

Figure 6.12: Comparisons of model responses to the path-change maneuver with measured responses: (a,c,e,g) loaded (15.3 km/h) and (b,d,f,h) unloaded (19.2 km/h)

6.4 Methodologies for coupled analyses of ride and directional performances of the AFSV

The HPS design with compromise between multi-axes ride and directional performances of the

AFSV can be investigated using the integrated three-dimensional vehicle model, considering the contributions of AFS's kineto-dynamics and off-road terrain roughness. The AFS's kineto-dynamics contribute to the nonlinear yaw stiffness and damping of the AFSV, which have been reported to strongly affect the yaw oscillations [10, 132, 146]. The characteristics of vehicle yaw oscillations relate to yaw-plane stability performance as well as the lateral and yaw vibrations of the vehicle. The ride vibration responses of the AFSV primarily depend on the magnitude and spectral components of the left and right tracks' elevations, apart from the vehicle dimensions and inertia, and suspension and tire properties. The terrain roughness may also deteriorate the yaw- and roll-plane stability of the AFSV [20, 168]. The roll stability performance of off-road vehicles, however, is generally analyzed using the measures defined for road vehicles assuming negligible contributions due to tire's interactions with the rough terrain. Moreover, the directional stability limits may also be reduced to some extent by implementing the axle suspensions, while the axle suspension systems are significant in limiting the multi-axes ride vibrations [48, 132].

The field-measured ride vibrations of the AFSV prototype suggest dominance in the vertical direction (Figs. 6.9 and 6.10), although the reported ride vibrations during actual operations of AFSVs may experience comparable longitudinal and lateral vibrations [4, 15]. Concerning the human operator's health caution [1], the ride performance of the AFSV is evaluated on the basis of the dominant vertical acceleration of the front unit, which supports the driver cabin, using its frequency-weighted root-mean-square (RMS) acceleration value a_{wz}. The frequency weighting function W_k, defined in ISO 2631-1 [1], is applied for this purpose. The a_{wz} for the unsuspended AFSV were obtained as 1.26 m/s^2 and 1.15 m/s^2 for the unloaded and loaded conditions, respectively, which exceed the 8-hour limit value in accordance with HCGZ defined in [1]. This suggests the need for control of ride vibration via the seat and axle suspensions. The ride performance of the AFSV model with the HPS and the AFS subsystem models is evaluated under excitations arising from the synthesized 100 m long terrain tracks, as in [187, 188], at an average forward speed of 20 km/h.

The roll stability performance of the AFSV operating on the off-road terrain is evaluated only in the loaded case considering higher cg position of the loaded vehicle. The integrated vehicle model is simulated under a continuous steering maneuver idealized by a ramp steering wheel input at rate of 5 degree/s, as in [40, 168], in order to establish its dynamic roll stability threshold (DRT). The vehicle forward speed is selected as the maximum speed of the AFSV, 50 km/h. Owing to the relative roll DOF between the front and rear units (Fig. 6.2), the rear unit experiences relatively greater roll motions due to its higher cg position and rearward amplification tendency, which is widely observed in articulated vehicle combinations [40].

Figure 6.13 illustrates steering responses of the rear unit in terms of lateral acceleration and lateral load transfer ratio (LTR). The mean value of these responses gradually increase with the increasing steering input. The simulation is terminated when the AFSV's rear unit approaches the absolute rollover condition as the cg of rear unit aligns vertically with the line joining the rear tire-terrain contact center and the articulation joint, which is indicated as point C in Fig. 6.13, and it corresponds to LTR = 1. The steering responses, however, exhibit considerable oscillations due to the off-road terrain excitation, which make it difficult to identify the onset of a roll stability and the corresponding lateral acceleration and LTR using the criterion defined for smooth roadways. Furthermore, a sustained value of LTR near unity is observed between point A and point B, prior to the absolute rollover. The vehicle is considered to approach the critical roll stability margin during this sustained period (SP), while the corresponding lateral acceleration varies from 2 m/s^2 to 5.9 m/s^2. The dynamic roll stability threshold of the considered AFSV is thus measured by the RMS value of rear unit's lateral acceleration during the sustained period of LTR = 1 [168], which is termed as SP-DRT in this study. SP-DRT is obtained as 3.78 m/s^2 for the unsuspended AFSV operation on the off-road terrain.

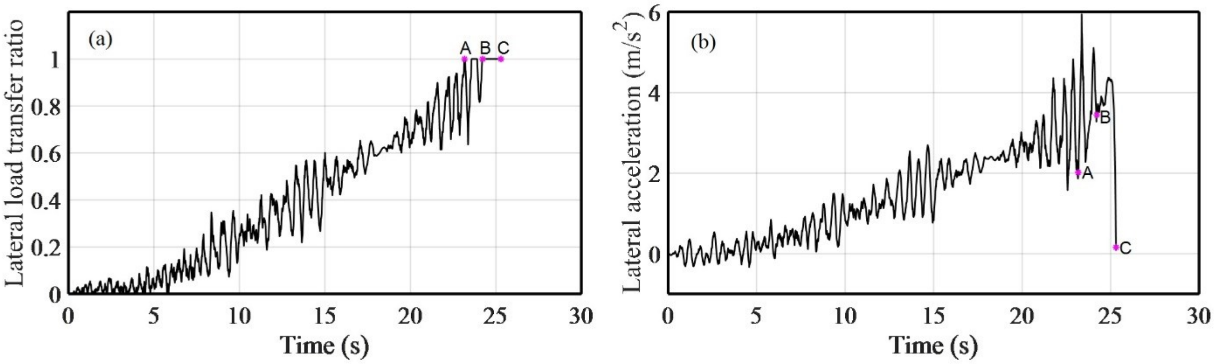

Figure 6.13: Lateral load transfer ratio (a) and lateral acceleration (b) of the rear unit of the AFSV

The yaw stability performance of the AFSV is evaluated in the loaded case as well on the basis of the articulation angle oscillation following a lateral perturbation idealized by a pulse steering wheel input, as in [132, 146]. The vehicle forward speed is also selected as the maximum speed of 50 km/h. The articulation angle response following the pulse steering is illustrated in Fig. 6.14. Slight oscillations in the articulation angle are observed prior to the steering input, applied at t=1 second, which is attributed to tire interactions with the rough terrain. The articulation oscillation after the 0.2-seconds pulse steering input is fitted to a single-DOF system response, in order to obtain the yaw-mode oscillation frequency and damping ratio of the AFSV [146]. The yaw-mode oscillation frequency ω_z, which has been reported to positively correlate with the yaw-plane stability of the AFSV, is selected to measure the yaw-plane stability limit. For the unsuspended vehicle, ω_z was obtained as 2.81 Hz.

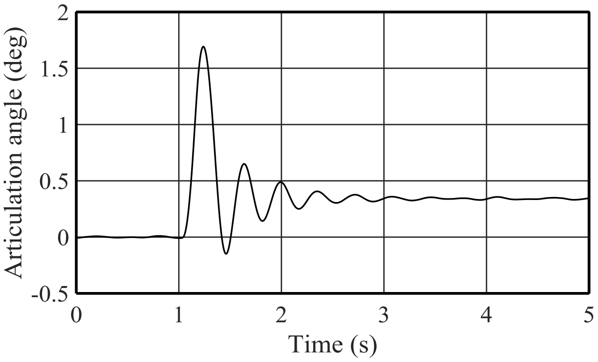

Figure 6.14: Articulation angle oscillation following a lateral perturbation

6.5 Sensitivity analyses and design optimization of front-axle hydro-pneumatic suspension

The nonlinearity and hysteresis in the stiffness and damping characteristics of the simple HPS design would contribute to the multi-performances of the AFSV in a highly complex manner. Parametric sensitivity analyses are thus performed for the integrated AFSV model to study the effects of HPS on the coupled ride and directional response characteristics of the vehicle. The results are used to formulate an optimization problem in an attempt to seek a more favorable design of the HPS system considering the ride as well as directional performances of the AFSV. Variations in main parameters of the HPS are considered for this purpose, which include: piston area A_{hc} of the HPS strut, which determines the gas volume and the effective suspension stiffness; and flow areas of check valves A_v and bleed orifices A_b, which affect the suspension damping property. Variations in A_{hc} influence not only the effective suspension stiffness but also the load carrying capacity. The gas charge pressure and the rod area A_{hr} are not altered in order to maintain identical load carrying capacity of the struts. While A_b relates to damping property in extension, both A_v and A_b determine the damping characteristics during compression, as seen in Eq. (6.18). Since the HPS is introduced for the front unit alone, its effects on the yaw and roll performances are not expected to be significant.

6.5.1 Sensitivity analyses

For the sensitivity analyses, the selected areas A_{hc}, A_v and A_b are varied one parameter at a time by ±15% and ±30% about their respective nominal values, listed in Table 6.3. Table 6.4 summarizes the ride vibration exposure, roll and yaw stability performance measures computed from the responses to terrain excitation and steering input, using the methodology presented in section 6.4, in terms of a_{wz}, *SP-DRT* and ω_z, respectively. Compared with the unsuspended AFSV prototype operating on the off-road terrain, implementing the nominal front-axle HPS is shown to reduce the a_{wz} by 30% and 25% for the unloaded and loaded cases, respectively, while the *SP-DRT* and ω_z are only slightly reduced. The observed effect of suspension on roll and yaw plane stability measures is significantly lower than those reported in [48, 132]. The reductions in the roll and yaw stability limits compared to the unloaded vehicle are relatively small (3.2% and 3.6%, respectively), since HPS is introduced in the front unit axle alone, while the roll and yaw motions are mostly affected by the rear unit with the load. Increasing A_{hc} reduces the vertical stiffness of the front unit suspension, which tends to deteriorate the roll stability. The variations in A_v and A_b and the resulting suspension damping, however, demonstrate nearly no effects on the directional stability of the AFSV, especially in the yaw plane.

The ride performances of both the loaded and unloaded vehicles, however, are quite sensitive to the HPS properties, as expected. The unloaded vehicle generally exhibit greater vibrations than the loaded case, as seen in Table 6.4. Since the payload alters the front-axle load of the AFSV only minimally, the vertical acceleration response spectra obtained for the loaded and unloaded cases exhibit dominance near 1 Hz and coupled with the pitch mode vibration around 1.5 Hz (Fig. 6.15). The variation in A_{hc} alters the suspension stiffness and thereby the dominant vibration frequencies. The 30% reduction in A_{hc} significantly increases the vibration magnitudes near 1 Hz, which results in 26% and 17% increase in a_{wz} for the unloaded and loaded vehicles, respectively. The 30% increase in A_{hc}, on the other hand, reduces vertical vibration response near 1 Hz, while the pitch motion of the AFSV increase considerably (near 1.5 Hz) due to the reduced front-axle HPS stiffness, as seen in Figs. 6.15(a) and 6.15(b). This leads to nearly 50% increase in a_{wz} for both the unloaded and loaded vehicles (Table 6.4).

The variations in A_v only slightly affect the ride performance in the unloaded case, as seen in Table 4, which is due to only partial contribution of A_v to the effective damping coefficient during suspension compression. The variations in A_b, however, strongly affect the effective suspension damping property, and thus the ride vibration response, as illustrated in Figs. 6.15(c) and 6.15(d) for the loaded and unloaded vehicle models, respectively. Increasing A_b yields lower effective damping and subsequently higher vibration in the vicinity of the vertical mode resonance frequency (< 1.2 Hz) but better vibration isolation at in the critical ride frequencies. The frequency-weighted ride vibration values thus decrease with increasing A_b, due to relatively lower weighting near the dominant frequency of 1 Hz.

Table 6.4: Results obtained from sensitivity analyses of the front-axle HPS system

Load condition	*Ride (a_{wz}, m/s^2)*						*Roll (SP-DRT, m/s^2)*			*Yaw (ω_z, Hz)*		
	unloaded			loaded			loaded			loaded		
Parameter	A_{hc}	A_v	A_b	A_{hc}	A_v	A_b	A_{hc}	A_v	A_b	A_{hc}	A_v	A_b
-30%	1.12	0.90	0.96	1.01	0.86	0.90	3.67	3.66	3.66	2.81	2.80	2.80
-15%	0.93	0.89	0.92	0.85	0.86	0.87	3.66	3.66	3.66	2.80	2.80	2.80
Nominal	0.89	0.89	0.89	0.86	0.86	0.86	3.66	3.66	3.66	2.80	2.80	2.80
15%	1.23	0.89	0.87	1.15	0.86	0.85	3.64	3.66	3.66	2.80	2.80	2.80
30%	1.34	0.89	0.86	1.26	0.86	0.84	3.63	3.65	3.65	2.80	2.80	2.80

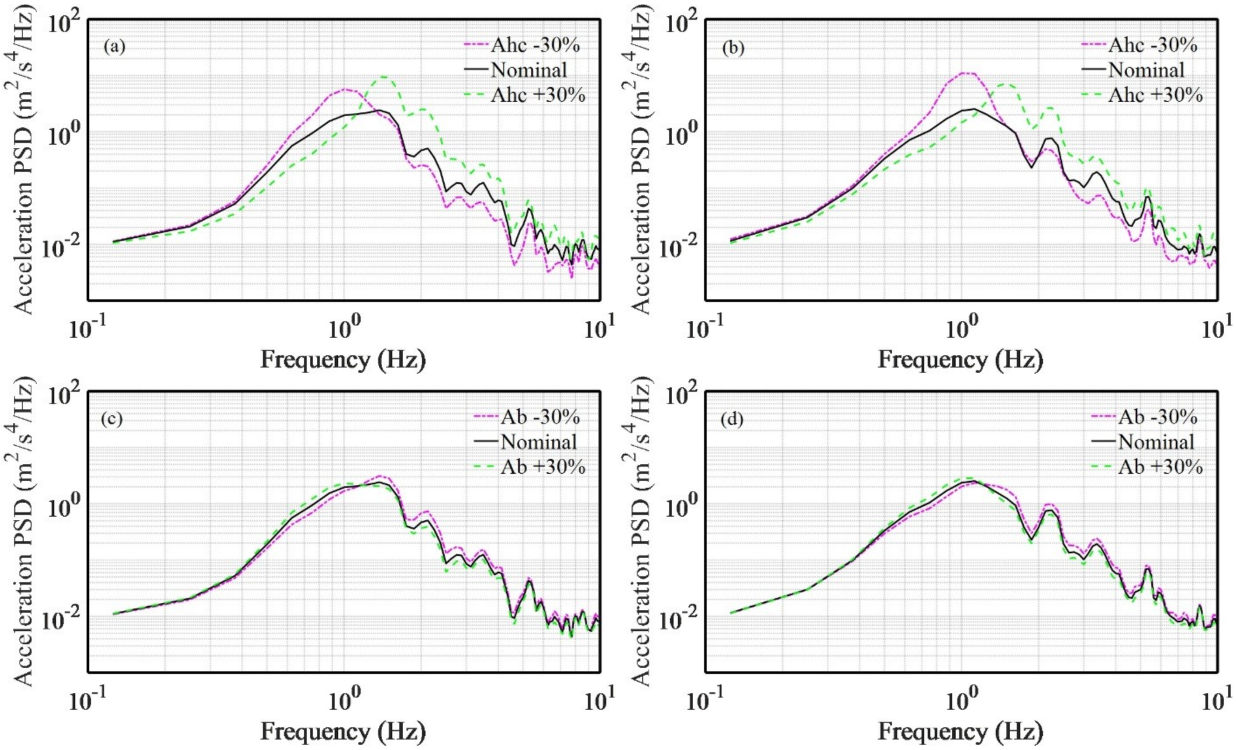

Figure 6.15: Effects of variations in A_{hc} and A_b on the PSD of vertical acceleration response of the front unit: (a,c) loaded and (b,d) unloaded

6.5.2 Design optimization

An optimal solution for the front-axle HPS is further attempted to seek improved ride performance, while preserving the roll and yaw directional performances. The results obtained from the sensitivity analyses suggest that the directional stability limits of the AFSV exhibit only slight sensitivity to the HPS's main parameters, when applied to front-axle alone. The HPS system may thus be optimized considering the ride vibration performance alone. The total suspension travel, d_s, however, must be limited so as to limit the maximum bounce and pitch motions of the vehicle. The optimization problem is thus formulated to minimize a composite objective function, as:

$$F(\chi) = \text{Minimize}\left[\frac{a_{wz}}{a_{wzn}} + \frac{d_s}{d_{sn}}\right] \tag{6.19}$$

where $\chi = [A_{hc}\ A_v\ A_b]$ is the selected design parameters vector; a_{wzn} and d_{sn} are the respective values of the vertical ride and peak-to-peak suspension travel obtained for the nominal HPS design. Moreover, it would be beneficial to limit the ride vibration level well within the HCGZ limit with respect to 8-hours daily exposure. The upper limit of 0.85 m/s^2 is thus selected. Furthermore, the strut piston area and the orifice sizes may be limited to feasible values. The strut piston should be wider enough than the strut rod, and the orifice diameters should be large enough to maintain the assumptions of short holes and turbulent flows through the check valves and bleed orifices. Inequality constraints are thus imposed on the weighted ride vibration acceleration as well as the design parameters, as:

$$\begin{gathered} a_{wz} \leq 0.85\ \mathrm{m}/s^2 \\ \chi \geq \ [0.026 \quad 4\times10^{-6} \quad 7\times10^{-6}]\ m^2 \end{gathered} \tag{6.20}$$

The constrained nonlinear optimization problem is solved using Genetic algorithm in the Matlab/Simulink Design Optimization toolbox [161]. The solutions are obtained for unloaded AFSV model considering relatively higher vibration levels in the unloaded condition. The resulting optimal design parameters are summarized in Table 6.5 together with the nominal parameters. It can be seen that optimal areas of the check valves A_v and bleed orifices A_b are substantially lower and higher, respectively, than the nominal values. The optimal piston area A_{hc} is increased by 11% compared to the nominal design, which increases the gas volume within the HPS strut and thereby decreases the effective suspension stiffness. While the suspension travel d_s is slightly decreased to 0.078 m although the suspension is softened compared to the nominal design, and the minimization function value is converged to 1.93. The weighted ride vibration a_{wz} (0.848 m/s^2) is converged to the vicinity of the upper limit imposed in Eq. (6.20), which is nearly 5% lower than that obtained for the nominal suspension and 33% lower compared to the unsuspended vehicle. The optimal HPS design thus reduces the vertical motion as well as the vibration exposure level of the AFSV. On the other hand, the vehicle directional stability performance measures (*SP-DRT* and ω_z)

obtained with the optimal HPS design, also presented in Table 6.5, are affected only slightly. This is consistent with the sensitivity analyses results in the previous subsection.

Table 6.5: Nominal and optimal HPS design parameters and vehicle ride response

Parameter	Nominal design	Optimal design	Objective	Nominal value	Optimal value
A_{hc} (m^2)	0.038	0.0474	a_{wz} (m/s^2)	0.89	0.848
A_v (mm^2)	8	4.28	*SP-DRT* (m/s^2)	3.66	3.63
A_b (mm^2)	11	27.3	ω_z, (Hz)	2.80	2.80
			d_s (m)	0.08	0.078
			$F(\chi)$	2	1.93

Furthermore, the effects of variations in load condition and forward speed (10 to 30 km/h) of the AFSV with optimal HPS design on the ride vibration and suspension travel are evaluated and presented in Fig. 6.16. The ride vibration response is evaluated in terms of the unweighted and weighted RMS values of the front unit's vertical acceleration. Since the HPS is optimized for the unloaded case, the unweighted and weighted RMS accelerations of the unloaded vehicle are generally comparable to those of the loaded vehicle in the speed range considered, although the loaded vehicle is usually reported to experience lower vibration [167]. This implies that the vibration magnitudes within the more critical frequency range are comparable both load conditions in the selected range of speeds. Increasing the forward speed, however, is shown to increase the unweighted and weighted accelerations as well as the suspension travel, irrespective of the load condition. This is attributed to increased terrain excitations near the critical ride frequencies with increasing vehicle speed. The suspension travel of the loaded vehicle is generally greater than that of the unloaded vehicle, as seen in Fig. 6.16(b), due to the increased axle load. The ride vibration of the AFSV exceeds the 8-hours HCGZ limit as the forward speed approaches 25 km/h or higher, as seen in Fig. 6.16(a). This suggests the need for secondary suspensions of the cabin and the seat.

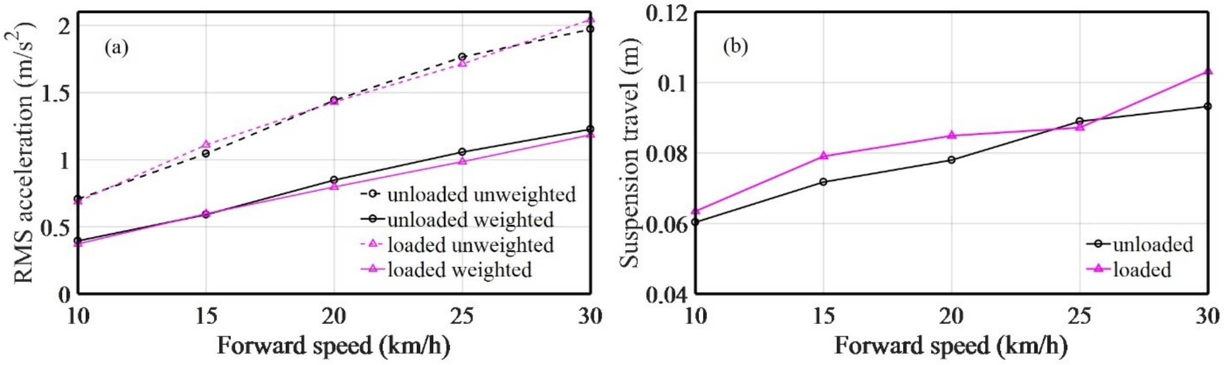

Figure 6.16: Effects of variations in load and speed on responses of the vehicle with optimal front-axle HPS: (a) frequency-weighted and unweighted RMS vertical acceleration; and (b) suspension travel

6.6 Conclusions

The ride vibration, and roll- and yaw-plane directional stability performances of an AFSV are investigated considering the contributions of the kineto-dynamics of the frame steering system, off-road terrain roughness and a hydro-pneumatic front-axle suspension. These performances of the off-road AFSV can be measured in terms of frequency-weighted vertical vibration of the front unit, RMS value of the lateral acceleration during the sustained lateral load transfer ratio period prior to absolute rollover of the rear unit, and yaw-mode oscillation frequency following a lateral perturbation, respectively. Implementing the front-axle hydro-pneumatic suspension was shown to preserve the directional stability limits, while reducing the ride vibration exposure of the human operators by nearly 30%, compared to the unsuspended AFSV prototype. Owing to suspension implementation to the front-axle alone, the results showed only minimal sensitivity of the roll and yaw stability measures to variations in suspension stiffness and damping characteristics. A ±30% variation in the strut piston area about the nominal value, however, showed significant effect on the frequency-weighted vertical acceleration, ranging from 20% to 50%, with only minimal effects on the directional stability performance limits (<4%). The optimal HPS design further attenuated the ride vibrations, irrespective of the payload variation of the AFSV. Increasing the forward speed, while operating on the off-road terrain, however, resulted in vibration exposure exceeding the defined HCGZ. This suggests the need for secondary suspension at the cabin and the seat, and consideration of suspension of both the axles. The directional stability performance limits of the AFSV were also shown to be only slightly affected by the optimal HPS design.

CHAPTER 7
CONCLUSIONS AND RECOMMENDATIONS

7.1 Major contributions and highlights of the dissertation research

This dissertation research presents systematic analytical and experimental studies for off-road vehicles to achieve enhanced ride performance while preserving the roll- and yaw-plane performances, especially for an articulated frame-steered vehicle (AFSV). An alternative roll stability performance measure is proposed considering the significant contributions of terrain tracks' elevations and spectral components. The hydro-mechanical articulated frame steering system (AFS) is investigated and the critical design features affecting the steering performances and the snaking stability in the yaw plane are identified. A simple and low-cost hydro-pneumatic suspension (HPS) strut is also studied considering the effects of gas-oil emulsion, so as to characterize its nonlinear stiffness and damping properties. The coupled ride and directional performance analyses of the AFSV, as well as the front-axle HPS suspension design optimization are subsequently conducted on the basis of an integrated three-dimensional vehicle model. The major highlights of the dissertation research are summarized below:

- A multi-body dynamic model of a mining vehicle is formulated and its roll dynamic behavior is investigated, while operating on off-road terrains.
- An alternative performance measure for assessing roll stability of off-road vehicles is proposed and the robustness of the proposed dynamic rollover threshold is illustrated.
- The parametric analyses of the off-road terrain properties on the proposed dynamic rollover threshold are conducted.
- A yaw-plane model of an articulated frame-steered mining vehicle is developed incorporating kineto-dynamics of the steering system and its validation is demonstrated using the field-measured data acquired from a 35 tons mining AFSV.
- The free yaw-oscillation and transient steering responses are characterized and the effects of steering strut parameters are investigated, and a design guidance for the articulated frame steering system is proposed.
- The objective measures of primary AFSV steering performances are identified considering the yaw oscillation/stability, steering power efficiency, and maneuverability, and a

methodology to determine the weights of different objective measures is presented using a three-level Analytic Hierarchy Process model

- An optimal design of the AFS is proposed to achieve improved yaw stability limit, steering power efficiency, and maneuverability.
- A simulation model of a simple and low-cost design of a hydro-pneumatic suspension (HPS) is formulated and its parameters are identified from the laboratory-measured data acquired for a prototype strut.
- The nonlinear stiffness and damping characteristics of HPS strut with gas-oil emulsion are obtained, and the effects of gas volume fraction within the emulsion on the resulting spring and damping forces of the HPS strut are investigated.
- A three-dimensional multi-body dynamic model of the articulated frame-steered mining vehicle is formulated integrating the hydro-mechanical AFS and hydro-pneumatic front-axle suspension subsystems to investigate multiple and coupled performance measures.
- The validity of the vehicle model is demonstrated using the field-measured data acquired on a prototype vehicle in terms of the multi-axes ride vibration and path-change directional responses.
- The coupled ride and directional performances of the AFSV are analyzed, and the front-axle HPS system is subsequently optimized.

7.2 Major conclusions

The major conclusions drawn from the analytical and experimental studies are summarized below:

- The dynamic rollover threshold of vehicle operating on rough terrains can be reliably estimated as the RMS lateral acceleration over the sustained period when the LTR remains near unity, prior to the absolute rollover.
- The vertical and roll excitations generated from the off-road terrains adversely affected the vehicle dynamic roll stability, especially the lower spatial frequency components of the terrain elevation.
- The free yaw-oscillations and transient steering characteristics of an AFSV were strongly affected by kineto-dynamic properties of the AFS system, although some of the design parameters suggested contradictory effects.

- Using fluids with higher fluid bulk modulus and increasing the steering arm length resulted in relatively higher the yaw stiffness of the AFS system, steering gain and rate of articulation with significantly lower articulation overshoot.
- The leakage flows and viscous seal friction within the steering struts resulted in rapid attenuation of yaw-oscillations without affecting the yaw stiffness. These also contributed to higher power dissipation and thereby lower steering gain and rate of articulation.
- The steering gain and rate of articulation were shown to be dominated by the strut kinematics.
- The solutions of the three-level Analytic Hierarchy Process model revealed greatest weight for the equivalent yaw stiffness or oscillation frequency compared to the other objective measures of the AFSV, namely, the strut length, damping ratio, steering gain, and response overshoot and articulation rate.
- The optimal AFS design revealed 24% gain in the yaw oscillation frequency, 7% gain in the yaw damping ratio and a more compact AFS system design with over 20% reduction in the strut length.
- The laboratory experiments revealed that the gas entrapment in the oil occurs rapidly under higher frequency operations and the mean gas volume fraction tended to saturate.
- The entrapped gas contributed to notable hysteresis in both the stiffness and damping properties, especially under higher operating pressures, while the effective stiffness and damping increased and decreased, respectively, with increasing gas volume fraction.
- The ride vibration, roll- and yaw-plane directional stability performance measures of the AFSV were shown to be coupled considering the contributions of the AFS's kineto-dynamics, off-road terrain roughness and the axle suspension.
- The coupled ride and directional performances of the off-road AFSV could be measured by the frequency-weighted vertical vibration of the front unit, RMS value of the lateral acceleration during the sustained lateral load transfer ratio period before absolute rollover of the rear unit, and yaw-mode oscillation frequency following a lateral perturbation.
- The sensitivity analyses results of the front-axle HPS suggested that variations in the suspension stiffness and damping characteristics mainly affected the vehicle ride vibrations, with minimal effect on the roll- and yaw-stability limits.

- The proposed optimal front-axle HPS could yield nearly 30% reduction in the WBV exposure compared to the conventional unsuspended vehicle with only slight reduction in the roll and yaw stability measures (below 4%).

7.3 Recommendations for future studies

The proposed three-dimensional model of the AFSV integrating the AFS and HPS subsystems can serve as an effective tool for predicting coupled ride and directional dynamics responses, and thereby facilitate axle suspension and steering system designs. The considered hydro-pneumatic suspension at the front axle offers an acceptable compromise between the ride vibration and directional stability performances of the AFSV. The front-axle suspended vehicle, however, showed excessive ride vibration exposure when operating at relatively higher speeds, although the directional stability performances are only slightly affected by the suspension system. The vibration exposure at speeds above 25 km/h exceeded the health-caution guidance limits for 8 hours daily exposure, which suggests the need for more effective primary and secondary suspensions. Additional efforts on novel suspension and steering system designs so as to achieve enhanced performances under broader ranges of payload and forward speed of the AFSV are thus highly desirable. Moreover, the considered HPS with gas-oil emulsion involves further challenges considering the instantaneous variations in temperature, gas volume fraction and hydraulic oil properties, especially during relatively higher velocity operations. Particular topics of future work may include the following:

- Due to highly nonlinear variations in stiffness and damping properties with the gas volume fraction for the HPS design considered in this study, further efforts are needed to identify more reliable relations among the gas volume fraction, properties of the emulsion and the fluid pressures.
- The variations in the free gas volume, fluid compressibility and temperature of the HPS would also affect the ride height. Design of a ride height control mechanism is thus desirable for such suspension systems.
- The effects of HPS strut temperature on the properties of gas and fluid and the resulting stiffness and damping characteristics need to be investigated.
- The integrated three-dimensional AFSV model presented in Chapter 6 can be extended with suspensions applied to both the axles, and secondary suspension at the cabin and the

seat, which would permit identifications of optimal primary and secondary suspension designs.

- The suspension struts within and cross-axle interconnections should be investigated to achieve further reductions in the vertical spring rates, while preserving high roll and pitch stiffness of the suspension.
- Owing to large size and load capacity of tires used in such vehicles, it is very difficult to obtain reliable tire parameters and thereby the tire model. Further efforts are strongly recommended to identify tire properties in terms of cornering, self-aligning, and lateral and longitudinal compliances so as develop a reliable tire model.
- Considering that the steering performance is directly affected by flow characteristics of the steering valve, it is recommended to undertake further studies with valves with relatively higher flow rates so as to achieve rapid steering rate.

REFERENCES

[1] ISO 2631-1: Mechanical vibration and shock – evaluation of human exposure to whole-body vibration – part 1: General requirements, (1997).

[2] Directive 2002/44/EC of the European Parliament, Minimum health and safety requirements regarding the exposure of workers to the risks arising from physical agents (vibration), (2002).

[3] T. Eger, J.M. Stevenson, S. Grenier, P. Boileau, M.P. Smets, Influence of vehicle size, haulage capacity and ride control on vibration exposure and predicted health risks for LHD vehicle operators, Journal of Low Frequency Noise, Vibration & Active Control 30 (2011) 45-62.

[4] V. Dentoni, G. Massacci, Occupational exposure to whole-body vibration: Unfavorable effects due to the use of old earth-moving machinery in mine reclamation, International Journal of Mining, Reclamation and Environment 27 (2013) 127-142.

[5] A.P. Cann, A.W. Salmoni, P. Vi, T.R. Eger, An exploratory study of whole-body vibration exposure and dose while operating heavy equipment in the construction industry, Applied Occupational and Environmental Hygiene 18 (2003) 999-1005.

[6] G. Owen, A. Hunter, A survey of tractor overturning accidents in the united kingdom, Journal of Occupational Accidents 5 (1983) 185-193.

[7] G. M. Owen and G. Gilfillan, "Survey of overturning accidents in England and wales, 1968-78," Scottish Institute of Agricultural Engineering, Tech. Rep. SIN/265, 1979.

[8] C.G. Drury, W.L. Porter, P.G. Dempsey, Patterns in mining haul truck accidents, Proceedings of the Human Factors and Ergonomics Society Annual Meeting, (2012) 2011-2015.

[9] B.R. Santos, W.L. Porter, A.G. Mayton, An analysis of injuries to haul truck operators in the US mining industry, Proceedings of the Human Factors and Ergonomics Society Annual Meeting, (2010) 1870-1874.

[10] A. Pazooki, S. Rakheja, D. Cao, Kineto-dynamic directional response analysis of an articulated frame steer vehicle, International Journal of Vehicle Design 65 (2014) 1-30.

[11] P. Dudziński, A. Skurjat, Directional dynamics problems of an articulated frame steer wheeled vehicles, Journal of KONES 19 (2012) 89-98.

[12] D.N.L. Horton, D.A. Crolla, Theoretical analysis of the steering behaviour of articulated frame steer vehicles, Vehicle System Dynamics 15 (1986) 211-234.

[13] K. Nevala, M. Jarviluoma, An active vibration damping system of a driver's seat for off-road vehicles, 4th Annual Conference on Mechatronics and Machine Vision in Practice, (1997) 38-43.

[14] X. Huang, S. Rakheja, Performance analysis of a relative motion based magneto-rheological damper controller for suspension seats, 4th International Conference on Micro- and Nanosystems, Montreal, Quebec, Canada, (2010) 39-48.

[15] R.J. Jack, M. Oliver, J.P. Dickey, S. Cation, G. Hayward, N. Lee-Shee, Six-degree-of-freedom whole-body vibration exposure levels during routine skidder operations, Ergonomics 53 (2010) 696-715.

[16] T. Eger, A. Salmoni, A. Cann, R. Jack, Whole-body vibration exposure experienced by mining equipment operators, Occupational Ergonomics 6 (2006) 121-127.

[17] S. Cation, R. Jack, M. Oliver, J.P. Dickey, N. Lee-Shee, Six degree of freedom whole-body vibration during forestry skidder operations, International Journal of Industrial Ergonomics 38 (2008) 739-757.

[18] N.L. Azad, A. Khajepour, J. McPhee, A survey of stability enhancement strategies for articulated steer vehicles, International Journal of Heavy Vehicle Systems 16 (2009) 26-48.

[19] Y. He, A. Khajepour, J. McPhee, X. Wang, Dynamic modelling and stability analysis of articulated frame steer vehicles, International Journal of Heavy Vehicle Systems 12 (2005) 28-59.

[20] A. Pazooki, S. Rakheja, D. Cao, Effect of terrain roughness on the roll and yaw directional stability of an articulated frame steer vehicle, SAE International Journal of Commercial Vehicles 6 (2013) 325-339.

[21] Y. Li, W. Sun, J. Huang, L. Zheng, Y. Wang, Effect of vertical and lateral coupling between tyre and road on vehicle rollover, Vehicle System Dynamics 51 (2013) 1216-1241.

[22] A. Pazooki, S. Rakheja, D. Cao, Modeling and validation of off-road vehicle ride dynamics, Mechanical Systems and Signal Processing 28 (2012) 679-695.

[23] D. Cao, S. Rakheja, C. Su, Roll-and pitch-plane coupled hydro-pneumatic suspension: Part 1: Feasibility analysis and suspension properties, Vehicle System Dynamics 48 (2010) 361-386.

[24] M. Bovenzi, A longitudinal study of low back pain and daily vibration exposure in professional drivers, Industrial Health 48 (2010) 584-595.

[25] N.L. Azad, J. McPhee, A. Khajepour, The effects of front and rear tires characteristics on the snaking behavior of articulated steer vehicles, Proceedings of IEEE Vehicle Power and Propulsion Conference, (2005) 274-279.

[26] European Committee for Standardization, "Mechanical vibration – guide to the health effects of vibration on the human body," Brussels, Tech. Rep. CEN Report 12349, 1996.

[27] M. Bovenzi, Low-back pain disorders and exposure to whole-body vibration in the workplace, Seminars in Perinatology 20 (1996) 38-53.

[28] S. Lings, C. Leboeuf-Yde, Whole-body vibration and low back pain: A systematic critical review of the epidemiological literature 1992-1999, International Archives of Occupational and Environmental Health 73 (2000) 290-297.

[29] M. Ekman, O. Johnell, L. Lidgren, The economic cost of low back pain in Sweden in 2001, Acta Orthopaedica 76 (2005) 275-284.

[30] H.R. Guo, S. Tanaka, W.E. Halperin, L.L. Cameron, Back pain prevalence in US industry and estimates of lost workdays, Journal of Public Health 87 (1999) 1029-1035.

[31] British Standards Institution, BS 6841 - Measurement and Evaluation of Human Exposure to Whole-Body Mechanical Vibration and Repeated Shock, 1987.

[32] S. Maeda, M. Morioka, Measurement of whole-body vibration exposure from garbage trucks, Journal of Sound and Vibration 215 (1998) 959-964.

[33] R.P. Blood, P.W. Rynell, P.W. Johnson, Vehicle design influences whole body vibration exposures: Effect of the location of the front axle relative to the cab, Journal of Occupational and Environmental Hygiene 8 (2011) 364-374.

[34] S. Milosavljevic, D.I. Mcbride, N. Bagheri, R.M. Vasiljev, R. Mani, A.B. Carman, B. Rehn, Exposure to whole-body vibration and mechanical shock: A field study of quad bike use in agriculture, Annals of Occupational Hygiene 55 (2011) 286-295.

[35] P. Xu, B. Bernardo, K. Tan, Optimal mounting design for cab vibration isolation, International Journal of Vehicle Design 57 (2011) 292-304.

[36] M. Park, T. Fukuda, T. Kim, S. Maeda, Health risk evaluation of whole-body vibration by ISO 2631-5 and ISO 2631-1 for operators of agricultural tractors and recreational vehicles. Industrial Health 51 (2013) 364-370.

[37] B. Rehn, T. Nilsson, B. Olofsson, R. Lundstrom, Whole-body vibration exposure and non-neutral neck postures during occupational use of all-terrain vehicles, Annals of Occupational Hygiene 49 (2005) 267-275.

[38] O.O. Okunribido, M. Magnusson, M.H. Pope, Low back pain in drivers: The relative role of whole-body vibration, posture and manual materials handling, Journal of Sound and Vibration 298 (2006) 540-555.

[39] I.J.H. Tiemessen, C.T.J. Hulshof, M.H.W. Frings-Dresen, Two way assessment of other physical work demands while measuring the whole body vibration magnitude, Journal of Sound and Vibration 310 (2008) 1080-1092.

[40] M. El-Gindy, An overview of performance measures for heavy commercial vehicles in north america, International Journal of Vehicle Design 16 (1995) 441-463.

[41] P. Liu, "Analysis, Detection and Early Warning Control of Dynamic Rollover of Heavy Freight Vehicles," Doctoral dissertation, Concordia University, 1999.

[42] A.G.M. Hunter, A review of research into machine stability on slopes, Safety Science 16 (1993) 325-339.

[43] M.G. Yisa, H. Terao, N. Noguchi, M. Kubota, Stability criteria for tractor-implement operation on slopes, Journal of Terramechanics 35 (1998) 1-19.

[44] J.E. Kelly, G.E. Rehkugler, Stablity criteria for operation on side slopes, ASAE Special Publication, Engineering a Safer Food Machine (1980) 145-157.

[45] N.L. Azad, A. Khajepour, J. McPhee, Effects of locking differentials on the snaking behaviour of articulated steer vehicles, International Journal of Vehicle Systems Modelling and Testing 2 (2007) 101-127.

[46] A. Rehnberg, L. Drugge, Influence of tyre properties on the ride dynamics of heavy off-road vehicles, Joint 9th Asia-Pacific ISTVS Conference and Annual Meeting of Japanese Society for Terramechanics, Sapporo, Japan, (2010) .

[47] D.A. Crolla, E.B. Maclaurin, Theoretical and practical aspects of the ride dynamics of off-road vehicles-part 1, Journal of Terramechanics 22 (1985) 17-25.

[48] A. Pazooki, S. Rakheja, D. Cao, A three–dimensional model of an articulated frame–steer vehicle for coupled ride and handling dynamic analyses, International Journal of Vehicle Performance 1 (2014) 264-297.

[49] A. Rehnberg, "Suspension design for off-road construction machine," Doctoral dissertation, KTH Royal Institute of Technology, 2011.

[50] N. L. Azad, "Dynamic modelling and stability controller development for articulated steer vehicles," Doctoral Thesis, University of Waterloo, 2006.

[51] H. B. Pacejka, Tyre and Vehicle Dynamics, Oxford: Butterworth-Heinemann, 2006.

[52] M. Gipser, R. Hofer, P. Lugner, Dynamical tyre forces response to road unevennesses, Vehicle System Dynamics 27 (1997) 94-108.

[53] X. Li, G. Wang, Z. Yao, Y. Yang, Research on lateral stability and rollover mechanism of articulated wheel loader, Mathematical and Computer Modelling of Dynamical Systems (2013) 1-16.

[54] X. Li, G. Wang, Z. Yao, J. Qu, Dynamic model and validation of an articulated steering wheel loader on slopes and over obstacles, Vehicle System Dynamics (2013) 1-19.

[55] D. Gee-Clough, Selection of tyre sizes for agricultural vehicles, Journal of Agricultural Engineering Research 25 (1980) 261-278.

[56] D.A. Crolla, Off-road vehicle dynamics, Vehicle System Dynamics 10 (1981) 253-266.

[57] H.B. Pacejka, E. Bakker, L. Nyborg, Tyre modelling for use in vehicle dynamics studies, SAE Paper no. 870421 (1987) .

[58] K. Guo, D. Lu, S. Chen, W.C. Lin, X. Lu, The UniTire model: A nonlinear and non-steady-state tyre model for vehicle dynamics simulation, Vehicle System Dynamics 43 (2005) 341-358.

[59] D.A. Crolla, D.N.L. Horton, R.M. Stayner, Effect of tyre modelling on tractor ride vibration predictions, Journal of Agricultural Engineering Research 47 (1990) 55-77.

[60] Q. Xiding, L. Jude, M. Yongxin, A modified point contact tire model for the simulation of vehicle ride quality, Journal of Terramechanics 30 (1993) 133-141.

[61] J.A. Lines, R.O. Peachey, Predicting the ride vibration of a simple unsuspended vehicle, Journal of Terramechanics 29 (1992) 207-221.

[62] D.N.L. Horton, D.A. Crolla, Handling behaviour of off-road vehicles, International Journal of Vehicle Design 5 (1984) 197-218.

[63] D.A. Crolla, A.S.A. El-Razaz, A review of the combined lateral and longitudinal force generation of tyres on deformable surfaces, Journal of Terramechanics 24 (1987) 199-225.

[64] M. McAllister, D. Gee-Clough, D. Evernden, An investigation into forces on undriven, angled wheels, National Institute of Agricultural Engineering, Departmental Note DN 1045 (1981) .

[65] G. Krick, Behaviour of tyres driven in soft ground with side slip, Journal of Terramechanics 9 (1973) 9-30.

[66] Z.J. Janosi, G. Wray, I.O. Kamm, Tire turning forces under on-and off-road conditions, 7th International Conference of International Society for Terrain-Vehicle Systems, (1981) .

[67] J. R. Ellis, Vehicle Dynamics, Business Books London, 1969.

[68] C. Oertel, On modeling contact and friction calculation of tyre response on uneven roads, Vehicle System Dynamics 27 (1997) 289-302.

[69] Y. Choi, G. Gim, Improved UA tire model as a semi-empirical model, FISITA World Automotive Congress, Seoul, Republic of Korea, (2000) F2000G383.

[70] Adams Help, "Using FTire tire model," 2010.

[71] W. Smith, H. Peng, Modeling of wheel–soil interaction over rough terrain using the discrete element method, Journal of Terramechanics 50 (2013) 277-287.

[72] K. Xia, Finite element modeling of tire/terrain interaction: Application to predicting soil compaction and tire mobility, Journal of Terramechanics 48 (2011) 113-123.

[73] M. G. Bekker, Theory of Land Locomotion: The Mechanics of Vehicle Mobility, Ann Arbor: University of Michigan Press, 1956.

[74] S. Ohkubo, A. Oida, M. Yamazaki, Application of DEM to find the interaction between tire and soil. Nogyo Kikai Gakkai Nenji Taikai Koen Yoshi 58 (1999) 483-484.

[75] R. Ma, H. Chemistruck, J.B. Ferris, State-of-the-art of terrain profile characterization models, International Journal of Vehicle Design 61 (2013) 285-304.

[76] R. Lee, C. Sandu, Terrain profile modelling using stochastic partial differential equations, International Journal of Vehicle Systems Modelling and Testing 4 (2009) 318-356.

[77] H.M. Chemistruck, J.B. Ferris, D. Gorsich, Using a galerkin approach to define terrain surfaces, Journal of Dynamic Systems, Measurement, and Control 134 (2012) 021017.

[78] ISO, 8608 Mechanical Vibration – Road Surface Profiles – Reporting of Measured Data, Geneva: 1995.

[79] J. Y. Wong, Theory of Ground Vehicles, New York: John Wiley & Sons, 2002.

[80] A. Pazooki, D. Cao, S. Rakheja, P. Boileau, Ride dynamic evaluations and design optimisation of a torsio-elastic off-road vehicle suspension, Vehicle System Dynamics 49 (2011) 1455-1476.

[81] J.L. Logdanoff, F. Kozin, L.J. Cote, Atlas of off-road ground roughness PSDs and report on data acquisition techniques, ATAC Components Research and Development Laboratories Technical Report no.9387 (LL109) (1996) .

[82] D. Ammon, Problems in road surface modelling, Vehicle System Dynamics 20 (1992) 28-41.

[83] K.M.A. Kamash, J.D. Robson, The application of isotropy in road surface modelling, Journal of Sound and Vibration 57 (1978) 89-100.

[84] A.N. Heath, Modelling and simulation of road roughness, 11th IAVSD Symposium, Kingston, (1989) 275-284.

[85] L. Sun, J. Su, Modeling random fields of road surface irregularities, Road Materials and Pavement Design 2 (2001) 49-70.

[86] H. Zhang, Computer prediction of automobile ride comfort dynamics, Automotive Engineering 8 (1986) 21-31.

[87] K. Bogsjö, Coherence of road roughness in left and right wheel-path, Vehicle System Dynamics 46 (2008) 599-609.

[88] Y. Zhang, J. Zhang, Numerical simulation of stochastic road process using white noise filtration, Mechanical Systems and Signal Processing 20 (2006) 363-372.

[89] P. Boileau, "A study of secondary suspensions and human driver response to whole-body vehicular vibration and shock," Doctoral dissertation, Concordia University, 1995.

[90] S. Rakheja, S. Sankar, Improved off-road tractor ride via passive cab and seat suspensions, Journal of Vibration Acoustics Stress and Reliability in Design 106 (1984) 305-313.

[91] S. Sankar, M. Afonso, Design and testing of lateral seat suspension for off-road vehicles, Journal of Terramechanics 30 (1993) 371-393.

[92] I. Hostens, K. Deprez, H. Ramon, An improved design of air suspension for seats of mobile agricultural machines, Journal of Sound and Vibration 276 (2004) 141-156.

[93] P. Donati, Survey of technical preventative measures to reduce whole-body vibration effects when designing mobile machinery, Journal of Sound and Vibration 253 (2002) 169-183.

[94] X.Q. Ma, S. Rakheja, C. Su, Damping requirement of a suspension seat subject to low frequency vehicle vibration and shock, International Journal of Vehicle Design 47 (2008) 133-156.

[95] I.J. Tiemessen, C.T. Hulshof, M.H. Frings-Dresen, An overview of strategies to reduce whole-body vibration exposure on drivers: A systematic review, International Journal of Industrial Ergonomics 37 (2007) 245-256.

[96] A. Achen, J. Toscano, R. Marjoram, K. St Clair, B. Mcmahon, A. Goelz, S. Shutto, Semi-active vehicle cab suspension using magnetorheological (MR) technology, Proceedings of the JFPS International Symposium on Fluid Power, (2008) 561-564.

[97] D. Hilton, P. Moran, Experiments in improving tractor operator ride by means of a cab suspension, Journal of Agricultural Engineering Research 20 (1975) 433-448.

[98] Y. Kang, W. Zhang, S. Rakheja, Relative kinematic and handling performance analyses of independent axle suspensions for a heavy-duty mining truck, International Journal of Heavy Vehicle Systems 22 (2015) 114-136.

[99] A. Rehnberg, Vehicle dynamic analysis of wheel loaders with suspended axles, Int. J. Vehicle Systems Modelling and Testing 3 (2008) 168-188.

[100] P. Hansson, Working space requirement for an agricultural tractor axle suspension, Biosystems Engineering 81 (2002) 57-71.

[101] P. Hansson, Rear axle suspensions with controlled damping on agricultural tractors, Computers and Electronics in Agriculture 15 (1996) 123-147.

[102] P.S. Els, N.J. Theron, P.E. Uys, M.J. Thoresson, The ride comfort vs. handling compromise for off-road vehicles, Journal of Terramechanics 44 (2007) 303-317.

[103] D.N.L. Horton, D.A. Crolla, Theoretical analysis of a semi active suspension fitted to an off-road vehicle, Vehicle System Dynamics 15 (1986) 351-372.

[104] D. Cao, S. Rakheja, C. Su, Roll-and pitch-plane-coupled hydro-pneumatic suspension. part 2: Dynamic response analyses, Vehicle System Dynamics 48 (2010) 507-528.

[105] R.W. Goldman, M. El-Gindy, B.T. Kulakowski, Rollover dynamics of road vehicles: Literature survey, International Journal of Heavy Vehicle Systems 8 (2001) 103-141.

[106] R. Kamnik, F. Boettiger, K. Hunt, Roll dynamics and lateral load transfer estimation in articulated heavy freight vehicles, Proceedings of the Institution of Mechanical Engineers, Part D: Journal of Automobile Engineering 217 (2003) 985-997.

[107] E. Dahlberg, A. Stensson, The dynamic rollover threshold-a heavy truck sensitivity study, International Journal of Vehicle Design 40 (2006) 228-250.

[108] J. Preston-Thomas, J. Woodrooffe, A feasibility study of a rollover warning device for heavy trucks, Transport Canada Publication no. TP 10610E (1990) .

[109] A.G. Nalecz, Z. Lu, K.L. d'Entremont, An investigation into dynamic measures of vehicle rollover propensity, SAE Technical Paper 930831 (1993) .

[110] A. Bozorgebrahimi, R. Hall, M. Morin, Equipment size effects on open pit mining performance, International Journal of Surface Mining, Reclamation and Environment 19 (2005) 41-56.

[111] R. Jois, Haul road design and road safety, QRC H&S Conference, (2011) 1-9.

[112] O.M. Gonzalez, J.C. Jauregui, A. Lozano, G. Herrera, Effect of road profile on heavy vehicles with air suspension, International Journal of Heavy Vehicle Systems 14 (2007) 98-110.

[113] MSC Adams Documentation, "Tire models contact methods," 2010.

[114] B. Duprey, M. Sayers, T. Gillespie, Simulation of the performance based standards (PBS) low-speed 90 turn test in TruckSim by jumping back in time, SAE Technical Paper 2013-01-2374 (2013) .

[115] Y. He, J. Yang and W. M. Zhang, "YCK50R design manual," University of Science and Technology Beijing, Department of Vehicle Engineering, 2011 (Unpublished).

[116] Y. He, "Performance Analysis and Parameter Optimization of Mining Truck Hydro-pneumatic Suspension Based on Ride Comfort," Doctoral Thesis, University of Science and Technology Beijing, 2013.

[117] K. Wang, "Dynamic analysis of a tracked snowplowing vehicle and assessment of ride quality," Master Thesis, Concordia University, 1998.

[118] S. Rakheja, K. Wang, R. Bhat, P.-. Boileau, Enhancement of ride vibration environment of tracked sidewalk snowploughs: Vehicle modelling and analysis, International Journal of Vehicle Design 30 (2002) 193-222.

[119] J.E. Bernard, C.L. Clover, Tire modeling for low-speed and high-speed calculations, SAE Technical Paper 950311 (1995) .

[120] ISO/TC108/SC2/WG4 N57, Reporting Vehicle Road Surface Irregularities, 1982.

[121] H.M. Ngwangwa, P.S. Heyns, Application of an ANN-based methodology for road surface condition identification on mining vehicles and roads, Journal of Terramechanics 53 (2014) 59-74.

[122] Y. Fujimoto, Spectrum analysis of road roughness for earthmoving machinery, Journal of Terramechanics 20 (1983) 43-60.

[123] M. W. Sayers, Dynamic Terrain Inputs to Predict Structural Integrity of Ground Vehicles, 1988.

[124] P. Uys, P.S. Els, M. Thoresson, Suspension settings for optimal ride comfort of off-road vehicles travelling on roads with different roughness and speeds, Journal of Terramechanics 44 (2007) 163-175.

[125] K. Shin and J. Hammond, Fundamentals of Signal Processing for Sound and Vibration Engineers, John Wiley & Sons, 2008.

[126] P. Dudziński, Design characteristics of steering systems for mobile wheeled earthmoving equipment, Journal of Terramechanics 26 (1989) 25-82.

[127] C. Altafini, Why to use an articulated vehicle in underground mining operations, Proceedings of the IEEE International Conference on Robotics and Automation, Detroit, (1999) 3020-3025.

[128] Z. Yao, G. Wang, X. Li, J. Qu, Y. Zhang, Y. Yang, Dynamic simulation for the rollover stability performances of articulated vehicles, Proceedings of the Institution of Mechanical Engineers, Part D: Journal of Automobile Engineering 228 (2014) 771-783.

[129] P. Liu, J. Caroux, Steer laws for steerable trailer axles to reduce tire wear, SAE International Journal of Commercial Vehicles 4 (2011) 31-39.

[130] M.M. Islam, Y. He, S. Zhu, Q. Wang, A comparative study of multi-trailer articulated heavy-vehicle models, Proceedings of the Institution of Mechanical Engineers, Part D: Journal of Automobile Engineering 229 (2015) 1200-1228.

[131] Y. Yin, S. Rakheja, J. Yang, P. Boileau, Analysis of a flow volume regulated frame steering system and experimental verifications, SAE Technical Paper 2015-01-2740 (2015) .

[132] A. Rehnberg, L. Drugge, A.S. Trigell, Snaking stability of articulated frame steer vehicles with axle suspension, International Journal of Heavy Vehicle Systems 17 (2010) 119-138.

[133] L. Chen, Y. Shieh, Jackknife prevention for articulated vehicles using model reference adaptive control, Proceedings of the Institution of Mechanical Engineers, Part D: Journal of Automobile Engineering 225 (2011) 28-42.

[134] S. S. Rao, Mechanical Vibrations, Prentice Hall, 2010.

[135] R. Sharp, M.A. Fernandez, Car-caravan snaking: Part 1: The influence of pintle pin friction, Proceedings of the Institution of Mechanical Engineers, Part C: Journal of Mechanical Engineering Science 216 (2002) 707-722.

[136] J. Darling, D. Tilley, B. Gao, An experimental investigation of car—trailer high-speed stability, Proceedings of the Institution of Mechanical Engineers, Part D: Journal of Automobile Engineering 223 (2009) 471-484.

[137] W. Wang, D. Yu, Y. Huang, Z. Zhou, R. Xu, A locomotive's dynamic response to in-service parameter variations of its hydraulic yaw damper, Nonlinear Dynamics 77 (2014) 1485-1502.

[138] W. Smith, N. Zhang, Hydraulically interconnected vehicle suspension: Optimization and sensitivity analysis, Proceedings of the Institution of Mechanical Engineers, Part D: Journal of Automobile Engineering 224 (2010) 1335-1355.

[139] W. Sochacki, Modelling and analysis of damped vibration in hydraulic cylinder, Mathematical and Computer Modelling of Dynamical Systems 21 (2015) 23-37.

[140] B. Nau, An historical review of studies of polymeric seals in reciprocating hydraulic systems, Proceedings of the Institution of Mechanical Engineers, Part J: Journal of Engineering Tribology 213 (1999) 215-226.

[141] G.K. Nikas, R.S. Sayles, Study of leakage and friction of flexible seals for steady motion via a numerical approximation method, Tribology International 39 (2006) 921-936.

[142] J. Dixon, The Shock Absorber Handbook, John Wiley & Sons, 2008.

[143] F. Han, Personal communications – steering valve flow characteristics, Xuzhou Construction Machinery Group (XCMG) China (2014 (Unpublished)) .

[144] X. Ding, S. Mikaric, Y. He, Design of an active trailer-steering system for multi-trailer articulated heavy vehicles using real-time simulations, Proceedings of the Institution of Mechanical Engineers, Part D: Journal of Automobile Engineering 227 (2013) 643-655.

[145] J. Yang, B. Zhang and W. M. Zhang, Design Manual of the 35 T Articulated Mining Dump Truck, Document, University of Science and Technology Beijing, Beijing, People's Republic of China: 2013.

[146] Y. Yin, S. Rakheja, J. Yang, P. Boileau, Effect of articulated frame steering on the transient yaw responses of the vehicle, Proceedings of the Institution of Mechanical Engineers, Part D: Journal of Automobile Engineering (2017) 0954407017702987.

[147] Q. Wei, B. Zhu, B. Jing, H. Liu, M. Liu, Optimization design of loader steering mechanism based on MATLAB, IEEE 10th International Conference on Computer-Aided Industrial Design & Conceptual Design, Wenzhou, (2009) 751-754.

[148] Z. Zhao, J. Wang, Fuzzy optimal design of articulated dump truck's steering mechanism, 2011 International Conference on Consumer Electronics, Communications and Networks (CECNet), XianNing, (2011) 4093-4096.

[149] B.K.S. Thulasiraman, G. Arumugam, N.G. Sadali, I. Neelamegan, Steering linkage optimization of articulated construction equipment, The 1st International and 16th National Conference on Machines and Mechanisms (iNaCoMM2013), IIT Roorkee, India, (2013) 404-411.

[150] R.T. Marler, J.S. Arora, Survey of multi-objective optimization methods for engineering, Structural and Multidisciplinary Optimization 26 (2004) 369-395.

[151] I.Y. Kim, O. De Weck, Adaptive weighted-sum method for bi-objective optimization: Pareto front generation, Structural and Multidisciplinary Optimization 29 (2005) 149-158.

[152] R.T. Marler, J.S. Arora, The weighted sum method for multi-objective optimization: New insights, Structural and Multidisciplinary Optimization 41 (2010) 853-862.

[153] Y. He, M.M. Islam, S. Zhu, T. Hu, A design synthesis framework for directional performance optimization of multi-trailer articulated heavy vehicles with trailer lateral dynamic control systems, Proceedings of the Institution of Mechanical Engineers, Part D: Journal of Automobile Engineering 0 (2016) 1-30.

[154] T.L. Saaty, Decision-making with the AHP: Why is the principal eigenvector necessary, European Journal of Operational Research 145 (2003) 85-91.

[155] N.L. Azad, A. Khajepour, J. McPhee, Analysis of jackknifing in articulated steer vehicles, Vehicle Power and Propulsion, (2005) 86-90.

[156] J. Yu, Z. Chen, Y. Lu, The variation of oil effective bulk modulus with pressure in hydraulic systems, Journal of Dynamic Systems, Measurement, and Control 116 (1994) 146-150.

[157] S. Kim, H. Murrenhoff, Measurement of effective bulk modulus for hydraulic oil at low pressure, Journal of Fluids Engineering 134 (2012) 021201.

[158] J. Lee, H. Shin, H. Jo, A study of the effects of entrained air in a hydraulic brake actuator, Proceedings of the Institution of Mechanical Engineers, Part D: Journal of Automobile Engineering 222 (2008) 285-292.

[159] T.L. Saaty, A scaling method for priorities in hierarchical structures, Journal of Mathematical Psychology 15 (1977) 234-281.

[160] J. Arora, Introduction to Optimum Design, Academic Press, 2004.

[161] Matlab R2016b, "Simulink Design Optimization Documentation," 2016.

[162] K.R. Davey, Latin hypercube sampling and pattern search in magnetic field optimization problems, IEEE Transactions on Magnetics 44 (2008) 974-977.

[163] M. Franchini, G. Galeati, S. Berra, Global optimization techniques for the calibration of conceptual rainfall-runoff models, Hydrological Sciences Journal 43 (1998) 443-458.

[164] D. Cao, S. Rakheja, C. Sandu, Special issue on interdisciplinary aspects of vehicle system dynamics integration, 25 (2011) e1-e3.

[165] D. Cao, X. Song, M. Ahmadian, Editors' perspectives: Road vehicle suspension design, dynamics, and control, Vehicle System Dynamics 49 (2011) 3-28.

[166] C. Lee, B. Moon, Simulation and experimental validation of vehicle dynamic characteristics for displacement-sensitive shock absorber using fluid-flow modelling, Mechanical Systems and Signal Processing 20 (2006) 373-388.

[167] A. Rehnberg, L. Drugge, Ride comfort simulation of a wheel loader with suspended axles, International Journal of Vehicle Systems Modelling and Testing 3 (2008) 168-188.

[168] Y. Yin, S. Rakheja, P. Boileau, A roll stability performance measure for off-road vehicles, Journal of Terramechanics 64 (2016) 58-68.

[169] W.A. Smith, N. Zhang, W. Hu, Hydraulically interconnected vehicle suspension: Handling performance, Vehicle System Dynamics 49 (2011) 87-106.

[170] H. Ren, S. Chen, Y. Zhao, G. Liu, L. Yang, State observer-based sliding mode control for semi-active hydro-pneumatic suspension, Vehicle System Dynamics 54 (2016) 168-190.

[171] X. Sun, C. Yuan, Y. Cai, S. Wang, L. Chen, Model predictive control of an air suspension system with damping multi-mode switching damper based on hybrid model, Mechanical Systems and Signal Processing 94 (2017) 94-110.

[172] K. Guo, Y. Chen, Y. Yang, Y. Zhuang, Y. Jia, Modeling and simulation of a hydro-pneumatic spring based on internal characteristics, Second International Conference on Mechanic Automation and Control Engineering, Hohhot, (2011) 5910-5915.

[173] J. Yang, J.F. Zhao, Y.H. Shen, C.Y. Duan, Influence of variety of oil temperature on performance of hydro-pneumatic suspension, Applied Mechanics and Materials, (2011) 705-710.

[174] P. Els, B. Grobbelaar, Heat transfer effects on hydropneumatic suspension systems, Journal of Terramechanics 36 (1999) 197-205.

[175] Y. Shen, J. Zhao, J. Yang, X. Huang, Research on test and simulation of hydro-pneumatic suspension, International Conference on Consumer Electronics, Communications and Networks (CECNet), (2011) 678-681.

[176] P. Czop, D. SŁawik, A high-frequency first-principle model of a shock absorber and servo-hydraulic tester, Mechanical Systems and Signal Processing 25 (2011) 1937-1955.

[177] H. Gholizadeh, D. Bitner, R. Burton, G. Schoenau, Modeling and experimental validation of the effective bulk modulus of a mixture of hydraulic oil and air, Journal of Dynamic Systems, Measurement, and Control 136 (2014) 051013.

[178] D. Cao, S. Rakheja, C. Su, Pitch plane analysis of a twin-gas-chamber strut suspension, Proceedings of the Institution of Mechanical Engineers, Part D: Journal of Automobile Engineering 222 (2008) 1313-1335.

[179] S.F. Van Der Westhuizen, P.S. Els, Comparison of different gas models to calculate the spring force of a hydropneumatic suspension, Journal of Terramechanics 57 (2015) 41-59.

[180] K. Küçük, H.K. Yurt, K.B. Arıkan, H. İmrek, Modelling and optimization of an 8× 8 heavy duty vehicle's hydro-pneumatic suspension systemMpa, International Journal of Vehicle Design 71 (2016) 122-138.

[181] J. Swevers, F. Al-Bender, C.G. Ganseman, T. Projogo, An integrated friction model structure with improved presliding behavior for accurate friction compensation, IEEE Transactions on Automatic Control 45 (2000) 675-686.

[182] F. Al-Bender, V. Lampaert, J. Swevers, The generalized maxwell-slip model: A novel model for friction simulation and compensation, IEEE Transactions on Automatic Control 50 (2005) 1883-1887.

[183] M. Ruderman, T. Bertram, Two-state dynamic friction model with elasto-plasticity, Mechanical Systems and Signal Processing 39 (2013) 316-332.

[184] B. Armstrong and C. C. Wit, Friction Modeling and Compensation, CRC Press, 1995.

[185] MathWorks, "Friction in contact between moving bodies," *Matlab R2016b Documentation,* 2016.

[186] N.L. Azad, A. Khajepour, J. Mcphee, Robust state feedback stabilization of articulated steer vehicles, Vehicle System Dynamics 45 (2007) 249-275.

[187] T.H. Langer, T.K. Iversen, O.Ø Mouritsen, M.K. Ebbesen, M.R. Hansen, Suspension system performance optimization with discrete design variables, Structural and Multidisciplinary Optimization 47 (2013) 621-630.

[188] T.H. Langer, B.B. Christensen, O.Ø Mouritsen, M.R. Hansen, Optimization of front axle suspension system of articulated dump truck, 1st Joint International Conference on Multibody System Dynamics, (2010) .

[189] Y. Yin, S. Rakheja, J. Yang, P. Boileau, Characterization of a hydro-pneumatic suspension strut with gas-oil emulsion, Mechanical Systems and Signal Processing (2017 (submitted)) .

[190] MSC Software, "ADAMS help documentation," 2013.